ZR

ISSN 2095-8137 CN 53-1229/Q

Volume **41** Issue **2**
18 March **2020**

Zoological Research

Science Press

CODEN: DOYADI
www.zoores.ac.cn

ZOOLOGICAL RESEARCH

Volume 41, Issue 2 18 March 2020

CONTENTS

Review

Articles

Reports

Letters to the editor

Cover image: 9.4 T MRI of a rhesus macaque (*Macaca mulatta*) brain in the horizontal plane. Illustration by Huan-Zhi Chen

Cover design: Yang Niu

Zoological Research Website:http://www.zoores.ac.cn/

ZOOLOGICAL RESEARCH

Deciphering the puzzles of dog domestication

Zhe Zhang[1], Saber Khederzadeh[2,3], Yan Li[1,*]

[1] *State Key Laboratory for Conservation and Utilization of Bio-Resources in Yunnan*, *School of Life Sciences*, *Yunnan University*, *Kunming*, *Yunnan* 650091, *China*

[2] *State Key Laboratory of Genetic Resources and Evolution*, *Germplasm Bank of Wild Species*, *Kunming Institute of Zoology*, *Chinese Academy of Sciences*, *Kunming*, *Yunnan* 650223, *China*

[3] *Kunming College of Life Science*, *University of Chinese Academy of Sciences*, *Kunming*, *Yunnan* 650204, *China*

ABSTRACT

The domestic dog, as a highly successful domestication model, is well known as a favored human companion. Exploring its domestication history should provide great insight into our understanding of the prehistoric development of human culture and productivity. Furthermore, investigation on the mechanisms underpinning the morphological and behavioral traits associated with canid domestication syndrome is of significance not only for scientific study but also for human medical research. Current development of a multidisciplinary canine genome database, which includes enormous omics data, has substantially improved our understanding of the genetic makeup of dogs. Here, we reviewed recent advances associated with the original history and genetic basis underlying environmental adaptations and phenotypic diversities in domestic dogs, which should provide perspectives on improving the communicative relationship between dogs and humans.

Keywords: Dog; Domestication history; Adaptation; Phenotypic diversity, Domestic legacy

INTRODUCTION

Dogs, as the first domesticated mammal, have interacted with humans for thousands of years (Freedman & Wayne, 2017). This domestication occurred in two main phases: the initial domestication of the wild gray wolf to primary dog and the subsequent improvement of these indigenous dogs into various modern breeds. In the first phase, highly specific behaviors valued by nomadic hunter-gatherer societies, such as tracking and consuming prey, drove the initial evolution of primary dogs at the beginning of domestication (Ostrander et al., 2017). During this process, selection was not the only mechanism of evolution, as genetic drift likely also caused fit, unfit, or neutral alleles to become fixed due to bottleneck or founder effects (Doebley, 1989; Eyre-Walker et al., 1998). Moreover, features commonly associated with domestication were not selected directly but rather represented side effects of the relaxation of selection (Dobney & Larson, 2006). For example, domestication relaxed the selective pressure on male dogs to compete for mates. Thus, genes involved in producing traits relevant to this endeavor were no longer under selective pressure and thus became effectively neutral or even detrimental as they involved the diversion of resources from traits under selection such as tameness. With the advent of agricultural societies, dogs adapted to the introduction of starch within their diets, a crucial step in their evolution from the wolf (Arendt et al., 2016). Over the past few hundred years, phenotypic radiation among domesticated

---

Received: 05 July 2019; Accepted: 06 January 2020; Online: 09 January 2020

Foundation items: This work was supported by the Second Tibetan Plateau Scientific Expedition and Research (STEP) Program (2019QZKK0501), Strategic Priority Research Program of the Chinese Academy of Sciences (XDA2004010302), and National Natural Science Foundation of China (31860305). Y.L. was supported by the Young Academic and Technical Leader Raising Foundation of Yunnan Province

*Corresponding author, E-mail: liyan0910@ynu.edu.cn

DOI: 10.24272/j.issn.2095-8137.2020.002

dogs accelerated the breeding process, resulting in the development of nearly 400 breeds to fulfill specialized functions in human society, with clear morphological and behavioral differences, such as big or small, lean or squat, and independent or loyal (Freedman & Wayne, 2017). This breeding improvement was largely shaped by the extreme influence of artificial selection, with a dramatic increase in deleterious alleles, i.e., “domestic cost” (Cruz et al., 2008). The tremendous diversity in the morphology and behavior of present-day breeds illuminates the power and appeal of artificial selection, which has been widely used over a long period and exhibits inestimable potential.

Domestic dogs have spread to every corner of the world following human migration and thus adapted to highly distinct environments. This long-term accompaniment has not only promoted a much closer relationship between humans and dogs than with any other domesticated animal, but also similar genetics underlying as many as 360 diseases suffered by both, especially mental diseases (e.g., canine compulsive disorder, Alzheimer’s disease, epilepsy) (De Risio et al., 2015; Dewey et al., 2019; Ostrander et al., 2017; Shearin & Ostrander, 2010b), which may partially result from the same natural environmental pressures and similar social exposure. Therefore, dogs are good models for both evolutionary and pathological research.

Integrating molecular phylogenetics, bioinformatics, and biotechnology has helped to decipher puzzles about dog domestication history. Here, we summarized the progress of dog domestication, including the timing and origin, adaptation to different local environments, and genetic basis underlying phenotypic diversity, to highlight our current understanding of dog domestication and provoke enthusiasm for further breeding according to genetic information.

ORIGIN OF DOGS

Archaeological evidence demonstrates that the dog has been a human companion since the Mesolithic Age. Genomic sequencing data also suggest that initial dog domestication predated the advent of agriculture, occurring instead alongside hunter-gatherers (Freedman et al., 2014). Both genetic and phenotypic research has clearly demonstrated that the dog originated from an extinct gray wolf population and was domesticated in the Old World (Fan et al., 2016). However, there is ongoing debate regarding the geographic origin of monophylogeny or polyphylogeny due to discrepancies in study ideas and methods. Fortunately, growing evidence is shedding light on the origin and evolutionary trajectories of dogs.

Vilà and colleagues investigated dog origin based on mtDNA control region sequences and were the first to suggest a polyphyly origin from multiple ancestral wolf populations with backcrossing events after initial domestication (Vilà et al., 1997). Alternatively, Savolainen et al. (2002) proposed East Asia as the single origin center some 15 000 years ago due to the presence of rich genetic and phylogeographic variations and as the origin of the Australian Dingo (Savolainen et al., 2004). Furthermore, evidence also suggests that native American dogs originated from Old World dogs that crossed the Bering Strait following human activity during the late Pleistocene (Leonard et al., 2002). Although evidence that mtDNA haplotypes from African village dogs are as diverse as those from East Asia challenges the East Asian origin hypothesis (Boyko et al., 2009), this hypothesis is supported by previous diversity analyses on mitochondrial and Y chromosomes from an almost exhaustive sampling (Ding et al., 2012; Pang et al., 2009).

However, the East Asian origin hypothesis has been rebutted by nuclear genomic single nucleotide polymorphic (SNP) analysis, which supports a Mid-Asian origin (Vonholdt et al., 2010). The Mid-Asian origin hypothesis relies on two findings: (1) breeds of East Asian origin do not have the highest level of nuclear variability; and (2) most breeds share most haplotypes with Middle Eastern wolves. Nevertheless, this conclusion has been weakened by a lack of village dogs from the Yangtze River where the uniparentally inherited markers present the most genetic diversity (Ding et al., 2012; Pang et al., 2009) and by the significant bias of SNPs designed by array technology. Another study based on canid samples from Africa, Asia, Europe, the Middle East, and North America disproved the East Asian origin hypothesis through genomic resequencing analysis (Fan et al., 2016). However, subsequent genomic resequencing of canid samples across the Eurasian mainland elucidated an “Out of Southern East Asia” migration route, thus emphasizing an East Asian origin and predating the beginning of domestication by ~33 000 years ago (Wang et al., 2016). Research on ancient DNA has also suggested that the dog may have been domesticated independently in Eastern and Western Eurasia from distinct wolf populations. Western Eurasian dogs were then partially replaced by Eastern dogs following Near Eastern Neolithic farmer expansion into Europe (Frantz et al., 2016; Ollivier et al., 2018). American dogs likely originated in East Asia and dispersed into the Americas alongside people (Ni Leathlobhair et al., 2018), but they almost completely disappeared after the arrival of Europeans, leaving the closest detectable genetic legacy of canine transmissible venereal tumor to an individual 8 000 years ago.

Taken together, genetic material following different inheritance rules has been used to infer the origin of dogs. Genetic markers on mitochondrial DNA (mtDNA) and Y chromosomes are stably inherited from their maternal lineage and paternal lineage, respectively, which facilitates investigation of gene flow from maternal and paternal ancestors. However, the absence (or near absence) of recombination and the sensitivity of genetic drift make these markers defective at deciphering exact demographic history. Whole genomic SNP data have provided more information, especially on gene flow and incomplete lineage sorting (ILS), for phylogenetic reconstruction, resulting in inconsistent results to those obtained by mtDNA or Y chromosomes for dog domestication (Ding et al., 2012; Savolainen et al., 2002;

Vilà et al., 1997; Vonholdt et al., 2010). Fortunately, recent research incorporating different inherited markers has provided more convincing clues on the evolution of wild animals like mosquitoes and domestic animals like dogs and cattle (Frantz et al., 2016; Thawornwattana et al., 2018; Wu et al., 2018). Therefore, the incorporation of different genetic markers, in combination with large-scale samples across diverse geographic regions and time points, high-depth sequencing data, and the development of more advanced methodologies, will improve our understanding of the evolutionary origin and genetic makeup of dogs.

ADAPTATION TO DIFFERENT ENVIRONMENTS

The dog, which shares a closer relationship to humans than any other domestic animal, dispersed across the entire world following man and adapted to diverse local environments over a relatively short time period. The genetic mechanisms underlying adaptation have been widely considered by biologists. Here, we summarize the two main drivers: i.e., dietary change and environmental adaptation.

In the process of wolf to dog transformation, diet is thought to have played a crucial role. Unlike wolves, dogs can thrive on a diet rich in starch. Ten genes involved in digestion and fatty acid metabolism evolved rapidly during the domestication of dogs (Axelsson et al., 2013), providing evidence for domestication-induced changes in diet. Three genes (*AMY2B*, *MGAM*, *SGLT1*) have been identified as selective candidates that play key roles in the breakdown of starch. Different dog breeds possess a varying ability to process starch, which may be associated with copy number variations of the *AMY2B* gene influencing amylase activity (Arendt et al., 2014). The changes in *AMY2B* copy number in native dogs, modern breeds, and wolves across the world illustrate that a diet change involved a secondary shift, consistent with the development and spread of prehistoric agriculture in most parts of the world, rather than a single occurrence during initial domestication (Arendt et al., 2016).

In addition, environmental adaptation has also attracted the attention of biologists. The Tibetan Mastiff, which is a local breed native to the Tibetan plateau, has evolved special phenotypic traits adapted to high-altitude environments. Analysis of SNP array data has revealed several genes with selective signatures in the Tibetan Mastiff, especially the *EPAS1* gene, which is reported to influence environmental adaptation in Tibetan residents (Li et al., 2014b). Genomic resequencing of dogs from different altitudes has indicated that a G305S variant and non-synonymous mutations in *EPAS1* may decrease vascular resistance and thus promote oxygen transport (Gou et al., 2014). EPAS1 and HBB have further been identified as candidates for convergent hemoglobin adaptations to hypoxia between Tibetan people and the Tibetan dog (Wang et al., 2014). From the perspective of the X chromosome, which has been neglected in previous studies, the haplotype frequency of the *AMOT* gene is significantly correlated with altitude (Wu et al., 2016). Moreover, genome-wide scanning of the Tibetan Mastiff and Tibetan wolf indicate genetic introgression on *EPAS1* and *HBB* loci, implying the possibility that the Tibetan Mastiff acquired local adaptation quickly by secondary contact with its wild relative, the Tibetan wolf, although no such evidence has been found on the *AMOT* locus (Miao et al., 2017).

Another classic adaptation to the environment is the African dog's adaptation to malaria, which is pervasive on the African continent. Dogs migrated into Africa about 14 000 years ago. Liu et al. (2018) explored the genetic basis of adaptation to the tropical African environment through whole genome analyses of African indigenous dogs from Nigeria. Among the positively selected genes associated with immunity, angiogenesis, ultraviolet protection, as well as insulin secretion and sensitivity, the gene *ADGRE1* was found to confer African dogs with defense against *Plasmodium* infection (Liu et al., 2018). This gene is also associated with human immune response to malaria (Kariuki et al., 2013). Therefore, these results provide new clues on the convergent adaptation and evolution between humans and dogs.

PHENOTYPIC DIVERSITY AND DOMESTIC LEGACY OF MODERN BREEDS

With the development of human society and advancement of the industrial revolution, the demands of people became increasingly diverse, with bog breeding positively selected for two primary functions. First, certain dogs were bred to perform specific tasks to assist their human companions based on their distinct behaviors and functions. Second, other dogs were bred as ornamental pets to be integrated into human families. Presently, there are more than 400 dog breeds, which possess different morphological and behavioral characteristics. Here, we review their phenotypic diversity by examining behavioral and morphological phenotypes separately.

Behavioral phenotypes

Dog breeds are classified into seven groups according to their guarding, herding, obedience, and hunting abilities: i.e., gundogs, working dogs, herding dogs, hounds, terriers, and companion dogs. These behavioral traits have become fixed within breeds due to intensive artificial selection and are considered inheritable, as cross-bred dogs exhibit intermediate behavior from their purebred parents. A survey of over 10 000 German shepherd and Rottweiler individuals revealed a genetic contribution to 16 assessed behavioral traits (Saetre et al., 2006). Further genomic analysis also found the dopamine receptor to be associated with aggressive behavior among canine breeds (Ito et al., 2004). Canine compulsive disorder (CCD) is common in many breeds and exhibits a mechanism like that of human obsessive-compulsive disorder (OCD). The cadherin 2 (*CDH2*) gene is a crucial factor associated with CCD in Doberman pinschers (Dodman et al., 2010; Tang et al., 2014). Interestingly, variants in the *CDH2* gene may also contribute to OCD and Tourette disorder in humans (Moya et al., 2013). Moreover, population genetic analysis has suggested that *CDH2* influences circling behavior in Belgian Malinois (Cao et al., 2014).

In addition to the breed traits mentioned above, the behavioral transformation from fear-aggressiveness to tameness is believed to have been a prerequisite to initial dog domestication. An experiment on silver foxes reconstructed this behavioral transformation in a domestication model (Lindberg et al., 2005; Saetre et al., 2004) and several genetic loci were found to be associated with this change (Kukekova et al., 2011; Spady & Ostrander, 2007). However, intensive breeding and selection only occurred very recently in dogs, resulting in an extremely small gene pool, which may have led to misconception about the genetic changes associated with behavioral transformation. Several studies have focused on the Chinese indigenous dog, an outbred dog living in the original center of Asia that shows the most robust genetic diversity and is assumed to be closest to the primary dog. Genomic analysis on this outbred dog revealed the genetic basis for the rewiring of dog brains and convergent evolution between dogs and humans (Li et al., 2013, 2014a; Lindberg et al., 2005; Saetre et al., 2004; Wang et al., 2013).

Morphological diversity

The genetic mechanisms underlying the morphological differences among dogs have been deeply researched as morphological traits are easily observed and estimated. Parallel studies on morphological characters from model animals such as mice and humans have also revealed the genetic underpinnings of morphological diversity in dogs.

Body size, one of the most important quantitative traits under evolutionary scrutiny, varies more in dogs than in any other terrestrial mammal. For example, the Cane Corso and Yorkshire demonstrate a 30-fold difference in body size (Shearin & Ostrander, 2010a). Research on the Portuguese water dog identified insulin-like growth factor 1 (*IGF1*) as the gene that controls body size (Sutter et al., 2007), as also reported in mice and humans (Baker et al., 1993; Woods et al., 1996, 1997). Variants of fibroblast growth factor 4 (*FGF4*) are the cause of short legs in many breeds and are correlated with chondrodysplasia (Parker et al., 2009). Unlike the results from association mapping of quantitative traits in humans and domesticated plants, a simple genetic architecture appears to underlie morphological variation in dogs (Boyko et al., 2010). For example, integrative research on multiple breeds found that six genes (*GHR*, *HMGA2*, *SMAD2*, *STC2*, *IGF1*, and *IGF1R*) explain almost half of size variation in dog breeds with standard body weight (BSW) <41 kg (Rimbault et al., 2013). Moreover, a study of the X chromosome identified three genes (*IRS4*, *IGSF1*, and *ACSL4*) as responsible for body size variation in dogs with BSW >41 kg (Plassais et al., 2017).

Skull shape is another significant morphological trait found to be highly diversified among dog breeds. Analysis of skull shape among 374 dogs identified *SMOC2* as a crucial gene explaining approximately 36% of facial length variation (Marchant et al., 2017). Previous study on skull morphology associations also identified *BMP3* as a causative gene affecting cranial development and linked with brachycephaly in some breeds such as the pug and bulldog (Schoenebeck et al., 2012).

Dogs also exhibit tremendous coat diversity since their separation from their gray wolf ancestor. Whole-genome association analysis of 80 dog breeds identified three genes (*RSPO2*, *FGF5*, and *KRT71*) with an effect on coat growth, length, and curl (Cadieu et al., 2009). Furthermore, variants in the forkhead box transcription factor family (*FOX13*), which influence ectodermal development, are thought to be responsible for the hairless traits in Mexican and Peruvian hairless dogs and Chinese crested dogs (Drogemuller et al., 2008).

Three genes, namely agouti (*ASIP*), melanocortin 1 receptor (*MC1R*), and beta-defensin 103 (*CBD103*), are thought to encode the ligand-receptor system that controls pigment type-switching in dogs (Candille et al., 2007). The latter gene (*CBD103*), previously recognized as a component of innate immunity in most vertebrates, is predicted to play roles in functions associated with the melanocortin pathway in domestic dogs. More interestingly, North American wolves derived an allele in *CBD103*, resulting in a black coat color phenotype, through genetic introgression from dogs >500 years ago (Anderson et al., 2009). In addition, the *TYRP1*, *MITF*, and *SILV* genes are also thought to influence phenotypes like brown color, white spotting, and merle patterning (Clark et al., 2006; Karlsson et al., 2007; Schmutz et al., 2002). Detailed information about the allele patterns of genes involved in coat color and their associated phenotypes can be found in a previous review (Schmutz & Berryere, 2007).

Domestic legacy

During the progression of dog domestication, both the relaxation of selective pressure and accumulation of deleterious mutations from the hitchhiking-effect caused domestic legacy. On the one hand, breeders focused on the purification of varieties and ignored disease resistance in purebred dogs. Reduction in effective population size, mainly caused by breed purification, increased the fixation probability for many weakly deleterious mutations located close to functional loci under strong artificial selection (Cruz et al., 2008). On the other hand, selectively retained pleiotropic genes increased the risk of genetic diseases. For example, coat color-related sensorineural deafness has been widely described in numerous dog breeds (Webb & Cullen, 2010), and brachycephaly (flat-face) is commonly observed in breeds like the English bulldog, French bulldog, pug, Boston terrier, Pekingese, boxer, Shi Tzu and Cavalier King Charles spaniel (Dupre & Heidenreich, 2016). In addition, continuous circling, Alzheimer's disease, and epilepsy, which impact physical and mental wellbeing, are also commonly observed in dogs (De Risio et al., 2015; Dewey et al., 2019; Moon-Fanelli & Dodman, 1998). Therefore, a more detailed and robust understanding of the genomic make-up of dogs is required for ongoing breeding strategies to satisfy both changing human demands and increased ethical concerns regarding dog welfare.

CONCLUSIONS

With the development of sequencing technologies and decrease in associated costs, high-quality sequencing data can now provide much deeper insights into the evolutionary history of dogs. In addition, improvements in data exchange within canine research communities have helped elucidate the genetic mechanisms underpinning heredity and variation. For example, the International Dog10K Genomes Project, which started in 2015, has produced enormous -omics data of dog breeds from around the world. The Dog Genome SNP Database (DoGSD) has also provide information on the differences between dog and wolf genomes (Bai et al., 2015). In addition to the genomic databases, international dog clubs have also provided phenotypic information on more than 400 dog breeds (Ostrander et al., 2017). The iDog integrated resource not only contains all the information mentioned above (Tang et al., 2019), which incorporates sequence alignment tools and genome browsers, but can also supply the global dog research community with genomic sequence assemblies, genomic variations, phenotypic/disease traits, gene expression profiles, gene ontology, and homolog gene information. These resources will promote our understanding of the evolutionary and genetic mechanisms of domestic dogs and help elucidate the genetic underpinnings of human genetic diseases. Finally, as man's best friend, dogs deserve more attention and responsibility to promote their welfare. Dog owners should acquire professional knowledge on the different physical states of their companion. Veterinary associations should also help with the introduction of new policies, edicts, regulations, and positive humane solutions to benefit dogs.

COMPETING INTERESTS

The authors declare that they have no competing interests.

AUTHORS' CONTRIBUTIONS

Y.L proposed the research ideas and revised the manuscript. Z.Z. and S.K. reviewed the literature and drafted the manuscript. All authors read and approved the final version of the manuscript.

REFERENCES

Anderson TM, vonHoldt BM, Candille SI, Musiani M, Greco C, Stahler DR, Smith DW, Padhukasahasram B, Randi E, Leonard JA, Bustamante CD, Ostrander EA, Tang H, Wayne RK, Barsh GS. 2009. Molecular and evolutionary history of melanism in North American gray wolves. *Science*, **323**(5919): 1339−1343.

Arendt M, Cairns KM, Ballard JWO, Savolainen P, Axelsson E. 2016. Diet adaptation in dog reflects spread of prehistoric agriculture. *Heredity (Edinb)*, **117**(5): 301−306.

Arendt M, Fall T, Lindblad-Toh K, Axelsson E. 2014. Amylase activity is associated with AMY2B copy numbers in dog: implications for dog domestication, diet and diabetes. *Animal Genetics*, **45**(5): 716−722.

Axelsson E, Ratnakumar A, Arendt ML, Maqbool K, Webster MT, Perloski M, Liberg O, Arnemo JM, Hedhammar Å, Lindblad-Toh K. 2013. The genomic signature of dog domestication reveals adaptation to a starch-rich diet. *Nature*, **495**(7441): 360−364.

Bai B, Zhao WM, Tang BX, Wang YQ, Wang L, Zhang Z, Yang HC, Liu YH, Zhu JW, Irwin DM, Wang GD, Zhang YP. 2015. DoGSD: the dog and wolf genome SNP database. *Nucleic Acids Research*, **43**(D1): D777−D783.

Baker J, Liu JP, Robertson EJ, Efstratiadis A. 1993. Role of insulin-like growth factors in embryonic and postnatal growth. *Cell*, **75**(1): 73−82.

Boyko AR, Boyko RH, Boyko CM, Parker HG, Castelhano M, Corey L, Degenhardt JD, Auton A, Hedimbi M, Kityo R, Ostrander EA, Schoenebeck J, Todhunter RJ, Jones P, Bustamante CD. 2009. Complex population structure in African village dogs and its implications for inferring dog domestication history. *Proceedings of the National Academy of Sciences of the United States of America*, **106**(33): 13903−13908.

Boyko AR, Quignon P, Li L, Schoenebeck JJ, Degenhardt JD, Lohmueller KE, Zhao K, Brisbin A, Parker HG, vonHoldt BM, Cargill M, Auton A, Reynolds A, Elkahloun AG, Castelhano M, Mosher DS, Sutter NB, Johnson GS, Novembre J, Hubisz MJ, Siepel A, Wayne RK, Bustamante CD, Ostrander EA. 2010. A simple genetic architecture underlies morphological variation in dogs. *PLoS Biology*, **8**(8): e1000451.

Cadieu E, Neff MW, Quignon P, Walsh K, Chase K, Parker HG, VonHoldt BM, Rhue A, Boyko A, Byers A, Wong A, Mosher DS, Elkahloun AG, Spady TC, AndréC, Lark KG, Cargill M, Bustamante CD, Wayne RK, Ostrander EA. 2009. Coat variation in the domestic dog is governed by variants in three genes. *Science*, **326**(5949): 150−153.

Candille SI, Kaelin CB, Cattanach BM, Yu B, Thompson DA, Nix MA, Kerns JA, Schmutz SM, Millhauser GL, Barsh GS. 2007. A β-defensin mutation causes black coat color in domestic dogs. *Science*, **318**(5855): 1418−1423.

Cao X, Irwin DM, Liu YH, Cheng LG, Wang L, Wang GD, Zhang YP. 2014. Balancing selection on CDH2 may be related to the behavioral features of the belgian malinois. *PLoS One*, **9**(10): e110075.

Clark LA, Wahl JM, Rees CA, Murphy KE. 2006. Retrotransposon insertion in SILV is responsible for merle patterning of the domestic dog. *Proceedings of the National Academy of Sciences of the United States of America*, **103**(5): 1376−1381.

Cruz F, Vilà C, Webster MT. 2008. The legacy of domestication: accumulation of deleterious mutations in the dog genome. *Molecular Biology and Evolution*, **25**(11): 2331−2336.

De Risio L, Bhatti S, Muñana K, Penderis J, Stein V, Tipold A, Berendt M, Farqhuar R, Fischer A, Long S, Mandigers PJ, Matiasek K, Packer RM, Pakozdy A, Patterson N, Platt S, Podell M, Potschka H, Batlle MP, Rusbridge C, Volk HA. 2015. International veterinary epilepsy task force consensus proposal: diagnostic approach to epilepsy in dogs. *BMC Veterinary Research*, **11**: 148.

Dewey CW, Davies ES, Xie H, Wakshlag JJ. 2019. Canine cognitive dysfunction: pathophysiology, diagnosis, and treatment. *Veterinary Clinics of North America-Small Animal Practice*, **49**(3): 477−499.

Ding ZL, Oskarsson M, Ardalan A, Angleby H, Dahlgren LG, Tepeli C, Kirkness E, Savolainen P, Zhang YP. 2012. Origins of domestic dog in Southern East Asia is supported by analysis of Y-chromosome DNA. *Heredity*, **108**(5): 507−514.

Dobney K, Larson G. 2006. Genetics and animal domestication: new windows on an elusive process. *Journal of Zoology*, **269**(2): 261−271.

Dodman NH, Karlsson EK, Moon-Fanelli A, Galdzicka M, Perloski M, Shuster L, Lindblad-Toh K, Ginns EI. 2010. A canine chromosome 7 locus confers compulsive disorder susceptibility. *Molecular Psychiatry*, **15**(1): 8−10.

Doebley J. 1989. Isozymic evidence and the evolution of crop plants. *In*: Soltis DE, Soltis PS, Dudley TR (eds). Isozymes in Plant Biology. Dordrecht: Springer.

Drogemuller C, Karlsson EK, Hytönen MK, Perloski M, Dolf G, Sainio K, Lohi H, Lindblad-Toh K, Leeb T. 2008. A mutation in hairless dogs implicates FOXI3 in ectodermal development. *Science*, **321**(5895): 1462−1462.

Dupre G, Heidenreich D. 2016. Brachycephalic Syndrome. *Veterinary Clinics of North America-Small Animal Practice*, **46**(4): 691−707.

Eyre-Walker A, Gaut RL, Hilton H, Feldman DL, Gaut BS. 1998. Investigation of the bottleneck leading to the domestication of maize. *Proceedings of the National Academy of Sciences of the United States of America*, **95**(8): 4441−4446.

Fan Z, Silva P, Gronau I, Wang S, Armero AS, Schweizer RM, Ramirez O, Pollinger J, Galaverni M, Ortega Del-Vecchyo D, Du L, Zhang W, Zhang Z, Xing J, Vila C, Marques-Bonet T, Godinho R, Yue B, Wayne RK. 2016. Worldwide patterns of genomic variation and admixture in gray wolves. *Genome Research*, **26**(2): 163−73.

Frantz LA, Mullin VE, Pionnier-Capitan M, Lebrasseur O, Ollivier M, Perri A, Linderholm A, Mattiangeli V, Teasdale MD, Dimopoulos EA, Tresset A, Duffraisse M, McCormick F, Bartosiewicz L, Gál E, Nyerges ÉA, Sablin MV, Brehard S, Mashkour M, Bălăşescu A, Gillet B, Hughes S, Chassaing O, Hitte C, Vigne JD, Dobney K, Hänni C, Bradley DG, Larson G. 2016. Genomic and archaeological evidence suggest a dual origin of domestic dogs. *Science*, **352**(6290): 1228−1231.

Freedman AH, Gronau I, Schweizer RM, Ortega-Del Vecchyo D, Han E, Silva PM, Galaverni M, Fan Z, Marx P, Lorente-Galdos B, Beale H, Ramirez O, Hormozdiari F, Alkan C, Vilà C, Squire K, Geffen E, Kusak J, Boyko AR, Parker HG, Lee C, Tadigotla V, Wilton A, Siepel A, Bustamante CD, Harkins TT, Nelson SF, Ostrander EA, Marques-Bonet T, Wayne RK, Novembre J. 2014. Genome sequencing highlights the dynamic early history of dogs. *PLoS Genetics*, **10**(1): e1004016.

Freedman AH, Wayne RK. 2017. Deciphering the origin of dogs: From fossils to genomes. *Annual Review of Animal Biosciences*, **5**: 281−307.

Gou X, Wang Z, Li N, Qiu F, Xu Z, Yan DW, Yang SL, Jia J, Kong XY, Wei ZH, Lu SX, Lian LS, Wu CX, Wang XY, Li GZ, Ma T, Jiang Q, Zhao X, Yang JQ, Liu BH, Wei DK, Li H, Yang JF, Yan YL, Zhao GY, Dong XX, Li ML, Deng WD, Leng J, Wei CC, Wang C, Mao HM, Zhang H, Ding GH, Li YX. 2014. Whole-genome sequencing of six dog breeds from continuous altitudes reveals adaptation to high-altitude hypoxia. *Genome Research*, **24**(8): 1308−1315.

Ito H, Nara H, Inoue-Murayama M, Shimada MK, Koshimura A, Ueda Y, Kitagawa H, Takeuchi Y, Mori Y, Murayama Y, Morita M, Iwasaki T, Ôta K, Tanabe Y, Ito S. 2004. Allele frequency distribution of the canine dopamine receptor D4 gene exon III and I in 23 breeds. *Journal of Veterinary Medical Science*, **66**(7): 815−820.

Kariuki SM, Rockett K, Clark TG, Reyburn H, Agbenyega T, Taylor TE, Birbeck GL, Williams TN, Newton CRJC. 2013. The genetic risk of acute seizures in African children with falciparum malaria. *Epilepsia*, **54**(6): 990−1001.

Karlsson EK, Baranowska I, Wade CM, Salmon Hillbertz NH, Zody MC, Anderson N, Biagi TM, Patterson N, Pielberg GR, Kulbokas EJ, Comstock KE, Keller ET, Mesirov JP, von Euler H, Kampe O, Hedhammar A, Lander ES, Andersson G, Andersson L, Lindblad-Toh K. 2007. Efficient mapping of mendelian traits in dogs through genome-wide association. *Nature Genetics*, **39**(11): 1321−1328.

Kukekova AV, Trut LN, Chase K, Kharlamova AV, Johnson JL, Temnykh SV, Oskina IN, Gulevich RG, Vladimirova AV, Klebanov S, Shepeleva DV, Shikhevich SG, Acland GM, Lark KG. 2011. Mapping loci for fox domestication: deconstruction/reconstruction of a behavioral phenotype. *Behavior Genetics*, **41**(4): 593−606.

Leonard JA, Wayne RK, Wheeler J, Valadez R, Guillén S, Vilà C. 2002. Ancient DNA evidence for Old World origin of New World dogs. *Science*, **298**(5598): 1613−1616.

Li Y, von Holdt BM, Reynolds A, Boyko AR, Wayne RK, Wu DD, Zhang YP. 2013. Artificial selection on brain-expressed genes during the domestication of dog. *Molecular Biology and Evolution*, **30**(8): 1867−1876.

Li Y, Wang GD, Wang MS, Irwin DM, Wu DD, Zhang YP. 2014a. Domestication of the dog from the wolf was promoted by enhanced excitatory synaptic plasticity: A hypothesis. *Genome Biology and Evolution*, **6**(11): 3115−3121.

Li Y, Wu DD, Boyko AR, Wang GD, Wu SF, Irwin DM, Zhang YP. 2014b. Population variation revealed high-altitude adaptation of Tibetan mastiffs. *Molecular Biology and Evolution*, **31**(5): 1200−1205.

Lindberg J, Björnerfeldt S, Saetre P, Svartberg K, Seehuus B, Bakken M, Vilà C, Jazin E. 2005. Selection for tameness has changed brain gene expression in silver foxes. *Current Biology*, **15**(22): R915−R916.

Liu YH, Wang L, Xu T, Guo XM, Li Y, Yin TT, Yang HC, Hu Y, Adeola AC, Sanke OJ, Otecko NO, Wang M, Ma YP, Charles OS, Sinding MHS, Gopalakrishnan S, Samaniego JA, Hansen AJ, Fernandes C, Gaubert P, Budd J, Dawuda PM, Rueness EK, Jiang LB, Zhai WW, Gilbert MTP, Peng MS, Qi XP, Wang GD, Zhang YP. 2018. Whole-genome sequencing of African dogs provides insights into adaptations against tropical parasites. *Molecular Biology and Evolution*, **35**(2): 287−298.

Marchant TW, Johnson EJ, McTeir L, Johnson CI, Gow A, Liuti T, Kuehn D, Svenson K, Bermingham ML, Drögemüller M, Nussbaumer M, Davey MG, Argyle DJ, Powell RM, Guilherme S, Lang J, Ter Haar G, Leeb T, Schwarz T, Mellanby RJ, Clements DN, Schoenebeck JJ. 2017. Canine brachycephaly is associated with a retrotransposon-mediated missplicing of SMOC2. *Current Biology*, **27**(11): 1573−1584.

Miao B, Wang Z, Li Y. 2017. Genomic analysis reveals hypoxia adaptation in the Tibetan mastiff by introgression of the gray wolf from the Tibetan Plateau. *Molecular Biology and Evolution*, **34**(3): 734−743.

Moon-Fanelli AA, Dodman NH. 1998. Description and development of compulsive tail chasing in terriers and response to clomipramine treatment. *Journal of the American Veterinary Medical Association*, **212**(8): 1252−1257.

Moya PR, Dodman NH, Timpano KR, Rubenstein LM, Rana Z, Fried RL, Reichardt LF, Heiman GA, Tischfield JA, King RA, Galdzicka M, Ginns EI, Wendland JR. 2013. Rare missense neuronal cadherin gene (CDH2) variants in specific obsessive-compulsive disorder and Tourette disorder phenotypes. *European Journal of Human Genetics*, **21**(8): 850−854.

Ni Leathlobhair M, Perri AR, Irving-Pease EK, Witt KE, Linderholm A, Haile J, Lebrasseur O, Ameen C, Blick J, Boyko AR, Brace S, Cortes YN, Crockford SJ, Devault A, Dimopoulos EA, Eldridge M, Enk J, Gopalakrishnan S, Gori K, Grimes V, Guiry E, Hansen AJ, Hulme-Beaman A, Johnson J, Kitchen A, Kasparov AK, Kwon YM, Nikolskiy PA, Lope CP, Manin A, Martin T, Meyer M, Myers KN, Omura M, Rouillard JM, Pavlova EY, Sciulli P, Sinding MS, Strakova A, Ivanova VV, Widga C, Willerslev E, Pitulko VV, Barnes I, Gilbert MTP, Dobney KM, Malhi RS, Murchison EP, Larson G, Frantz LAF. 2018. The evolutionary history of dogs in the Americas. *Science*, **361**(6397): 81−85.

Ollivier M, Tresset A, Frantz LAF, Bréhard S, Bălăşescu A, Mashkour M, Boroneant A, Pionnier-Capitan M, Lebrasseur O, Arbogast RM, Bartosiewicz L, Debue K, Rabinovich R, Sablin MV, Larson G, Hänni C, Hitte C, Vigne JD. 2018. Dogs accompanied humans during the Neolithic expansion into Europe. *Biology Letters*, **14**(10).

Ostrander EA, Wayne RK, Freedman AH, Davis BW. 2017. Demographic history, selection and functional diversity of the canine genome. *Nature Reviews Genetics*, **18**(12): 705−720.

Pang JF, Kluetsch C, Zou XJ, Zhang AB, Luo LY, Angleby H, Ardalan A, Ekström C, Sköllermo A, Lundeberg J, Matsumura S, Leitner T, Zhang YP, Savolainen P. 2009. mtDNA data indicate a single origin for dogs south of Yangtze River, less than 16, 300 years Ago, from numerous wolves. *Molecular Biology and Evolution*, **26**(12): 2849−2864.

Parker HG, VonHoldt BM, Quignon P, Margulies EH, Shao S, Mosher DS, Spady TC, Elkahloun A, Cargill M, Jones PG, Maslen CL, Acland GM, Sutter NB, Kuroki K, Bustamante CD, Wayne RK, Ostrander EA. 2009. An expressed Fgf4 retrogene is associated with breed-defining chondrodysplasia in domestic dogs. *Science*, **325**(5943): 995−998.

Plassais J, Rimbault M, Williams FJ, Davis BW, Schoenebeck JJ, Ostrander EA. 2017. Analysis of large versus small dogs reveals three genes on the canine X chromosome associated with body weight, muscling and back fat thickness. *PLoS Genetics*, **13**(3): e1006661.

Rimbault M, Beale HC, Schoenebeck JJ, Hoopes BC, Allen JJ, Kilroy-Glynn P, Wayne RK, Sutter NB, Ostrander EA. 2013. Derived variants at six genes explain nearly half of size reduction in dog breeds. *Genome Research*, **23**(12): 1985−1995.

Saetre P, Lindberg J, Leonard JA, Olsson K, Pettersson U, Ellegren H, Bergström TF, Vila C, Jazin E. 2004. From wild wolf to domestic dog: gene expression changes in the brain. *Molecular Brain Research*, **126**(2): 198−206.

Saetre P, Strandberg E, Sundgren PE, Pettersson U, Jazin E, Bergström TF. 2006. The genetic contribution to canine personality. *Genes Brain and Behavior*, **5**(3): 240−248.

Savolainen P, Leitner T, Wilton AN, Matisoo-Smith E, Lundeberg J. 2004. A detailed picture of the origin of the Australian dingo, obtained from the study of mitochondrial DNA. *Proceedings of the National Academy of Sciences of the United States of America*, **101**(33): 12387−12390.

Savolainen P, Zhang YP, Luo J, Lundeberg J, Leitner T. 2002. Genetic evidence for an East Asian origin of domestic dogs. *Science*, **298**(5598): 1610−1613.

Schmutz SM, Berryere TG. 2007. Genes affecting coat colour and pattern in domestic dogs: a review. *Animal Genetics*, **38**(6): 539−549.

Schmutz SM, Berryere TG, Goldfinch AD. 2002. TYRP1 and MC1R genotypes and their effects on coat color in dogs. *Mammalian Genome*, **13**(7): 380−387.

Schoenebeck JJ, Hutchinson SA, Byers A, Beale HC, Carrington B, Faden DL, Rimbault M, Decker B, Kidd JM, Sood R, Boyko AR, Fondon JW, 3 rd, Wayne RK, Bustamante CD, Ciruna B, Ostrander EA. 2012. Variation of BMP3 contributes to dog breed skull diversity. *PLoS Genetics*, **8**(8): e1002849.

Shearin AL, Ostrander EA. 2010a. Canine morphology: hunting for genes and tracking mutations. *PLoS Biology*, **8**(3): e1000310.

Shearin AL, Ostrander EA. 2010b. Leading the way: canine models of genomics and disease. *Disease Models and Mechanisms*, **3**(1−2): 27−34.

Spady TC, Ostrander EA. 2007. Canid genomics: mapping genes for behavior in the silver fox. *Genome Research*, **17**(3): 259−263.

Sutter NB, Bustamante CD, Chase K, Gray MM, Zhao KY, Zhu L, Padhukasahasram B, Karlins E, Davis S, Jones PG, Quignon P, Johnson GS, Parker HG, Fretwell N, Mosher DS, Lawler DF, Satyaraj E, Nordborg M, Lark KG, Wayne RK, Ostrander EA. 2007. A single IGF1 allele is a major determinant of small size in dogs. *Science*, **316**(5821): 112−115.

Tang B, Zhou Q, Dong L, Li W, Zhang X, Lan L, Zhai S, Xiao J, Zhang Z, Bao Y, Zhang YP, Wang GD, Zhao W. 2019. iDog: an integrated resource for domestic dogs and wild canids. *Nucleic Acids Research*, **47**(D1): D793−D800.

Tang R, Noh HJ, Wang D, Sigurdsson S, Swofford R, Perloski M, Duxbury M, Patterson EE, Albright J, Castelhano M, Auton A, Boyko AR, Feng G, Lindblad-Toh K, Karlsson EK. 2014. Candidate genes and functional noncoding variants identified in a canine model of obsessive-compulsive disorder. *Genome Biology*, **15**(3): R25.

Thawornwattana Y, Dalquen D, Yang Z. 2018. Coalescent analysis of phylogenomic data confidently resolves the species relationships in the anopheles gambiae species complex. *Molecular Biology and Evolution*, **35**(10): 2512−2527.

Vilà C, Savolainen P, Maldonado JE, Amorim IR, Rice JE, Honeycutt RL, Crandall KA, Lundeberg J, Wayne RK. 1997. Multiple and ancient origins of the domestic dog. *Science*, **276**(5319): 1687−1689.

Vonholdt BM, Pollinger JP, Lohmueller KE, Han E, Parker HG, Quignon P, Degenhardt JD, Boyko AR, Earl DA, Auton A, Reynolds A, Bryc K, Brisbin A, Knowles JC, Mosher DS, Spady TC, Elkahloun A, Geffen E, Pilot M, Jedrzejewski W, Greco C, Randi E, Bannasch D, Wilton A, Shearman J, Musiani M, Cargill M, Jones PG, Qian Z, Huang W, Ding ZL, Zhang YP, Bustamante CD, Ostrander EA, Novembre J, Wayne RK. 2010. Genome-wide SNP and haplotype analyses reveal a rich history underlying dog domestication. *Nature*, **464**(7290): 898−902.

Wang GD, Fan RX, Zhai W, Liu F, Wang L, Zhong L, Wu H, Yang HC, Wu SF, Zhu CL, Li Y, Gao Y, Ge RL, Wu CI, Zhang YP. 2014. Genetic convergence in the adaptation of dogs and humans to the high-altitude environment of the tibetan plateau. *Genome Biology and Evolution*, **6**(8): 2122−2128.

Wang GD, Zhai W, Yang HC, Wang L, Zhong L, Liu YH, Fan RX, Yin TT, Zhu CL, Poyarkov AD, Irwin DM, Hytönen MK, Lohi H, Wu CI, Savolainen P, Zhang YP. 2016. Out of southern East Asia: the natural history of domestic dogs across the world. *Cell Research*, **26**(1): 21−33.

Wang GD, Zhai WW, Yang HC, Fan RX, Cao X, Zhong L, Wang L, Liu F, Wu H, Cheng LG, Poyarkov AD, Poyarkov NA, Tang SS, Zhao WM, Gao Y, Lv XM, Irwin DM, Savolainen P, Wu CI, Zhang YP. 2013. The genomics of selection in dogs and the parallel evolution between dogs and humans.

Nature Communications, **4**: 1860.

Webb AA, Cullen CL. 2010. Coat color and coat color pattern-related neurologic and neuro-ophthalmic diseases. *Canadian Veterinary Journal*, **51**(6): 653−657.

Woods KA, Camacho-Hübner C, Barter D, Clark AJ, Savage MO. 1997. Insulin-like growth factor I gene deletion causing intrauterine growth retardation and severe short stature. *Acta Paediatrica Supplement*, **86**(S423): 39−45.

Woods KA, Camacho-Hübner C, Savage MO, Clark AJ. 1996. Intrauterine growth retardation and postnatal growth failure associated with deletion of the insulin-like growth factor I gene. *New England Journal of Medicine*, **335**(18): 1363−1367.

Wu DD, Ding XD, Wang S, Wójcik JM, Zhang Y, Tokarska M, Li Y, Wang MS, Faruque O, Nielsen R, Zhang Q, Zhang YP. 2018. Pervasive introgression facilitated domestication and adaptation in the *Bos* species complex. *Nature Ecology & Evolution*, **2**(7): 1139−1145.

Wu H, Liu YH, Wang GD, Yang CT, Otecko NO, Liu F, Wu SF, Wang L, Yu L, Zhang YP. 2016. Identifying molecular signatures of hypoxia adaptation from sex chromosomes: A case for Tibetan Mastiff based on analyses of X chromosome. *Scientific Reports*, **6**: 35004.

ZOOLOGICAL RESEARCH

Review of the genus *Brachytarsophrys* (Anura: Megophryidae), with revalidation of *Brachytarsophrys platyparietus* and description of a new species from China

Yao Li[1], Dan-Dan Zhang[1], Zhi-Tong Lyu[1], Jian Wang[1], Yu-Long Li[1], Zu-Yao Liu[1], Hong-Hui Chen[1], Ding-Qi Rao[2], Zhi-Fang Jin[3], Chang-You Zhang[3], Ying-Yong Wang[1,*]

[1] *State Key Laboratory of Biocontrol / The Museum of Biology*, *School of Life Sciences*, *Sun Yat-Sen University*, *Guangzhou*, *Guangdong* 510275, *China*

[2] *State Key Laboratory of Genetic Resources and Evolution*, *Kunming Institute of Zoology*, *Chinese Academy of Sciences*, *Kunming*, *Yunnan* 650223, *China*

[3] *Jiangxi Jiulianshan National Nature Reserve*, *Ganzhou*, *Jiangxi* 341700, *China*

ABSTRACT

The genus-level recognition of monophyletic short-legged toads (*Brachytarsophrys*) has been recently implicated in the taxonomic debate of *Megophrys sensu lato*. In the present study, *Brachytarsophrys* is reasonably regarded as a distinct genus based on significant morphological differentiations and recent molecular analyses. Furthermore, a comprehensive review of this genus is performed, with two species groups proposed based on morphological differences and phylogenetic relationships. Particularly, *Brachytarsophrys platyparietus* is removed as a synonym of *Brachytarsophrys carinense* and considered a valid species due to significant genetic divergence and distinct morphological differences. In addition, a new species, *Brachytarsophrys orientalis* **sp. nov.**, is described based on a series of specimens collected from southeastern China. This work takes the member species of the genus *Brachytarsophrys* to seven, suggesting that the diversity of *Brachytarsophrys* is underestimated. In addition, the genus levels of other monophyletic groups within the subfamily Megophryinae are discussed.

Keywords: Genus level; Megophryinae; Morphology; Phylogeny; Revision

INTRODUCTION

Systematics of the subfamily Megophryinae have been debated for decades (Dubois, 1987; Dubois & Ohler, 1998; Fei et al., 2009; Fei & Ye, 2016; Frost et al., 2006; Jiang et al., 2003; Li & Wang, 2008; Rao & Yang, 1997; Zheng et al., 2004). Based on multilocus nuclear-gene and matrilineal

---

Received: 02 September 2019; Accepted: 04 March 2020; Online: 11 March 2020

Foundation items: This work was supported by the Project of Comprehensive Scientific Survey of Luoxiao Mountains Region of Ministry of Science and Technology, China (2013FY111500); Specimen Platform of Ministry of Science and Technology, China, teaching specimens sub-platform (2005DKA21403-JK); Animal Branch of the Germplasm Bank of Wild Species, Chinese Academy of Sciences (Large Research Infrastructure Funding); and Project of Scientific Investigation on Amphibian, Reptilian and Avian Animals in Jiangxi Jiulianshan National Nature Reserve

*Corresponding author, E-mail: wangyy@mail.sysu.edu.cn

DOI: 10.24272/j.issn.2095-8137.2020.033

mtDNA genealogy, three recent studies revealed highly similar phylogenetic relationships within Megophryinae, resolving the following monophyletic groups: i.e., Atympanophrys, Brachytarsophrys, Megophrys, Ophryophryne, Panophrys, Pelobatrachus, and Xenophrys (Chen et al., 2017; Liu et al., 2018; Mahony et al., 2017). However, disagreements remain regarding taxonomic proposals at the genus level among these monophyletic groups. Chen et al. (2017) considered the subfamily Megophryinae to be valid and composed of five genera: i.e., *Atympanophrys* Tian & Hu, 1983, *Brachytarsophrys* Tian & Hu, 1983, *Megophrys* Kuhl & Van Hasselt, 1822, *Ophryophryne* Boulenger, 1903, and *Xenophrys* Günther, 1864. Mahony et al. (2017) treated the entire Megophryinae subfamily as a single genus *Megophrys* and regarded the seven molecularly resolved clades in their phylogenetic tree as seven subgenera: i.e., *Atympanophrys*, *Brachytarsophrys*, *Megophrys*, *Ophryophryne*, *Panophrys* Rao & Yang, 1997, *Pelobatrachus* Beddard, 1908, and *Xenophrys*. Although the phylogenetic results of the above two studies are highly similar, the taxonomic proposals represent different views, and the focus of the taxonomic debate returns to the previous problem of morphological cognizance at the genus level.

The short-legged toad genus *Brachytarsophrys* within Megophryinae was established by Tian & Hu (1983), with *Leptobrachium carinense* Boulenger, 1889 as the type species. Based on a combination of morphological characteristics, *Brachytarsophrys* differs significantly from other groups within Megophryinae and has been regarded as a valid genus for a long time (Delorme et al., 2006; Fei et al., 2009; Fei & Ye, 2016; Frost et al., 2006; Pyron & Wiens, 2011; Xie & Wang, 2000; Zhao & Adler, 1993). Recent phylogenetic results have also confirmed *Brachytarsophrys* as a monophyletic lineage against other Megophryinae groups (Chen et al., 2017; Deuti et al., 2017; Liu et al., 2018; Mahony et al., 2017; Orlov et al., 2015; Poyarkov et al., 2017; Zhang et al., 2017). Therefore, we regard *Brachytarsophrys* as a distinct genus in this study.

Currently, the genus *Brachytarsophrys* is widely distributed in southern China, Myanmar, Vietnam, Laos, and northern Thailand, and contains five recognized species: i.e., *Brachytarsophrys carinense* (Boulenger, 1889), *Brachytarsophrys feae* (Boulenger, 1886), *Brachytarsophrys intermedia* (Smith, 1921), *Brachytarsophrys chuannanensis* Fei, Ye & Huang, 2001, and *Brachytarsophrys popei* Zhao, Yang, Chen, Chen & Wang, 2014. Rao & Yang (1997) also described *Brachytarsophrys platyparietus* as a species from northern Yunnan and considered that the previous records of *B. carinense* from southern and southwestern China should be *B. platyparietus*, with *B. carinense* being endemic to Myanmar and Thailand. However, after examining a series of specimens from China and a single specimen (MNHN 1893.0527) from Yado, Myanmar, Fei et al. (2009) temporarily treated *B. platyparietus* as a synonym of *B. carinense*, though also suggested that the validity of *B. platyparietus* requires further research and evidence.

In the present work, a series of *Brachytarsophrys* specimens and samples were collected from multiple localities (Figure 1A), covering potential unnamed populations and all recognized species. The phylogenetic relationships among *Brachytarsophrys* congeners were reconstructed and detailed morphological comparisons were performed, leading to a comprehensive review of this genus. Both the morphological comparisons and molecular results confirm that *B. platyparietus* should be re-considered as a valid species (see below for supplementary description). In addition, populations of *Brachytarsophrys* from Jiangxi and Fujian in southeastern China are revealed as a new species, named *Brachytarsophrys orientalis* **sp. nov**., based on morphological and molecular differences, thus demonstrating that *Brachytarsophrys* diversity is underestimated.

MATERIALS AND METHODS

Morphological characters

Measurements followed the protocols described by Fei et al. (2009) with digital calipers to the nearest 0.1 mm. These measurements were as follows: SVL: Snout–vent length (from tip of snout to vent); HDL: Head length (from tip of snout to posterior of articulation of jaw); HDW: Head width (maximum distance between both sides of articulation of jaw); SKL: Skull length (from tip of snout to posterior margin of occipital); SNT: Snout length (from tip of snout to anterior corner of eye); IOD: Interorbital distance (minimum distance between upper eyelids); IND: Internasal distance (distance between nares); ED: Eye diameter (eyeball diameter parallel to axis of body); HND: Hand length (from distal end of radioulnar to tip of finger III); RAD: Radioulnar length (from flexed elbow to proximal margin of outer palmar tubercle); TIB: Tibia length (from outer surface of flexed knee to heel); FTL: Foot length (from distal end of tibia to tip of toe IV); BL: Body length (from tip of snout to origin of tail in tadpole); TL: Tail length (from origin to tip of tail in tadpole). To show body size variation among adult males, we plotted the boxplot of SVL in R-3.6.2 (R Core Team, 2019).

The toe webbing formula followed the protocol described by Savage (1975). To describe toe webbing of *Brachytarsophrys* species accurately, the location of the web on the phalange articulation was designated as follows: - (distal part of phalange articulation); none (middle part of phalange articulation); + (proximal part of phalange articulation); ++ (lower part of phalange articulation) (Figure 2).

Sex was determined by observation of secondary sexual characters, i.e., presence of internal vocal sac openings and nuptial spines in males. Tadpole stage was identified following Gosner (1960).

Comparative morphological data of all recognized *Brachytarsophrys* species were obtained from the literature (Boulenger, 1889, 1890, 1908; Fei & Ye, 2001; Fei et al., 2009; Smith, 1921; Taylor, 1962; Zhao et al., 2014) and from examined specimens of *B. feae*, *B. chuannanensis*, and *B. popei*.

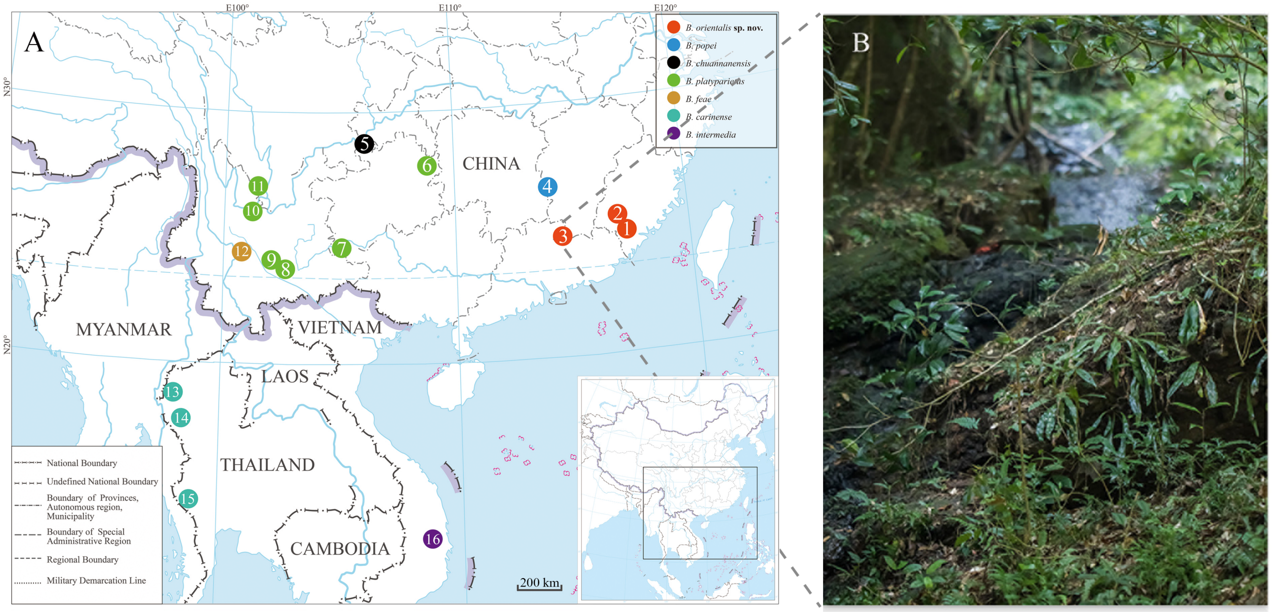

Figure 1 Collection localities of samples used in this study and habitat of *Brachytarsophrys orientalis* sp. nov.

A: Localities of *Brachytarsophrys orientalis* **sp. nov.**: 1: Huboliao Nature Reserve, Fujian; 2: Shanghang County, Fujian; 3: Jiulianshan Nature Reserve, Jiangxi. Localities of *B. popei*; 4: Taoyuandong Nature Reserve, Hunan. Localities of *B. chuannanensis*; 5: Hejiang County, Sichuan. Localities of *B. platyparietus*; 6: Mt. Fanjing, Guizhou; 7: Mt. Jinzhong, Guangxi; 8: Shiping County, Yunnan; 9: Mt. Mopan, Yunnan; 10: Dayao County, Yunnan; 11: Yanbian County, Yunnan. Localities of *B. feae*; 12: Jingdong County, Yunnan. Localities of *B. carinense*; 13: Mae Surin NP., Mae Hong Son, Thailand; 14: Omkoi, Chiang Mai, Thailand; 15: Thong Pha Phum, Kanchanaburi, Thailand. Localities of *B. intermedia*; 16: Krong Pa, Gia Lai, Vietnam. B: Habitat of *Brachytarsophrys orientalis* **sp. nov.** in Jiulianshan Nature Reserve, Jiangxi Province.

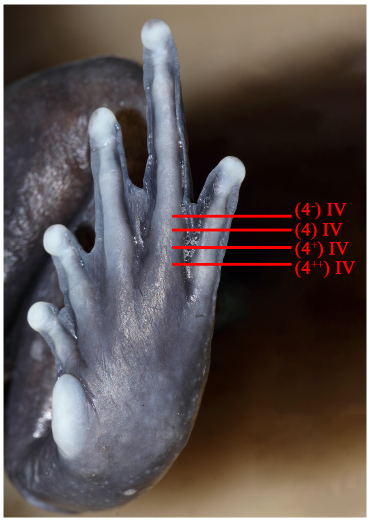

Figure 2 Location of web on phalange articulation

(4^-) IV: Distal part of articulation between fourth phalange and metatarsal; (4) IV: Middle part of articulation between fourth phalange and metatarsal; (4^+) IV: Proximal part of articulation between fourth phalange and metatarsal; (4^{++}) IV: Lower part of articulation between fourth phalange and metatarsal.

All specimens were fixed in 10% buffered formalin, then transferred to 75% ethanol for preservation, and deposited in The Museum of Biology, Sun Yat-Sen University (SYS) and Chengdu Institute of Biology (CIB), Chinese Academy of Sciences (CAS), China. Other collection abbreviations for specimens or samples include the Kunming Institute of Zoology (KIZ), CAS, China; Muséum National d'Histoire Naturelle (MNHN), France; and Royal Ontario Museum (ROM), Canada.

Molecular sampling

For molecular analyses, a total of 28 *Brachytarsophrys* samples were used, including 11 samples from the five recognized species (*B. carinense*, *B. feae*, *B. intermedia*, *B. chuannanensis*, and *B. popei*), one topotype sample of *B. platyparietus*, and 16 samples of unidentified species. Additionally, one sequence of *B. carinense* and out-group sequences of *Atympanophrys shapingensis* (Liu, 1950) and *Xenophrys mangshanensis* (Fei & Ye, 1990) were obtained from GenBank and incorporated into our dataset (Figure 1A and Table 1). All muscle samples were taken from euthanized specimens and then preserved in 95% ethanol before fixation.

Extraction, polymerase chain reaction (PCR), and sequencing

DNA was extracted from muscle tissue using an extraction kit from Tiangen Biotech (Beijing) Co., Ltd. (China). Partial cytochrome c oxidase I (*COI*) and cytochrome b (cyt *b*) genes were amplified using the primers listed in Table 2. PCR amplifications were performed in a 20 µl reaction volume with

Table 1 Localities, voucher information, and GenBank accession Nos. of all samples used in this study

ID	Species	Localities (*: Type locality)	Specimen No.	*COI*	cyt *b*
1	*Brachytarsophrys orientalis* **sp. nov.**	*China: Jiulianshan Nature Reserve, Longnan County, Jiangxi	SYS a004225	MT162625	MT162650
2	*Brachytarsophrys orientalis* **sp. nov.**	*China: Jiulianshan Nature Reserve, Longnan County, Jiangxi	SYS a004226	MT162626	MT162651
3	*Brachytarsophrys orientalis* **sp. nov.**	*China: Jiulianshan Nature Reserve, Longnan County, Jiangxi	SYS a004227	MT162627	MT162652
4	*Brachytarsophrys orientalis* **sp. nov.**	*China: Jiulianshan Nature Reserve, Longnan County, Jiangxi	SYS a004228	MT162628	MT162653
5	*Brachytarsophrys orientalis* **sp. nov.**	*China: Jiulianshan Nature Reserve, Longnan County, Jiangxi	SYS a004486	MT162629	MT162654
6	*Brachytarsophrys orientalis* **sp. nov.**	*China: Jiulianshan Nature Reserve, Longnan County, Jiangxi	SYS a005451	MT162632	MT162655
7	*Brachytarsophrys orientalis* **sp. nov.**	China: Gutian Township, Shanghang County, Fujian	SYS a003249	MT162623	MT162648
8	*Brachytarsophrys orientalis* **sp. nov.**	China: Huboliao Nature Reserve, Nanjing County, Fujian	SYS a003340	MT162624	MT162649
9	*Brachytarsophrys carinense*	Thailand: Doi Chiang Dao, Chiang Mai	K3001	KR087626	–
10	*Brachytarsophrys carinense*	Thailand: Omkoi, Chiang Mai	KIZ024170	MT162640	MT162663
11	*Brachytarsophrys carinense*	Thailand: Mae Surin NP., Mae Hong Son	KIZ024429	MT162641	MT162664
12	*Brachytarsophrys carinense*	Thailand: Thong Pha Phum, Kanchanaburi	KIZ024640	MT162642	MT162665
13	*Brachytarsophrys chuannanensis*	*China: Zihuai Township, Hejiang County, Sichuan	SYS a004926	MT162630	–
14	*Brachytarsophrys chuannanensis*	*China: Zihuai Township, Hejiang County, Sichuan	SYS a004927	MT162631	–
15	*Brachytarsophrys feae*	China: Jingdong County, Yunnan	SYS a003912	MH406362	MH407192
16	*Brachytarsophrys feae*	China: Jingdong County, Yunnan	SYS a003913	MH406363	MH407193
17	*Brachytarsophrys intermedia*	Vietnam: Krong Pa, Gia Lai	ROM 23794	MT162643	MT162666
18	*Brachytarsophrys platyparietus*	*China: Duodihe, Dayao county, Yunnan	SYS a005919	MT162633	MT162656
19	*Brachytarsophrys platyparietus*	China: Mt. Jinzhong, Longlin County, Guangxi	SYS a002236	MT162622	MT162647
20	*Brachytarsophrys platyparietus*	China: Mt. Fanjing, Tongren City, Guizhou	YPX43968	MT162644	MT162667
21	*Brachytarsophrys platyparietus*	China: Mt. Mopan, Xinping County, Yunnan	SYS a007774	MT162634	MT162657
22	*Brachytarsophrys platyparietus*	China: Mt. Mopan, Xinping County, Yunnan	SYS a007775	MT162635	MT162658
23	*Brachytarsophrys platyparietus*	China: Mt. Mopan, Xinping County, Yunnan	SYS a007776	MT162636	MT162659
24	*Brachytarsophrys platyparietus*	China: Mt. Mopan, Xinping County, Yunnan	SYS a007777	MT162637	MT162660
25	*Brachytarsophrys platyparietus*	China: Yilong Township, Shiping County, Yunnan	SYS a007790	MT162638	MT162661
26	*Brachytarsophrys platyparietus*	China: Yumen Township, Yanbian County, Sichuan	SYS a007853	MT162639	MT162662
27	*Brachytarsophrys popei*	*China: Taoyuandong Nature Reserve, Yanling County, Hunan	SYS a001864	MH406361	MH407191
28	*Brachytarsophrys popei*	*China: Taoyuandong Nature Reserve, Yanling County, Hunan	SYS a001865	MT162620	MT162645
29	*Brachytarsophrys popei*	*China: Taoyuandong Nature Reserve, Yanling County, Hunan	SYS a001866	MT162621	MT162646
30	*Atympanophrys shapingensis*	China: Mt. Wawu, Hongya County, Sichuan	SYS a005310	MH406352	MH407182
31	*Atympanophrys shapingensis*	China: Zhaojue County, Sichuan	SYS a005339	MH406359	MH407189
32	*Xenophrys mangshanensis*	China: Mt. Dayao, Jinxiu County, Guangxi	SYS a004870	MH406323	MH407153
33	*Xenophrys mangshanensis*	China: Mt. Dayao, Jinxiu County, Guangxi	SYS a004871	MH406324	MH407154

–: Not available.

Table 2 Primer pairs used in this study

Gene	Forward primer	Reverse primer	References
COI	Chmf4 (5'-TYTCWACWAAYCAYAAAGAYATCGG-3')	Chmr4 (5'-ACYTCRGGRTGRCCRAARAATCA-3')	Che et al., 2012
COI	Dglco (5'-GGTCAACAAATCATAAAGAYATYGG-3')	Dghco (5'-TAAACTTCAGGGTGACCAAARAAYCA-3')	Meyer et al., 2005
cyt *b*	PFGlu14140L(5'-GAAAAACCACTGTTGTHHYTCAACTA-3')	PFThr15310 (5'-CGGYTTACAAGACCGRTGCTTT-3')	Zhang et al., 2013

the following cycling conditions: initial denaturing step at 95 °C for 4 min; 35 cycles of denaturing at 95 °C for 40 s, annealing at 50 °C for 40 s, and extension at 72 °C for 1 min; and final extension step at 72 °C for 10 min. PCR products were purified with spin columns. The purified products were sequenced with both forward and reverse primers using the BigDye Terminator Cycle Sequencing Kit according to the guidelines of the manufacturer on an ABI Prism 3730 automated DNA sequencer from Shanghai Majorbio Biopharm Technology Co., Ltd. (China). All sequences were deposited in GenBank (Table 1).

Phylogenetic analyses

Sequences were aligned using ClustalX 2.0 (Thompson et al., 1997) with default parameters in MEGA 6 (Tamura et al., 2013). The two gene segments (627 base pairs (bp) for *COI* and 1 050 bp for cyt *b*) were concatenated seriatim into a 1 677 bp sequence and further divided into two partitions based upon each gene. The two partitions were tested respectively in jModelTest 2.1.2 (Darriba et al., 2012) based on Akaike information criteria, resulting in the both best-fitting nucleotide substitution models of GTR+G+I. Phylogenetic trees were constructed using maximum likelihood (ML) implemented in RaxmlGUI 1.3 (Silvestro & Michalak, 2012) and Bayesian inference (BI) in MrBayes 3.2.4 (Ronquist et al., 2012). For ML analysis, the majority rule consensus tree was calculated with 1 000 bootstrap replicates. For BI analysis, two independent runs with four Markov Chain Monte Carlo simulations were performed for 10 million iterations, with sampling every 1 000 generations and the first 25% of samples discarded as burn-in. Convergence of the Markov Chain Monte Carlo simulations was assessed by checking the average standard deviation of split frequencies between two runs using Tracer v.1.4 (http://tree.bio.ed.ac.uk/software/tracer/). We also calculated uncorrected pairwise genetic distances (*P*-distance) in MEGA 6.

RESULTS

The ML and BI analyses, which resulted in essentially identical topologies, were integrated, as shown in Figure 3. All major nodes were sufficiently supported with Bayesian posterior probabilities (BPP) >0.95 and maximum likelihood bootstrap supports (BS) >90. The mean *P*-distances among all *Brachytarsophrys* species are given in Table 3.

All *Brachytarsophrys* samples were clustered into two major, deeply divergent, and strongly supported monophyletic groups (BPP=1.00, BS=100), designated in this study as Group I and Group II, respectively. Group I was composed of species from the Indochina Peninsula, namely, *B. carinense* and *B. intermedia*. All samples from China formed Group II, which could be divided into two clades with strong node

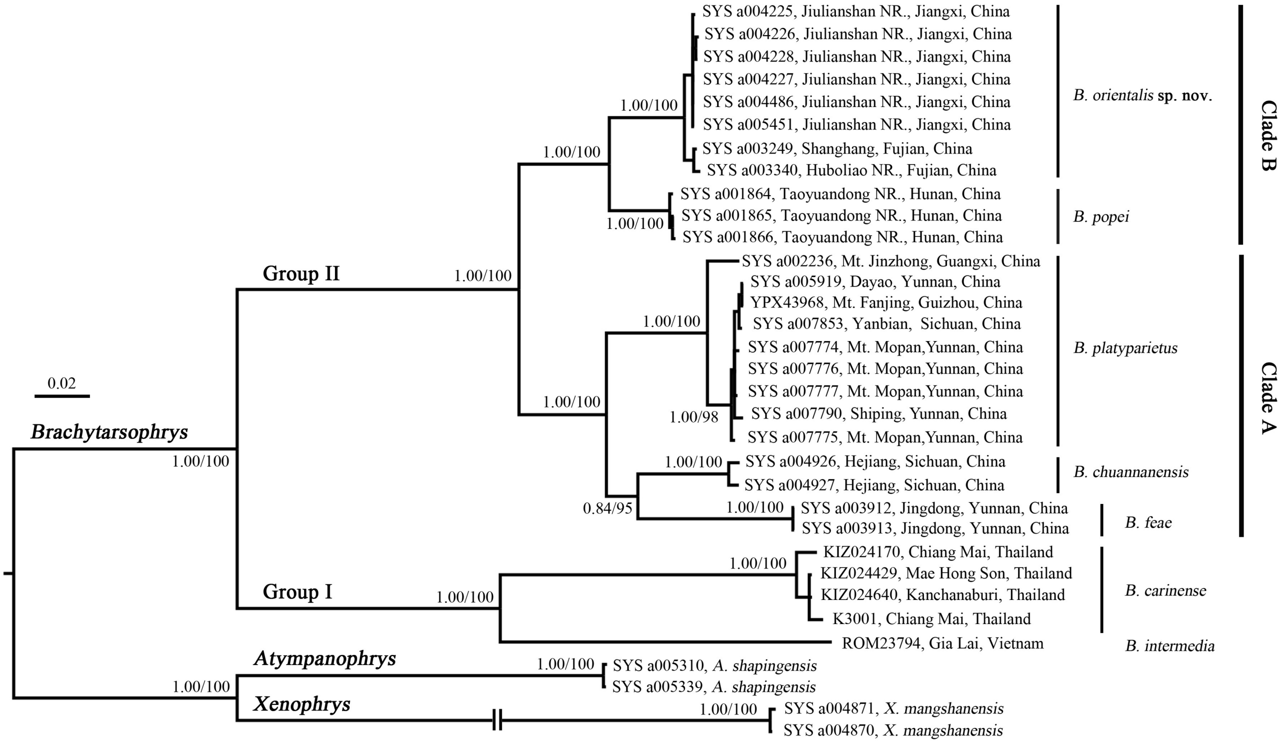

Figure 3 Bayesian inference and maximum-likelihood phylogenies

Numbers before slashes are Bayesian posterior probabilities, and numbers after slashes are maximum-likelihood bootstrap supports.

Table 3 Uncorrected *P*-distances (mean, in %) among species of the genus *Brachytarsophrys* based on partial mitochondrial *COI* gene

ID	Species	1–8	9–12	13–14	15–16	17	18–26	27–29
1–8	*Brachytarsophrys orientalis* **sp. nov.**	0.3						
9–12	*B. carinense*	15.8	0.6					
13–14	*B. chuannanensis*	8.5	14.7	0.5				
15–16	*B. feae*	9.4	15.3	6.3	0.0			
17	*B. intermedia*	15.7	12.1	16.3	15.2	–		
18–26	*B. platyparietus*	8.4	14.6	5.8	6.8	15.9	0.5	
27–29	*B. popei*	4.3	15.8	8.7	10.4	15.7	7.7	0.1

support (BPP=1.00, BS=100), representing populations from southwestern and southeastern China and designated as clade A and clade B, respectively.

In clade A, the topotype sample of "*B. platyparietus*" from Dayao County clustered with eight samples from multiple localities in southwestern China to form a monophyletic lineage with strong node support (BPP=1.00, BS=100) and small divergence (mean *P*-distance 0.5%), representing the "*B. platyparietus*" lineage. This lineage was the sister taxon to (*B. chuannanensis*+*B. feae*) with strong node support (BPP=1.00, BS=100), but was distant from *B. carinense* in phylogeny. In clade B, *Brachytarsophrys* samples from Jiangxi and Fujian were grouped into a monophyletic lineage with strong node support (BPP=1.00, BS=100) and small divergence (mean *P*-distance 0.3%). This was the sister taxon to *B. popei* with moderate genetic difference (mean *P*-distance 4.3%) and represented a separately evolving undescribed lineage.

The measurements and body proportions of *Brachytarsophrys* species are shown in Table 4, and the boxplot of adult male SVL is shown in Figure 4 (*B. carinense* data were insufficient and excluded). The morphological comparisons within *Brachytarsophrys* are shown in Table 5.

Adult male body size varies significantly among *Brachytarsophrys* congeners. The specimens from southeastern China are significantly smaller than that from southwestern China and Indochina. *Brachytarsophrys popei* possesses the smallest body size (SVL 70.7–83.5 mm), although the undescribed *Brachytarsophrys* species partly overlaps (SVL 76.8–82.7 mm). The undescribed specimens also present a combination of morphological characteristics not observed in other known congeners, including small body size (SVL 76.8–82.7 mm in seven adult males), moderate webbing, and absence of transversal stripes on chest in tadpoles. Therefore, based on the morphological and molecular differences, these specimens are proposed as a new species, *Brachytarsophrys orientalis* **sp. nov.**, in this study.

Furthermore, the specimens of "*B. platyparietus*" differ from all known congeners by numerous small, conical, horny tubercles on pectoral region, lateral belly to lower flank of body, ventral surface, and rear of limbs, and by absence of dermal ridge or glandular fold on dorsum. Rao & Yang (1997) found that the previously reported populations of *B. carinense* in China lacked paired elongate granular folds on dorsum, and besides their geographical distribution range was separated by another valid species (*B. feae*). Therefore, they suggested that the Chinese populations of *B. carinense* should be a distinct species (*B. platyparietus*), with *B. carinense* only being distributed in Myanmar and Thailand (Boulenger, 1889; Taylor, 1962). Our study supports this suggestion. Thus, the "*B. platyparietus*" lineage should be recognized as a distinct valid species within the genus (supplementary description on this species is given below). Currently, the species *B. platyparietus* is recognized from eastern and northern Yunnan, southern Sichuan, western Guangxi, and northeastern Guizhou.

DISCUSSION

In morphology, *Brachytarsophrys* differs significantly from other groups within Megophryinae by a combination of morphological characters (see Systematics below). Phylogenetically, *Brachytarsophrys* is a monophyletic group (Chen et al., 2017; Deuti et al., 2017; Mahony et al., 2017; Poyarkov et al., 2017; Zhang et al., 2017) and differentiated from other groups within Megophryinae with a series of geological and ecological changes ca. 38.94 million years ago (Liu et al., 2018). Ecologically, *Brachytarsophrys* species usually hide in deep crevices between rocks or boulders in streams during the breeding season (Fei & Ye, 2001; Fei et al., 2009; Smith, 1921; Taylor, 1962; Zhao et al., 2014), which is different from other species of Megophryinae (Wang et al., 2019; Yang et al., 2018). Therefore, *Brachytarsophrys* exhibits significant differences from other groups of Megophryinae in every aspect and should be considered a distinct genus.

For the two Megophryinae taxonomic proposals suggested by Chen et al. (2017) and Mahony et al. (2017), Chen's suggestion is inapposite because the genus *Xenophrys* (including *Panophrys*) is not monophyletic and the genus *Ophryophryne* is inserted between *Xenophrys* and *Panophrys*. The treatment by Mahony et al. (2017) is also controversial as it underrated the significant differences among several groups of Megophryinae, for instance, the species of *Brachytarsophrys*. Regarding the recognition of genus *Brachytarsophrys* and the principle of monophyly, these taxonomic conflicts may be resolved by elevation of the seven subgenera proposed by Mahony et al. (2017) to genus level, which fulfills the following three criteria to be descriptively useful: reasonably compact, monophyletic, and ecologically, morphologically, or biogeographically distinct (Gill et al., 2005).

The revalidation of *B. platyparietus* and the discovery of *Brachytarsophrys orientalis* **sp. nov**. take the members of the genus to seven species. Based on the morphological differences and phylogenetic relationships, we propose two species groups within *Brachytarsophrys*: i.e., (1) *Brachytarsophrys carinense* group (Group I in Figure 3), characterized by presence of dermal ridge or glandular fold on dorsum and large body size, including two species, *B. carinense* and *B. intermedia*; (2) *Brachytarsophrys feae* group (Group II in Figure 3), characterized by absence of dermal ridge or glandular fold on dorsum and large or small body size, including five species, *B. chuannanensis*, *B. feae*, *Brachytarsophrys orientalis* **sp. nov**., *B. platyparietus*, and *B. popei*.

Key to species of genus *Brachytarsophrys*

For identification, the seven species of *Brachytarsophrys* can be distinguished as follows:

1a) Presence of dermal ridge or glandular fold on dorsum..**2** (*B. carinense* group)

Table 4 Measurements (in mm; minimum−maximum, mean±*SD*) and body proportions of examined specimens of *Brachytarsophrys*

	Brachytarsophrys orientalis **sp. nov.**		*B. popei*		*B. platyparietus*		*B. chuannanensis*	*B. feae*	*B. intermedia*	
	M (*n*=7)	F (*n*=1)	M (*n*=13)	F (*n*=1)	M (*n*=6)	F (*n*=3)	M (*n*=12)	M (*n*=5)	M (*n*=7)	F (*n*=1)
SVL	76.8–82.7 (79.9±2.6)	88.6	70.7–83.5 (76.9±3.5)	86.2	88.5–113.0 (101.8±9.6)	118.5–131.0 (124.8±6.3)	91.4–109.4 (105.3 in CIB 98A0045)	78.5–94.9 (86.9±7.4)	86.0–103.0 (95.6±6.1)	92.0
HDL	32.8–35.0 (33.6±0.7)	40.8	29.8–34.2 (32.2±1.3)	36.0	37.1–47.0 (42.0±3.9)	46.5–52.5 (49.1±3.1)	44.8 in CIB 98A0045	31.5–35.9 (33.8±1.6)	–	–
SKL	20.1–21.5 (20.9±0.5)	24.6	17.7–20.6 (19.6±1.0)	21.2	23.9 in SYS a005919	30.6 in SYS a002236	–	21.0–23.3 (22.1±0.9)	23.0–28.0 (25.3±1.5)	27.0
HDW	39.1–42.3 (40.8±1.4)	48.8	36.0–40.8 (39.1±1.6)	42.5	43.1–57.0 (50.8±5.2)	55.7–61.0 (58.9±2.8)	54.1 in CIB 98A0045	37.7–44.4 (41.3±2.4)	44.0–51.0 (47.3±2.3)	50.0
SNT	9.0–10.6 (9.8±0.6)	12.2	8.5–10.3 (9.6±0.5)	10.6	9.9 in SYS a005919	13.5 in SYS a002236	–	9.2–10.5 (9.7±0.5)	11.0–13.0 (12.0±0.6)	12.0
IND	7.6–9.0 (8.4±0.5)	9.5	7.0–8.7 (7.8±0.4)	8.2	8.2 in SYS a005919	10.3 in SYS a002236	–	7.3–8.7 (8.3±0.6)	–	–
IOD	8.9–13.6 (12.0±1.7)	14.6	11.1–14.0 (12.0±1.2)	13.9	10.6 in SYS a005919	14.0 in SYS a002236	–	8.8–13.9 (11.0±2.0)	12.0–13.0 (12.4±0.5)	13.0
ED	8.5–10.7 (9.8±0.9)	10.4	7.8–10.6 (9.3±1.0)	9.8	8.7 in SYS a005919	9.9 in SYS a002236	–	7.6–11.3 (9.1±1.4)	–	–
HND	20.0–22.5 (21.3±0.8)	22.6	18.6–21.6 (19.8±1.0)	20.5	26.7 in SYS a005919	32.1 in SYS a002236	–	21.3–24.0 (22.7±1.0)	23.0–27.0 (24.4±1.3)	25.0
RAD	14.7–19.7 (17.5±1.7)	17.4	15.6–17.9 (16.9±0.8)	17.3	17.6 in SYS a005919	23.2 in SYS a002236	–	17.0–19.1 (17.8±0.9)	–	–
TIB	31.1–33.5 (32.1±1.0)	33.1	28.0–33.5 (30.8±1.6)	31.4	34.3 in SYS a005919	43.8 in SYS a002236	42.7 in CIB 98A0045	31.3–36.6 (33.6±1.9)	32.0–39.0 (35.9±2.1)	36.0
FTL	46.9–50.5 (48.4±1.1)	51.0	42.0–49.7 (46.1±2.3)	49.5	57.4 in SYS a005919	70.6 in SYS a002236	–	47.1–50.9 (48.9±1.4)	–	–
HDL/SVL	0.41–0.43 (0.42±0.01)	0.46	0.40–0.43 (0.42±0.01)	0.42	0.39–0.45 (0.41±0.02)	0.39–0.40 (0.39±0.01)	0.43 in CIB 98A0045	0.37–0.42 (0.39±0.02)	–	–
HDW/SVL	0.49–0.53 (0.51±0.01)	0.55	0.47–0.53 (0.51±0.02)	0.49	0.46–0.54 (0.50±0.03)	0.47–0.48 (0.47±0.01)	0.51 in CIB 98A0045	0.45–0.53 (0.48±0.03)	0.47–0.51 (0.50±0.02)	0.54
HDW/SKL	1.89–2.02 (1.95±0.05)	1.98	1.89–2.24 (2.00±0.09)	2.00	1.80 in SYS a005919	1.96 in SYS a002236	–	1.73–1.96 (1.87±0.10)	1.82–1.92 (1.87±0.04)	1.85
HDW/HDL	1.17–1.26 (1.22±0.04)	1.20	1.18–1.26 (1.21±0.03)	1.18	1.16–1.24 (1.21±0.03)	1.16–1.24 (1.20±0.04)	1.21 in CIB 98A0045	1.20–1.25 (1.22±0.02)	–	–
SNT/HDL	0.27–0.31 (0.29±0.01)	0.30	0.28–0.31 (0.30±0.01)	0.29	0.27 in SYS a005919	0.28 in SYS a002236	–	0.27–0.31 (0.29±0.02)	–	–
SNT/SVL	0.12–0.13 (0.12±0.01)	0.14	0.12–0.13 (0.13±0.00)	0.12	0.10 in SYS a005919	0.11 in SYS a002236	–	0.10–0.12 (0.11±0.01)	0.12–0.13 (0.13±0.00)	0.13
IND/IOD	0.60–0.92 (0.71±0.11)	0.65	0.60–0.71 (0.65±0.03)	0.59	0.77 in SYS a005919	0.74 in SYS a002236		0.61–0.94 (0.77±0.15)	–	–
IND/HDW	0.19–0.23 (0.21±0.02)	0.19	0.18–0.21 (0.20±0.01)	0.19	0.19 in SYS a005919	0.17 in SYS a002236	–	0.18–0.22 (0.20±0.01)	–	–
IOD/HDW	0.22–0.32 (0.29±0.04)	0.30	0.29–0.35 (0.31±0.02)	0.33	0.25 in SYS a005919	0.23 in SYS a002236	–	0.23–0.31 (0.26±0.03)	–	–
ED/HDL	0.26–0.32 (0.29±0.02)	0.25	0.25–0.33 (0.29±0.02)	0.27	0.23 in SYS a005919	0.20 in SYS a002236	–	0.24–0.31 (0.27±0.03)	–	–
ED/SVL	0.11–0.14 (0.12±0.01)	0.12	0.11–0.14 (0.12±0.01)	0.11	0.09 in SYS a005919	0.08 in SYS a002236	–	0.09–0.12 (0.10±0.02)	–	–
HND/SVL	0.25–0.28 (0.27±0.01)	0.26	0.24–0.28 (0.26±0.01)	0.24	0.28 in SYS a005919	0.26 in SYS a002236	–	0.25–0.29 (0.26±0.02)	0.23–0.27 (0.26±0.01)	0.27
RAD/SVL	0.19–0.24 (0.22±0.02)	0.20	0.20–0.24 (0.22±0.01)	0.20	0.19 in SYS a005919	0.19 in SYS a002236	–	0.19–0.23 (0.21±0.02)	–	–
TIB/SVL	0.39–0.42 (0.40±0.01)	0.37	0.38–0.43 (0.40±0.01)	0.36	0.36 in SYS a005919	0.35 in SYS a002236	0.41 in CIB 98A0045	0.36–0.42 (0.39±0.02)	0.35–0.41 (0.37±0.02)	0.39
FTL/SVL	0.58–0.65 (0.61±0.03)	0.58	0.57–0.63 (0.60±0.02)	0.57	0.61 in SYS a005919	0.57 in SYS a002236	–	0.53–0.61 (0.57±0.03)	–	–
References	This study		Zhao et al., 2014		Rao & Yang, 1997; this study		Fei & Ye, 2001; this study	This study	Smith, 1921	

F: Female; M: Male. –: Not available.

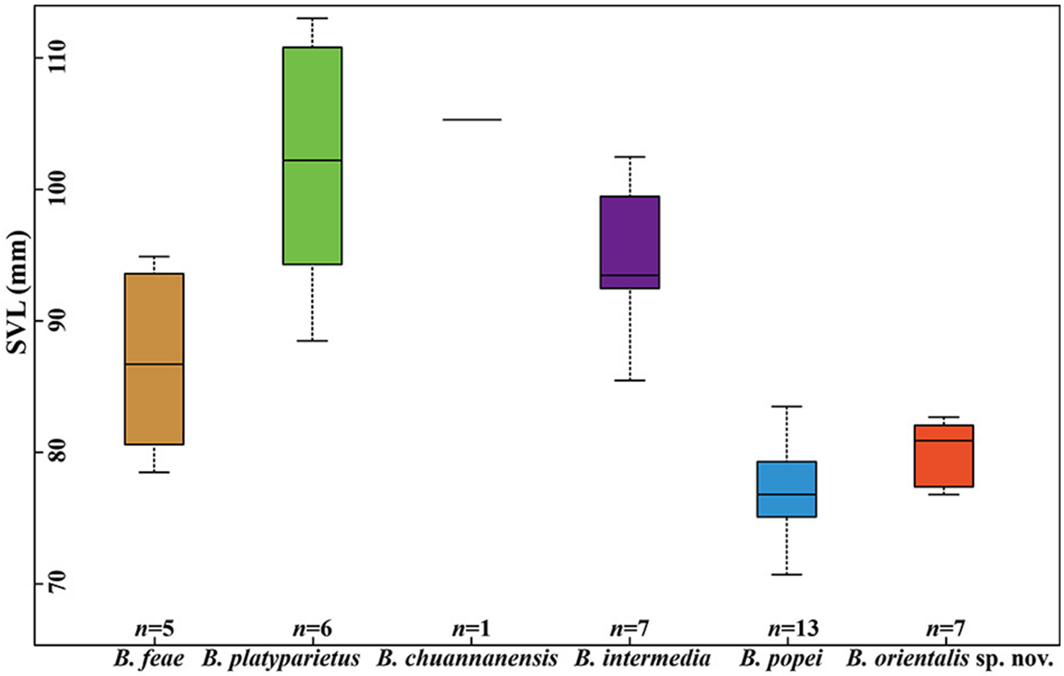

Figure 4 Boxplot of SVL showing body size variation among adult *Brachytarsophrys* males (data deficiency of *B. chuannanensis* and *B. carinense*)

Horizontal lines within each box represent median, and boxes encompass 75th and 25th percentile.

1b) Absence of dermal ridge or glandular fold on dorsum..**3** (*B. feae* group)

2a) Large body size, SVL 124.0–168.0 mm in females, 91.6–123.0 mm in males, tibiotarsal articulation reaching to axilla in females, to commissure of jaw in males.... .... *B. carinense*

2b) Moderate body size, SVL 92.0 mm in females, 86.0–103.0 mm in males, tibiotarsal articulation nearly reaching commissure of jaw..................................*B. intermedia*

3a) Pectoral region, lateral belly to lower flank of body, ventral surface, and rear of limbs with dense small, conical, horny tubercles...*B. platyparietus*

3b) Pectoral region, lateral belly to lower flank of body, ventral surface, and rear of limbs without horny tubercles...**4**

4a) Toe webbing rudimentary..**5**

4b) Toe webbing well developed...**6**

5a) Inter metatarsal tubercle approximately equal to first toe...*B. chuannanensis*

5b) Inter metatarsal tubercle longer than first toe.... ....*B. feae*

6a) Tongue feebly notched, smaller webbing, free web margin of IV toe only reaching base of articulation between fourth phalange and metatarsal, formula (4) IV (4)...... ....*Brachytarsophrys orientalis* **sp. nov.**

6b) Tongue deeply notched, larger webbing, free web margin of IV toe far beyond articulation between fourth phalange and metatarsal, formula (3⅔) IV (3⅔)...................... .... *B. popei*

SYSTEMATICS

Family Megophryidae Bonaparte, 1850
Subfamily Megophryinae Bonaparte, 1850
Genus *Brachytarsophrys* Tian & Hu, 1983

Type species: *Leptobrachium carinense* Boulenger, 1889

Diagnosis: (1) Large body size, habitus thickset and stout; (2) head enormous, and extremely depressed, head width approximately twice skull length; (3) presence of transverse groove, defining head behind; (4) tympanum hidden; (5) maxillary teeth present; (6) pupil vertical; (7) upper eyelid with several conical tubercles, one elongated, forming conical or flattened horn; (8) hindlimbs short and strongly thickset, heels not meeting, separated by greater distance; (9) toes with webbing and fringes; (10) inhabits deep crevices between rocks or boulders of streams during breeding season.

Suggested common name: Short-Legged Toads (in English) / Duan Tui Chan (短腿蟾 in Chinese).

Distribution: Tropical and subtropical eastern and southeastern mainland Asia, including southern China, Myanmar, Vietnam, Laos, and northern Thailand.

Remarks: The genus *Brachytarsophrys* was established with designating *Leptobrachium carinense* Boulenger, 1889 as the type species (Tian & Hu, 1983). However, from the original literature, the examined specimen of *L. carinense* by Tian & Hu (1983) was collected from Jingdong, Yunnan, China, and should not be identified as *B. carinense* but as *B. feae* (Boulenger, 1886).

Table 5 Diagnostic characters separating the seven *Brachytarsophrys* species from each other

Morphological characters	*Brachytarsophrys orientalis* **sp. nov.**	*B. popei*	*B. carinense*	*B. platyparietus*	*B. chuannanensis*	*B. feae*	*B. intermedia*
SVL of males (in mm)	76.8–82.7	70.7–83.5	91.6–123.0	88.5–113.0	91.4–109.4	78.5–94.9	86.0–103.0
SVL of females (in mm)	88.6	86.2	124.0–168.0	118.5–131.0	–	–	92.0
Tongue	Feebly notched behind	Deeply notched behind	Feebly notched behind	Feebly notched behind	Feebly notched behind	Feebly notched behind	Feebly notched behind
Dermal ridge or glandular fold on dorsum	Absent	Absent	Dermal ridge on dorsum	Absent	Absent	Absent	Glandular fold on dorsum
Small, conical, horny tubercles	Absent	Absent	Absent	Present on pectoral region, lateral belly to lower flank of body, ventral surface, and rear of limbs	Absent	Absent	Absent
Stellate bony	Absent	Absent	Stellate bony deposits in skin of parietal region and anterior part of dorsum	Absent	Absent	Stellate bony deposits on each side of parietal region	Absent
Webbing formula of male	I (1½)-(2) II (1½)-(3) III (2½)-(4) IV (4)-(2) V	I (1½)-(2) II (1½)-(3) III (2½)-(3⅔) IV (3⅔)-(2) V	–	I (1½)-(2^{+}) II (1½)-(3) III (2⅓)-(3⅔) IV (3⅔)-(2^{-}) V	I (1½)-(2^{++}) II (2)-(3^{++}) III (3)-(4) IV (4^{++})-(2½) V	I (2)-(2^{++}) II (2^{-})-(3) III (2⅔)-(4) IV (4)-(2⅔) V	–
Webbing formula of female	I (2)-(2^{+}) II (1⅔)-(3) III (3^{-})-(4) IV (4^{+})-(2½) V	I (1½)-(2^{+}) II (1½)-(3) III (2½)-(4^{-}) IV (4^{-})-(2) V	–	I (1½)-(2^{+}) II (1½)-(3) III (2⅔)-(4^{-}) IV (4^{-})-(2⅔) V	–	–	–
Lateral fringes on toes of male	One third as broad as distal toe phalanx	One fourth as broad as distal toe phalanx	–	Half as broad as distal toe phalanx	One fifth as broad as distal toe phalanx in CIB 98A0045	One fourth as broad as distal toe phalanx	–
Lateral fringes on toes of female	One sixth as broad as distal toe phalanx	One fifth as broad as distal toe phalanx	–	One fourth as broad as distal toe phalanx	–	–	–
Position of tibiotarsal articulation reaching	Commissure of jaw	Commissure of jaw	Axilla in females, angle of mouth in males	Commissure of jaw	Shoulder or commissure of jaw	Shoulder in females, commissure of jaw in males	Commissure of jaw
Transversal stripe on chest in tadpole	Absent	A transversal stripe on chest	–	–	A transversal stripe on chest	Several transversal stripes on chest	–

–: Not available.

Brachytarsophrys carinense **group**

Brachytarsophrys carinense **(Boulenger, 1889)**

Leptobrachium carinense: Boulenger, 1889.
Megophrys carinensis: Bourret, 1942.
Brachytarsophrys carinensis: Tian & Hu, 1983; Rao & Yang, 1997.
Megophrys (*Brachytarsophrys*) *carinensis*: Dubois, 1987.
Brachytarsophrys carinense: Delorme et al., 2006.
Megophrys (*Brachytarsophrys*) *carinense*: Mahony et al., 2017.

Syntypes: BMNH and NHMW 2291.1-2 (according to Häupl & Tiedemann (1978)) and MSNG 29689 (designated lectotype by Capocaccia (1957)), collected from western slopes of Karens Mountains (800 m a.s.l.), East of Toungoo, Myanmar.

Diagnosis: Based on the original description of Boulenger (1889) and supplementary description of Taylor (1962) and Mahony et al. (2017). (1) Large body size, SVL 124.0–168.0 mm in females, 91.6–123.0 mm in males; (2) head enormous, extremely depressed, head width nearly twice skull length; (3) tongue large, feebly notched behind; (4) canthus rostralis distinct, loreal region to temporal region very oblique; (5) tympanum hidden; (6) maxillary teeth present, vomerine teeth present on two widely-separated vomerine ridges; (7) digits without subarticular tubercles, tibiotarsal articulation reaching axilla in females, commissure of mouth in males; (8) very large, flat, oval inner metatarsal tubercle; (9) toes one third webbed; (10) presence of transverse fold separating head from body; (11) upper eyelid with two to four horn-like conical tubercles; (12) oblique dermal ridge on each side of anterior part of dorsum; (13) stellate bony deposits in skin of parietal region and anterior part of dorsum; (14) single subgular vocal sac in males.

Suggested common name: Broad-Headed Short-Legged Toad (in English) / Kuan Tou Duan Tui Chan (宽头短腿蟾 in Chinese).

Distribution and habitats: Currently, *B. carinense* is recognized from southern Myanmar and adjacent northern Thailand at elevations of 800 m and upwards. This toad hides in crevices between rocks or between the roots of shrubs during the day (Boulenger, 1889; Taylor, 1962).

Brachytarsophrys intermedia **(Smith, 1921)**

Megalophrys intermedius: Smith, 1921.
Megophrys intermedia: Bourret, 1942.
Brachytarsophrys intermedia: Rao & Yang, 1997.
Megophrys (*Brachytarsophrys*) *intermedia*: Mahony et al., 2017.

Syntypes: BMNH (11 specimens—formerly M. Smith) 2067, 2073, 2075–76, 2078, 2085–86, adult males, 2070, adult female, 2083–84, young females, and 2074, without gender data, collected from the Langbian Plateau (1 500 m a.s.l.), Vietnam.

Diagnosis: Based on the original description of Smith (1921). (1) Medium body size, SVL 92.0 mm in one adult female, 86.0–103.0 mm in seven adult males; (2) head enormous and depressed, head width nearly twice skull length; (3) tongue feebly notched behind; (4) maxillary teeth present, vomerine teeth present on two widely-separated vomerine ridges; (5) snout round, not protruding beyond margin of lower jaw, canthus rostralis distinct; (6) loreal region to temporal region very oblique; (7) tympanum hidden; (8) presence of transverse groove behind head, separating head from body; (9) digits without subarticular tubercles, tibiotarsal articulation reaching to commissure of jaw; (10) large, flat, oval inner metatarsal tubercles; (11) toes one third to one half webbed, web extending as fringe along either side of toes; (12) paired oblique glandular folds on dorsum; (13) upper eyelid with several conical tubercles, one enlarged to form long horn.

Suggested common name: Annam Short-Legged Toad (in English) / Yue Nan Duan Tui Chan (越南短腿蟾 in Chinese).

Distribution and habitats: The species occurs in the central highlands of southern Vietnam and Laos at elevations above 900 m. Most specimens have been discovered in deep crevices between the rocks or boulders of streams. Loud, harsh male croaks can be heard at all times of the day and night (Smith, 1921).

Brachytarsophrys feae **group**

Brachytarsophrys chuannanensis **Fei, Ye & Huang, 2001**

(Figure 5)

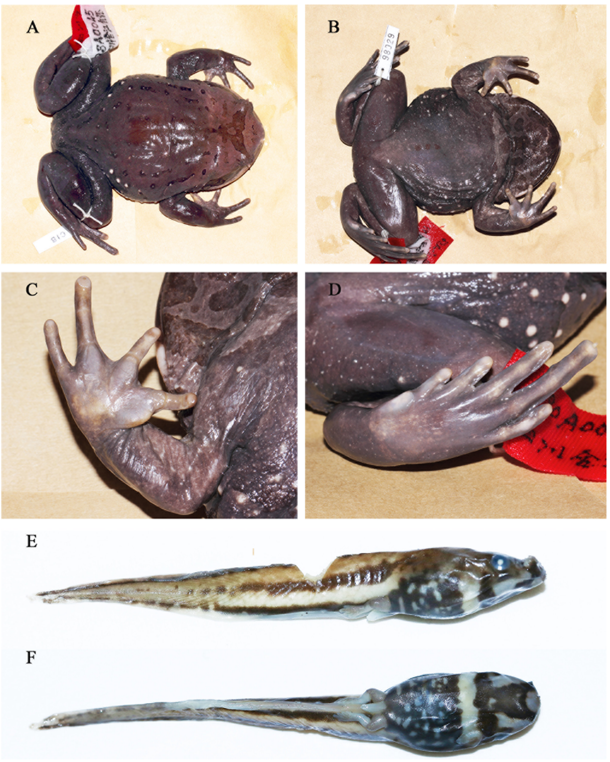

Figure 5 General aspect of *Brachytarsophrys chuannanensis*

A: Dorsolateral view of adult male holotype CIB 98A0045 in preservative; B: Ventral view of holotype CIB 98A0045 in preservative; C, D: Hand and foot of holotype CIB 98A0045 in preservative; E, F: Ventral view of 38th stage tadpole of *B. chuannanensis*.

Brachytarsophrys chuannanensis: Fei & Ye, 2001.
Megophrys (*Brachytarsophrys*) *chuannanensis*: Mahony et al., 2017.

Holotype: CIB 98A0045, adult male, collected from Zihuai (E105°49′, N28°48′; 850 m a.s.l.), Hejiang County, Sichuan Province, China.

Paratypes: Eleven adult males without specimen number data.

Examined specimens: One specimen. Holotype CIB 98A0045.

Diagnosis: Based on the original description of Fei & Ye (2001) and examined specimen. (1) Large body size, SVL 91.4–109.4 mm in 12 adult males; (2) head enormous and depressed, head width nearly twice skull length; (3) maxillary teeth well developed, vomerine teeth present on two widely-separated vomerine ridges; (4) snout round, slightly protruding beyond margin of lower jaw; (5) tympanum hidden; (6) toes with rudimentary webbing; (7) heels not meeting; (8) tibiotarsal articulation reaching to shoulder or posterior margin of mouth; (9) inner metatarsal tubercle approximately equal to first toe; (10) upper eyelids with several small tubercles, one enlarged, forming horn; (11) presence of transverse groove, defining head behind; (12) male with single subgular vocal sac, dorsal surface of first and second finger bases with black brown nuptial pad; (13) tadpole with a transversal stripe on ventral surface.

Suggested common name: Southern Sichuan Short-Legged Toad (in English) / Chuan Nan Duan Tui Chan (川南短腿蟾 in Chinese).

Distribution and habitats: The species is distributed in Hejiang and Junlian counties, Sichuan Province, southwestern China, at 800 to 1 400 m a.s.l.. Specimens are found in or near montane streams surrounded by lush vegetation. They usually hide in crevices between rocks or dirt burrows in streams during the day. Males emit a series of croaks at about 23:00h. The spawning season is around the middle of May (Fei & Ye, 2001).

***Brachytarsophrys feae* (Boulenger, 1886)** (Figure 6)
Megalophrys feae: Boulenger, 1886.
Leptobrachium feae: Boulenger, 1889.
Megophrys feae: Gee & Boring, 1929.
Brachytarsophrys feae: Rao & Yang, 1997.
Megophrys (*Brachytarsophrys*) *feae*: Mahony et al., 2017.

Holotype: MSNG 29763, female (according to Capocaccia (1957)), collected from Khakhyen Hills, East of Bhamò, Myanmar.

Examined specimens: Five specimens. SYS a001770–1771, adult males, collected from Zhenyuan County, Yunnan Province, China; SYS a003912–3914, adult males, collected from Jingdong County, Yunnan Province, China.

Figure 6 General aspect of *Brachytarsophrys feae*
A: Dorsolateral view of adult male SYS a003914 in life; B: Ventral view of adult male SYS a003914 in life; C, D: Hand and foot of adult male SYS a003914 in life; E: Ventral view of 44th stage tadpole of *B. feae*.

Diagnosis: Based on the original description of Boulenger (1886), supplementary description of Fei et al. (2009), and examined specimens. (1) Moderate body size, SVL 78.5–94.9 mm in five adult males; (2) head enormous, extremely depressed, head width approximately twice skull length; (3) tongue pyriform, feebly notched behind; (4) maxillary teeth present, vomerine teeth present on two vomerine ridges; (5) canthus rostralis indistinct, loreal region concave, temporal region oblique; (6) tympanum hidden; (7) tibiotarsal articulation reaching axilla or commissure of jaw; (8) very large, flat, oval inner metatarsal tubercle, longer than first toe; (9) toes with rudimentary webbing; (10) upper eyelid with several small tubercles, one enlarged, forming horn; (11) absence of dermal ridge on dorsum; (12) stellate bony deposits on each side of parietal region; (13) male with single subgular vocal sac, dorsal surface of first and second finger bases with black brown nuptial pad; (14) tadpole with several transversal stripes on ventral surface.

Suggested common name: Fea 's Short-Legged Toad (in English) / Fei Shi Duan Tui Chan (费氏短腿蟾 in Chinese).

Distribution and habitats: This species is currently recognized from northern Myanmar and Yunnan Province in southwestern China at 650 to 2 100 m a.s.l.. Specimens are found in montane streams, under rocks or deep burrows surrounded by moist evergreen broadleaf forests. Male individuals begin to emit a series of croaks in April. The spawning season is from May to June (Fei & Ye, 2009; this study).

***Brachytarsophrys popei* Zhao, Yang, Chen, Chen & Wang, 2014** (Figure 7)
Brachytarsophrys popei: Zhao et al., 2014.
Megophrys (*Brachytarsophrys*) *popei*: Mahony et al., 2017.

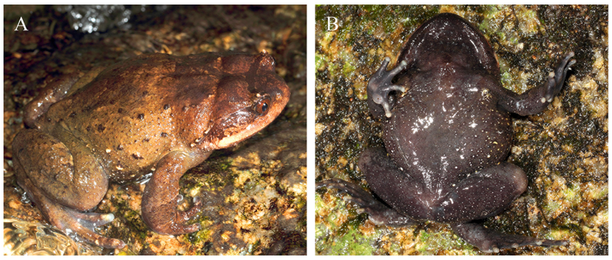

Figure 7 General aspect of *Brachytarsophrys popei*

A: Dorsolateral view of adult male holotype SYS a001867 in life; B: Ventral view of holotype SYS a001867 in life.

Holotype: SYS a001867, adult male, collected from Taoyuandong Nature Reserve (N26°30′8.79″, E114°03′38.27″; 1 045 m a.s.l.), Yanling County, Hunan Province, China.

Paratypes: SYS a001864–1866, adult males, collected from same locality as holotype; SYS a001874, 1876–1878, adult males, SYS a001875, adult female, collected from Mount Jinggang (N26°29'51.85", E114°04'50.68"; 923 m–1 270 m a.s.l.), Jinggangshan City, Jiangxi Province, China; SYS a000583–0585, 0588–0589, adult males, collected from Nanling Nature Reserve (N24°56'14.19", E113°0'13.12"; 1 089 m–1 304 m a.s.l.), Ruyuan County, Guangdong Province, China.

Examined specimens: Nine specimens. Holotype SYS 001867 and paratypes SYS a001864–1866, SYS a001874–1878.

Diagnosis: Based on the original description of Zhao et al. (2014) and examined specimens. (1) Relatively small body size, SVL 86.2 mm in one adult female, 70.7–83.5 mm in 13 adult males; (2) head enormous, and extremely depressed, head width approximately twice skull length; (3) tongue pyriform, deeply notched behind; (4) maxillary teeth present, vomerine teeth present on two vomerine ridges; (5) tympanum hidden; (6) heels not meeting; (7) tibiotarsal articulation reaching to commissure of jaw; (8) toes about one third to two thirds webbed in males; (9) upper eyelid with several tubercles, one enlarged, forming horn; (10) males with single subgular vocal sac, first and second finger bases with dense tiny black nuptial spines; (11) tadpole with a transverse white stripe on chest reaching spiracle.

Suggested common name: Pope's Short-Legged Toad (in English) / Po Pu Duan Tui Chan (珀普短腿蟾 in Chinese).

Distribution and habitats: *Brachytarsophrys popei* populations occur in Taoyuandong Nature Reserve, Hunan Province, adjacent Mt. Jinggang, Jiangxi Province, and Nanling Reserve, Guangdong Province, southeastern China, at 900 to 1 300 m a.s.l.. The species can be found under rocks in montane streams surrounded by moist subtropical evergreen broadleaf forests. Males emit a series of croaks from July to September (Zhao et al., 2014).

Figure 8 General aspect of *Brachytarsophrys platyparietus*

A: Dorsolateral view of adult male SYS a005919 in life; B: Ventral view of adult male SYS a005919 in life; C, D: Hand and foot of adult male SYS a005919 in life.

***Brachytarsophrys platyparietus* Rao & Yang, 1997**
(Figure 8)

Brachytarsophrys platyparietus: Rao & Yang, 1997.
Brachytarsophrys carinensis: Fei et al., 2009.
Brachytarsophrys carinense: Chen et al., 2017.

Holotype: KIZ 90275, adult male, collected from Duodihe, Santai Township, Dayao County, Yunnan Province, China.

Paratypes: KIZ 90274, adult male, and KIZ 90276, adult female, collected from same locality as holotype.

Examined specimens: Thirteen specimens. KIZ 91001, 91002, 90267, 90273, adult males, KIZ 90270, adult female, and SYS a005919, adult male, collected from same locality as holotype; SYS a007774–7777, adult males, collected from Mt. Mopan, Xinping Yi and Dai Autonomous County, Yunnan Province, China; SYS a007790, adult male, collected from Yilong Township, Shiping County, Yunnan Province, China; SYS a007853, adult male, collected from Yumen Township, Yanbian County, Sichuan Province, China; SYS a002236, adult female, collected from Mt. Jinzhong, Longlin Various Nationalities Autonomous County, Guangxi Zhuang Autonomous Region, China.

Revision of diagnosis: *Brachytarsophrys platyparietus* differs from other known congeners by the following combination of morphological characters: (1) relatively large body size, SVL 118.5–131.0 mm in three adult females, SVL 88.5–113.0 mm in six adult males; (2) head enormous, slightly flattened, head width nearly 1.2 times as long as head length, and nearly twice skull length; (3) tibiotarsal articulation reaching to commissure of jaw in males and females; (4) outer metatarsal tubercle absent, inner metatarsal tubercle approximately equal to first toe; (5) slightly larger webbing, from distal metatarsals to basal toes, webbing formula I (1½)-(2^{+}) II (1½)-(3) III (2⅓)-(3⅔) IV (3⅔)-(2^{-}) V in males; (6) lateral fringes of males more developed than those of females, nearly half as broad as distal toe phalanx in males; (7) horn-shaped tubercle on upper eyelid extremely elongate, forming a long pointed and compressed horn in female; (8) dorsum and flank of body without dermal ridge; (9) numerous small, conical, horny tubercles scattered on pectoral region, lateral belly to lower flank of body, ventral surface, and rear of limbs.

Comparisons: *Brachytarsophrys platyparietus* has been treated as a synonym of *B. carinense*, but differs significantly from *B. carinense* by a combination of the following characters: dermal ridge on dorsal surface absent (vs. present in *B. carinense*); stellate bony deposits in skin absent (vs. stellate bony deposits in skin of parietal region and anterior part of dorsum in *B. carinense*); large warts on dorsal limbs present, but dermal ridges absent (vs. slight oblique dermal ridges across limbs in *B. carinense*); first finger longer than second (vs. first finger not extending beyond second in *B. carinense*); tibiotarsal articulation reaching commissure of jaw in females (vs. reaching axilla in females of *B. carinense*).

Brachytarsophrys platyparietus differs from all remaining congeners by a combination of the following characters: numerous small, conical, horny tubercles on pectoral region, lateral belly to lower flank of body, ventral surface, and rear of limbs (Figure 9 and Table 5). *Brachytarsophrys platyparietus* differs from *B. feae* by slightly larger webbing, from distal metatarsals to basal toes, webbing formula I (1½)-(2^{+}) II (1½)-(3) III (2⅓)-(3⅔) IV (3⅔)-(2^{-}) V in males (vs. smaller webbing, from distal metatarsals to basal toes, webbing formula I (2)-(2^{++}) II (2^{-})-(3) III (2⅔)-(4) IV (4)-(2⅔) V in males of *B. feae*); lateral fringes on toes wide, nearly half as broad as distal toe phalanx in males (vs. narrow, less than one fourth of distal toe phalanx in males of *B. feae*); stellate bony deposits absent (vs. stellate bony deposits on each side of parietal region in *B. feae*); inner metatarsal tubercle approximately equal to first toe (vs. inner metatarsal tubercle longer than first toe in *B. feae*). *Brachytarsophrys platyparietus* differs from *B. chuannanensis* by foot with slightly larger webbing, from distal metatarsals to basal toes, webbing formula I (1½)-(2^{+}) II (1½)-(3) III (2⅓)-(3⅔) IV (3⅔)-(2^{-}) V in males (vs. smaller webbing, from distal metatarsals to basal toes, webbing formula I (1½)-(2^{++}) II (2)-(3^{++}) III (3)-(4) IV (4^{++})-(2½) V in holotype CIB 98A0045 of *B. chuannanensis*); wide lateral fringes on toes, nearly half as broad as distal toe phalanx in males (vs. narrow, less than one fifth of distal toe phalanx in holotype CIB 98A0045 of *B. chuannanensis*).

Figure 9 Numerous small, conical, horny tubercles in *Brachytarsophrys platyparietus*.

A, B: Conical horny tubercles in adult male SYS a005919; C, D: Conical horny tubercles in adult female SYS a002236.

Brachytarsophrys platyparietus differs from *B. popei* by a combination of the following characters: large body size, SVL 118.5–131.0 mm in three adult females, SVL 88.5–113.0 mm in six adult males (vs. 86.2 mm in one adult female, 70.7–83.5 mm in 13 adult males in *B. popei*); outer metacarpal tubercles absent (vs. present in *B. popei*); horn-shaped tubercle on upper eyelid extremely elongate, pointed, and compressed in females (vs. relatively short, blunt, and conical in females of *B. popei*). *Brachytarsophrys platyparietus* differs from *B. intermedia* by oblique glandular fold on dorsum absent (vs. present in *B. intermedia*); folds across limbs absent (vs. present in *B. intermedia*).

Description of topotype specimen: SYS a005919, adult male. Body stout, large body size, SVL 94.3 mm; head enormous and flattened, head width nearly 1.2 times as long as head length, and nearly twice skull length (HDW/SKL ratio 1.80); two visible, large rounded bulges on occipital region, forming broad longitudinal concave groove along middle line across occiput, and distinct transverse groove, defining head behind; snout short (SNT/SVL ratio 0.10), rounded in dorsal view, slightly protruding beyond margin of lower jaw; canthus rostralis rounded; loreal region oblique, slightly concave; nostril oval, close to tip of snout; internasal distance significantly smaller than interorbital distance (IND/IOD ratio 0.77); pupil vertical; temporal region oblique; tympanum completely hidden; choanae partly concealed by maxillary shelves; maxillary teeth well developed; vomerine teeth present on two vomerine ridges between choanae; vomerine ridges long, posterior level behind posterior level of choanae, widely separated by large distance approximately two times as long as length of one ridge; tongue pyriform, feebly notched behind.

Forelimbs short and moderately robust; hands short (HND/SVL ratio 0.28); relative finger lengths II<I<IV<III; tips of digits round, slightly dilated; no webbing or lateral fringes on fingers; no subarticular tubercles and no outer metacarpal tubercle, inner metacarpal tubercle significantly enlarged.

Hindlimbs short and robust (TIB/SVL ratio 0.36); tibiotarsal articulation reaching commissure of jaw when hindlimbs stretched alongside body; heels not meeting, separated by 8.0 mm when hindlimbs flexed at right angles to axis of body; relative toe lengths I<II<V<III<IV; tips of toes round, moderately dilated; no subarticular tubercles; no tarsal gland; inter metatarsal tubercle prominent, elongate, approximately equal to first toe, outer metatarsal tubercle absent; slightly larger webbing, from distal metatarsals to basal toes, webbing formula I (1½)-(2^{+}) II (1½)-(3) III (2⅓)-(3⅔) IV (3⅔)-(2^{-}) V; webbing extending as wide fringe along either side of toes, nearly half as broad as distal toe phalanx.

Dorsal skin of head smooth; upper eyelid with several large conical tubercles, middle one extremely elongate, forming long conical horn; supratympanic fold distinct, from posterior corner of eye to upper arm insertion on each side; dorsum and flank of body slightly rough without dermal ridge, scattered with some large glandular warts and small tubercles; pair of symmetrical conical warts on front of shoulders; dorsal limbs with several large warts and small tubercles, not arranged in row; ventral surface of head, body, and limbs smooth, with several glandular warts arranged on rear of thigh and around vent; numerous small, conical, horny tubercles scattered on pectoral region, lateral belly to lower flank of body, ventral surface, and rear of limbs; pectoral gland and femoral gland invisible.

Measurements (in mm): SVL 94.3, HDL 37.1, SKL 23.9, HDW 43.1, SNT 9.9, IND 8.2, IOD 10.6, ED 8.7, HND 26.7, RAD 17.6, TIB 34.3, FTL 57.4.

Coloration: In life, dorsal surface of head brown with dark blotches and stripes; wide dark brown stripe bordered with yellow between eyes, pair of short oblique discontinuous dark stripes bordered with yellow above shoulder; warts and tubercles light-colored bordered with yellow; eyes surrounded by star-shaped dark brown marking bordered with yellow; temporal region under supratympanic fold with broad dark brown stripe bordered with light yellow; dorsal digits with black cross-bars; chin, throat, pectoral region brown with faint dark blotches, two large longitudinal dark stripes edged with yellow on lateral throat; pupils black; iris brownish red.

In preservative, dorsal and ventral surfaces dark brown, yellow border edge on stripes between eyes, above shoulder, and on lateral throat faded to light yellow, inter metatarsal tubercle faded to grayish-white.

Variation: Measurements are given in Table 4 and variations are as follows: SYS a007776 and SYS a007777, slightly larger webbing, toe webbing formula I (1½)-(2) II (1½)-(3) III (2½)-(3½) IV (3½)-(2) V. SYS a002236, adult female, heels not meeting, separated by 9.5 mm; foot webbing and lateral fringes of toes slightly smaller than those of adult male specimens, toe webbing formula I (1½)-(2^+) II (1½)-(3) III (2⅔)-(4^-) IV (4^-)-(2⅔) V; webbing extending as fringe along either side of toes, nearly one fourth as broad as distal toe phalanx; yellowish brown body.

Male secondary sexual characteristics: Male with single subgular vocal sac; dorsal surface of first and second finger bases with indistinct, not elevated nuptial pad, bearing dense tiny black nuptial spines (in preservative).

Suggested common name: Flat-Headed Short-Legged Toad (in English) / Ping Tou Duan Tui Chan (平头短腿蟾 in Chinese).

Distribution and habitats: Currently, *Brachytarsophrys platyparietus* is recognized from Duodihe of Dayao County, Mt. Mopan of Xinping County, Yilong Township of Shiping County, Mt. Jinzhong of Longlin County, Mt. Fanjing of Tongren City, Yumen Township of Yanbian County, indicating its potential distribution areas, which range across central southwestern China at around 2 000 m a.s.l.. These toads inhabit montane streams surrounded by moist subtropical evergreen broadleaf forests. Some adult males have been found near batches of eggs attached to the bottom of a rock, suggesting that adult males may exhibit egg protection behavior (Figure 10).

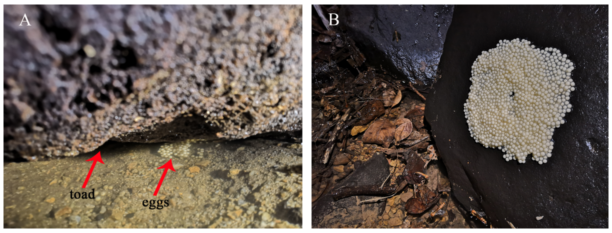

Figure 10 Egg protection behavior in *Brachytarsophrys platyparietus*

A: Under rock, adult male on left protected eggs on right; B: Eggs of *B. platyparietus.*

***Brachytarsophrys orientalis* sp. nov. Y Li, Lyu, J Wang & YY Wang** (Figure 11)

Holotype: SYS a004227, adult male, collected by Jian Wang and Hai-Long He, on 4 August 2015 from Jiulianshan Nature Reserve (N24°34'47", E114°26'9"; 400 m a.s.l.), Longnan County, Jiangxi Province, China.

Paratypes: Five specimens from the same locality as the holotype: SYS a004225/ CIB 110009, SYS a004226 and 4228, adult males, same collection data as holotype; SYS a004486, adult female, collected by Jiang Wang and Hai-Long He on 22 September 2015; SYS a005451, adult male, collected by Zhi-Tong Lyu and Hai-Long He on 21 August 2016.

Other examined specimens: SYS a003249, adult male, collected by Run-Lin Li on 20 August 2014 from Gutian Township (N25°13'11", E116°49'43"; 700 m a.s.l.), Shanghang County, Fujian Province, China; SYS a003340, adult male, collected by Zhi-Tong Lyu and Zu-Yao Liu on 22 August 2014 from Huboliao Natural Reserve (N24°40'28", E117°5'21"; 200 m a.s.l.), Nanjing County, Fujian Province, China; SYS

Figure 11 General aspect of *Brachytarsophrys orientalis* sp. nov.

A: Dorsolateral view of adult male holotype SYS a004227 in life; B: Ventral view of holotype SYS a004227 in life; C, D: Hand and foot of holotype SYS a004227 in life.

a004622, tadpole in stage 36, collected from same locality as holotype by Jian Wang, Zhi-Tong Lyu and Hai-Long He on 01 April 2016.

Diagnosis: *Brachytarsophrys orientalis* **sp. nov.** is characterized by the following combination of morphological characters: (1) relatively small body size, SVL 88.6 mm in single adult female, SVL 76.8–82.7 mm in seven adult males; (2) head enormous and depressed, head width nearly 1.2 times as long as head length and nearly twice skull length; (3) tongue pyriform, feebly notched behind; (4) heels not meeting; (5) tibiotarsal articulation reaching to commissure of jaw; (6) outer metatarsal tubercle absent, inner metatarsal tubercle approximately equal to first toe; (7) smaller webbing, from distal metatarsals to basal toes, webbing formula I (1½)-(2) II (1½)-(3) III (2½)-(4) IV (4)-(2) V in males; (8) lateral fringes of males more developed than those of females, nearly one third as broad as distal toe phalanx in males; (9) absence of a transversal stripe on chest in tadpole.

Comparisons: Comparative data of *Brachytarsophrys orientalis* **sp. nov**. with other congeners are listed in Table 5. *Brachytarsophrys orientalis* **sp. nov**. differs from its sister taxon *B. popei* by the following characters: tongue feebly notched (vs. tongue deeply notched in *B. popei*); smaller webbing, webbing formula I (1½)-(2) II (1½)-(3) III (2½)-(4) IV (4)-(2) V in males, I (2)-(2$^+$) II (1⅔)-(3) III (3$^-$)-(4) IV (4$^+$)-(2½) V in females (vs. slightly larger webbing, webbing formula I (1½)-(2) II (1½)-(3) III (2½)-(3⅔) IV (3⅔)-(2) V in males, I (1½)-(2$^+$) II (1½)-(3) III (2½)-(4$^-$) IV (4$^-$)-(2) V in females of *B. popei*) (Figure 12A–D); transversal stripe on chest in tadpole absent (vs. a transversal stripe reaching spiracle in *B. popei*) (Figure 12E–H).

Brachytarsophrys orientalis **sp. nov**. differs from the remaining five congeners by the following combination of morphological characters: small body size, SVL 88.6 mm in one adult female, SVL 76.8–82.7 mm in seven adult males (vs. 124.0–168.0 mm in adult females, 91.6–123.0 mm in adult males in *B. carinense*; 118.5–131.0 mm in three adult females, 88.5–113.0 mm in six adult males in *B. platyparietus*; 91.4–109.4 mm in 12 adult males in *B. chuannanensis*; 92.0 mm in one adult female, 86.0–103.0 mm in seven adult males in *B. intermedia*). *Brachytarsophrys orientalis* **sp. nov**. further differs from *B. platyparietus* by absence of numerous small, conical, horny tubercles on pectoral region, lateral belly to lower flank of body, ventral surface, and rear of limbs (vs. present in *B. platyparietus*). *Brachytarsophrys orientalis* **sp. nov**. further differs from *B. chuannanensis* and *B. feae* by lateral fringes on toes wide, nearly one third as broad as distal toe phalanx in males (vs. narrow, less than one fourth of distal toe phalanx in males of *B. feae*, less than one fifth in *B. chuannanensis*); transversal stripe on chest in tadpoles absent (vs. transversal stripe reaching spiracle in tadpole in *B. chuannanensis* and *B. feae*). *Brachytarsophrys orientalis* **sp. nov**. differs from *B. carinense* and *B. intermedia* by lack of dermal ridge on dorsum (vs. oblique dermal ridge on each side of anterior half dorsum in *B. carinense*, oblique glandular fold on dorsum in *B. intermedia*).

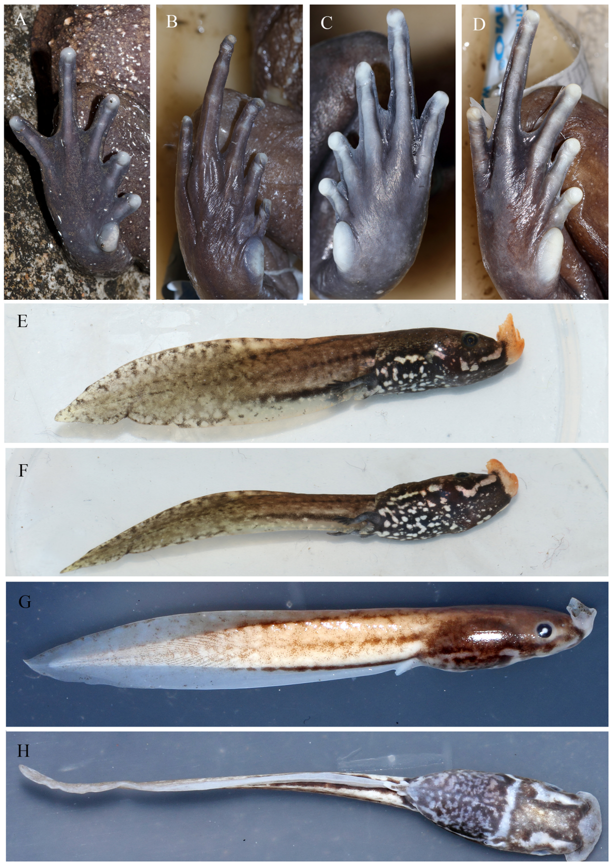

Figure 12 Morphological differences between *Brachytarsophrys orientalis* sp. nov. and *B. popei*

A: Sole of feet in male holotype SYS a004227 of *Brachytarsophrys orientalis* **sp. nov**.; B: Sole of feet in female paratype SYS a004486 of *Brachytarsophrys orientalis* **sp. nov**.; C: Sole of feet in male holotype SYS a001867 of *B. popei*; D: Sole of feet in female paratype SYS a001875 of *B. popei*; E, F: Ventral view of 36th stage tadpole of *Brachytarsophrys orientalis* **sp. nov.**; G, H: Ventral view of 29th stage tadpole of *B. popei*.

Description of holotype: Body stout, moderate body size, SVL 82.7 mm; head enormous and depressed, head width nearly 1.2 times as long as head length, and nearly twice skull length (HDW/SKL ratio 1.98); two visible large rounded bulges on occipital region, forming broad longitudinal concave groove along middle line across occiput, and distinct transverse groove, defining head behind; snout short (SNT/SVL ratio 0.12) and round, slightly protruding beyond margin of lower jaw; canthus rostralis indistinct, not sharp; loreal region oblique, slightly concave; nostril oval, close to tip of snout; internasal distance smaller than interorbital distance (IND/IOD ratio 0.63); pupil vertical; temporal region oblique, slightly concave; tympanum hidden; maxillary teeth well developed; vomerine teeth present on two vomerine ridges between choanae; vomerine ridges long, posterior level behind posterior level of choanae, widely separated by large distance approximately 1.5 times as long as length of one ridge; tongue pyriform, feebly notched behind.

Forelimbs short and moderately robust; hands short (HND/SVL ratio 0.26); relative finger lengths II<I<IV<III; tips of digits round, slightly dilated; no webbing or lateral fringes on fingers; no subarticular tubercles; inner metacarpal tubercle significantly enlarged, outer metacarpal tubercle slightly enlarged.

Hindlimbs short and robust (TIB/SVL ratio 0.40); tibiotarsal articulation reaching commissure of jaw when hindlimbs stretched alongside body; heels not meeting, separated by 5.6 mm when hindlimbs flexed at right angles to axis of body; relative toe lengths I<II<V<III<IV; tips of toes round, moderately dilated; no subarticular tubercles; no tarsal glands; inter metatarsal tubercle prominent, elongate, approximately equal to first toe, outer metatarsal tubercle absent; smaller webbing, from distal metatarsals to basal toes; webbing formula I (1½)-(2) II (1½)-(3) III (2½)-(4) IV (4)-(2) V; webbing extending as wide fringe along either side of toes, nearly one third as broad as distal toe phalanx.

Dorsal skin of head smooth; upper eyelids with several large conical tubercles, one enlarged, forming horn; supratympanic fold distinct, from posterior corner of eye to upper arm insertion on each side; dorsum and flank of body slightly rough, scattered with some large glandular warts and small tubercles; dorsal limbs with some small tubercles; ventral surface of head, body, and limbs smooth, some tubercles arranged on rear of thigh and around vent; pectoral gland distinct and irregular, femoral gland indistinct.

Measurements (in mm): SVL 82.7, HDL 33.8, SKL 21.3, HDW 42.2, SNT 10.3, IND 8.6, IOD 13.6, ED 10.2, HND 21.6, RAD 19.7, TIB 33.3, FTL 48.6.

Coloration: In life, dorsal surface of head and body brown with dark blotches and stripes; irregular dark brown V-shaped marking between eyes, some small dark blotches on posterior of occiput forming distinct wide streak; dark tubercles on dorsum, cream yellow tubercles on sides of body; upper lip light brown; tympanic region brown; some irregular black blotches on dorsal limbs; dorsal digits with brown blotches and cream white blotches; ventral surface grayish brown with small white granular spots; pectoral gland yellowish; tip of digits, metacarpal tubercles, and inner metatarsal tubercle pale; pupils black; iris brownish.

In preservative, dorsal and ventral surfaces dark brown; upper lip cream; irregular dark brown V-shaped marking becoming indistinct, pectoral gland and tubercles fading to grayish-white.

Description of tadpole: Body slender, oval; tail depth slightly larger than body depth; dorsal fin arising just before origin of tail, tapering gradually to narrow, pointed tip; tail 2.2 times as long as body length, BL 12.3 mm and TL 27.6 mm in 36th stage tadpole (Figure 12E–F). Eyes large, lateral; nostrils dorsolateral; spiracle on left side of body, closer to eye than to end of body; anal tube long, attached to ventral fin; oral disk with lips expanded vertically forming dorsally oriented funnel.

Body brown; two short, longitudinal white stripes on sides of ventral surface of head; posteriorly absent transversal white stripe on chest; two short longitudinal white stripes along sides of body; belly mottled with dense white speckles between two longitudinal stripes; tail with three short dark longitudinal stripes, one at base of dorsal fin, one at base of ventral fin, one on middle line of tail of tadpole.

Variation: Measurements of type series are given in Table 4. All specimens were similar in morphology and color pattern. The female paratype SYS a004486 differs from males by foot webbing and lateral fringes of toes slightly smaller than those of adult male specimens, toe webbing formula I (2)-(2^{+}) II (1⅔)-(3) III (3^{-})-(4) IV (4^{+})-(2½) V in female; webbing extending as fringe along either side of toes, nearly one sixth as broad as distal toe phalanx; yellowish brown body. Enlarged tubercles on edge of upper eyelid longer in SYS a004225 and SYS a004226.

Male secondary sexual characteristics: Male with single subgular vocal sac; nuptial pad on dorsal surface of first and second fingers, nuptial spines black (in preservative).

Etymology: The specific name "*orientalis*" refers to the distribution of the new species, which is the easternmost species within the genus *Brachytarsophrys*.

Suggested common name: Oriental Short-Legged Toad (in English) / Dong Fang Duan Tui Chan (东方短腿蟾 in Chinese).

Distribution and habitats: Currently, *Brachytarsophrys orientalis* **sp. nov.** is only known from the Jiulianshan Nature Reserve in Jiangxi Province and Gutian Township and Huboliao Nature Reserve in Fujian Province, China, at 200 to 700 m a.s.l.. This species is found under rocks in montane streams surrounded by moist subtropical evergreen broadleaf forests (Figure 1B). All male individuals were observed in August and emitted a series of croaks from hidden positions.

NOMENCLATURAL ACTS REGISTRATION

The electronic version of this article in portable document format represents a published work according to the International Commission on Zoological Nomenclature (ICZN), and hence the new names contained in the electronic version are effectively published under that Code from the electronic edition alone (see Articles 8.5–8.6 of the Code). This published work and the nomenclatural acts it contains have been registered in ZooBank, the online registration system for the ICZN. The ZooBank LSIDs (Life Science Identifiers) can be resolved and the associated information can be viewed through any standard web browser by appending the LSID to the prefix http://zoobank.org/.

Publication LSID:
urn:lsid:zoobank.org:pub:745F3A5C-9D92-4D60-981D-1380E0EEB845.

Brachytarsophrys orientalis LSID:
urn:lsid:zoobank.org:act:B93B722F-40C3-40D0-8C7A-879DBD5CC25F.

SCIENTIFIC FIELD SURVEY PERMISSION INFORMATION

Permission for field surveys in Jiulianshan National Nature Reserve, Longnan County, Jiangxi Province was granted by the Jiangxi Jiulianshan National Nature Reserve Administration.

COMPETING INTERESTS

The authors declare that they have no competing interests.

AUTHOR CONTRIBUTIONS

Y.Y.W and D.D.Z conceived and designed the study. Y.L, Z.T.L, J.W, Y.L.L, Z.Y.L, H.H.C, D.Q.R, Z.F.J and C.Y.Z collected materials. Y.L performed the experiments, analyzed the data and prepared the manuscript. D.D.Z, Z.T.L, J.W, and Y.Y.W revised the manuscript. All authors read and approved the final version of the manuscript.

ACKNOWLEDGEMENTS

We thank the Kunming Institute of Zoology and Chengdu Institute of Biology, Chinese Academy of Sciences, for allowing us to examine preserved specimens. We thank Run-Lin Li, Jia-He Li, Hai-Long He, Cheng-Yi Liu, Rong-Hua Huang, and Xiao-Jiang Pan for their help with fieldwork, and Jia-He Li for help with laboratory work. We are grateful to the editors and reviewers for providing constructive comments on our work, and to Dr. Christine Watt for polishing the manuscript.

REFERENCES

Boulenger GA. 1886. Description of a new frog of the genus *Megalophrys*. *Annali del Museo Civico di Storia Naturale di Genova*, **4**: 512−513.

Boulenger GA. 1889. Description of a new batrachian of the genus *Leptobrachium*, obtained by M. L. Fea in the Karens Mountains, Burma. *Annali del Museo Civico de Storia Naturale di Genova*, **2**(7): 748−750.

Boulenger GA. 1890. The Fauna of British India, including Ceylon and Burma: Reptilia and Batrachia. London: Thacker, Spink & CO. and Thacker & CO. Limited.

Boulenger GA. 1908. A revision of the Oriental pelobatid batrachians (genus *Megalophrys*). *Proceedings of the Zoological Society of London*, **78**(2): 407−430.

Bourret R. 1942. Les Batraciens de l 'Indochine. Hanoi: Institut Océanographique de l'Indochine. (in French)

Capocaccia L. 1957. Catalogo dei tipi di anfibi del Museo Civico di Storia Naturale di Genova. *Annali del Museo Civico di Storia Naturale di Genova. Serie 3*, **69**: 208−222.

Che J, Chen HM, Yang JX, Jin JQ, Jiang K, Yuan ZY, Murphy RW, Zhang YP. 2012. Universal COI primers for DNA barcoding amphibians. *Molecular Ecology Resources*, **12**(2): 247−258.

Chen JM, Zhou WW, Poyarkov NA Jr, Stuart BL, Brown RM, Lathrop A, Wang YY, Yuan ZY, Jiang K, Hou M, Chen HM, Suwannapoom C, Nguyen SN, van Duong T, Papenfuss TJ, Murphy RW, Zhang YP, Che J. 2017. A novel multilocus phylogenetic estimation reveals unrecognized diversity in Asian horned toads, genus *Megophrys sensu lato* (Anura: Megophryidae). *Molecular Phylogenetics and Evolution*, **106**: 28−43.

Darriba D, Taboada GL, Doallo R, Posada D. 2012. jModelTest 2: more models, new heuristics and high-performance computing. *Nature Methods*, **9**(8): 772.

Delorme M, Dubois A, Grosjean S, Ohler A. 2006. Une nouvelle ergotaxinomie des Megophryidae (Amphibia, Anura). *Alytes*, **24**(1-4): 6−21.

Deuti K, Grosjean S, Nicolas V, Vasudevan K, Ohler A. 2017. Nomenclatural puzzle in early *Xenophrys* nomina (Anura, Megophryidae) solved with description of two new species from India (Darjeeling hills and Sikkim). *Alytes*, **34**: 20−48.

Dubois A. 1987. Miscellanea taxinomica batrachologica. *Alytes*, **5**: 7−95.

Dubois A, Ohler A. 1998. A new species of *Leptobrachium (Vibrissaphora)* from northern Vietnam, with a review of the taxonomy of the genus *Leptobrachium* (Pelobatidae, Megophyinae). *Dumerilia*, **4**(14): 1−32.

Fei L, Ye CY. 2001. The Colour Handbook of the Amphibians of Sichuan. Beijing: Chinese Forestry Press. (in Chinese)

Fei L, Hu SQ, Ye CY, Huang YZ. 2009. Fauna Sinica. Amphibia. Vol. 2. Anura. Beijing: Science Press. (in Chinese)

Fei L, Ye CY. 2016. Amphibians of China. Vol. 1. Beijing: Science Press.

Frost DR, Grant T, Faivovich J, Bain RH, Haas A, Haddad CFB, De Sá RO, Channing A, Wilkinson M, Donnellan SC, Raxworthy CJ, Campbell JA, Blotto BL, Moler P, Drewes RC, Nussbaum RA, Lynch JD, Green DM, Wheeler WC. 2006. The amphibian tree of life. *Bulletin of the American Museum of natural History*, **297**: 1−291.

Gee NG, Boring AM. 1929. Check list of Chinese Amphibia with notes on geographical distribution. *Peking Natural History Bulletin*, **4**: 15−51.

Gill FB, Slikas B, Sheldon FH. 2005. Phylogeny of titmice (Paridae): II. Species relationships based on sequences of the mitochondrial cytochrome-B gene. *The Auk*, **122**(1): 121–143.

Gosner KL. 1960. A simplified table for staging anuran embryos and larvae with notes on identification. *Herpetologica*, **16**: 183−190.

Häupl M, Tiedemann F. 1978. Vertebrata 1. Typenkatalog der Herpetologischen Sammlung. *Kataloge der Wissenschaftlichen Sammlungen des Naturhistorischen Museums in Wien*, **2**: 7−34.

Jiang JP, Yuan FR, Xie F, Zheng ZH. 2003. Phylogenetic relationships of some species and genera in Megophryids inferred from partial sequences of mitochondrial 12S and 16S rRNA genes. *Zoological Research*, **24**(4): 241−248. (in Chinese)

Li C, Wang YZ. 2008. Taxonomic review of *Megophrys* and *Xenophrys*, and a proposal for Chinese species (Megophryidae, Anura). *Acta Zootaxonomica Sinica*, **33**(1): 104−106. (in Chinese)

Liu ZY, Chen GL, Zhu TQ, Zeng ZC, Lyu ZT, Wang J, Messenger K, Greenberg AJ, Guo ZX, Yang ZH, Shi SH, Wang YY. 2018. Prevalence of cryptic species in morphologically uniform taxa-fast speciation and evolutionary radiation in Asian toads. *Molecular Phylogenetics and Evolution*, **127**: 723−731.

Mahony S, Foley NM, Biju SD, Teeling EC. 2017. Evolutionary history of the Asian Horned Frogs (Megophryinae): integrative approaches to timetree dating in the absence of a fossil record. *Molecular Biology and Evolution*, **34**(3): 744−771.

Meyer CP, Geller JB, Paulay G. 2005. Fine scale endemism on coral reefs: archipelagic differentiation in turbinid gastropods. *Evolution*, **59**(1): 113−125.

Orlov NL, Poyarkov NA Jr, Nguyen TT. 2015. Taxonomic notes on *Megophrys* frogs (Megophryidae: Anura) of Vietnam, with description of a new species. *Russian Journal of Herpetology*, **22**(3): 206−218.

Poyarkov NA Jr, van Duong T, Orlov NL, Gogoleva SS, Vassilieva AB, Nguyen LT, Nguyen VDH, Nguyen SN, Che J, Mahony S. 2017. Molecular, morphological and acoustic assessment of the genus *Ophryophryne* (Anura, Megophryidae) from Langbian Plateau, southern Vietnam, with description of a new species. *ZooKeys*, **672**: 49−120.

Pyron RA, Wiens JJ. 2011. A large-scale phylogeny of Amphibia including over 2800 species, and a revised classification of extant frogs, salamanders, and caecilians. *Molecular Phylogenetics and Evolution*, **61**(2): 543−583.

R Core Team. 2019. R:A language and environment for statistical computing. R Foundation for Statistical Computing, Vienna, Austria. URL https://www.R-project.org/.

Rao DQ, Yang DT. 1997. The variation in karyotypes of *Brachytarsophrys* from China with a discussion of the classification of the Genus. *Asiatic Herpetological Research*, **7**: 103−107.

Ronquist F, Teslenko M, Van Der Mark P, Ayres DL, Darling A, Höhna S, Larget B, Liu L, Suchard MA, Huelsenbeck JP. 2012. Mrbayes 3.2: Efficient bayesian phylogenetic inference and model choice across a large model space. *Systematic Biology*, **61**(3): 539−542.

Savage JM. 1975. Systematics and distribution of the Mexican and Central American stream frogs related to Eleutherodactylus rugulosus. *Copeia*, **2**: 254−306.

Silvestro D, Michalak I. 2012. RaxmlGUI: A graphical front-end for RAxML. *Organisms Diversity and Evolution*, **12**(4): 335−337.

Smith MA. 1921. New or little-known reptiles and batrachians from southern Annam (Indo-China). *Proceeding of the Zoological Society of London*, **91**(2): 423−440.

Tamura K, Stecher G, Peterson D, Filipski A, Kumar S. 2013. MEGA6: Molecular evolutionary genetics analysis version 6.0. *Molecular Biology and Evolution*, **30**(12): 2725−2729.

Taylor EH. 1962. The amphibian Fauna of Thailand. *University of Kansas Science Bulletin*, **43**: 265−599.

Thompson JD, Gibson TJ, Plewniak F, Jeanmougin F, Higgins DG. 1997. The CLUSTAL_X windows interface: flexible strategies for multiple sequence alignment aided by quality analysis tools. *Nucleic Acids Research*, **25**(24): 4876−4882.

Tian WS, Hu QX. 1983. Taxonomic study on genus *Megophrys*, with descriptions of two new genera. *Acta Herpetologica Sinica*, **2**(2): 41−48. (in Chinese)

Wang J, Lyu ZT, Liu ZY, Liao CK, Zeng ZC, Zhao J, Li YL, Wang YY. 2019. Description of six new species of the subgenus *Panophrys* within the genus *Megophrys* (Anura, Megophryidae) from southeastern China based on molecular and morphological data. *ZooKeys*, **851**(1986): 113−164.

Xie F, Wang ZW. 2000. Review of the systematics of pelobatids. *Cultum Herpetologica Sinica*, **8**: 356−370.

Yang JH, Wang J, Wang YY. 2018. A new species of the genus *Megophrys* (Anura: Megophryidae) from Yunnan Province, China. *Zootaxa*, **4413**(2): 325−338.

Zhang P, Liang D, Mao RL, Hillis DM, Wake DB, Cannatella DC. 2013. Efficient sequencing of anuran mtDNAs and a mitogenomic exploration of the phylogeny and evolution of frogs. *Molecular Biology and Evolution*, **30**: 1899−1915.

Zhang YN, Li G, Xiao N, Li JQ, Pan T, Wang H, Zhang BW, Zhou J. 2017. A new species of the genus *Xenophrys* (Amphibia: Anura: Megophryidae) from Libo County, Guizhou, China. *Asian Herpetological Research*, **8**(2): 75−85.

Zhao EM, Adler K. 1993. Herpetology of China. Oxford: Society for the Study of Amphibians and Reptiles.

Zhao J, Yang JH, Chen GL, Chen CQ, Wang YY. 2014. Description of a new species of the genus *Brachytarsophrys* Tian and Hu, 1983 (Amphibia: Anura: Megophryidae) from Southern China based on molecular and morphological data. *Asian Herpetological Research*, **5**(3): 150−160.

Zheng YC, Zeng XM, Yuan YZ, Liu ZJ. 2004. Phylogenetic positions of *Ophryophryne* and four *Leptobrachium* group genera in Megophryidae (Anura). *Sichuan Journal of Zoology*, **23**(3): 290−295. (in Chinese)

ZOOLOGICAL RESEARCH

Mudskipper interleukin-34 modulates the functions of monocytes/macrophages via the colony-stimulating factor-1 receptor 1

Hai-Yu Shen[1,2], Yan Zhou[1,2], Qian-Jin Zhou[1,2,3,*], Ming-Yun Li[1,2], Jiong Chen[1,2,3,*]

[1] *State Key Laboratory for Managing Biotic and Chemical Threats to the Quality and Safety of Agro-products*, *Ningbo University*, *Ningbo*, *Zhejiang* 315211, *China*

[2] *Laboratory of Biochemistry and Molecular Biology*, *School of Marine Sciences*, *Ningbo University*, *Ningbo*, *Zhejiang* 315832, *China*

[3] *Key Laboratory of Applied Marine Biotechnology of Ministry of Education*, *Ningbo University*, *Ningbo*, *Zhejiang* 315832, *China*

ABSTRACT

Interleukin-34 (IL-34) is a novel cytokine that plays an important role in innate immunity and inflammatory processes by binding to the colony-stimulating factor-1 receptor (CSF-1R). However, information on the function of IL-34 in fish remains limited. In the present study, we identified an IL-34 homolog from mudskippers (*Boleophthalmus pectinirostris*). *In silico* analysis showed that the mudskipper IL-34 (BpIL-34) was similar to other known IL-34 variants in sequence and structure and was most closely related to an orange-spotted grouper (*Epinephelus coioides*) homolog. *BpIL-34* transcripts were constitutively expressed in various tissues, with the highest level of expression found in the brain. *Edwardsiella tarda* infection significantly up-regulated the mRNA expression of *BpIL-34 in the mudskipper tissues.* The recombinant mature BpIL-34 peptide (rBpIL-34) was purified and used to produce anti-rBpIL-34 IgG. Western blot analysis combined with PNGase F digestion revealed that native BpIL-34 in monocytes/macrophages (MOs/MΦs) was N-glycosylated. *In vitro*, rBpIL-34 treatment enhanced the phagocytotic and bactericidal activity of mudskipper MOs/MΦs, as well as the mRNA expression of pro-inflammatory cytokines like tumor necrosis factor α (*BpTNF-α*) and *BpIL-1β* in these cells. Furthermore, the knockdown of mudskipper *CSF-1R1* (*BpCSF-1R1*), but not mudskipper *BpCSF-1R2*, significantly inhibited the rBpIL-34-mediated enhanced effect on MO/MΦ function. In conclusion, our results indicate that mudskipper BpIL-34 modulates the functions of MOs/MΦs via BpCSF-1R1.

Keywords: Interleukin-34; Mudskipper; Monocyte/macrophage function; *Edwardsiella tarda*; Colony-stimulating factor-1 receptor

INTRODUCTION

Cytokines comprise a large group of proteins, peptides, and

Received: 03 January 2020; Accepted: 04 March 2020; Online: 04 March 2020

Foundation items: The study was supported by the National Natural Science Foundation of China (31972821; 31772876), the Program of Zhejiang Provincial Natural Science Foundation of China (LZ18C190001), Science and Technology Department of Zhejiang Province (LGN18C180002), Natural Science Foundation of Ningbo City (2018A610342), and the K.C. Wong Magna Fund in Ningbo University

*Corresponding authors, E-mail: mumu2325@163.com; jchen1975@163.com

DOI: 10.24272/j.issn.2095-8137.2020.026

glycoproteins that are secreted by specific cells of the immune system to mediate and regulate immunity, inflammation, and hematopoiesis (Wang & Secombes, 2013; Zou & Secombes, 2016). There are many types of cytokines including chemokines, interferons, interleukins, lymphokines, and tumor necrosis factor. In recent years, considerable progress has been made in the cloning, sequencing, and functional analysis of fish cytokine genes (Ogryzko et al., 2014; Secombes & Zou, 2017; Wang & Secombes, 2013). Our increasing knowledge on the regulation of fish immune responses by cytokines and their potential use as candidate drugs for disease control in aquaculture makes fish cytokine biology an attractive and rapidly expanding field (Secombes, 2016).

In a brilliant study that aimed to understand the system of secreted proteins and receptors involved in cell–cell signaling, interleukin 34 (IL-34), a secreted protein with high functional selectivity that stimulates monocyte survival, was identified as the second ligand of the colony-stimulating factor-1 receptor (CSF-1R) (Lin et al., 2008). The IL-34 structure is comprised of two β strands, four short helices, and four long helices, with an antiparallel four-helix core homologous to that of CSF-1 (Ma et al., 2012). CSF-1 is a cytokine that controls the production, differentiation, and function of macrophages, and CSF-1R mediates most, if not all, of the biological effects of CSF-1 (Liu et al., 2012; Nakamichi et al., 2013). IL-34 binds to CSF-1R with higher affinity than that of CSF-1 and induces the enhanced phosphorylation of CSF-1R and stronger activation of signaling pathways (Chihara et al., 2010). In addition, IL-34, but not CSF-1, binds to two other receptors, namely PTP-*ζ* and syndecan-1 (Baghdadi et al., 2018). PTP-*ζ* is a chondroitin sulfate proteoglycan, with expression restricted to the brain (neural progenitors and glial cells) and kidney (Masteller & Wong, 2014). IL-34 binds to the extracellular domains of PTP-ζ, resulting in the activation of several signaling pathways that regulate cell proliferation, motility, and clonogenicity (Baghdadi et al., 2018). The binding of IL-34 to syndecan-1 modulates the activation of CSF-1R and appears to be involved in the regulation of myeloid cell migration (Vasek et al., 2016). IL-34 and CSF-1 are equivalent in their ability to induce macrophage differentiation but exhibit different polarization potentials (Baghdadi et al., 2018). In contrast to CSF-1, IL-34 has a restricted pattern of expression (Nandi et al., 2012) and seems to be required for the generation of a restricted set of tissue-specific macrophages, including microglia and Langerhans cells, two types of phagocytes present in the brain and skin, respectively (Greter et al., 2012; Nakamichi et al., 2013; Wang et al., 2012). Over the past decade, accumulating evidence has shown that IL-34 exerts potent immunomodulatory effects under many pathological states such as infections, inflammatory diseases, autoimmune diseases, cancer, transplant rejection, and neurological diseases (Baghdadi et al., 2018; Grayfer & Robert, 2014, 2015; Kim & Turka, 2015; Masteller & Wong, 2014).

In fish, single copies of the *IL-34* gene have been found in the genome of rainbow trout (*Oncorhynchus mykiss*), zebrafish (*Danio rerio*), fugu (*Takifugu rubripes*), orange-spotted grouper (*Epinephelus coioides*), large yellow croaker (*Larimichthys crocea*), and grass carp (*Ctenopharyngodon idella*) (Mo et al., 2015; Wang et al., 2013, 2018; Xue et al., 2019). To date, however, information on the expression of *IL-34* in fish is still limited. Analysis of gene expression in tissues showed that *IL-34* is constitutively expressed in rainbow trout, large yellow croaker, and grass carp, with highest expression in the spleen (Wang et al., 2013, 2018; Xue et al., 2019); however, in orange-spotted grouper, the highest level of expression is reported in the brain (Mo et al., 2015). Furthermore, *IL-34* expression is tightly associated with pathogen stimulation. For example, studies on rainbow trout and grouper have demonstrated that parasitic infection can lead to elevated *IL-34* transcript levels in tissues, especially in infected sites (Mo et al., 2015; Wang et al., 2013). Stimulation by viral or bacterial pathogens has also been shown to up-regulate the expression of *IL-34* in large yellow croaker (Wang et al., 2018), golden pompano (*Trachinotus ovatus*) (Wu et al., 2019), and grass carp (Xue et al., 2019). However, the functions and underlying mechanisms of IL-34 in fish immune responses remain unclear. Recent study showed that recombinant grass carp IL-34 produced in bacteria and HEK293T cells has a stimulatory effect on the expression of *IL-1β*, *IL-6*, and *IL-8* but inhibits the expression of *IL-10* and *TGF-β* in primary head kidney macrophages (Xue et al., 2019), suggesting that IL-34 is a pro-inflammatory cytokine. Another study on zebrafish showed that ectopically expressed IL-34 can induce macrophage migration to the liver *in vivo* (Jiang et al., 2019). As putative receptors for IL-34, CSF-1Rs have already been identified as specific markers of macrophages in some teleost fish species, such as gilthead seabream (*Sparus aurata*) (Roca et al., 2006), goldfish (*Carassius auratus*) (Katzenback & Belosevic, 2012), ayu (*Plecoglossus altivelis*) (Chen et al., 2016b), and grass carp (Chen et al., 2015). Unlike mammals, teleost fish commonly possess two *CSF-1R* genes (*CSF-1R1* and *CSF-1R2*), which are widely expressed in tissues, including the head kidney and spleen (Chen et al., 2015, 2016b; Dan et al., 2013; Honda et al., 2005; Katzenback & Belosevic, 2012; Mulero et al., 2008; Williams et al., 2002). A soluble form of CSF-1R has also been described in goldfish, which is important in the regulation of leucocyte-related immune responses (Rieger et al., 2013, 2014, 2015). However, the relationship between IL-34 and CSF-1Rs in fish has not been investigated to date.

Mudskipper fish (*Boleophthalmus pectinirostris*) are usually found in soft mudflat estuaries and coastal waters after ebb tides. Their behavioral, physiological, and morphological characteristics have become specialized and adapted to an amphibious lifestyle (You et al., 2018). The complete genomic sequences of mudskippers show many immune genes for adaptations to their complex habitats (You et al., 2014). *Edwardsiella tarda* is a gram-negative, facultative anaerobic bacterium that infects multifarious hosts, including fish, amphibians, and humans (Slaven et al., 2001; Xu & Zhang, 2014). Bacterial infections cause large aquacultural losses in

Asia, especially in China and Japan (Xu & Zhang, 2014). Our previous report showed that intraperitoneal infection with *E. tarda* is lethal to mudskippers (Chen et al., 2016a). Given the importance of IL-34 in anti-bacterial innate immune responses, studies on the biological function and mechanism of IL-34 in mudskippers against *E. tarda* infection are crucial. In this study, we identified an *IL-34* gene (*BpIL-34*) in mudskippers based on genomic sequences and investigated mRNA expression in the tissues of healthy and *E. tarda*-infected fish. Moreover, we prepared the recombinant mature peptide of BpIL-34 (rBpIL-34) and determined its effect on monocyte/macrophage (MO/MΦ) functions, including phagocytosis, bactericidal activity, and cytokine mRNA expression. Furthermore, two mudskipper *CSF-1R* genes (*BpCSF-1R1* and *BpCSF-1R2*) were identified, with the effect of *BpCSF-1R1* and *BpCSF-1R2* knockdown on BpIL-34-activated MO/MΦ functions also investigated. These findings should provide new insights into IL-34 as a drug candidate for controlling biological diseases in fish.

MATERIALS AND METHODS

Fish maintenance

Healthy mudskippers without visible pathological symptoms, weighing 35–40 g each, were purchased from a commercial farm in Ningbo city, China. The fish were kept at a salinity of 10 and temperature of 24–26 °C in a filtered-water recirculating system. The fish were allowed two weeks to acclimatize to laboratory conditions. In addition, they were randomly selected for polymerase chain reaction (PCR) determination of *E. tarda* in blood and liver with *E. tarda*-specific primers gyrBF (5′–TGGCGACACCGAGCAGA–3′) and gyrBR (5′–ACAAACGCCTTAATCCCACC–3′) and showed to be *E. tarda*-free (Guan et al., 2017). All experiments were performed according to the Experimental Animal Management Law of China and approved by the Animal Ethics Committee of Ningbo University.

Molecular characterization of *BpIL-34* cDNA

The cDNA sequence of *BpIL-34* was retrieved from our transcriptome data of mudskipper by BLAST search (http://blast.ncbi.nlm.nih.gov/Blast.cgi) and verified in mudskipper genomic sequences (You et al., 2014). The molecular weight and isoelectric point of putative BpIL-34 were calculated using the ExPASy Compute pI/MW tool (https://www.expasy.org/tools). SignalP 5.0 (http://www.cbs.dtu.dk/services/SignalP/) was used to predict the sequence of the signal peptide. SMART (http://smart.embl-heidelberg.de/) was used to predict the domain architecture of the putative protein. Potential N-glycosylation sites were predicted using the NetNGlyc1.0 Server (http://www.cbs.dtu.dk/services/NetNGlyc/). Multiple sequence alignments were performed and analyzed using ClustalW (http://clustalw.ddbj.nig.ac.jp/). Phylogenetic tree analysis was conducted with MEGA v5.0 (Tamura et al., 2011). The related *IL-34* and *CSF-1* sequences are listed in Table 1.

In vivo bacterial challenge and tissue collection

In vivo E. tarda challenge was performed on the mudskippers as described previously (Guan et al., 2017). The *E. tarda* strain MCCC 235 (purchased from the Marine Culture Collection of China) was cultured in Tryptic Soy Broth (TSB) medium at 28 °C with shaking and collected in the logarithmic growth phase. The fish were then intraperitoneally injected with 1.0×10^4 colony forming units (CFUs) of live *E. tarda* per fish, with the control group treated with the same volume of phosphate-buffered saline (PBS). At 4, 8, 12, and 24 h post-injection (hpi), the liver, spleen, kidney, and brain were collected. The tissues of healthy fish without treatment, including the kidney, muscle, liver, skin, spleen, gill, brain, and intestine, were also collected. Prior to tissue dissection, fish were anesthetized with 0.03% (v/v) ethylene glycol monophenyl ether and sacrificed.

Quantitative real-time PCR (qRT-PCR)

Total RNA was extracted from fish tissues and MOs/MΦs using RNAiso reagent (TaKaRa, Dalian, China). After treatment with DNase I (TaKaRa, Dalian, China), first-strand cDNA was synthesized using AMV reverse transcriptase (TaKaRa, Dalian, China). qRT-PCR was performed on an ABI StepOne Real-Time PCR System (Applied Biosystems, Foster City, USA) using SYBR premix Ex Taq II (TaKaRa, Dalian, China) as described previously (Chen et al., 2019). The primers used are listed in Table 2. The reaction mixture was incubated for 5 min at 94 °C, and then subjected to 40 amplification cycles of 30 s at 94 °C, 30 s at 60 °C, and 30 s at 72 °C, followed by melting curve analysis for 30 s at 94 °C, 30 s at 72 °C, and 30 s at 94 °C. Relative gene expression of *BpIL-34* in healthy or *E. tarda*-infected samples was calculated using the $2^{-\Delta CT}$ and $2^{-\Delta\Delta CT}$ methods, respectively, and the data were normalized to *Bp18S rRNA* levels. Each PCR run was performed with four samples and repeated three times.

Prokaryotic expression and purification of recombinant mature BpIL-34 (rBpIL-34)

The primers BpIL-34pF (5′-CGGAATTCGCCCCCACTCCTTCGAGC-3′, underline indicates an introduced *Eco*R I site) and BpIL-34pR (5′-CCGCTCGAGTCAGCTTTTTGTGTTCACATTCT-3′, underline indicates an introduced *Xho* I site) were designed to amplify the sequence encoding the mature BpIL-34 (mBpIL-34) peptide. After digestion with *Eco*R I and *Xho* I, the amplicon was cloned into the pET-28a vector and the constructed plasmid (pET28a-mBpIL-34) was subsequently transformed into *Escherichia coli* BL21 (DE3). Here, rBpIL-34 was overexpressed by the induction of isopropyl-β-D-thiogalactopyranoside (IPTG) and subsequently purified using a Ni-NTA column (TaKaRa, Dalian, China) according to the manufacturer's instructions. Endotoxin in the recombinant proteins was detected using the *Limulus amebocyte* lysate test and was found to be less than 0.1 EU/mg after toxin removal with an endotoxin-removal column (Pierce, Rockford, USA).

Antibody preparation and Western blot assays

Antibody production was performed as reported previously

Table 1 IL-34 and CSF-1 sequences used for multiple sequence alignment and phylogenetic tree analysis

GenBank accession No.	Species		Gene
	Latin name	English name	
XM_020935293	*Boleophthalmus pectinirostris*	Mudskipper	*IL-34*
NM_001128701	*Danio rerio*	Zebrafish	*IL-34*
KM350155	*Epinephelus coioides*	Orange-spotted grouper	*IL-34*
NM_001257301	*Oncorhynchus mykiss*	Rainbow trout	*IL-34*
XM_030427145	*Sparus aurata*	Gilthead seabream	*IL-34*
NM_001305607	*Takifugu rubripes*	Tiger puffer	*IL-34*
XM_020104586	*Paralichthys olivaceus*	Japanese flounder	*IL-34*
XM_019360775	*Oreochromis niloticus*	Nile tilapia	*IL-34*
XM_010743578	*Larimichthys crocea*	Large yellow croaker	*IL-34*
XM_014124241	*Salmo salar*	Atlantic salmon	*IL-34*
XM_017465109	*Ictalurus punctatus*	Channel catfish	*IL-34*
XM_019087026	*Cyprinus carpio*	Common carp	*IL-34*
XM_011476357	*Oryzias latipes*	Japanese rice fish	*IL-34*
XM_027161223	*Tachysurus fulvidraco*	Yellow catfish	*IL-34*
XM_013138989	*Esox lucius*	Northern pike	*IL-34*
XM_026287434	*Carassius auratus*	Goldfish	*IL-34*
XM_007249177	*Astyanax mexicanus*	Mexican tetra	*IL-34*
MK297321	*Ctenopharyngodon idella*	Grass carp	*IL-34*
XM_020456685	*Oncorhynchus kisutch*	Coho salmon	*IL-34*
XM_024802984	*Maylandia zebra*	Zebra mbuna	*IL-34*
NM_152456	*Homo sapiens*	Human	*IL-34*
NM_001135100	*Mus musculus*	Mouse	*IL-34*
NM_001025766	*Rattus norvegicus*	Rat	*IL-34*
NM_001285975	*Sus scrofa*	Pig	*IL-34*
XM_022419217	*Canis lupus familiaris*	Dog	*IL-34*
XM_023637306	*Equus caballus*	Horse	*IL-34*
XM_018260639	*Xenopus laevis*	African clawed frog	*IL-34*
XM_003641892	*Gallus gallus*	Chicken	*IL-34*
XM_019535589	*Crocodylus porosus*	Crocodile	*IL-34*
NM_001100324	*Bos taurus*	Cattle	*IL-34*
NM_001114480	*Danio rerio*	Zebrafish	*CSF-1*
NM_001080076	*Danio rerio*	Zebrafish	*CSF-1-2*
NM_001124394	*Oncorhynchus mykiss*	Rainbow trout	*CSF-1*
NM_001160476	*Oncorhynchus mykiss*	Rainbow trout	*CSF-1-2*
KM350156	*Epinephelus coioides*	Orange-spotted grouper	*CSF-1-2*
NM_001280600	*Xenopus laevis*	African clawed frog	*CSF-1*
XM_017000369	*Homo sapiens*	Human	*CSF-1*
XM_024984551	*Bos taurus*	Cattle	*CSF-1*
XM_008761428	*Rattus norvegicus*	Rat	*CSF-1*
NM_001113530	*Mus musculus*	Mouse	*CSF-1*
NM_001193295	*Gallus gallus*	Chicken	*CSF-1*

(Chen et al., 2019). Briefly, purified rBpIL-34 was used as an immunogen to produce antiserum in Institute of Cancer Research (ICR) mice. Protein A agarose beads (Invitrogen, Shanghai, China) were used to precipitate IgG (anti-rBpIL-34 IgG) from the antisera. The IgG from saline-injected ICR mice (isotype IgG) was also purified.

Western blotting was performed to detect native rBpIL-34 in mudskipper MOs/MΦs using anti-rBpIL-34 IgG as per previous research (Chen et al., 2019). Briefly, protein samples were resolved by SDS-PAGE and transferred to a polyvinylidene fluoride membrane. Anti-rBpIL-34 IgG was used as the primary antibody at a 1:1 000 dilution, followed by horseradish peroxidase (HRP)-labeled goat anti-mouse IgG (1:5 000) as the secondary antibody. Proteins were visualized using an

Table 2 Oligonucleotide primers used in the qRT-PCR analysis of mudskipper genes

Gene	GenBank accession No.	Primer	Nucleotide sequence (5′–3′)
BpIL-34	XM_020935293	BpIL-34RF	GCAGGAGCTTCCAGAGTCAG
		BpIL-34RR	CCTCCAATGGGACCTGTCAC
BpIL-1β	KX492895	BpIL-1βF	ACGAGTGGTGAATGTGGTCA
		BpIL-1βR	GAACTGAGGTTGTGCTGCAA
BpTNF-α	KX492896	BpTNF-αF	GGACAACAACGAGATCGTGA
		BpTNF-αR	GTTCCACCGTGTGACTGATG
BpIL-6	XM_020932674	BpIL-6F	GCAGCACGTCAGAAGATGAGA
		BpIL-6R	TCTCTGAGAAACTCGTGCAGC
BpTGF-β	XM_020928521	BpTGF-βF	TCAAAGGACACTTGCACAGC
		BpTGF-βR	CAGGGCCAAGATCTGTGAAT
BpIL-10	XM_020936977	BpIL-10F	GTGGAGGGGTTCCCTCTAAG
		BpIL-10R	GTGCGGAGGTAAAAGCTCAG
Bp18S rRNA	KX492897	Bp18SF	GGCCGTTCTTAGTTGGTGGA
		Bp18SR	CCCGGACATCTAAGGGCATC
BpCSF-1R1	XM_020921963	BpCSF-1R1F	GGCCCACGTGTAAGGAGAAT
		BpCSF-1R1R	TACTCCTCCCTCTGCACCTC
BpCSF-1R2	XM_020941064	BpCSF-1R2F	GTCTTGAGGTTGGACTCGGG
		BpCSF-1R2R	CTCACACCTGTCGGTGAGTC

enhanced chemiluminescence (ECL) kit from Amersham (GE Healthcare, Pittsburgh, USA). To determine whether native BpIL-34 is N-glycosylated, denatured proteins of mudskipper MOs/MΦs were treated with PNGase F (New England Biolabs, Beverly, USA) at 37 °C overnight and analyzed by Western blotting.

Primary culture of mudskipper kidney-derived MOs/MΦs

Mudskipper kidney-derived MOs/MΦs were isolated and cultured as described previously (Ding et al., 2019). Briefly, fish kidney leukocyte-enriched fractions were obtained using Ficoll-Hypaque PREMIUM (1.077 g/mL; GE Healthcare, USA). After washing twice with RPMI1640, the MOs/MΦs were cultured in 35 mm dishes at a concentration of $2×10^7$ cells/mL. Cells (2 mL) were then incubated for at least 12 h at 24 °C with 5% CO_2. Non-adherent cells were washed off, and adherent cells were incubated in complete medium (RPMI 1640, 5% mudskipper serum, 5% fetal bovine serum (FBS), 100 U/mL penicillin, 100 μg/mL streptomycin) at 24 °C with 5% CO_2. The purity of the isolated mudskipper MOs/MΦs was greater than 95%, as measured by Wright-Giemsa staining.

RNA interference (RNAi)

Target gene siRNAs, *BpCSF-1R1* siRNA (BpCSF-1R1si, 5′-GCCAACGCCUCAAUCACAUTT-3′) and *BpCSF-1R2* siRNA (BpCSF-1R2si, 5′-GCAGCAAUGAGAAUCACUUTT-3′), as well as mismatched control siRNA (MsiRNA, 5′-UUCUCCG AACGUGUCACGUTT-3′), were designed and synthesized by Invitrogen. The transfection of cells with siRNA was performed using Lipofectamine RNAiMAX (Invitrogen) according to the manufacturer's protocols. Briefly, 5 μL of lipofectamine RNAiMAX in 250 μL of Opti-MEM (Invitrogen) was mixed with 100 pmoL siRNA in 250 μL of Opti-MEM. The mixture was then incubated for 20 min at room temperature before adding it to MOs/MΦs at a final siRNA concentration of 40 nmol/L. Media were changed to complete media after 5.5-h incubation, and cells were cultured for another 48 h before collection for expression analysis. qRT-PCR confirmed the knockdown of *BpCSF-1R1* and *BpCSF-1R2* mRNA. The primers used are listed in Table 2.

Phagocytosis assay

Mudskipper MO/MΦ phagocytosis assays using *E. tarda* were performed as described previously (Chen et al., 2016a). Briefly, *E. tarda* were collected in the logarithmic growth phase, labeled with fluorescein isothiocyanate (FITC) (Sigma, Saint Louis, USA), and designated FITC-*E. tarda*. The MOs/MΦs were cultured in 6-well plates at a concentration of $2×10^6$ cells/mL and each well contained a 2-mL cell suspension. The MOs/MΦs were treated with 10.0 μg/mL rBpIL-34 or the same volume of PBS for 12 h. The heat-killed FITC-*E. tarda* were then added at a multiplicity of infection (MOI) of 10 and incubated for another 30 min. After washing extensively with sterile PBS to remove extracellular particles from the cells, Trypan Blue (0.4%) was used to quench fluorescence outside the cell. The engulfed bacteria were examined by flow cytometry using a Gallios Flow Cytometer (Beckman Coulter, Miami, USA). The relative mean fluorescence intensity (MFI) of bacteria engulfed by the cells was analyzed using FlowJo software. The MFIs of the PBS- and rBpIL-34-treated groups were expressed as fold-change relative to that without bacteria, and the MFI of the PBS-treated group was assigned a value of 100. Another set of assays were conducted with the addition of the siRNA reagents. After transfection with BpCSF-1R1si, BpCSF-1R2si, or MsiRNA for 48 h, MOs/MΦs were treated with 10.0 μg/mL rBpIL-34 for 12 h. The remaining steps were performed as described above. The MFIs of the rBpIL-34- and siRNA-treated groups were expressed as fold-change relative to that without bacteria, and the MFI of the rBpIL-34-treated group was assigned a value of 100.

Bacterial killing assay

A bacterial killing assay was performed as described previously (Chen et al., 2018). Briefly, 4×10^6 MOs/MΦs were treated with 10.0 μg/mL rBpIL-34 or the same volume of PBS for 12 h. Live FITC-*E. tarda* were added at a MOI of 10 and incubated for another 30 min. Bacterial uptake by MOs/MΦs was allowed to occur for 30 min at 24 °C in an atmosphere with 5% CO_2. Non-internalized *E. tarda* were removed by extensive washing with sterile PBS. One set of samples (uptake group) was collected for RNA extraction, whereas the other set of samples (kill group) was further incubated for 1.5 h to facilitate bacterial killing before cell lysis. Cells were subjected to classic RNA isolation and subsequent qRT-PCR assays for *E. tarda* using the primers gyrBF and gyrBR (Guan et al., 2017). The Ct values, based on standard curves generated previously, were used to calculate the total CFUs/mL in all samples. Bacterial survival was determined by dividing the number of CFUs in the kill group by that in the uptake group. Four independent experiments were carried out. In addition, another set of assays were conducted with the addition of siRNA reagents. After transfection with BpCSF-1R1si, BpCSF-1R2si, or MsiRNA for 48 h, MOs/MΦs were treated with 10.0 μg/mL rBpIL-34 for 12 h. The remaining steps were performed as described above.

Cytokine mRNA expression analysis in MOs/MΦs

After transfection with BpCSF-1R1si, BpCSF-1R2si, and MsiRNA, MOs/MΦs were treated with 10.0 μg/mL rBpIL-34 for 12 h; MOs/MΦs without any treatment were used as a blank control. qRT-PCR was carried out as described in Section 2.4 with target gene-specific primers (Table 2). The mRNA expression levels of *BpTNF-α*, *BpIL-1β*, *BpIL-6*, *BpTGF-β*, and *BpIL-10* were normalized to those of *Bp18S rRNA*. Four independent experiments were performed.

Statistical analysis

All data are described as means±standard error of the mean (*SEM*). Data were analyzed by one-way analysis of variance (ANOVA) or Student's *t*-test using SPSS v13.0 (SPSS Inc, Chicago, IL, USA). A *P*-value of 0.05 was considered statistically significant.

RESULTS

Sequence identification of BpIL-34

The cDNA sequence of *BpIL-34* was obtained from the DDBJ/EMBL/GenBank databases under accession No. XM_020935293. The sequence was 1 169 nucleotides (nt) in length and possessed an open reading frame (ORF) of 642 nt, which was predicted to encode a 213-amino acid (aa) polypeptide with a calculated MW of 25.0 kDa and an isoelectric point (pI) of 8.57. Sequence analyses revealed that BpIL-34 possessed a 24-aa N-terminal signal peptide, and the mature peptide was comprised of 189 aa, with a calculated MW of 22.4 kDa. Multiple alignment showed that BpIL-34 contained five highly conserved cysteine residues (Cys32, Cys177, Cys182, Cys187, and Cys197), four of which formed two disulfide bonds (Cys32-Cys187 and Cys182-Cys197) (Figure 1). Two potential N-glycosylation sites (Asn39 and Asn71) were found in BpIL-34 (Figure 1). BpIL-34 was also found to contain a conserved motif with multiple cationic amino acid residues (RKx [R/K] K) at aa position 203–207, similar to that in other fish homologs (Liu et al., 2012) (Figure 1).

Sequence comparisons showed that BpIL-34 shared the highest aa identity (78.4%) with the orange-spotted grouper IL-34. A phylogenetic tree was constructed based on the complete aa sequences of IL-34, with the CSF-1 sequences serving as an outgroup (Figure 2). Results showed that fish IL-34 grouped together to form a cluster distinct from the mammalian IL-34 cluster (Figure 2). The fish and mammalian IL-34 clusters formed a clade that was well separated from the CSF-1 clade (Figure 2).

Tissue *BpIL-34* mRNA expression in response to *E. tarda* infection

The relative mRNA expression of *BpIL-34* in selected tissues was detected by qRT-PCR. In healthy fish, *BpIL-34* transcripts were detected in all tested tissues, with the highest level observed in the brain, followed by the gill and intestine (Figure 3A). Upon *E. tarda* infection, *BpIL-34* mRNA expression rapidly increased in the four selected tissues (brain, liver, spleen, and kidney) compared to that in the control group, and the highest level of up-regulation (45.7-fold) was found in the kidney at 12 hpi (Figure 3B–E).

Prokaryotic expression and purification of rBpIL-34 and antibody preparation

After induction by IPTG, recombinant rBpIL-34 was overexpressed in *E. coli* BL21 (DE3). The size of rBpIL-34 obtained based on SDS-PAGE analysis was ~26 kDa, similar to the calculated value (22.4 kDa for the mBpIL-34 plus 3.83 kDa for 6×His-tag; Figure 4A). rBpIL-34 was purified by affinity chromatography using an Ni-NTA column, with purity not less than 96% (data not shown). Purified rBpIL-34 was then used to immunize mice, and anti-rBPIL-34 IgG was purified from antisera. As determined by Western blot analysis, the MW of native BpIL-34 in mudskipper MOs/MΦs was approximately 32 kDa, which was converted to a 25-kDa band after PNGase F digestion (Figure 4B).

Effect of rBpIL-34 on phagocytotic and bacterial killing activity of MOs/MΦs

MOs/MΦs play a pivotal role in immune responses in fish against invasion by pathogens, and phagocytosis and intracellular bacterial killing are the main biological functions of MOs/MΦs (Lu & Chen, 2019). Consequently, we investigated the effects of rBpIL-34 on the functions of mudskipper MOs/MΦs. Phagocytosis of FITC-*E. tarda* by rBpIL-34-treated MOs/MΦs was significantly higher (up to 3.18-fold) than that in

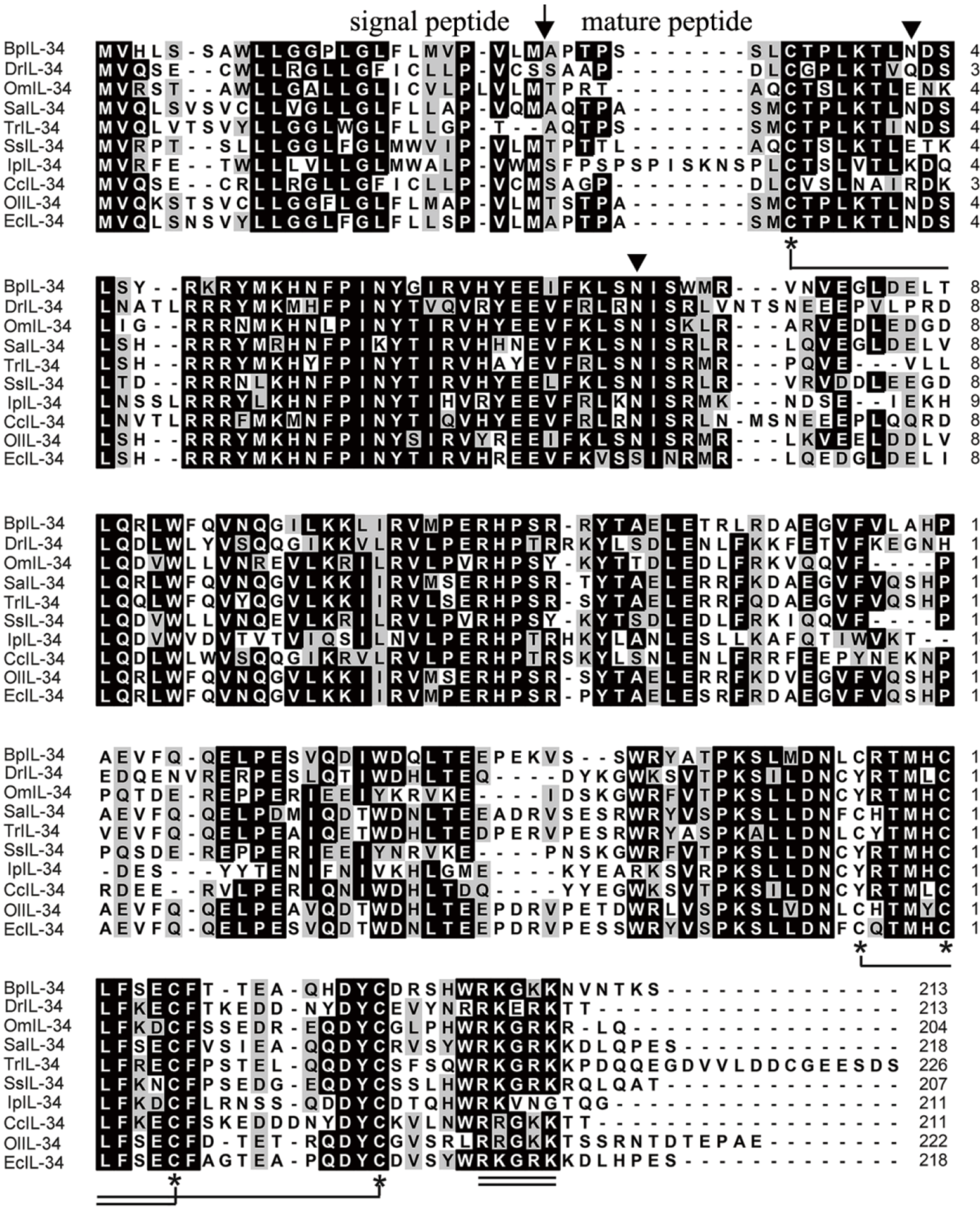

Figure 1 Multiple alignment of amino acid sequences of BpIL-34 and related fish IL-34 sequences

Threshold for shading was >60%; similar residues are marked with a gray shadow, identical residues with a black shadow, and alignment gaps with "-". BpIL-34: Mudskipper IL-34; DrIL-34: Zebrafish IL-34; OmIL-34: Rainbow trout IL-34; SaIL-34: Gilthead seabream IL-34; TrIL-34: Tiger puffer IL-34; SsIL-34: Atlantic salmon IL-34; IpIL-34: Channel catfish IL-34; CcIL-34: Common carp IL-34; OlIL-34: Japanese rice fish IL-34; EcIL-34: Orange-spotted grouper IL-34. Predicted cleavage site for signal peptide is marked as "↓". Five conserved cysteine residues are marked as "*". Two cysteine residues joined by solid line represent disulfide bond. Possible N-linked glycosylation sites of BpIL-34 are indicated by "▼". RKx [R/K] K motif is double underlined. GenBank accession Nos. of sequences used are presented in Table 1.

the PBS-treated group (Figure 5A). In addition, qRT-PCR measurement of intracellular *E. tarda* CFUs in mudskipper MOs/MΦs showed that the bacterial survival rate in the rBpIL-34-treated group (36.12%±1.54%) was much lower than that in the PBS-treated group (75.36%±3.97%; Figure 5B).

Effect of rBpIL-34 on cytokine mRNA expression in MOs/MΦs

We also investigated the effects of rBpIL-34 on mRNA expression of typical inflammatory cytokines (pro-inflammatory cytokines: *BpTNF-α*, *BpIL-1β*, and *BpIL-6*; anti-inflammatory

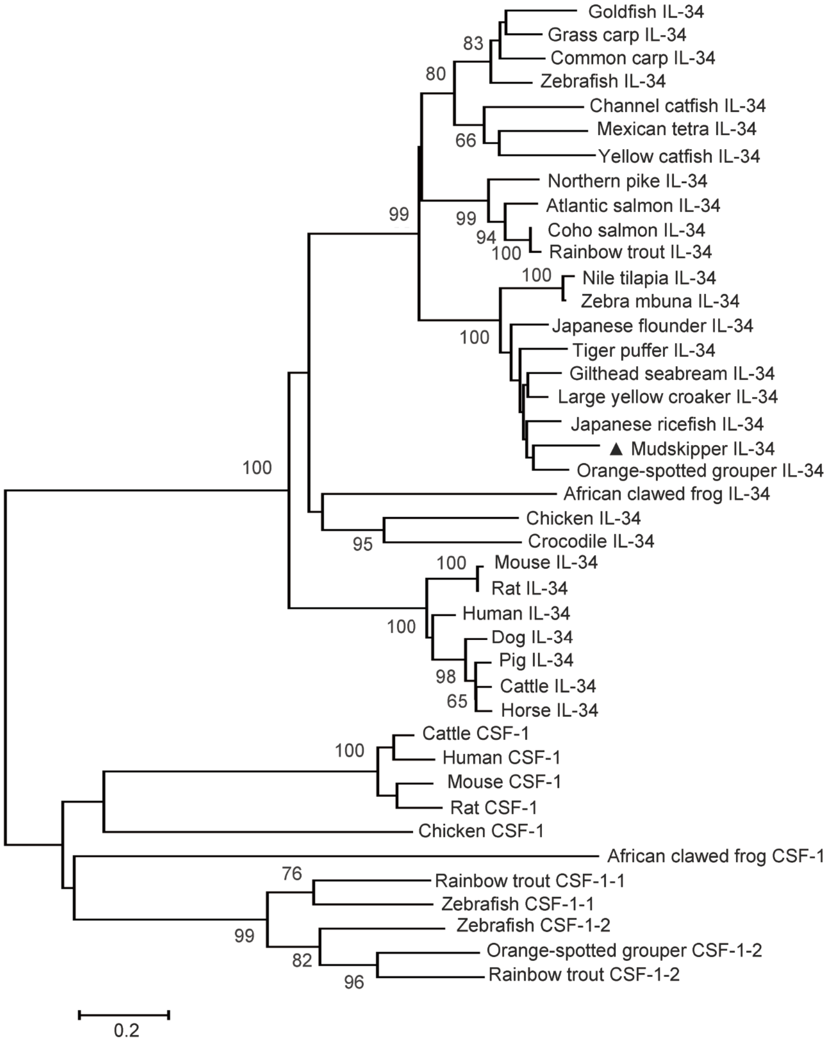

Figure 2 Phylogenetic tree analysis of complete amino acid sequences of IL-34 and CSF-1 using neighbor-joining method

CSF-1 sequences as an outgroup. Percentage of bootstrap values is shown next to branches based on 1 000 bootstrap replications (shown only when >60%). Scale bar represents number of substitutions per base position. Site of mudskipper IL-34 is indicated by "▲". GenBank accession Nos. of sequences used are listed in Table 1.

cytokines: *BpTGF-β* and *BpIL-10*) in mudskipper MOs/MΦs. qRT-PCR showed that the mRNA expression levels of *BpTNF-α*, *BpIL-1β*, and *BpIL-6* were up-regulated 7.36-, 3.01-, and 1.42-fold, respectively, in MOs/MΦs treated with rBpIL-34 compared to those in the control group (Figure 6). No significant change was found in the mRNA expression of *BpTGF-β* between the rBpIL-34-treated and control groups; however, *BpIL-10* mRNA expression was down-regulated 0.67-fold in the rBpIL-34-treated group compared to that in the control group (Figure 6).

Effect of *BpCSF-1R1* and *BpCSF-1R2* knockdown on rBpIL-34-enhanced phagocytotic and bacterial killing activity of MOs/MΦs

As CSF-1R is reportedly the receptor of IL-34 in mammals (Ségaliny et al., 2015; Wang et al., 2012) and mudskippers have two *CSF-1R* genes, we further determined whether *BpCSF-1R1* or *BpCSF-1R2* knockdown would influence the rBpIL-34-enhanced phagocytotic and bacterial killing activity of mudskipper MOs/MΦs. Firstly, we used RNAi to knock down the expression of *BpCSF-1R1* and *BpCSF-1R2* in MOs/MΦs. When MOs/MΦs were transfected with BpCSF-1R1si, the mRNA expression of *BpCSF-1R1* decreased to 29.17%±6.31% of control levels at 48 h, whereas *BpCSF-1R2* expression showed no significant change (Figure 7B, C). Similarly, when MOs/MΦs were transfected with BpCSF-1R2si, the mRNA expression of *BpCSF-1R2* decreased to 21.66%±1.11% of control levels at 48 h, whereas *BpCSF-1R1* expression showed no significant change (Figure 7B, C). These results suggest that the target genes *BpCSF-1R1* and *BpCSF-1R2* were effectively and specifically knocked down. The transfection of MsiRNA had no obvious effect on either

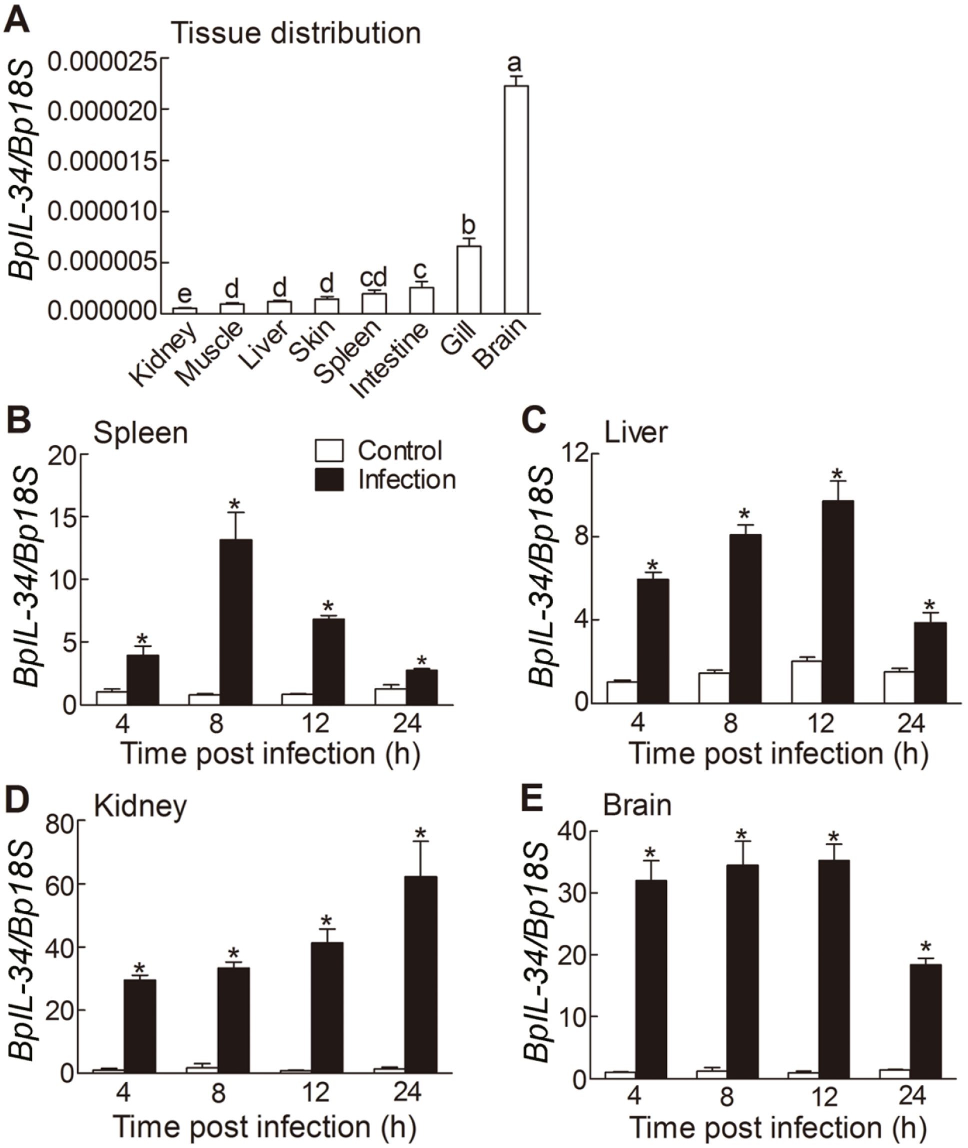

Figure 3 qRT-PCR analysis of *BpIL-34* mRNA expression in tissues of healthy (A) and *Edwardsiella tarda*-infected mudskippers (B–E)

A: *BpIL-34* mRNA expression relative to that of *Bp18S rRNA* was calculated using $2^{-\Delta CT}$ method. Values denoted by different letters are significantly different when compared by ANOVA (P<0.05); n=4. B–E: *BpIL-34* mRNA expression relative to that of *Bp18S rRNA* was calculated using $2^{-\Delta\Delta CT}$ method. Tissues were collected at 4, 8, 12, and 24 h after bacterial infection. Data are expressed as means±*SEM*; n=4, *: P<0.05.

BpCSF-1R1 or *BpCSF-1R2* expression (Figure 7B, C).

We then used BpCSF-1R1si and BpCSF-1R2si to explore whether BpCSF-1R1 and BpCSF-1R2 mediated the enhancing effect of rBPIL-34 on the phagocytotic and bacterial killing activity of MOs/MΦs. After BpCSF-1R1si transfection, MOs/MΦs treated with rBpIL-34 showed a significant decrease in phagocytosis of *E. tarda* (0.16-fold) compared to that in the control group (normal MO/MΦs treated with rBpIL-34), whereas MsiRNA or BpCSF-1R2si transfection resulted in no obvious changes (Figure 8A). On the other hand, the bacterial survival rate in *BpCSF-1R1*-knockdown MOs/MΦs after rBPIL-34 treatment was significantly increased (2.15-fold) compared to that in the control group (normal MO/MΦ treated with rBpIL-34), with MsiRNA or BpCSF-1R2si transfection resulting in no obvious changes (Figure 8B).

Effect of *BpCSF-1R1* and *BpCSF-1R2* knockdown on rBpIL-34-altered cytokine mRNA expression in MOs/MΦs

qRT-PCR analysis showed that *BpCSF-1R1* knockdown decreased the mRNA expression of *BpTNF-α*, *BpIL-1β*, and *BpIL-6* in mudskipper MOs/MΦs treated with rBpIL-34 by approximately 0.31-, 0.36-, and 0.49-fold, respectively, compared to levels in the MsiRNA-treated control group (Figure 9), whereas *BpTGF-β* and *BpIL-10* mRNA expression

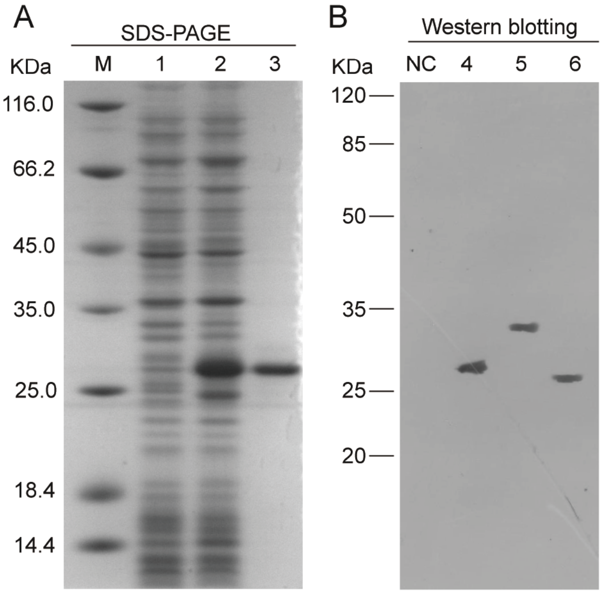

Figure 4 Prokaryotic expression and Western blot analysis of BpIL-34

A: SDS-PAGE analysis of prokaryotically expressed rBpIL-34. Lane M: Protein marker; 1, 2: Crude protein extracts from BL21 (DE3) transformed with pET-28a-BpIL-34 plasmid before and after IPTG induction, respectively; 3: Purified rBpIL-34. B: Western blot analysis of BpIL-34 using anti-rBpIL-34 IgG. NC: Negative control; 4: Purified rBpIL-34; 5: Proteins extracted from mudskipper MOs/MΦs; 6: Proteins extracted from mudskipper MOs/MΦs with PNGase F digestion.

was not obviously changed (Figure 9). *BpCSF-1R2* knockdown had no noticeable effect on the mRNA levels of all selected cytokines in MOs/MΦs compared to those in the control group (Figure 9).

DISCUSSION

IL-34 is a recently discovered cytokine identified as the second ligand of CSF-1R (Lin et al., 2008). Over the past decade, accumulating evidence has shown that IL-34 exerts potent immunomodulatory effects in many physiological and pathological states. However, studies on the function of IL-34 in teleosts are limited. In this study, we identified an *IL-34* homolog sequence from mudskippers. Sequence analysis revealed that BpIL-34 had structural similarities to other fish IL-34 homologs. Phylogenetic tree analysis showed that BpIL-34 belonged to the IL-34 clade and was most closely related to an orange-spotted grouper homolog. It has been reported that the C-terminal region of IL-34 is heavily glycosylated via O-linked glycans in humans (Felix et al., 2013), but this region is not found in fish IL-34 homologs (Xue et al., 2019). In contrast, two to six potential N-glycosylation sites are present in each fish IL-34 homolog (Wang et al., 2013). Our results showed that the native BpIL-34 in cells was N-glycosylated. Glycosylation plays an important role in functions such as intracellular transport, ligand binding, structural stability, and signal transduction (Huang et al., 2015). Recent study has shown that this post-translational glycosylation does not appear to influence the functions of recombinant grass carp IL-34 as the effects of both bacteria-derived rCiIL-34 and HEK293T cell-derived rCiIL-34 on fish MOs/MΦs are similar (Xue et al., 2019). Signatures of positive selection are also found in mammalian IL-34 (Neves et al., 2014), which might be explained by the multitude of biological processes involving IL-34.

Gene expression patterns commonly reflect functions. *IL-34* expression is mainly detected in the skin and central nervous system in mice (Wang et al., 2012). In fish, like rainbow trout, large yellow croaker, and grass carp, *IL-34* is constitutively expressed in various tissues, with highest expression found in the spleen (Wang et al., 2013, 2018; Xue et al., 2019), or the brain in the case of orange-spotted grouper (Mo et al., 2015). *IL-34* expression is tightly associated with pathogen stimulation. Most studies have shown that pathogen infection increases *IL-34* transcript levels in tissues, especially at the infected sites (Mo et al., 2015; Wang et al., 2013, 2018; Wu et al., 2019; Xue et al., 2019). However, a significant decrease in the expression of IL-34 in hepatitis B virus (HBV) patients has also been identified (Cheng et al., 2017). Changes in *IL-34* expression, either increase or decrease, are involved in disease pathogenesis, and are correlated with progression, severity, and chronicity (Baghdadi et al., 2018). In this study, we determined that *BpIL-34* transcripts were constitutively expressed in all tested tissues, with the highest level found in the brain. This result is in accordance with that reported in the orange-spotted grouper (Mo et al., 2015) and in mammals (Wang et al., 2012). IL-34 is a tissue-restricted ligand of CSF-1R and is required for the development of Langerhans cells and microglia in mammals (Wang et al., 2012); moreover, it can protect blood-brain barrier integrity by restoring expression levels of tight junction proteins (Jin et al., 2014). Fish IL-34 may also exhibit such functions. Upon *E. tarda* infection, the *BpIL-34* mRNA level was significantly up-regulated in the liver, spleen, kidney, and brain, in accordance with that reported in fish previously (Mo et al., 2015; Wang et al., 2013; Wu et al., 2019; Xue et al., 2019), suggesting that *BpIL-34* may be involved in mudskipper immune responses against *E. tarda*.

MO/MΦ plays key roles in the fish protection system, and phagocytosis, the killing of invading bacteria, and production of cytokines are their main effector functions (Lu & Chen, 2019; Zou & Secombes, 2016). IL-34 was first identified as a potent activator of MO and MΦ via CSF-1R based on functional screening of the extracellular proteome (Lin et al., 2008). In the African clawed frog (*Xenopus laevis*), recombinant IL-34-derived MΦs not only display higher bactericidal activity than control cells but also exhibit potent antiviral activity against FV3 ranavirus, which is dependent on reactive oxygen production (Grayfer & Robert, 2014, 2015). Intriguingly, recombinant CSF-1-treated rather than recombinant IL-34-treated MΦs are more phagocytic for both tadpoles and adult frogs (Grayfer & Robert, 2014, 2015). IL-34

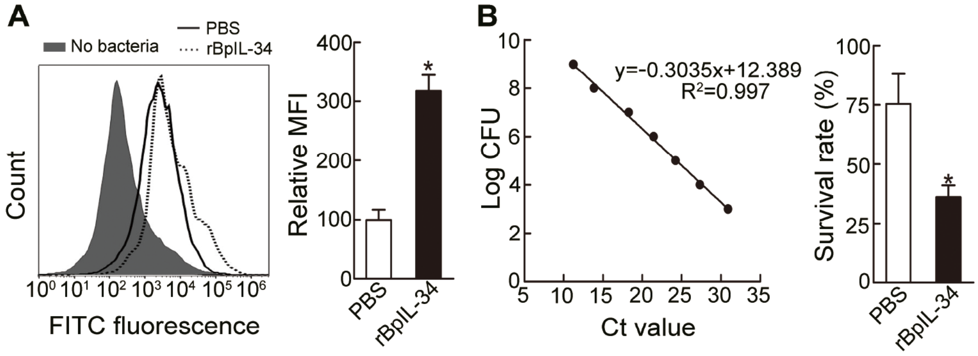

Figure 5 Effects of rBpIL-34 on phagocytosis and bacterial killing of *Edwardsiella tarda* by mudskipper MO/MΦs

A: Effect of rBpIL-34 on phagocytosis of *E. tarda* by MOs/MΦs. Mudskipper MOs/MΦs were pre-treated with PBS or rBpIL-34 before adding FITC-*E. tarda* (MOI=10). After an additional 30 min incubation, phagocytosis of FITC-*E. tarda* was determined by flow cytometry. MFI is presented as fold-change over the value for PBS-treated group, which was assigned a unit of 100. B: Effect of rBpIL-34 on bacterial killing of *E. tarda* by MOs/MΦs. MOs/MΦs were infected with live *E. tarda* after treatment with PBS or rBpIL-34, and viability of *E. tarda* (MOI=10) was determined by qRT-PCR. Killing of *E. tarda* by mudskipper MOs/MΦs was measured using CFU assay based on a standard curve. Data are expressed as means±*SEM*; *n*=4, *: *P*<0.05.

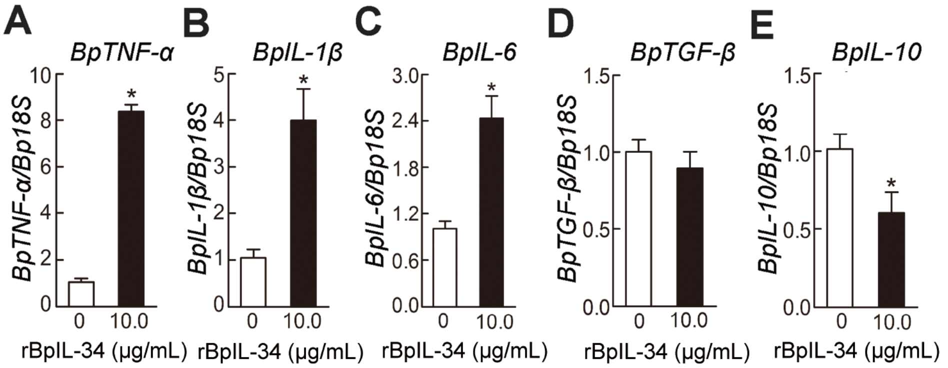

Figure 6 Effects of rBpIL-34 on mRNA expression of *BpTNF-α* (A), *BpIL-1β* (B), *BpIL-6* (C), *BpTGF-β* (D), and *BpIL-10* (E) in mudskipper MOs/MΦs

MOs/MΦs were treated with rBpIL-34 for 12 h. PBS-treated group was used as the control. mRNA expression levels of selected cytokines were normalized to those of *Bp18S rRNA*. Data are expressed as means±*SEM*; *n*=4, *: *P*<0.05.

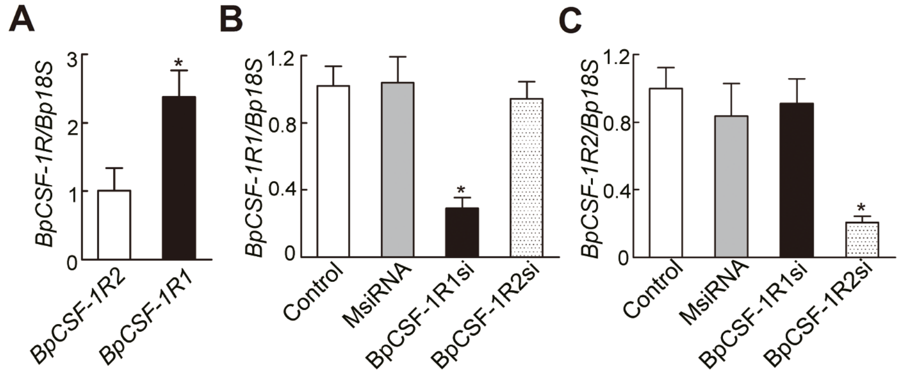

Figure 7 RNAi-mediated gene knockdown of *BpCSF-1R1* and *BpCSF-1R2* in mudskipper MOs/MΦs

A: qRT-PCR analysis of mRNA expression of *BpCSF-1R1* and *BpCSF-1R2* in primary MOs/MΦs. B: qRT-PCR analysis of *BpCSF-1R1* transcripts in BpCSF-1R1si- or BpCSF-1R2si-transfected MOs/MΦs. C: qRT-PCR analysis of *BpCSF-1R2* transcripts in BpCSF-1R1si- or BpCSF-1R2si-transfected MOs/MΦs. MsiRNA-transfected MOs/MΦs group was used as the control. mRNA levels of *BpCSF-1R1* and *BpCSF-1R2* were normalized to those of *Bp18S rRNA*. Data are expressed as means±*SEM*; *n*=4, *: *P*<0.05.

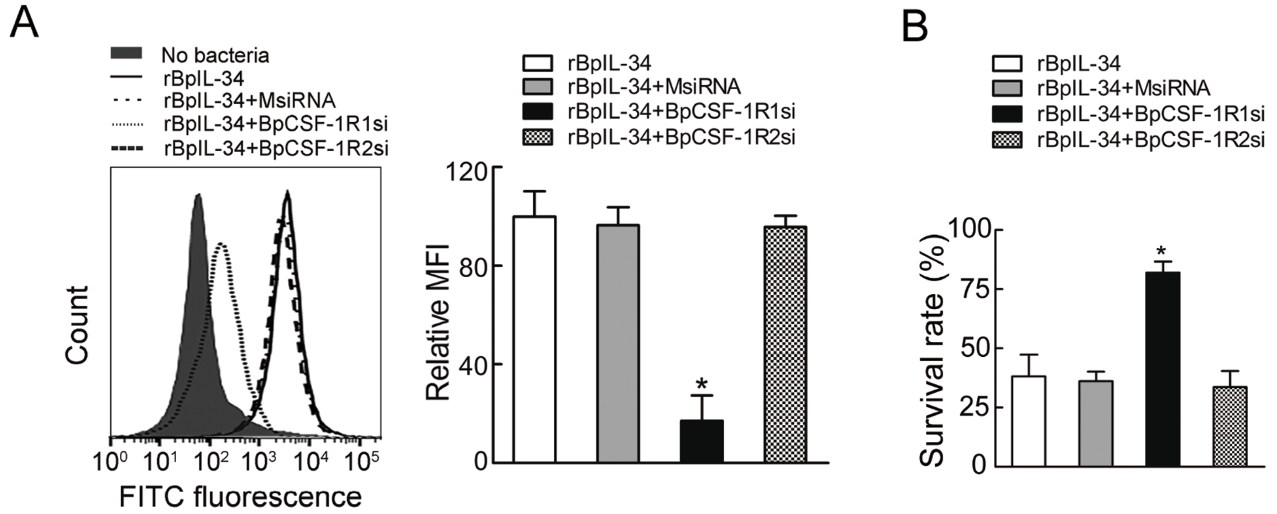

Figure 8 Effects of *BpCSF-1R1* and *BpCSF-1R2* knockdown on rBpIL-34-enhanced phagocytosis and bacterial killing of *Edwardsiella tarda* by mudskipper MOs/MΦs

A: Effect of *BpCSF-1R1* or *BpCSF-1R2* knockdown on rBpIL-34-enhanced phagocytosis of *E. tarda* by mudskipper MOs/MΦs. After transfection with BpCSF-1R1si, BpCSF-1R2si, or MsiRNA (control) for 48 h, mudskipper MOs/MΦs were treated with rBpIL-34 for 12 h. Normal MOs/MΦs treated with rBpIL-34 (rBpIL-34 group) were used as controls. Thereafter, FITC-*E. tarda* were added at a MOI of 10 and incubated for an additional 30 min. Phagocytosis of FITC-*E. tarda* was determined by flow cytometry. Mean fluorescence intensity (MFI) is presented as a fold-change over value for rBpIL-34 group, which was assigned a value of 100. B: Effect of *BpCSF-1R1* and *BpCSF-1R2* knockdown on rBpIL-34-enhanced bacterial killing of *E. tarda* by mudskipper MOs/MΦs. After transfection with BpCSF-1R1si, BpCSF-1R2si, or MsiRNA for 48 h, mudskipper MOs/MΦs were treated with rBpIL-34 for 12 h. Normal MOs/MΦs treated with rBpIL-34 (rBpIL-34 group) were used as controls. Live *E. tarda* were added at a MOI of 10 and incubated for an additional 30 min. Killing of *E. tarda* by mudskipper MOs/MΦs was measured using a CFU assay based on standard curve. Data are expressed as means±*SEM*; *n*=4, *: *P*<0.05.

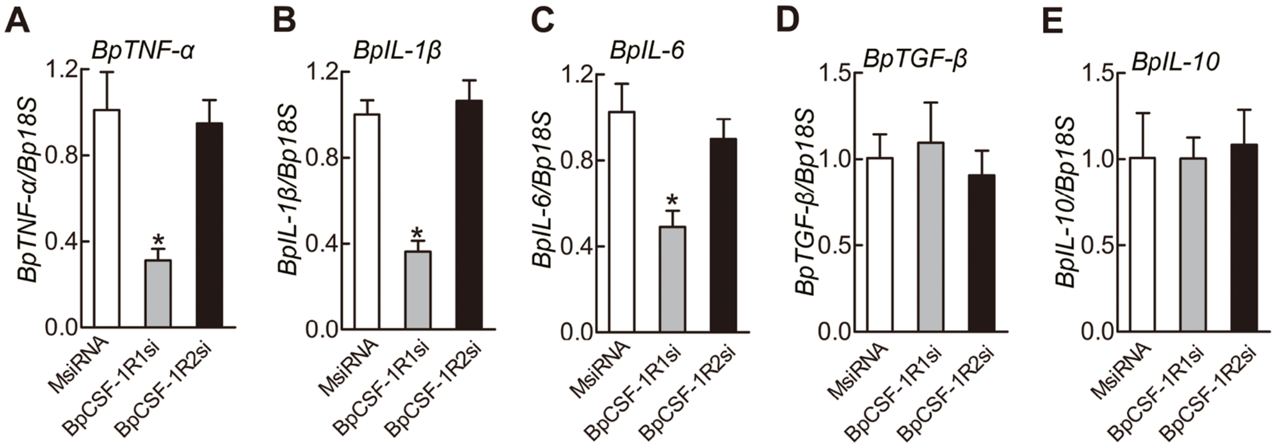

Figure 9 Effects of *BpCSF-1R1* and *BpCSF-1R2* knockdown on rBpIL-34-altered mRNA expression of selected cytokines in MOs/MΦs

Mudskipper MOs/MΦs were pre-treated with BpCSF-1R1si, BpCSF-1R2si, or MsiRNA (control) and further incubated with rBpIL-34 for 12 h. MsiRNA-treated group was used as the control. mRNA levels of *BpTNF-α* (A), *BpIL-1β* (B), *BpIL-6* (C), *BpTGF-β* (D), and *BpIL-10* (E) were normalized to those of *Bp18S rRNA*. Data are expressed as means±*SEM*; *n*=4, *: *P*<0.05.

also activates microglia (tissue-resident MΦs of the central nervous system) to rescue neurons by enhancing the phagocytosis of toxicants or damaged debris (Suzumura, 2013; Wang & Colonna, 2014). In this study, we showed that rBpIL-34-derived mudskipper MOs/MΦs displayed increased phagocytic and bactericidal activities compared to those of the PBS-treated control group, suggesting that rBpIL-34 could activate these cells and possibly drive their differentiation. Cytokines are signaling proteins that regulate a wide range of biological functions, and macrophages are a major source of many cytokines. Studies have shown that IL-34 can alter cytokine expression in vertebrate species. For example, IL-34 treatment can induce the up-regulation of IL-6, CXCL10, IL-8, and CCL2 in human whole blood (Eda et al., 2010) and increased TNF-α expression in lamina propria mononuclear cells (Franzè et al., 2015). Furthermore, the addition of IL-34 to primary lung fibroblasts can significantly promote IL-6 and IL-8 expression in a dose- and time-dependent manner (Zhou et al., 2018). Treatment with chicken IL-34 increases the expression of Th1 and Th17 cytokines in chicken cell lines (Truong et al., 2018). In grass carp, *in vitro* IL-34 treatment up-regulates the expression of IL-1β, IL-6, and IL-8 but inhibits the expression of IL-10 and TGF-β1 in MΦs (Xue et al., 2019). Here, we determined that rBpIL-34-derived MOs/MΦs expressed higher levels of *BpTNF-α*, *BpIL-1β*, and *BpIL-6* and lower levels of *BpIL-10* compared to that in the PBS-treated control group, coinciding well with previous reports (Eda et al., 2010; Franzè et al., 2015; Truong et al., 2018; Xue et al., 2019; Zhou et al., 2018). These results suggest that IL-34 promotes the differentiation of mudskipper MO/MΦ into the pro-inflammatory phenotype.

CSF-1R is critical for the proliferation, survival, and differentiation of MΦs, as its knockdown results in the marked depletion of MΦs in most tissues (Dai et al, 2002; Droin & Solary, 2010). In addition, CSF-1R signaling controls development of the MΦ lineage under steady conditions and during certain inflammatory reactions (Lenzo et al, 2012). CSF-1R is a major receptor of IL-34 in mammals (Baghdadi et al., 2018; Jeannin et al., 2018; Peyraud et al., 2017). For example, in human whole blood, the IL-34-enhanced mRNA expression levels of *IL-6* and chemokines such as *MCP-1* are inhibited by GW2580, a CSF-1R kinase inhibitor (Eda et al., 2010). In this study, we determined that BpCSF-1R1, but not BpCSF-1R2, mediated the enhancing effects of rBpIL-34 on MO/MΦ phagocytosis, bactericidal activity, and pro-inflammatory cytokine mRNA expression. Interestingly, although rBpIL-34 inhibited the mRNA expression of the anti-inflammatory cytokine *BpIL-10* in MOs/MΦs, knockdown of *BpCSF-1R1* and *BpCSF-1R2* had no significant effect on *BpIL-10* mRNA expression in mudskipper MOs/MΦs compared to that in the MsiRNA-treated control group, suggesting that the inhibitory effect of rBPIL-34 on *BpIL-10* mRNA expression was independent of BpCSF-1R1 and BpCSF-1R2. To our knowledge, this is the first report to show that CSF-1R1 mediates the functions of IL-34 in fish MOs/MΦs.

In summary, we identified an IL-34 homolog from mudskippers. *BpIL-34* mRNA expression was up-regulated in mudskipper tissue upon *E. tarda* infection. *In vitro*, rBpIL-34 treatment not only enhanced the phagocytotic and bactericidal activity of mudskipper MOs/MΦs but also elevated the mRNA levels of pro-inflammatory cytokines. Results of RNAi suggested that BpCSF-1R1, but not BpCSF-1R2, mediated the effects of rBpIL-34. However, further investigations are needed to determine the underlying intracellular signaling pathways associated with IL-34.

COMPETING INTERESTS

The authors declare that they have no competing interests.

AUTHORS' CONTRIBUTIONS

H.Y.S., Q.J.Z, and J.C. conceived and designed the experiments. H.Y.S., Y.Z., and Q.J.Z performed the experiments. H.Y.S., Q.J.Z, and J.C. analyzed the data and wrote the manuscript. M.Y.L. and J.C. reviewed and corrected the manuscript. All authors read and approved the final version of the manuscript.

REFERENCES

Baghdadi M, Umeyama Y, Hama N, Kobayashi T, Han N, Wada H, Seino KI. 2018. Interleukin-34, a comprehensive review. *Journal of Leukocyte Biology*, **104**(5): 931−951.

Chen J, Chen Q, Lu XJ, Chen J. 2016a. The protection effect of LEAP-2 on the mudskipper (*Boleophthalmus pectinirostris*) against *Edwardsiella tarda* infection is associated with its immunomodulatory activity on monocytes/macrophages. *Fish & Shellfish Immunology*, **59**: 66−76.

Chen J, Nie L, Chen J. 2018. Mudskipper (*Boleophthalmus pectinirostris*) hepcidin-1 and hepcidin-2 present different gene expression profile and antibacterial activity and possess distinct protective effect against *Edwardsiella tarda* infection. *Probiotics and Antimicrobial Proteins*, **10**(2): 176−185.

Chen K, Shi YH, Chen J, Li MY. 2019. A soluble FcγR homolog inhibits IgM antibody production in ayu spleen cells. *Zoological Research*, **40**(5): 404−415.

Chen Q, Lu XJ, Chen J. 2015. Identification and functional characterization of the CSF1R gene from grass carp *Ctenopharyngodon idellus* and its use as a marker of monocytes/macrophages. *Fish & Shellfish Immunology*, **45**(2): 386−398.

Chen Q, Lu XJ, Li MY, Chen J. 2016b. Molecular cloning, pathologically-correlated expression and functional characterization of the colonystimulating factor 1 receptor (CSF-1R) gene from a teleost, *Plecoglossus altivelis*. *Zoological Research*, **37**(2): 96−102.

Cheng ST, Tang H, Ren JH, Chen X, Huang AL, Chen J. 2017. Interleukin-34 inhibits hepatitis B virus replication *in vitro* and *in vivo*. *PLoS One*, **12**(6): e0179605.

Chihara T, Suzu S, Hassan R, Chutiwitoonchai N, Hiyoshi M, Motoyoshi K, Kimura F, Okada S. 2010. IL-34 and M-CSF share the receptor Fms but are not identical in biological activity and signal activation. *Cell Death & Differentiation*, **17**(12): 1917−1927.

Dai XM, Ryan GR, Hapel AJ, Dominguez MG, Russell RG, Kapp S, Sylvestre V, Stanley ER. 2002. Targeted disruption of the mouse colony-stimulating factor 1 receptor gene results in osteopetrosis, mononuclear phagocyte deficiency, increased primitive progenitor cell frequencies, and reproductive defects. *Blood*, **99**(1): 111−120.

Dan XM, Zhong ZP, Li YW, Luo XC, Li AX. 2013. Cloning and expression analysis of grouper (*Epinephelus coioides*) M-CSFR gene post *Cryptocaryon irritans* infection and distribution of M-CSFR$^+$ cells. *Fish & Shellfish Immunology*, **35**(2): 240−248.

Ding FF, Li CH, Chen J. 2019. Molecular characterization of the NK-lysin in a teleost fish, *Boleophthalmus pectinirostris*: Antimicrobial activity and immunomodulatory activity on monocytes/macrophages. *Fish & Shellfish*

Immunology, **92**: 256−264.

Droin N, Solary E. 2010. Editorial: CSF1R, CSF-1, and IL-34, a "ménage à trois" conserved across vertebrates. *Journal of Leukocyte Biology*, **87**(5): 745−747.

Eda H, Zhang J, Keith RH, Michener M, Beidler DR, Monahan JB. 2010. Macrophage-colony stimulating factor and interleukin-34 induce chemokines in human whole blood. *Cytokine*, **52**(3): 215−220.

Felix J, Elegheert J, Gutsche I, Shkumatov AV, Wen YR, Bracke N, Pannecoucke E, Vandenberghe I, Devreese B, Svergun DI, Pauwels E, Vergauwen B, Savvides SN. 2013. Human IL-34 and CSF-1 establish structurally similar extracellular assemblies with their common hematopoietic receptor. *Structure*, **21**(4): 528−539.

Franzè E, Monteleone I, Cupi ML, Mancia P, Caprioli F, Marafini I, Colantoni A, Ortenzi A, Laudisi F, Sica G, Sileri P, Pallone F, Monteleone G. 2015. Interleukin-34 sustains inflammatory pathways in the gut. *Clinical Science*, **129**(3): 271−280.

Grayfer L, Robert J. 2014. Divergent antiviral roles of amphibian (*Xenopus laevis*) macrophages elicited by colony-stimulating factor-1 and interleukin-34. *Journal of Leukocyte Biology*, **96**(6): 1143−1153.

Grayfer L, Robert J. 2015. Distinct functional roles of amphibian (*Xenopus laevis*) colony-stimulating factor-1- and interleukin-34-derived macrophages. *Journal of Leukocyte Biology*, **98**(4): 641−649.

Greter M, Lelios I, Pelczar P, Hoeffel G, Price J, Leboeuf M, Kündig TM, Frei K, Ginhoux F, Merad M, Becher B. 2012. Stroma-derived interleukin-34 controls the development and maintenance of langerhans cells and the maintenance of microglia. *Immunity*, **37**(6): 1050−1060.

Guan F, Lu XJ, Li CH, Chen J. 2017. Molecular characterization of mudskipper (*Boleophthalmus pectinirostris*) hypoxia-inducible factor-1α (HIF-1α) and analysis of its function in monocytes/macrophages. *PLoS One*, **12**(5): e0177960.

Honda T, Nishizawa T, Uenobe M, Kohchi C, Kuroda A, Ototake M, Nakanishi T, Yokomizo Y, Takahashi Y, Inagawa H, Soma GI. 2005. Molecular cloning and expression analysis of a macrophage-colony stimulating factor receptor-like gene from rainbow trout, *Oncorhynchus mykiss*. *Molecular Immunology*, **42**(1): 1−8.

Huang ZL, Chen S, Liu JC, Xiao J, Yan J, Feng H. 2015. IFNa of black carp is an antiviral cytokine modified with N-linked glycosylation. *Fish & Shellfish Immunology*, **46**(2): 477−485.

Jeannin P, Paolini L, Adam C, Delneste Y. 2018. The roles of CSFs on the functional polarization of tumor-associated macrophages. *The FEBS Journal*, **285**(4): 680−699.

Jiang YY, Chen JH, Yen K, Xu J. 2019. Ectopically expressed IL-34 can efficiently induce macrophage migration to the liver in zebrafish. *Zebrafish*, **16**(2): 165−170.

Jin SJ, Sonobe Y, Kawanokuchi J, Horiuchi H, Cheng Y, Wang Y, Mizuno T, Takeuchi H, Suzumura A. 2014. Interleukin-34 restores blood-brain barrier integrity by upregulating tight junction proteins in endothelial cells. *PLoS One*, **9**(12): e115981.

Katzenback BA, Belosevic M. 2012. Colony-stimulating factor-1 receptor protein expression is a specific marker for goldfish (*Carassius auratus* L.) macrophage progenitors and their differentiated cell types. *Fish & Shellfish Immunology*, **32**(3): 434−445.

Kim JI, Turka LA. 2015. Transplant tolerance: a new role for IL-34. *Journal of Clinical Investigation*, **125**(10): 3751−3753.

Lenzo JC, Turner AL, Cook AD, Vlahos R, Anderson GP, Reynolds EC, Hamilton JA. 2012. Control of macrophage lineage populations by CSF-1 receptor and GM-CSF in homeostasis and inflammation. *Immunology & Cell Biology*, **90**(4): 429−440.

Lin HS, Lee E, Hestir K, Leo C, Huang MM, Bosch E, Halenbeck R, Wu G, Zhou A, Behrens D, Hollenbaugh D, Linnemann T, Qin MM, Wong J, Chu KT, Doberstein SK, Williams LT. 2008. Discovery of a cytokine and its receptor by functional screening of the extracellular proteome. *Science*, **320**(5877): 807−811.

Liu H, Leo C, Chen XY, Wong BR, Williams LT, Lin HS, He XL. 2012. The mechanism of shared but distinct CSF-1R signaling by the non-homologous cytokines IL-34 and CSF-1. *Biochimica et Biophysica Acta (BBA) - Proteins and Proteomics*, **1824**(7): 938−945.

Lu XJ, Chen J. 2019. Specific function and modulation of teleost monocytes/macrophages: polarization and phagocytosis. *Zoological Research*, **40**(3): 146−150.

Ma XL, Lin WY, Chen YM, Stawicki S, Mukhyala K, Wu Y, Martin F, Bazan JF, Starovasnik MA. 2012. Structural basis for the dual recognition of helical cytokines IL-34 and CSF-1 by CSF-1R. *Structure*, **20**(4): 676−687.

Masteller EL, Wong BR. 2014. Targeting IL-34 in chronic inflammation. *Drug Discovery Today*, **19**(8): 1212−1216.

Mo ZQ, Li YW, Zhou L, Li AX, Luo XC, Dan XM. 2015. Grouper (*Epinephelus coioides*) IL-34/MCSF2 and MCSFR1/MCSFR2 were involved in mononuclear phagocytes activation against *Cryptocaryon irritans* infection. *Fish & Shellfish Immunology*, **43**(1): 142−149.

Mulero I, Pilar Sepulcre M, Roca FJ, Meseguer J, García-Ayala A, Mulero V. 2008. Characterization of macrophages from the bony fish gilthead seabream using an antibody against the macrophage colony-stimulating factor receptor. *Developmental & Comparative Immunology*, **32**(10): 1151−1159.

Nakamichi Y, Udagawa N, Takahashi N. 2013. IL-34 and CSF-1: similarities and differences. *Journal of Bone and Mineral Metabolism*, **31**(5): 486−495.

Nandi S, Gokhan S, Dai XM, Wei SW, Enikolopov G, Lin HS, Mehler MF, Stanley ER. 2012. The CSF-1 receptor ligands IL-34 and CSF-1 exhibit distinct developmental brain expression patterns and regulate neural progenitor cell maintenance and maturation. *Developmental Biology*, **367**(2): 100−113.

Neves F, Abrantes J, Steinke JW, Esteves PJ. 2014. Maximum-likelihood approaches reveal signatures of positive selection in IL genes in mammals. *Innate Immunity*, **20**(2): 184−191.

Ogryzko NV, Renshaw SA, Wilson HL. 2014. The IL-1 family in fish: swimming through the muddy waters of inflammasome evolution. *Developmental & Comparative Immunology*, **46**(1): 53−62.

Peyraud F, Cousin S, Italiano A. 2017. CSF-1R inhibitor development: current clinical status. *Current Oncology Reports*, **19**(11): 70.

Rieger AM, Konowalchuk JD, Havixbeck JJ, Robbins JS, Smith MK, Lund JM, Barreda DR. 2013. A soluble form of the CSF-1 receptor contributes to the inhibition of inflammation in a teleost fish. *Developmental & Comparative Immunology*, **39**(4): 438−446.

Rieger AM, Hanington PC, Belosevic M, Barreda DR. 2014. Control of CSF-1 induced inflammation in teleost fish by a soluble form of the CSF-1 receptor. *Fish & Shellfish Immunology*, **41**(1): 45−51.

Rieger AM, Havixbeck JJ, Belosevic M, Barreda DR. 2015. Teleost soluble CSF-1R modulates cytokine profiles at an inflammatory site, and inhibits neutrophil chemotaxis, phagocytosis, and bacterial killing. *Developmental & Comparative Immunology*, **49**(2): 259−266.

Roca FJ, Sepulcre MP, López-Castejón G, Meseguer J, Mulero V. 2006. The colony-stimulating factor-1 receptor is a specific marker of macrophages from the bony fish gilthead seabream. *Molecular Immunology*, **43**(9): 1418−1423.

Secombes CJ. 2016. What's new in fish cytokine research?. *Fish & Shellfish Immunology*, **53**: 1−3.

Secombes CJ, Zou J. 2017. Evolution of interferons and interferon receptors. *Frontiers in Immunology*, **8**: 209.

Ségaliny AI, Brion R, Brulin B, Maillasson M, Charrier C, Téletchéa S, Heymann D. 2015. IL-34 and M-CSF form a novel heteromeric cytokine and regulate the M-CSF receptor activation and localization. *Cytokine*, **76**(2): 170−181.

Slaven EM, Lopez FA, Hart SM, Sanders CV. 2001. Myonecrosis caused by *Edwardsiella tarda*: a case report and case series of extraintestinal *E. tarda* infections. *Clinical Infectious Diseases*, **32**(10): 1430−1433.

Suzumura A. 2013. Neuron-microglia interaction in neuroinflammation. *Current Protein & Peptide Science*, **14**(1): 16−20.

Tamura K, Peterson D, Peterson N, Stecher G, Nei M, Kumar S. 2011. MEGA5: molecular evolutionary genetics analysis using maximum likelihood, evolutionary distance, and maximum parsimony methods. *Molecular Biology and Evolution*, **28**(10): 2731−2739.

Truong AD, Hong Y, Lee J, Lee K, Kil DY, Lillehoj HS, Hong YH. 2018. Interleukin-34 regulates Th1 and Th17 cytokine production by activating multiple signaling pathways through CSF-1R in chicken cell lines. *International Journal of Molecular Sciences*, **19**(6): 1665.

Vasek MJ, Garber C, Dorsey D, Durrant DM, Bollman B, Soung A, Yu JS, Perez-Torres C, Frouin A, Wilton DK, Funk K, DeMasters BK, Jiang XP, Bowen JR, Mennerick S, Robinson JK, Garbow JR, Tyler KL, Suthar MS, Schmidt RE, Stevens B, Klein RS. 2016. A complement-microglial axis drives synapse loss during virus-induced memory impairment. *Nature*, **534**(7608): 538−543.

Wang LP, Jiang LH, Wu CW, Lou B. 2018. Molecular characterization and expression analysis of large yellow croaker (*Larimichthys crocea*) interleukin-12A, 16 and 34 after poly I: C and *Vibrio anguillarum* challenge. *Fish & Shellfish Immunology*, **74**: 84−93.

Wang TH, Kono T, Monte MM, Kuse H, Costa MM, Korenaga H, Maehr T, Husain M, Sakai M, Secombes CJ. 2013. Identification of IL-34 in teleost fish: differential expression of rainbow trout IL-34, MCSF1 and MCSF2, ligands of the MCSF receptor. *Molecular Immunology*, **53**(4): 398−409.

Wang TH, Secombes CJ. 2013. The cytokine networks of adaptive immunity in fish. *Fish & Shellfish Immunology*, **35**(6): 1703−1718.

Wang YM, Szretter KJ, Vermi W, Gilfillan S, Rossini C, Cella M, Barrow AD, Diamond MS, Colonna M. 2012. IL-34 is a tissue-restricted ligand of CSF1R required for the development of Langerhans cells and microglia. *Nature Immunology*, **13**(8): 753−760.

Wang YM, Colonna M. 2014. Interkeukin-34, a cytokine crucial for the differentiation and maintenance of tissue resident macrophages and Langerhans cells. *European Journal of Immunology*, **44**(6): 1575−1581.

Williams H, Brenner S, Venkatesh B. 2002. Identification and analysis of additional copies of the platelet-derived growth factor receptor and colony stimulating factor 1 receptor genes in fugu. *Gene*, **295**(2): 255−264.

Wu Y, Zhou YC, Cao ZJ, Sun Y, Chen Y, Xiang YJ, Wang L, Zhang SN, Guo WL. 2019. Comparative analysis of the expression patterns of IL-1β, IL-11, and IL-34 in golden pompano (*Trachinotus ovatus*) following different pathogens challenge. *Fish & Shellfish Immunology*, **93**: 863−870.

Xu TT, Zhang XH. 2014. *Edwardsiella tarda*: an intriguing problem in aquaculture. *Aquaculture*, **431**: 129−135.

Xue YJ, Jiang XY, Gao JD, Li X, Xu JW, Wang JY, Gao Q, Zou J. 2019. Functional characterisation of interleukin 34 in grass carp *Ctenopharyngodon idella*. *Fish & Shellfish Immunology*, **92**: 91−100.

You XX, Bian C, Zan QJ, Xu X, Liu X, Chen JM, Wang JT, Qiu Y, Li WJ, Zhang XH, Sun Y, Chen SX, Hong WS, Li YX, Cheng SF, Fan GY, Shi CC, Liang J, Tom Tang Y, Yang CY, Ruan ZQ, Bai J, Peng C, Mu Q, Lu J, Fan MJ, Yang S, Huang ZY, Jiang XT, Fang XD, Zhang GJ, Zhang Y, Polgar G, Yu H, Li J, Liu ZJ, Zhang GQ, Ravi V, Coon SL, Wang J, Yang HM, Venkatesh B, Wang J, Shi Q. 2014. Mudskipper genomes provide insights into the terrestrial adaptation of amphibious fishes. *Nature Communications*, **5**(1): 5594.

You XX, Chen JM, Bian C, Yi YH, Ruan ZQ, Li J, Zhang XH, Yu H, Xu JM, Shi Q. 2018. Transcriptomic evidence of adaptive tolerance to high environmental ammonia in mudskippers. *Genomics*, **110**(6): 404−413.

Zhou J, Sun XY, Zhang J, Yang Y, Chen DP, Cao J. 2018. IL-34 regulates IL-6 and IL-8 production in human lung fibroblasts *via* MAPK, PI3K-Akt, JAK and NF-κB signaling pathways. *International Immunopharmacology*, **61**: 119−125.

Zou J, Secombes CJ. 2016. The function of fish cytokines. *Biology*, **5**(2): 23.

ZOOLOGICAL RESEARCH

Comparative analysis of diverse toxins from a new pharmaceutical centipede, *Scolopendra mojiangica*

Zi-Chao Liu[1,3,#], Jin-Yang Liang[2,5,#], Xin-Qiang Lan[1,2,5], Tao Li[1,4], Jia-Rui Zhang[2,7], Fang Zhao[1,4,6], Geng Li[1,4], Pei-Yi Chen[1,4], Yun Zhang[2,*], Wen-Hui Lee[2,*], Feng Zhao[1,4,6,*]

[1] *Key Laboratory of Ethnic Medical Resources Research and Southeast Asian International Cooperation of Yunnan Universities*, *Department of Biology and Chemistry*, *Puer University*, *Puer*, *Yunnan* 665000, *China*

[2] *Key Laboratory of Animal Models and Human Disease Mechanisms of the Chinese Academy of Sciences* & *Yunnan Province*, *Kunming Institute of Zoology*, *Chinese Academy of Sciences*, *Kunming*, *Yunnan* 650223, *China*

[3] *Engineering Research Center for Exploitation and Utilization of Leech Resources in Universities of Yunnan Province*, *School of Agronomy and Life Sciences*, *Kunming University*, *Kunming*, *Yunnan* 650214, *China*

[4] *Key Laboratory of Active Molecules and Drug Development*, *Puer University*, *Puer*, *Yunnan* 665000, *China*

[5] *Kunming College of Life Science*, *University of Chinese Academy of Sciences*, *Kunming*, *Yunnan* 650204, *China*

[6] *Institute of Comparative Study of Traditional Materia Medica*, *Institute of Integrative Medicine of Fudan University*, *Shanghai* 200032, *China*

[7] *Nanshan College*, *Guangzhou Medical University*, *Guangzhou*, *Guangdong* 511436, *China*

ABSTRACT

As the oldest venomous animals, centipedes use their venom as a weapon to attack prey and for protection. Centipede venom, which contains many bioactive and pharmacologically active compounds, has been used for centuries in Chinese medicine, as shown by ancient records. Based on comparative analysis, we revealed the diversity of and differences in centipede toxin-like molecules *between Scolopendra mojiangica*, a substitute pharmaceutical material used in China, and *S. subspinipes mutilans*. More than 6 000 peptides isolated from the venom were identified by electrospray ionization-tandem mass spectrometry (ESI-MS/MS) and inferred from the transcriptome. As a result, in the proteome of *S. mojiangica*, 246 unique proteins were identified: one in five were toxin-like proteins or putative toxins with unknown function, accounting for a lower percentage of total proteins than that in *S. mutilans*. Transcriptome mining identified approximately 10 times more toxin-like proteins, which can characterize the precursor structures of mature toxin-like peptides. However, the constitution and quantity of the toxin transcripts in these two centipedes were similar. In toxicity assays, the crude venom showed strong insecticidal and hemolytic activity. These findings highlight the extensive diversity of toxin-like

---

Open Access

Received: 15 October 2019; Accepted: 06 December 2019; Online: 31 December 2019

Foundation items: This work was supported by grants from the Chinese National Natural Science Foundation (81860696, 31560596, 81373945, and 31360516), Yunnan Applied Basic Research Projects (2016FD076), Key Research Program of the Chinese Academy of Sciences (KJZD-EW-L03), "Yunling Scholar" Program, Yunnan Provincial Training Programs of Youth Leader in Academic and Technical Reserve Talent (2019HB058), and Puer University (2017XJKT12 & CXTD011)

[#] Authors contributed equally to this work

*Corresponding authors, E-mail: zhangy@mail.kiz.ac.cn; leewh@mail.kiz.ac.cn; zhaofeng@mail.kiz.ac.cn

DOI: 10.24272/j.issn.2095-8137.2020.019

proteins in *S. mojiangica* and provide a new foundation for the medical-pharmaceutical use of centipede toxin-like proteins.

Keywords: Centipede; Toxins; Pharmaceutical use; Proteotranscriptomic analysis

INTRODUCTION

As one of the oldest and most important predatory arthropods, the centipede has a fossil record that extends back 420 million years (Undheim & King, 2011). Approximately 3 300–3 500 centipede species have been found, with distribution worldwide and in most provinces of China (Rong et al., 2015). Centipede venom, which is secreted from venom glands in the first pair of limbs (Edgecombe & Giribet, 2007), is essential for survival, not only for subduing and killing prey but also for defense against predators.

Animal venom has long been considered a rich source of pharmacological and novel therapeutics (Kalia et al., 2015; Smith et al., 2013; Zhang, 2015). Furthermore, dried centipedes have been used medicinally for centuries, as shown in ancient Chinese medical records. Recently, an increasing number of studies have shown that centipede venom contains various functional components, including a rich reservoir of structural and pharmacological peptides (Hakim et al., 2015; Undheim et al., 2015, 2016). In addition, because of their excellent chemical and pharmacological activities, particularly as neurotoxins and ion channel inhibitors, centipede toxins have received further attention (Liu et al., 2012; Yang et al., 2012, 2013, 2015). Several antimicrobial peptides and specific toxins have also been identified in centipede venom (Chen et al., 2014; Hou et al., 2013; Peng et al., 2010; Yang et al., 2012). Interestingly, centipede toxins are expressed outside the venom gland and are involved in gene recruitment processes (Zhao et al., 2018a). These venom peptides have significant chemical, thermal, and biological stability, which enable researchers to adapt their functions for therapeutic use.

Therefore, centipede venom research is of great interest for investigating putative toxins. These toxins can act on a range of molecular targets, including voltage-gated sodium (Na_V), potassium (K_V), and calcium (Ca_V) channels (Liu et al., 2012; Yang et al., 2012). However, biochemical studies on centipede toxins are not nearly as extensive as studies on other venomous animals, such as snakes, spiders, and scorpions (Undheim et al., 2016), and complete data on centipede venom toxins, peptides, and protein sequences are currently limited to a small number of species (Hakim et al., 2015; Undheim et al., 2016). One potential reason is that most centipede species are considered too small to obtain enough venom for activity testing or high-throughput drug screening. Omics analysis of venom or venom glands is one approach for probing toxin molecular diversity. Specifically, to identify new putative proteins and enable comparison across species, large-scale sequencing of a broad array of centipede venom should be applied to further confirm the complexity of venom (Gonzalez-Morales et al., 2014; Liu et al., 2012; Rong et al., 2015).

Previous centipede research has mainly focused on *Scolopendra mutilans* (Zhao et al., 2018a), and occasionally on *S. subspinipes subspinipes*, *S. viridis*, and *S. dehaani* (Liu et al., 2012). To date, however, no comprehensive research has been reported on the new pharmaceutical centipede, *S. mojiangica* (Wang et al., 1997), which is used as a substitute medicinal material in traditional Chinese medicine. Therefore, a fully integrated approach combining transcriptomics and proteomics is essential for understanding the differences among pharmaceutical centipedes, including venom composition and toxin diversity. Here, in-depth proteotranscriptomic analyses (combined proteomic and transcriptomic analyses) were used to study centipede venom, and the protein/peptide composition of the dissected venom gland from *S. mojiangica* was described. Complete comparative analyses of the protein compounds and toxin distribution in the venom or venom gland of *S. mojiangica* and *S. mutilans* were also presented based on RNA-Seq and MS datasets.

MATERIALS AND METHODS

Animals and ethics

Adult *S. mojiangica* (both sexes) were collected from Mojiang (N23°27', E101°41'), Yunnan Province, China. All centipede (*S. mojiangica*) studies were reviewed and approved by the Animal Care and Use Committee of Puer University (ACUP. 531068520180126, approved on 17 September 2018).

Venom collection and sample preparation

The venom of *S. mojiangica* was collected as per our previous method. Briefly, a 3 V alternating current (AC) was used to stimulate the venom glands in the first pair of centipede limbs (Liu et al., 2012). The venom samples were stored at −20 °C until use. A 300 mg *S. mojiangica* venom sample was solubilized in 3 mL of Tris-HCl buffer. The venom solution was then loaded on a Sephacryl S-100HR (HiprepTM26/60, 71-1247-00-EG, GE Healthcare, USA) gel filtration column with a flow rate of 0.5 mL/h. Thirteen peaks (named P1−13) were obtained from this procedure (Supplementary Figure S1).

The proteins/peptides contained in the venom were pre-denatured with 500 μL of 25 nmol/L NH_4HCO_3 and separated with a 3 kDa cut-off ultrafiltration tube. The low molecular weight (<3 kDa) proteins/peptides were collected and desalinated before peptidomic analysis. Proteins/peptides with molecular weights greater than 3 kDa were applied to SDS-PAGE gels for separation. One half of each sample was mixed with extraction buffer (0.25% acetic acid and protease inhibitor cocktail) and disrupted with a sonicator (Hielscher Ultrasound Technology, Germany). To further separate these samples, 12% gel with protein ladder (Thermo, ref. 26614, USA) SDS-PAGE was used, followed by staining with GelCode Blue Stain (Thermo ref. 24592, USA) and destaining with Milli-Q water (Millipore, USA). We excised six bands from each lane for in-gel trypsin digestion. Samples were extracted with 100% acetonitrile, desalinated, lyophilized, and stored at −80 °C until further electrospray ionization-tandem mass spectrometry (ESI-MS/MS) analysis.

RNA extraction, sequencing, and transcriptome analysis

A total of 260 mg of venom gland was preserved in liquid nitrogen after collection from *S. mojiangica* until use. RNA extraction and cDNA library construction were performed according to our previous work (Zhao et al., 2014a, 2014b). cDNA from the *S. mojiangica* venom gland was sequenced using the Illumina HiSeq™ 2000 (USA), and the short-read assembly program SOAPdenovo-Trans (v1.03) was run with default parameters to complete *de novo* transcriptome assembly. Overlaps with certain lengths and connected paired-end reads were combined in the program to form contigs. The sequence clustering software TGICL was used to splice sequences and remove redundant sequences to produce the complete assembly of contigs of each sample (Pertea et al., 2003), and the longest possible non-redundant unigenes were produced. The TGICL parameters were the same as the parameters used in our previous work (Zhao et al., 2014b).

HPLC fractionation and mass spectrometry

After in-gel digestion, candidate fractionation samples were loaded onto an EASY-nLC HPLC system (Thermo Fisher Scientific, USA) equipped with a binary rapid separation nano-flow pump and ternary loading pump. Mobile phase eluent A (0.1% TFA contained in ddH_2O) and mobile phase eluent B ($ACN/ddH_2O/TFA$ 90/10/0.08% (v/v/v)) were used. Samples were applied to a Thermo Scientific EASY loading column (2 cm×100 μm, 5 μm −C18, USA) by the auto-sampler and analytical column (75 μm×100 mm, 3 μm −C18), respectively, with a flow rate of 250 nL/min. With linear stepwise gradients (0′–5% B, 5′−5% B, 12.5′−20% B, 62.5′−70% B, 63.5′−99% B, 65′−99% B, 66′−5% B and 72′−5% B), we separated the peptides with the column. Starting at 20% eluent B, 1.25 mL/5 min of each fraction was collected and lyophilized.

We selected the data-dependent mode of the Q Exactive instrument (Thermo Finnigan, USA), which then switched between full scan MS and MS/MS acquisition automatically. Based on the predictive automatic gain control (AGC) of the previous full scan, we accumulated 3×10^6 target value ions and acquired 70 000 (m/z 200) resolution of full scan MS spectra (m/z 300−1 800) in the Orbitrap. In addition, 15 s was set as the dynamic exclusion value. We isolated and fragmented the 10 most intense multiply charged ions ($z\geq2$) sequentially by higher-energy collisional dissociation (HCD) with a fixed resolution of 17 500 (m/z 200) and an injection time of 60 ms for the MS2 scanning method. The mass spectrometric conditions were as follows: 2 kV spray voltage, no sheath and auxiliary gas flow, 250 °C heated capillary temperature, 27 eV normalized HCD collision energy, and 0.1% underfill ratio. A total of 1×10^5 counts was set as the ion selection threshold for MS/MS.

Data processing and bioinformatics analysis

Using Proteome Discoverer (version 1.4), RAW data files were produced. Mascot v2.2 was used as the search tool to generate peak lists in our transcriptome database. Trypsin was chosen as an enzyme, and two missed cleavages were allowed. The MS/MS search criteria were as follows: MS polypeptide tolerance 2×10^4 mg/m³ and MS/MS mode 0.1 Da. The aminomethylation of cysteine was statically modified and the oxidation of methionine was dynamically modified. High confidence peptides were used for protein identification, generating a 1% false discovery rate (FDR) threshold. Only unique peptides with high confidence were used for protein identification.

All unigenes in our centipede database were annotated with BLASTX and searched against known databases, as presented in our previous study (Zhao et al., 2014a, 2014b, 2018a). Unigenes were aligned with high-priority databases and annotated with a given description instead of aligning with a low-priority database. Gene Ontology (GO) annotation was carried out using the Blast2GO (Conesa et al., 2005) software suite v2.5.0. In these searches, the BLASTX cut-off was set to $1e^{-6}$. The BLAST tool was used to search the toxin database and annotate the toxin with Tox-Prot in UniProtKB (02 February 2019, 6 822 sequences) and the animal toxin database platform ATDB (He et al., 2008), with the toxins then verified by phylogenetic analyses. The grouped sequences were aligned using MUSCLE v3.8.31 (Edgar, 2010). MrBayes 3.2.7 was used for phylogenetic analyses with maximum likelihood. The values were estimated by ultrafast bootstrap using 10 000 iterations. The resulting trees were analysed with MEGA 7 (Kumar et al., 2016), which was also used to automatically plot expression values and detection in venom.

Comparative expression analysis was performed as follows: comparison of RNA-Seq data of venom glands of various species was performed using Bowtie v0.12.7 (Langmead et al., 2009) and TopHat v2.0.6 (Trapnell et al., 2009) for mapping. Gene expression values were calculated from the expected number of fragments per kilobase of transcript sequence per million base pairs sequenced (FPKM) (Trapnell et al., 2010). The FPKM values for genes from every tissue were determined by rSeq (Jiang & Wong, 2009). The graphs and statistical analyses were performed using GraphPad Prism v5.0 (La Jolla, USA) and R v3.3.2. Here, $P<0.05$ was considered statistically significant.

Insect bioassays and hemolytic assays

Insect bioassays were performed according to the method in Yang et al. (2012). Freeze-dried crude venom powder was dissolved in insect saline (concentrations in deionized water: 140 mmol/L NaCl, 5 mmol/L KCl, 4 mmol/L $NaHCO_3$, 1 mmol/L $MgCl_2$, 0.75 mmol/L $CaCl_2$, 5 mmol/L HEPES) and injected into grasshoppers (*Locusta migratoria manilensis*; mass 700–900 mg) and mealworms (*Tenebrio molitor* larvae; mass 190–210 mg). Ants (*Tetramorium spp.*, adults; mass 35–55 mg) were fed with same venom.

Using human, mouse, and rabbit red blood cells (RBCs), hemolytic activity was assayed as described previously (Liu et al., 2012; Zhao et al., 2018b). Briefly, serial dilutions of the samples were incubated with washed RBCs (3%) at 37 °C for 30 min and then centrifuged. The resulting supernatant was measured at an absorbance of 540 nm. Maximum hemolysis was determined by adding 1% Triton X-100 to the cell samples.

RESULTS

Phylogeny of scolopendrid centipedes and isolation of venom gland

Original Chinese medicinal centipedes include *S. mutilans*, *S. multidens*, *S. mojiangica*, and *S. negrocapitis* (Wang et al., 1997). Here, we studied the novel substitutional pharmaceutical centipede, *S. mojiangica*, with comparative analysis of active molecules. *Scolopendra mojiangica* showed a relatively close relationship to *S. negrocapitis*, *S. mutilans*, and *S. multidens* (Figure 1A), though a smaller body size than *S. mutilans*, *S. dehaani*, and *S. multidens*. Similar to other species, it also uses venom to attack prey and in defense.

The protocol for isolating venom glands from *S. mojiangica* was described in our previous study (Liu et al., 2012). Healthy adult centipedes (n=280) without injury were selected, and the venom glands were dissected from their first pair of limbs. After that, 3 V AC was used to stimulate the venom gland and ensure that more toxins were included, so that proteome coverage could be improved. The isolated venom glands were then further processed (Figure 1B). A portion of each sample was used to obtain the proteome by SDS-PAGE analysis. Protein bands from the venom gland were excised for in-gel digestion and subjected to ESI-MS/MS analysis. The remaining portion of each sample was used to extract RNA, followed by RNA-Seq analysis of the transcriptome.

Proteomic analysis of venom components

A total of 246 proteins were identified in *S. mojiangica* at 95% coverage by ESI-MS/MS analysis (Supplementary Table S1; Figure 2A). In the proteome, 73.6% of proteins (n=181) were cellular components and 19.1% of proteins (n=47) were unknown functional proteins, which were putative venom toxins. Only 18 proteins were identified as toxin-like proteins, including neurotoxins, K^+ channel inhibitors, and blarina toxins (Figure 2B; Table 1). Although we obtained more proteins in *S. mojiangica* than in *S. mutilans* and *S. viridis* with proteomic analysis, the detected toxin-like proteins in *S. mojiangica* represented a lower percentage of total proteins than those identified in *S. mutilans* in our previous study (Figure 2C). In the venom proteome, most of the identified proteins showed a molecular weight of less than 50 kDa, similar to the proteome of *S. mutilans* (Figure 2D). Thus, the centipedes contained notably small functional molecules for potential pharmaceutical use, as expected. Based on peptide detection, 23.2% of proteins consisted of six or more unique peptides (Supplementary Figure S2). In addition, the more enriched the peptides assembled into proteins, the more comprehensive was the proteome obtained.

Transcriptomic analysis of venom components

We acquired 43 381 437 clean reads assembled into 132 597

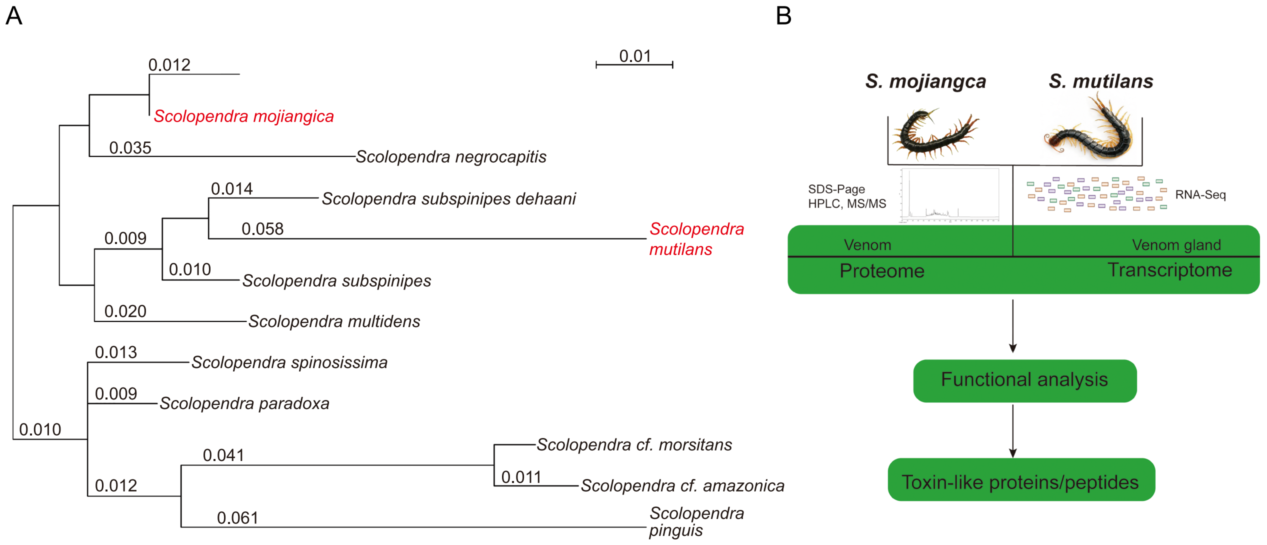

Figure 1 Proteomic and transcriptomic analyses of new pharmaceutical centipede

A: Molecular phylogenetic analysis of centipede, *S. mojiangica*, by maximum likelihood based on *COI* genes. Red labels correspond to two centipedes in our study, and posterior probabilities are assigned to nodes. B: Workflow for proteomic and transcriptomic analyses of centipede, *S. mojiangica*. Venom was processed and subjected to SDS-PAGE followed by in-gel digestion. Samples were then analysed in a separate ESI-MS/MS assay. For transcriptomic analysis, venom glands (not venom) were used for high-throughput sequencing. Functional analysis was combined with proteomic and transcriptomic data.

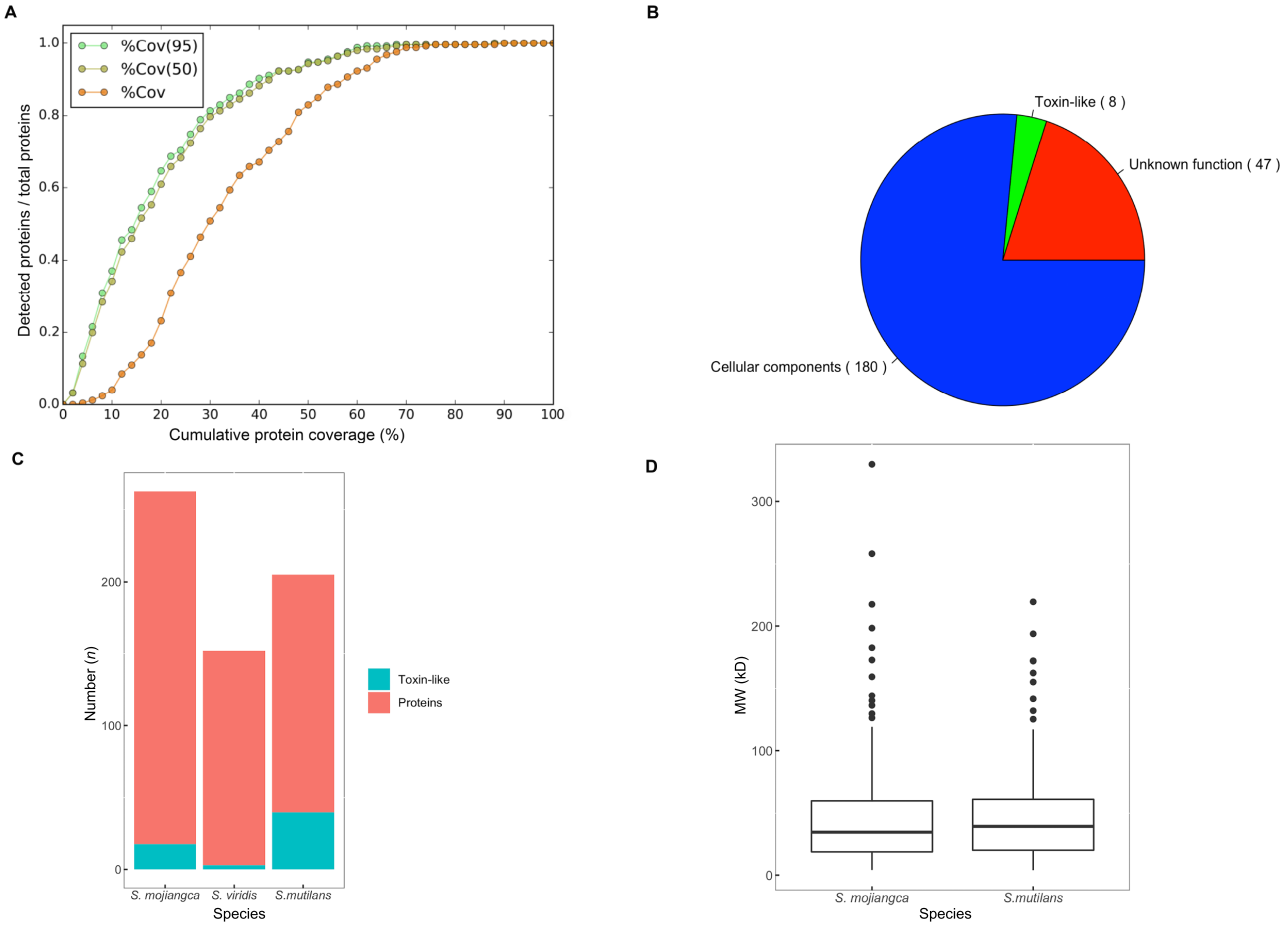

Figure 2 Profiles of *S. mojiangica* proteome

A: Cumulative distribution of protein peptide coverage. Horizontal axis shows protein peptide coverage, and vertical axis shows protein ratio. B: Pie chart of identified proteins from our *S. mojiangica* proteome. C: Comparison of toxin-like proteins determined by proteomic analysis among three centipedes: i.e., *S. mojiangica*, *S. viridis* (Gonzalez-Morales et al., 2014), and *S. mutilans* (Zhao et al., 2018a). D: Distribution of molecular weights of proteome proteins.

contigs from the venom gland using the Trinity program. As a result, the transcriptome data consisted of 107 642 putative gene objects (all unigenes) ranging from 101 bp to 9 184 bp, with an average length of 423 bp. The number of unigenes larger than 500 bp was 24 219. The largest unigenes were 9 184 bp in size, and the N50 of the unigenes was 214 bp (Supplementary Figure S3 and Table S2).

For comparative analysis, the venom gland transcriptome from *S. mojiangica* showed many transcripts (*n*=46 571) with high similarity to those of *S. mutilans*. Notably, however, most transcripts showed low similarity between the two centipede species (Figure 3A). In the transcriptomic expression analysis, the read count of each transcript in *S. mojiangica* and *S. mutilans* showed biases for gene expression, with higher expressed transcripts in *S. mojiangica* (Figure 3B). Functional annotation analyses of these transcripts were combined with Blast searching and phylogenetic analyses to obtain toxin-like unigenes. In total, 410 toxin-like transcripts were identified in the transcriptome of *S. mojiangica*, more than that identified in *S. mutilans* (342 transcripts). Furthermore, these transcripts were divided into 34 categories, mainly consisting of alpha-latrocrustotoxin, delta-latroinsectotoxin, ion channel inhibitors, and alpha-latrotoxin (Figure 3C).

Comparative determination of centipede toxins

As expected, we identified 34 kinds of toxin-like unigenes (*n*=342) from the transcriptome of *S. mutilans* using the same annotation method as that of *S. mojiangica* (Figure 4A). In total, 11 of these toxin-like unigenes encoded the most transcripts in the two centipedes. With gene expression analyses, most toxin-like unigenes showed no differential expression between *S. mojiangica* and *S. mutilans*, except for four toxin-like unigenes (i.e., alpha-latrotoxin, hopsarin-D, metalloproteinase, and trocarin) (Figure 4B).

Finally, we determined the toxicity and performed crude isolation of the centipede venom. The crude centipede venom

Table 1 Toxin-like proteins/peptides identified from venom proteome of *S. mojiangica* centipede

Sequence ID	GenBank accession No.	Sequence description	Category	Peptides	E-Value	MW (kD)	Calc. pI	FPKM
ScoMo_singlet48841	AT0003236	Blarina toxin precursor (EC 3.4.21.-)	Blarina toxin	9	1.00E-37	21.61	4.15	92.54
ScoMo_singlet50899	AT0003766	Mucrofibrase-5 precursor (EC 3.4.21.-)	Mucrofibrase-5	11	4.00E-16	14.40	9.93	3 454.74
ScoMo_singlet71394	AT0002263	Pseudechetoxin-like protein precursor	Pseudechetoxin	276	9.00E-42	28.74	9.86	7 195.57
ScoMo_contig2076	gi|429840589	K+ channel inhibitor	Channel inhibitor	617	4.00E-164	62.76	9.15	1.37
ScoMo_singlet78309	AT0000117	Latisemin precursor	Latisemin	412	2.00E-22	20.89	7.96	0.00
ScoMo_contig4762	AT0003236	Blarina toxin precursor (EC 3.4.21.-)	Blarina toxin	108	1.00E-44	28.58	6.5	15 173.32
ScoMo_singlet45908	AT0003741	Thrombin-like enzyme contortrixobin (EC 3.4.21.-)	Serine proteinase	109	1.00E-41	44.94	5.08	1 685.57
ScoMo_singlet67462	AT0000120	Pseudecin precursor	Pseudechetoxin	66	5.00E-32	23.71	8.91	14 111.58
ScoMo_singlet72573	AT0000552	Hopsarin-D (EC 3.4.21.6)	Hopsarin-D	93	1.00E-121	85.15	6.53	132.70
ScoMo_singlet76606	AT0000554	Trocarin precursor (EC 3.4.21.6)	Trocarin	38	3.00E-138	84.92	6.17	60.34
ScoMo_singlet25641	AT0000552	Hopsarin-D (EC 3.4.21.6)	Hopsarin-D	46	5.00E-20	27.21	4.6	184.53
ScoMo_singlet69905	AT0000554	Trocarin precursor (EC 3.4.21.6)	Trocarin	14	4.00E-107	40.69	5.28	1 245.366
ScoMo_singlet57737	AT0003404	Zinc metalloproteinase fibrolase (EC 3.4.24.72)	Metalloproteinase	20	4.00E-16	35.21	8.13	48.71
ScoMo_singlet8256	AT0000762	Alpha-latrocrustotoxin	Alpha-latrocrustotoxin	10	0	50.48	6.79	136.27
ScoMo_singlet68890	AT0000552	Hopsarin-D (EC 3.4.21.6)	Hopsarin-D	13	5.00E-75	42.03	7.88	161.84
ScoMo_singlet7846	gi|392295725	Omega-slptx-ssm2a neurotoxin precursor	Neurotoxin	11	8.00E-36	8.56	4.93	16 647.01
ScoMo_singlet55496	gi|501293796	Cathepsin L	Cathepsin L	180	1.00E-155	37.30	6.35	2.83
ScoMo_singlet39956	AT0000554	Trocarin precursor (EC 3.4.21.6)	Trocarin	12	4E-09	4.64	3.79	5.55

MW: Molecular Weight; Calc. pI: The calculated isoelectric point (pI); FPKM: Fragments Per Kilobase of exon model per Million mapped fragments.

exhibited strong insecticidal action (Figure 5A), and the crude venom had a similar potency as the venom of *S. mutilans*. The crude venom and its fractions eluted from the S-100HR column (Supplementary Figure S1; Figure 5B) showed hemolytic activity. The elution of peak 1 (P1) showed high hemolytic activity on human RBCs when 1 mg/mL protein/peptide was incubated for 4 h. In contrast, peaks 3, 5, and 6 (P3, P5, and P6) had lower hemolytic activity than that of P1 and crude venom.

DISCUSSION

Due to long-term evolutionary fine-tuning, venom toxins exhibit high specificity and potency for molecular targets that are not often found in natural or synthetic small molecules, and thus animal toxins are valuable pharmacological tools (King, 2011, 2013). There are many cases in which venom toxin has been used as a pharmacological molecule, e.g., snake venom, dried toad skin secretions (Chan Su), tarantula venom, and cobra venom used as traditional Ayurvedic, Chinese, Mexican, and Central and South American medicines, respectively (Harvey, 2014; King, 2011). These traditional medicines have been used to treat arthritis, gastrointestinal ailments, asthma, polio, multiple sclerosis, rheumatism, severe pain, and trigeminal neuralgia, or as a diuretic anesthetic and anti-cancer agent. Centipede venom has different biomedical properties and represents a vast reservoir of toxins, similar to venom from other animals. Due to its origins in one of the oldest venomous arthropods, centipede venom displays excellent activities and good prospects for drug development (Undheim et al., 2016; Zhang, 2015). Importantly, the centipede is a traditional Chinese medicine with an application history of more than 2 000 years (Chen & Yu, 1999; Zhao et al., 2018a). In China, pharmaceutically applied centipedes include *S. mutilans*, *S. multidens*, *S. dehaani*, and *S. negrocapitis*, with *S. mojiangica* (Wang et al., 1997) very occasionally used as a substitute. Our results showed that the venom toxicity of this centipede is strong in comparison to that of *S. mutilans*, a commonly used centipede in medicine.

In our previous study, the centipede showed diverse protein or peptide components, with the most abundant toxins in the

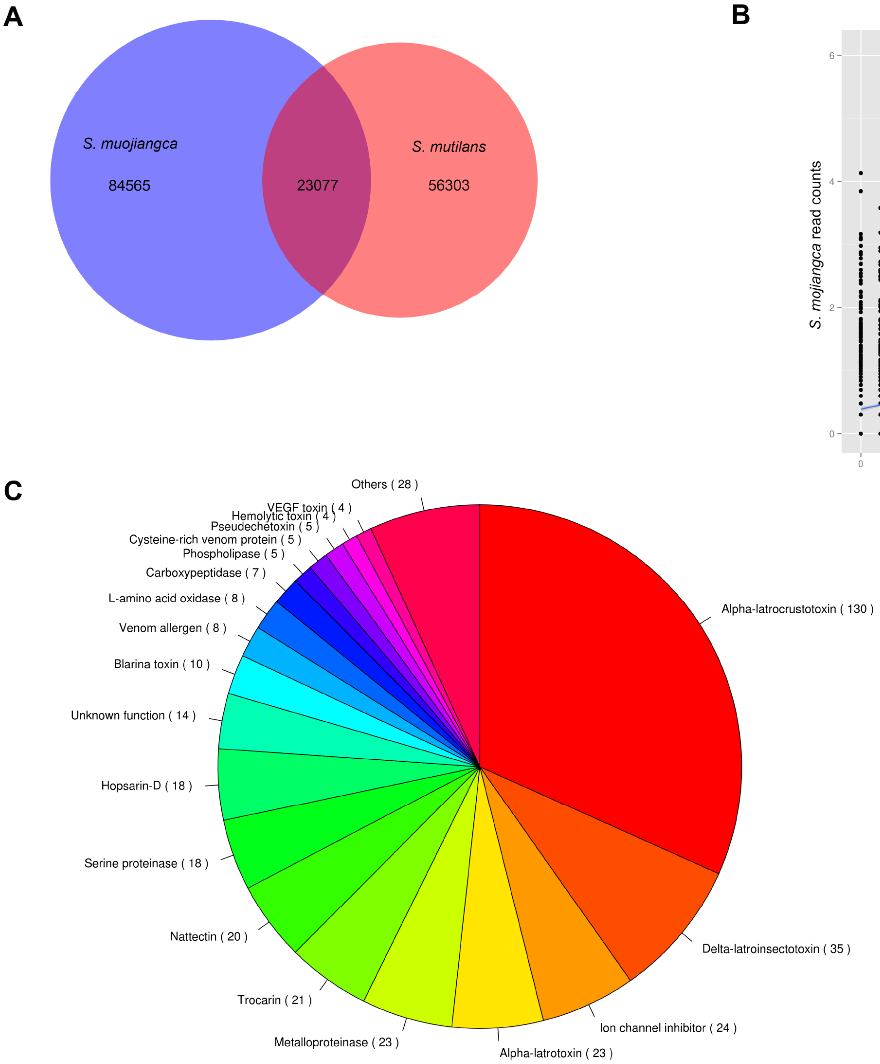

Figure 3 Identification of toxins from transcriptome of venom gland in centipedes

A: Comparison of transcripts identified in venom glands from two centipedes, *S. mojiangica* and *S. mutilans*, with transcriptomic analysis. B: Expression of all transcripts in venom glands of *S. mojiangica* and *S. mutilans*. Read counts reflect quantification accuracy of differential expression by mapping reads to transcripts and read counting. C: Pie chart of venom toxin-like proteins/peptides identified in transcriptomes of *S. mojiangica* and *S. mutilans*. In total, 410 and 342 venom toxin-like proteins/peptides were identified from *S. mojiangica* and *S. mutilans*, respectively, using transcriptomic analysis.

venom and torso tissues found to be more highly expressed than other active molecules using our method (Liu et al., 2012; Zhao et al., 2018a). Here, based on proteomic detection, we showed that the toxin-like proteins in *S. mojiangica* accounted for a lower percentage of total proteins than that in *S. mutilans*. However, there was a similar constitution and quantity of toxin transcripts in these two centipedes. We used high-throughput ESI-MS/MS and RNA-Seq technology to investigate the diversity of novel venom proteins, especially low-abundance peptides/proteins not detected using conventional methods (Savitski et al., 2005). Most of the detected proteins were identified as potentially active molecules with low molecular weights and unknown functions. In addition, each detected protein contained at least six peptides in the proteome dataset. The proteomic results for *S. mojiangica* were very similar to the protein detection results for *S. mutilans*. More than 400 toxin-like proteins/peptides were identified by transcriptome analysis in the centipede, but not detected in the proteome. Thus, most putative toxins in centipede venom may have low levels of expression in *S. mojiangica* and *S. mutilans*. In conclusion, centipede venom contains a surprising variety of toxin-like proteins/peptides.

Regarding toxin distribution, based on transcriptomic analysis, we identified more toxin transcripts in *S. mojiangica*

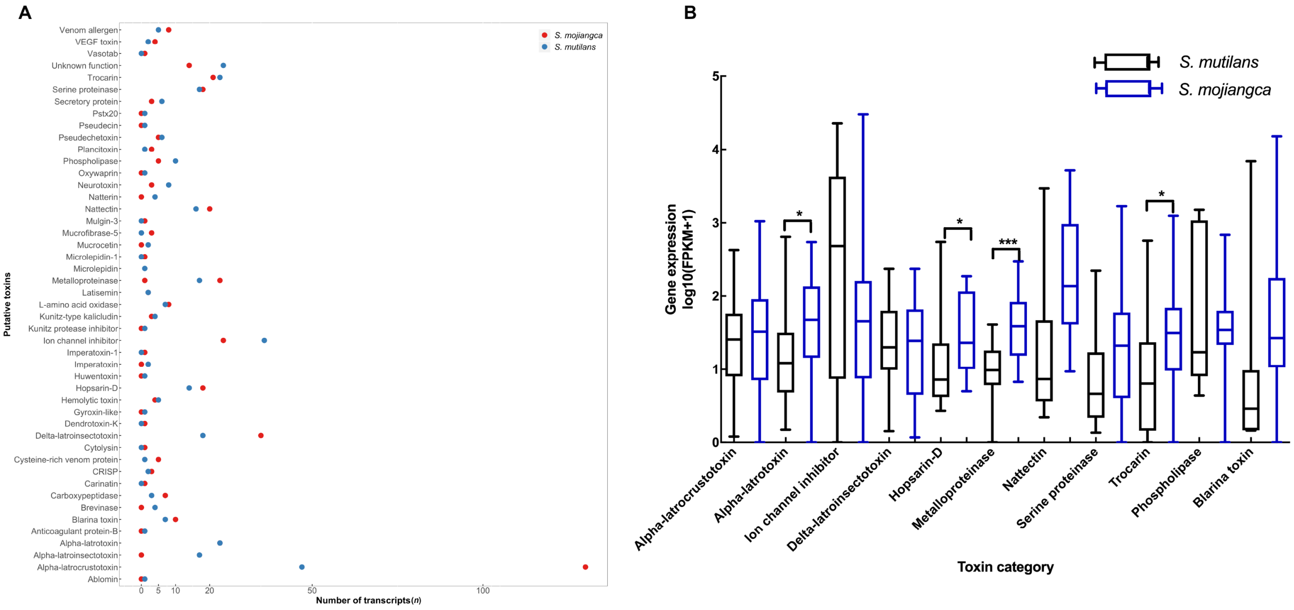

Figure 4 Comparison of toxin-like molecules distributed in centipedes *S. mojiangica* and *S. mutilans*

A: Distribution of identified toxin-like molecules in *S. mojiangica* and *S. mutilans*. Toxin-like transcripts (n=410) in *S. mojiangica* were divided into 34 categories. Blue dots represent transcripts of *S. mutilans* and red dots represent transcripts of *S. mojiangica*. B: Main components of toxin-like molecules expressed in *S. mojiangica* and *S. mutilans*. Transcriptomic analysis showed only four types of toxin-like molecules with differential gene expression between *S. mojiangica* and *S. mutilans*.

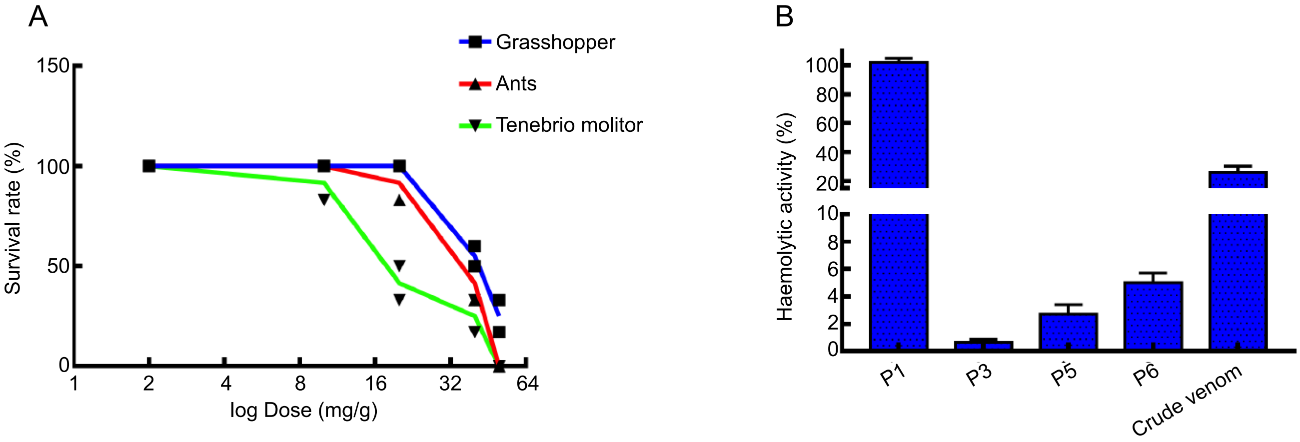

Figure 5 Insecticidal activity of crude centipede venom

A: Insecticidal activity of crude centipede venom. B: Hemolytic activity of elution of crude centipede venom. Peaks 1, 3, 5, and 6 at concentrations of 1 mg/mL were incubated with human red blood cells for 30 min at 37 °C, and absorbance of supernatant was measured at 540 nm.

than in *S. mutilans*. Most toxins did not show significantly differential expression between *S. mojiangica* and *S. mutilans*, including that of ion channel inhibitors and serine proteinases. The centipede *S. mojiangica* demonstrated higher gene expression of metalloproteinase, trocarin, hopsarin-D, and alpha-latrotoxin compared to *S. mutilans*. Therefore, *S. mojiangica* could be substituted for *S. mutilans* in medical use. These results indicate that *S. mojiangica* venom could be a rich source of pharmacologically and medically useful compounds.

Usually, we can obtain approximately 0.2–0.5 mg of crude venom from a single adult *S. mutilans* centipede over a period of two weeks. However, one adult *S. mojiangica* yielded less than 0.1 mg of crude venom in the same period. Therefore, it was difficult to study the venom components, including their pharmaceutical activity or medicinal application. In addition to the current annotation methods of centipede toxins, our results revealed that a wide variety of toxin-like active molecules were expressed in the venom gland by combining Blast alignment with the existing toxin databases and phylogenetic reconstruction of toxin relationships. Theoretically, this method may produce false positives, especially for proteins with low abundance and expression when using high-throughput proteomic and transcriptomic analyses with ESI-MS/MS and RNA-Seq technology. However, we used previously established approaches to maximize the search for functional proteins. Our results provide good evidence that the use of this substitute medicinal centipede is an appropriate medical option. Importantly, our data provide important clues to improve the use of the centipede as a traditional Chinese medicine.

CONCLUSIONS

Here, we used omics techniques to determine the profiles of venom components and toxin-like molecules in a new pharmaceutical centipede, *S. mojiangica*. We performed in-depth proteomic analysis of venom and deduced full-length protein sequences by combining proteome and transcriptome databases. We obtained more than 400 toxin-like molecules with potent activity. With gene expression and inter-species comparative analysis, we identified a broad and diverse composition of toxin-like molecules, which may play key roles in the functions of centipede venom. Our results indicate that this centipede is valuable for medicinal use and drug development, like other centipede species. Furthermore, our methods could improve the application of the centipede as a traditional Chinese medicine.

SUPPLEMENTARY DATA

Supplementary data to this article can be found online.

COMPETING INTERESTS

The authors declare that they have no competing interests.

AUTHORS' CONTRIBUTIONS

F.Z., W.H.L., and Y.Z. conceived the study. F.Z. wrote the paper and performed data and bioinformatics analyses. Z.C.L., J.Y.L., X.Q.L., T.L., J.R.Z., F.Z., G.L., and P.Y.C. performed all experiments. All authors read and approved the final version of the manuscript.

ACKNOWLEDGMENTS

We thank the members of our research groups for providing technical assistance and participating in discussions.

REFERENCES

Chen K, Yu B. 1999. Certain progress of clinical research on Chinese integrative medicine. *Chinese Medical Journal (Engl)*, **112**(10): 934−937.

Chen M, Li J, Zhang F, Liu Z. 2014. Isolation and characterization of SsmTx-I, a Specific Kv2.1 blocker from the venom of the centipede *Scolopendra Subspinipes Mutilans* L. Koch. *Journal of Peptide Science*, **20**(3): 159−164.

Conesa A, Gotz S, Garcia-Gomez JM, Terol J, Talon M, Robles M. 2005. Blast2GO: a universal tool for annotation, visualization and analysis in functional genomics research. *Bioinformatics*, **21**(18): 3674−3676.

Edgar RC. 2010. Quality measures for protein alignment benchmarks. *Nucleic Acids Research*, **38**(7): 2145−2153.

Edgecombe GD, Giribet G. 2007. Evolutionary biology of centipedes (Myriapoda: Chilopoda). *Annual Review of Entomology*, **52**: 151−170.

Gonzalez-Morales L, Pedraza-Escalona M, Diego-Garcia E, Restano-Cassulini R, Batista CV, Gutierrez Mdel C, Possani LD. 2014. Proteomic characterization of the venom and transcriptomic analysis of the venomous gland from the Mexican centipede *Scolopendra viridis*. *Journal of Proteomics*, **111**: 224−237.

Hakim MA, Yang S, Lai R. 2015. Centipede venoms and their components: resources for potential therapeutic applications. *Toxins (Basel)*, **7**(11): 4832−4851.

Harvey AL. 2014. Toxins and drug discovery. *Toxicon*, **92**: 193−200.

He QY, He QZ, Deng XC, Yao L, Meng E, Liu ZH, Liang SP. 2008. ATDB: a uni-database platform for animal toxins. *Nucleic Acids Research*, **36**.

Hou H, Yan W, Du K, Ye Y, Cao Q, Ren W. 2013. Construction and expression of an antimicrobial peptide scolopin 1 from the centipede venoms of *Scolopendra subspinipes mutilans* in *Escherichia coli* using SUMO fusion partner. *Protein Expression and Purification*, **92**(2): 230−234.

Jiang H, Wong WH. 2009. Statistical inferences for isoform expression in RNA-Seq. *Bioinformatics*, **25**(8): 1026−1032.

Kalia J, Milescu M, Salvatierra J, Wagner J, Klint JK, King GF, Olivera BM, Bosmans F. 2015. From foe to friend: using animal toxins to investigate ion channel function. *Journal of Molecular Biology*, **427**(1): 158−175.

King G. 2013. Venoms to drugs: translating venom peptides into therapeutics. *Australian Biochemist*, **44**(3): 13−16.

King GF. 2011. Venoms as a platform for human drugs: translating toxins into therapeutics. *Expert Opinion on Biological Therapy*, **11**(11): 1469−1484.

Kumar S, Stecher G, Tamura K. 2016. MEGA7: molecular evolutionary genetics analysis version 7.0 for bigger datasets. *Molecular Biology and Evolution*, **33**(7): 1870−1874.

Langmead B, Trapnell C, Pop M, Salzberg SL. 2009. Ultrafast and memory-efficient alignment of short DNA sequences to the human genome. *Genome Biology*, **10**(3): R25.

Liu ZC, Zhang R, Zhao F, Chen ZM, Liu HW, Wang YJ, Jiang P, Zhang Y, Wu Y, Ding JP, Lee WH, Zhang Y. 2012. Venomic and transcriptomic analysis of centipede *Scolopendra subspinipes dehaani*. *Journal of Proteome Research*, **11**(12): 6197−6212.

Peng K, Kong Y, Zhai L, Wu X, Jia P, Liu J, Yu H. 2010. Two novel antimicrobial peptides from centipede venoms. *Toxicon*, **55**(2-3): 274−279.

Pertea G, Huang X, Liang F, Antonescu V, Sultana R, Karamycheva S, Lee Y, White J, Cheung F, Parvizi B, Tsai J, Quackenbush J. 2003. TIGR Gene Indices clustering tools (TGICL): a software system for fast clustering of large EST datasets. *Bioinformatics*, **19**(5): 651−652.

Rong M, Yang S, Wen B, Mo G, Kang D, Liu J, Lin Z, Jiang W, Li B, Du C, Yang S, Jiang H, Feng Q, Xu X, Wang J, Lai R. 2015. Peptidomics combined with cDNA library unravel the diversity of centipede venom. *Journal of Proteomics*, **114**: 28−37.

Savitski MM, Nielsen ML, Kjeldsen F, Zubarev RA. 2005. Proteomics-grade de novo sequencing approach. *Journal of Proteome Research*, **4**(6):

2348−2354.

Smith JJ, Herzig V, King GF, Alewood PF. 2013. The insecticidal potential of venom peptides. *Cellular and Molecular Life Sciences: CMLS*, **70**(19): 3665−3693.

Trapnell C, Pachter L, Salzberg SL. 2009. TopHat: discovering splice junctions with RNA-Seq. *Bioinformatics*, **25**(9): 1105−1111.

Trapnell C, Williams BA, Pertea G, Mortazavi A, Kwan G, Van Baren MJ, Salzberg SL, Wold BJ, Pachter L. 2010. Transcript assembly and quantification by RNA-Seq reveals unannotated transcripts and isoform switching during cell differentiation. *Nature Biotechnol*, **28**(5): 511−515.

Undheim EA, Fry BG, King GF. 2015. Centipede venom: recent discoveries and current state of knowledge. *Toxins (Basel)*, **7**(3): 679−704.

Undheim EA, Jenner RA, King GF. 2016. Centipede venoms as a source of drug leads. *Expert Opinion on Drug Discovery*, **11**(12): 1139−1149.

Undheim EA, King GF. 2011. On the venom system of centipedes (Chilopoda), a neglected group of venomous animals. *Toxicon*, **57**(4): 512−524.

Wang K, Fang H, Ye M, Chen H, Zhu Y, Fang H. 1997. Investigation on the resources of medicinal centipedes and identification on their commodities. *Journal of Chinese Medicinal Materials*, **20**(9): 450−452.

Yang S, Liu Z, Xiao Y, Li Y, Rong M, Liang S, Zhang Z, Yu H, King GF, Lai R. 2012. Chemical punch packed in venoms makes centipedes excellent predators. *Molecular and Cellular Proteomics*, **11**(9): 640−650.

Yang S, Xiao Y, Kang D, Liu J, Li Y, Undheim EA, Klint JK, Rong M, Lai R, King GF. 2013. Discovery of a selective NaV1.7 inhibitor from centipede venom with analgesic efficacy exceeding morphine in rodent pain models. *Proceedings of the Natlional Academy of Sciences of the Untied States of America*, **110**(43): 17534−17539.

Yang S, Yang F, Wei N, Hong J, Li B, Luo L, Rong M, Yarov-Yarovoy V, Zheng J, Wang K, Lai R. 2015. A pain-inducing centipede toxin targets the heat activation machinery of nociceptor TRPV1. *Nature Communications*, **6**: 8297.

Zhang Y. 2015. Why do we study animal toxins?. *Zoological Research*, **36**(4): 183−222.

Zhao F, Guo X, Wang Y, Liu J, Lee WH, Zhang Y. 2014a. Drug target mining and analysis of the Chinese tree shrew for pharmacological testing. *PLoS One*, **9**(8): e104191.

Zhao F, Lan X, Li T, Xiang Y, Zhao F, Zhang Y, Lee WH. 2018a. Proteotranscriptomic analysis and discovery of the profile and diversity of toxin-like proteins in centipede. *Molecular and Cellular Proteomics*, **17**(4): 709−720.

Zhao F, Lan XQ, Du Y, Chen PY, Zhao J, Zhao F, Lee WH, Zhang Y. 2018b. King cobra peptide OH-CATH30 as a potential candidate drug through clinic drug-resistant isolates. *Zoological Research*, **39**(2): 87−96.

Zhao F, Yan C, Wang X, Yang Y, Wang G, Lee W, Xiang Y, Zhang Y. 2014b. Comprehensive transcriptome profiling and functional analysis of the frog (*Bombina maxima*) immune system. *DNA Research*, **21**(1): 1−13.

ZOOLOGICAL RESEARCH

Co-localization of two-color rAAV2-retro confirms the dispersion characteristics of efferent projections of mitral cells in mouse accessory olfactory bulb

Ning Zheng[1,2,#], Zhi-Zhong Wang[3,#], Song-Wei Wang[3,#], Fang-Jia Yang[4], Xu-Tao Zhu[1], Chen Lu[4], Anne Manyande[5], Xiao-Ping Rao[1,*], Fu-Qiang Xu[1,2,6,*]

[1] *Center of Brain Science*, *State Key Laboratory of Magnetic Resonance and Atomic and Molecular Physics*, *National Center for Magnetic Resonance in Wuhan*, *Key Laboratory of Magnetic Resonance in Biological Systems*, *Wuhan Institute of Physics and Mathematics*, *Innovation Academy for Precision Measurement Science and Technology*, *Chinese Academy of Sciences*, *Wuhan*, *Hubei* 430071, *China*

[2] *University of the Chinese Academy of Sciences*, *Beijing* 100049, *China*

[3] *Department of Automation*, *School of Electrical Engineering*, *Zhengzhou University*, *Zhengzhou*, *Henan* 450001, *China*

[4] *School of Life Science*, *Wuhan University*, *Wuhan*, *Hubei* 430072, *China*

[5] *School of Human and Social Sciences*, *University of West London*, *Middlesex TW89GA*, *UK*

[6] *Divisions of Biomedical Photonics*, *Wuhan National Laboratory for Optoelectronics*, *Wuhan*, *Hubei* 430074, *China*

ABSTRACT

The accessory olfactory bulb (AOB), located at the posterior dorsal aspect of the main olfactory bulb (MOB), is the first brain relay of the accessory olfactory system (AOS), which can parallelly detect and process volatile and nonvolatile social chemosignals and mediate different sexual and social behaviors with the main olfactory system (MOS). However, due to its anatomical location and absence of specific markers, there is a lack of research on the internal and external neural circuits of the AOB. This issue was addressed by single-color labeling and fluorescent double labeling using retrograde rAAVs injected into the bed nucleus of the stria terminalis (BST), anterior cortical amygdalar area (ACo), medial amygdaloid nucleus (MeA), and posteromedial cortical amygdaloid area (PMCo) in mice. We demonstrated the effectiveness of this AOB projection neuron labeling method and showed that the mitral cells of the AOB exhibited efferent projection dispersion characteristics similar to those of the MOB. Moreover, there were significant differences in the number of neurons projected to different brain regions, which indicated that each mitral cell in the AOB could project to a different number of neurons in different cortices. These results provide a circuitry basis to help understand the mechanism by which pheromone information is encoded and decoded in the AOS.

Keywords: Accessory olfactory bulb; Efferent projections; Retrograde rAAVs; Projection neuron labeling; Dispersion characteristics; Circuitry basis

Received: 18 September 2019; Accepted: 25 December 2019; Online: 31 December 2019

Foundation items: This work was supported by the National Natural Science Foundation of China (31400946, 31771156, 91632303/H09, 91732304 and 31830035) and Strategic Priority Research Program of the Chinese Academy of Sciences (XDB32030200)

#Authors contributed equally to this work

*Corresponding authors, E-mail: raoxiaoping0902@wipm.ac.cn; fuqiang.xu@wipm.ac.cn

DOI: 10.24272/j.issn.2095-8137.2020.020

INTRODUCTION

Most animals rely heavily on their chemosensory perception to interact with their surroundings, with a variety of odor molecules carrying a wealth of information. Chemical senses, based on the detection of molecules, trigger physiological, reproductive, and social responses, and play essential roles in foraging and avoidance, escaping from predators, and locating suitable mating partners (Su et al., 2009). Terrestrial vertebrates have two anatomically distinct and functionally overlapping (in part) olfactory systems: i.e., the main olfactory system (MOS) and accessory olfactory system (AOS), which can, in parallel, detect and process volatile and nonvolatile social chemosignals and mediate different sexual and social behaviors through different receptors and signal transduction pathways (Spehr et al., 2006). The AOS is a relatively "simple" combination of neural circuits with complex information processing mechanisms and is directly related to neuroendocrine changes, emotional changes, and social/sexual behaviors, making it an ideal model for studying chemical sensory coding (Mohrhardt et al., 2018).

The vomeronasal organ (VNO), which comprises the peripheral sensory structure of the AOS, plays a major role in detecting both hetero- and con-specific social cues that convey information about identity, gender, social rank, and sexual state (Ackels et al., 2016). The VNO is a bilaterally symmetrical, cylindrical organ encased in a bony capsule on the anterior nasal septum. It is blind posteriorly with a crescent-shaped sensory epithelium located at the medial wall of the organ and a large blood vessel running laterally to the lumen. Furthermore, depending on the species, it opens anteriorly into either the nasal or oral cavity to allow entry of chemosignals, especially nonvolatile chemical cues, after direct physical contact of the snout with odor sources (Doving & Trotier, 1998; Dulac & Torello, 2003; Halpern & Martinez-Marcos, 2003). Within the VNO, sensory neurons can be categorized into two segregated subpopulations organized in separate layers of the vomeronasal epithelium. Cells expressing type-I vomeronasal receptors (V1Rs) or formyl peptide receptors (FPRs) and Gi proteins in the apical layer project to the anterior part of the accessory bulb (aAOB). However, cells in the basal layer expressing type-II vomeronasal receptors (V2Rs) and Go proteins project to the posterior part of the AOB (pAOB) (Dulac & Torello, 2003; Riviere et al., 2009). The V1R/FPR-expressing cells are responsive to small hydrophobic molecules, such as volatile urinary components or pathogenic molecules emitted by sick animals (Leinders-Zufall et al., 2000; Riviere et al., 2009). The sensory neurons expressing V2Rs, which contain a large N-terminal domain and form ligand binding sites, respond to proteinaceous components (Breer et al., 2006; Krieger et al., 1999; Leinders-Zufall et al., 2004).

The AOB, located at the posterior dorsal aspect of the main olfactory bulb (MOB), is the first brain relay of the AOS and has a compact laminar structure approximately 1.5 mm (anterior-posterior) by 0.6 mm (medial-lateral) in surface area (Holy, 2018). The AOB shares many similarities with the larger MOB in broad classes of neuronal populations, layered organization, and connectivity. Yet, the AOB and MOB also show notable differences with respect to cytoarchitecture, glomerular formation, and physiological and morphological properties of projection neurons (Dulac & Wagner, 2006; Larriva-Sahd, 2008; Mohrhardt et al., 2018; Moriya-Ito et al., 2013; Urban & Castro, 2005; Yokosuka, 2012; Yoles-Frenkel et al., 2018; Yonekura & Yokoi, 2008). Each mitral cell contains multiple thick glomerular (or primary) dendrites toward multiple glomeruli (ranging between 2 and 10) (Takami & Graziadei, 1991; Urban & Castro, 2005; Yonekura & Yokoi, 2008). This unique organization is markedly distinct from that in the MOB, where each mitral cell contacts a single glomerulus (Su et al., 2009). Moreover, the thin secondary (accessory) dendrites, emanating from the cell body, are shorter and fewer in number than in the MOB mitral cells (Mohrhardt et al., 2018).

However, due to its anatomical location and absence of specific markers, there is a lack of research on the internal and external neural circuits of the AOB. For example, projection of the MOB is characterized by one-to-many, that is, the axonal branches of individual mitral cells can reach all olfactory cortices (Nagayama et al., 2010). This indicates that the encoded and transmitted odor information may be similar, but different olfactory cortices may have different odor decoding mechanisms, which eventually lead to the perception of odorants. The question is, does the AOB have similar projection characteristics as the MOB? Although the fine structure and configuration of these projections have been investigated in the MOB (Ghosh et al., 2011; Miyamichi et al., 2011; Nagayama et al., 2010; Sosulski et al., 2011), the projection characteristics of mitral cells in the AOB remain unknown.

In the present study, we successfully infected the mitral cell layer of the AOB (MiA) with rAAV2-retro absorbed by their terminal axons in different accessory olfactory cortices, including the bed nucleus of the stria terminalis (BST), anterior cortical amygdalar area (ACo), medial amygdaloid nucleus (MeA), and posteromedial cortical amygdaloid area (PMCo), thus indicating the effectiveness of this method for AOB projection neuron labeling. We then used two-color rAAV2-retro to achieve the co-labeling of mitral cells in the AOB from two different cortices. Results showed that the projection patterns of mitral cells in the AOB were like those of the MOB. Hence, the decoding mechanism of pheromones in the AOS may be similar to that in the MOS. Moreover, there may be significant differences in the number of neurons projected to the same area in different brain regions, indicating that each mitral cell in the AOB could project to a different number of neurons in different cortices.

MATERIALS AND METHODS

Animals

All surgical and experimental procedures were conducted in accordance with the guidelines of the Animal Care and Use

Committees at the Wuhan Institute of Physics and Mathematics, Chinese Academy of Sciences (reference No.: WIPM-(2014)39). Adult male C57BL/6 mice (15–40 weeks old, purchased from Hunan SJA Laboratory Animal Company, China) were housed in a specific pathogen-free facility under a controlled room temperature (22±2 °C), humidity (60%–80%), and 12 h:12 h light/dark cycle. Food and water were available *ad libitum*.

Virus injection

Recombinant rAAV2-retro-Ef1α-EYFP-WPRE-pA and rAAV2-retro-Ef1α-mCherry-WPRE-pA were prepared by BrainVTA (China). Animals were anesthetized with chloral hydrate (400 mg/kg), and then placed in a stereotaxic apparatus (RWD, China). During surgery and virus injection, anesthesia was maintained with isoflurane (1%). The skull above the target areas was thinned with a dental drill and removed carefully. Injections were administered with a syringe pump (Quintessential Stereotaxic Injector, USA) connected to a glass micropipette with a tip diameter of 10–15 mm. rAAV2-retro (80 nL, 1×10^{13} vg/mL) was injected (8 nL/min) respectively into the accessory olfactory cortex of adult C57 mice with the following coordinates: BST (AP, 0 mm; ML, –0.6 mm; DV, –4.5 mm), ACo (AP, –0.58 mm; ML, –2.35 mm; DV, –5.7 mm), MeA (AP, –1.1 mm; ML, –2.0 mm; DV, –5.0 mm), PMCo (AP, –3.08 mm; ML, –3.2 mm; DV, –5.25 mm). Four weeks after virus infection, the animals were transcardially perfused with physiological saline followed by 4% paraformaldehyde (PFA).

Tissue section preparation, imaging, and data analysis

Brains were removed, post-fixed in PFA overnight, and dehydrated in 30% (w/v) sucrose for 3 d. The AOB was sagittally sectioned and the accessory olfactory cortex was coronally sectioned on a cryostat microtome (NX50, Thermo, USA). Sequential whole-brain sections (50 μm thick) were transferred into antifreeze solution (50% PBS, 30% ethylene glycol, 20% glycerol) in 24-well plates for storage at −25 °C. For fluorescent imaging, they were wet-mounted with DAPI, sealed with nail polish, and imaged with the VS120 virtual microscopy slide-scanning system (Olympus, Japan). All slices of the AOB were photographed and the number of labeled cells was counted, with the posterior cortex sampled at intervals of 300 μm. The acquired images were processed with Adobe Photoshop CS4 and Adobe Illustrator CS6.0 for illustrations. For cell counting in ImageJ, the boundaries of brain regions were delineated manually based on the Allen Brain Atlas and Mouse Brain Atlas (Fourth Edition) and the labeled neurons were quantified by the cell counter plug-in. For all statistical analyses in SPSS (v13.0), we first verified that all data were normally distributed using the one-sample Kolmogorov-Smirnov test, then calculated the mean value, standard deviation, and standard error of each group, with one-way ANOVA followed by *post-hoc* test used to determine statistical differences between groups. Statistical significance was set at *P*<0.001, *P*<0.01, and *P*<0.05. Numbers of labeled neurons and co-labeling percentages were presented as means±*SD* and means±*SEM*, respectively. Graphs were made using GraphPad Prism (v7.0).

RESULTS

AOB projects to BST, ACo, MeA, and PMCo

To verify the effectiveness of labeling the mitral cells of the AOB, we injected retrograde tracers into different accessory olfactory cortices of mice. The primary data showed that the MiA could be labeled by cholera toxin B (CTB, not shown) or by rAAV2-retro injected in the BST, ACo, MeA, and PMCo (Figure 1A–H). These results indicated that the AOB could project to the BST, ACo, MeA, and PMCo. In addition, we found that the number of infected neurons in the MiA per slice varied in different retrograde-labeled brain regions (Figure 1I). Among them, the infected neurons were greatest in MeA and PMCo labeling (MeA: 111.06±74.39, PMCo: 117.12±82.213), followed by ACo labeling (ACo: 48.3±36.943), and finally BST labeling (BST: 26.05±20.061), with significant differences found between them (one-way ANOVA followed by *post-hoc* test; BST vs. ACo: *P*=0.198; BST vs. MeA: *P*<0.001; BST vs. PMCo: *P*<0.001; ACo vs. MeA: *P*<0.001; ACo vs. PMCo: *P*<0.001; MeA vs. PMCo, *P*=0.375) (Figure 1I).

AOB projects to BST and PMCo simultaneously

To test the features of the efferent axonal fibers of the AOB in mice, we used rAAV2-retro with different fluorescent protein elements, which do not repel each, to infect the same neurons (Zhu et al., 2020). Specifically, rAAV2-retro-Ef1α-EYFP-WPRE-pA and rAAV2-retro-Ef1α-mCherry-WPRE-pA were injected into two different accessory olfactory cortices simultaneously to achieve retrograde co-labeling of the AOB.

We first injected rAAV2-retro-Ef1α-EYFP-WPRE-pA into the BST (Figure 2B) and rAAV2-retro-Ef1α-mCherry-WPRE-pA into the PMCo (Figure 2C). The two kinds of rAAV2-retro showed overlapping into the MiA after four weeks (Figure 2D–F). We found that the percentage of co-labeled neurons in the MiA among all labeled neurons was higher in BST labeling than in PMCo labeling (BST vs. PMCo: 40.539%±6.850% vs. 5.80%±1.709%; one-way ANOVA, *F*=24.219, *P*<0.001, *n*=3) (Figure 2G). In addition, fluorescent markers of different colors appeared at both injection sites (not shown), indicating mutual regulation between the BST and PMCo.

AOB projects to ACo and PMCo simultaneously

In addition, we injected rAAV2-retro-Ef1α-EYFP-WPRE-pA into the ACo (Figure 3B) and rAAV2-retro-Ef1α-mCherry-WPRE-pA into the PMCo (Figure 3C). The two kinds of rAAV2-retro demonstrated overlapping in the MiA after four weeks (Figure 3D–F). We found that the percentage of co-labeled neurons in the MiA among all labeled neurons was greater in ACo labeling than in PMCo labeling (ACo vs. PMCo: 63.792%±4.578% vs. 19.758%±3.142%; one-way ANOVA, *F*=62.882, *P*<0.001, *n*=3) (Figure 3G). In addition, fluorescent markers of different colors appeared at both injection sites (Figure 3B, C), indicating mutual regulation between the ACo and PMCo.

AOB projects to PMCo and MeA simultaneously

We injected rAAV2-retro-Ef1α-mCherry-WPRE-pA into the MeA (Figure 4B) and rAAV2-retro-Ef1α-EYFP-WPRE-pA into

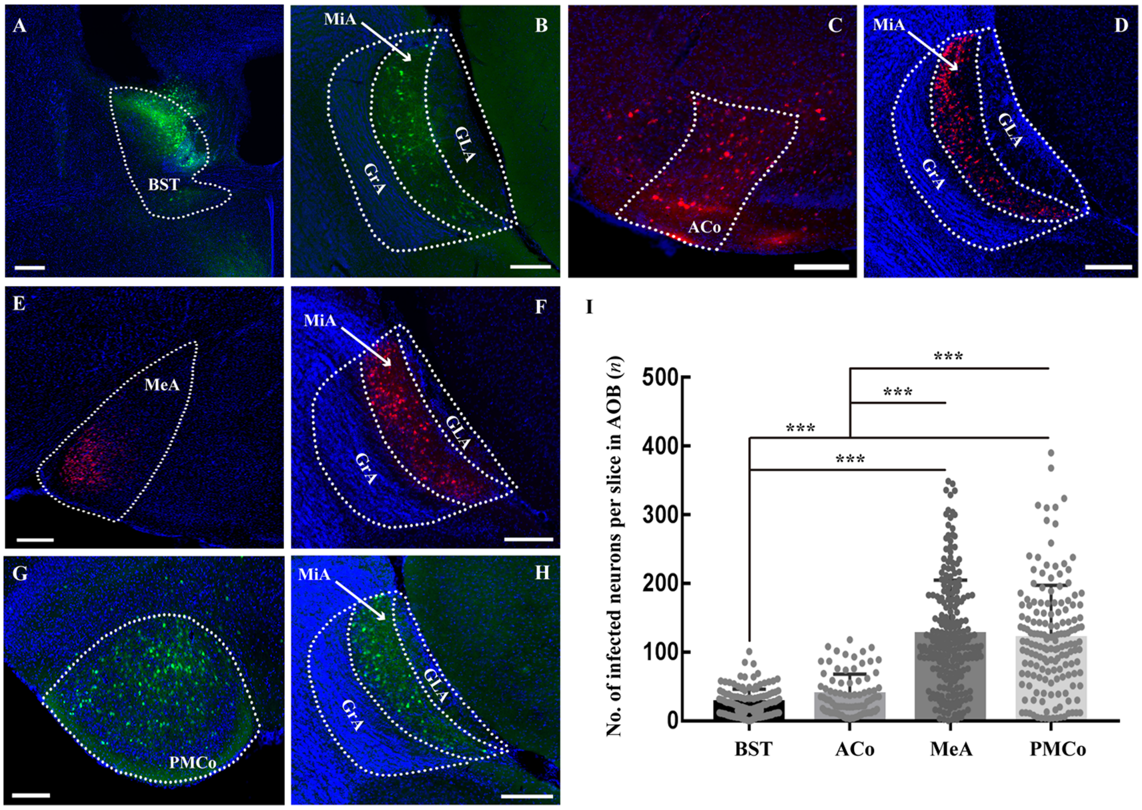

Figure 1 Mitral cell layer of AOB (MiA) projecting to BST, ACo, MeA, and PMCo

A, B: BST was injected with rAAV2-retro-Ef1α-EYFP-WPRE-pA (in green) (A) and MiA was labeled after four weeks (B). C, D: ACo was injected with rAAV2-retro-Ef1α-mCherry-WPRE-pA (in red) (C) and MiA was labeled after four weeks (D). E, F: MeA was injected with rAAV2-retro-Ef1α-mCherry-WPRE-pA (in red) (E) and MiA was labeled after four weeks (F). G, H: PMCo was injected with rAAV2-retro-Ef1α-EYFP-WPRE-pA (in green) (G) and MiA was labeled after four weeks (H). I: No. of infected neurons in MiA per slice varied in different retrograde-labeled brain regions. ***: $P<0.001$. Scale bars: 200 μm. $n=10, 6, 16, 11$.

the PMCo (Figure 4C). The two kinds of rAAV2-retro showed overlapping in the MiA after four weeks (Figure 4D–F). We found that the percentage of co-labeled neurons in the MiA among all labeled neurons was higher in PMCo labeling than in MeA labeling (PMCo vs. MeA: 95.836%±0.763% vs. 34.954%±2.494%; one-way ANOVA, $F=544.944$, $P<0.001$, $n=3$) (Figure 4G). In addition, fluorescent markers of different colors appeared at both injection sites (Figure 4B, C), indicating mutual regulation between the PMCo and MeA.

AOB projects to BST and MeA simultaneously

We injected rAAV2-retro-Ef1α-EYFP-WPRE-pA into the BST (Figure 5B) and rAAV2-retro-Ef1α-mCherry-WPRE-pA into the MeA (Figure 5C). The two kinds of rAAV2-retro showed overlapping in the MiA after four weeks (Figure 5D–F). We found that the percentage of co-labeled neurons in the MiA among all labeled neurons was greater in BST labeling than in MeA labeling (BST vs. MeA: 70.645%±3.288% vs. 13.888%±0.848%; one-way ANOVA, $F=284.577$, $P<0.001$, $n=3$) (Figure 5G). In addition, fluorescent markers of different colors appeared at both injection sites (Figure 5B, C), indicating mutual regulation between the BST and MeA.

AOB projects to ACo and MeA simultaneously

We injected rAAV2-retro-Ef1α-EYFP-WPRE-pA into the ACo (Figure 6B) and rAAV2-retro-Ef1α-mCherry-WPRE-pA into the MeA (Figure 6C). The two kinds of rAAV2-retro demonstrated overlapping in the MiA after four weeks (Figure 6D–F). We found that the percentage of co-labeled neurons in the MiA among all labeled neurons was greater in MeA labeling than in ACo labeling (ACo vs. MeA: 38.538%±2.460% vs. 15.685%±2.531%; one-way ANOVA, $F=41.919$, $P<0.001$, $n=3$) (Figure 6G). In addition, green fluorescent markers appeared at the MeA (Figure 6C), indicating projections from the MeA to ACo. Red fluorescent markers were found at the ACo (not shown), indicating mutual regulation between the ACo and MeA.

DISCUSSION

We used rAAV2-retro to successfully label AOB projection neurons in the MiA from the BST, ACo, MeA, and PMCo, and further adopted two-color rAAV2-retro to achieve co-labeling of mitral cells in the AOB. We demonstrated that a single neuron in the MiA could project to at least two different brain

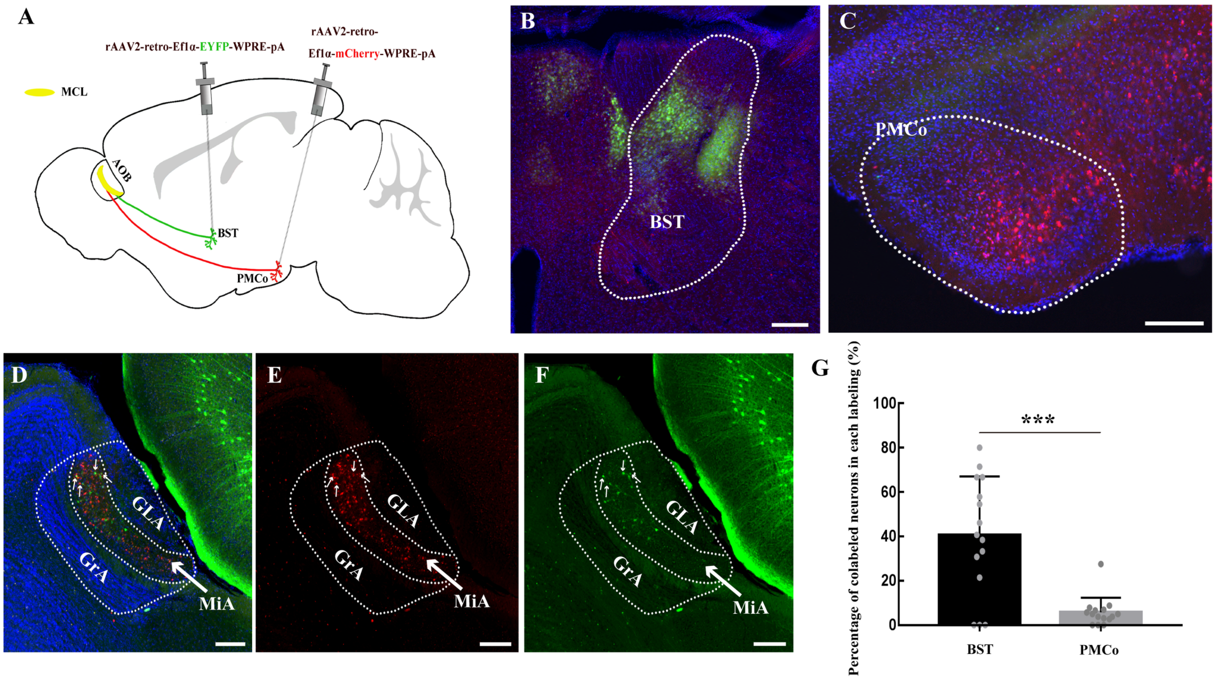

Figure 2 MiA projecting into BST and PMCo simultaneously

A: Schematic. B: Injection site of rAAV2-retro-Ef1α-EYFP-WPRE-pA (in green) in BST. C: Injection site of rAAV2-retro-Ef1α-mCherry-WPRE-pA (in red) in PMCo. D–F: Two kinds of rAAV2-retro overlapped in MiA after four weeks (arrows indicate co-labeled neurons). G: Percentages of co-labeled neurons in MiA among all labeled neurons in BST and PMCo labeling, respectively. ***: $P<0.001$. Scale bars: 200 μm. $n=3$.

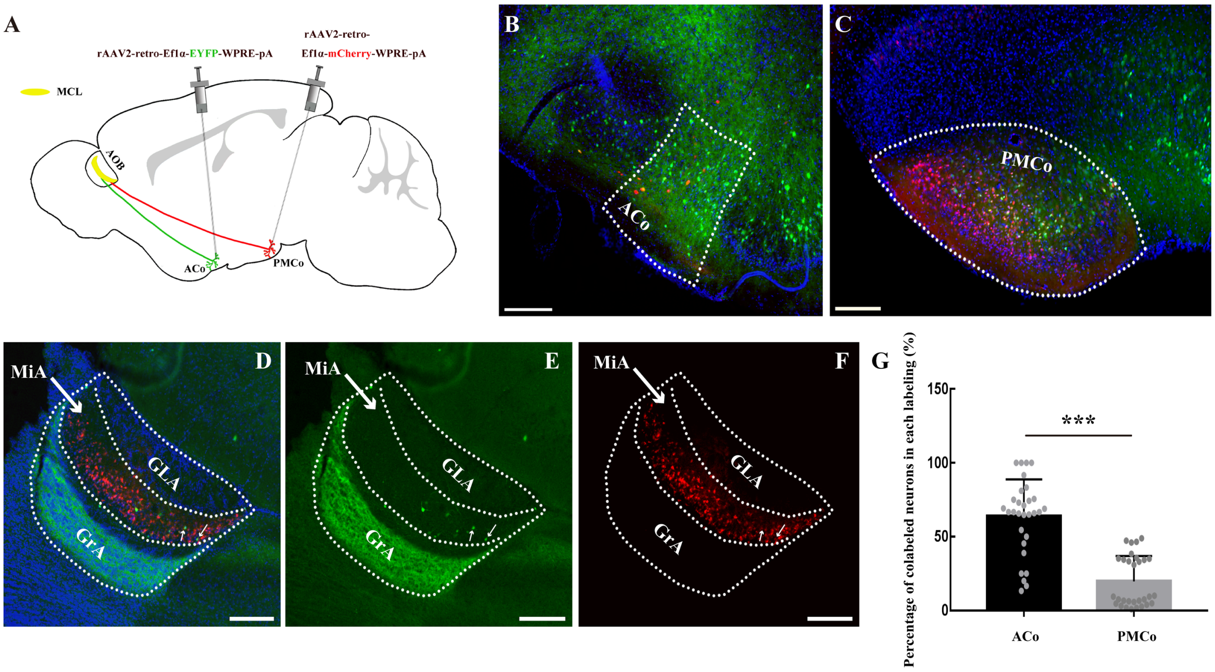

Figure 3 MiA projecting into ACo and PMCo simultaneously

A: Schematic. B: Injection site of rAAV2-retro-Ef1α-EYFP-WPRE-pA (in green) in ACo. C: Injection site of rAAV2-retro-Ef1α-mCherry-WPRE-pA (in red) in PMCo. D–F: Two kinds of rAAV2-retro overlapped in MiA after four weeks (arrows indicate co-labeled neurons). G: Percentages of co-labeled neurons in MiA among all labeled neurons in ACo and PMCo labeling, respectively. ***: $P<0.001$. Scale bars: 200 μm. $n=3$.

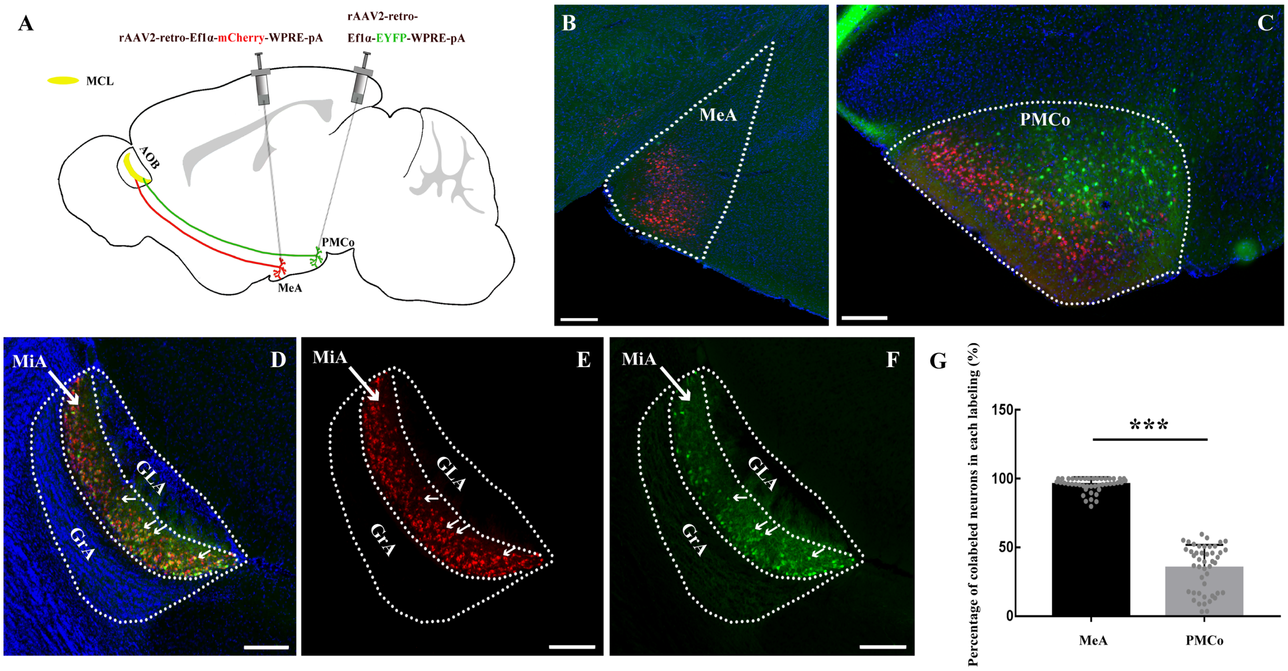

Figure 4 MiA projecting into PMCo and MeA simultaneously

A: Schematic. B: Injection site of rAAV2-retro-Ef1α-mCherry-WPRE-pA (in red) in MeA. C: Injection site of rAAV2-retro-Ef1α-EYFP-WPRE-pA (in green) in PMCo. D–F: Two kinds of rAAV2-retro overlapped in MiA after four weeks (arrows indicate co-labeled neurons). G: Percentages of co-labeled neurons in MiA among all labeled neurons from MeA and PMCo, respectively. ***: *P*<0.001. Scale bars: 200 μm. *n*=3.

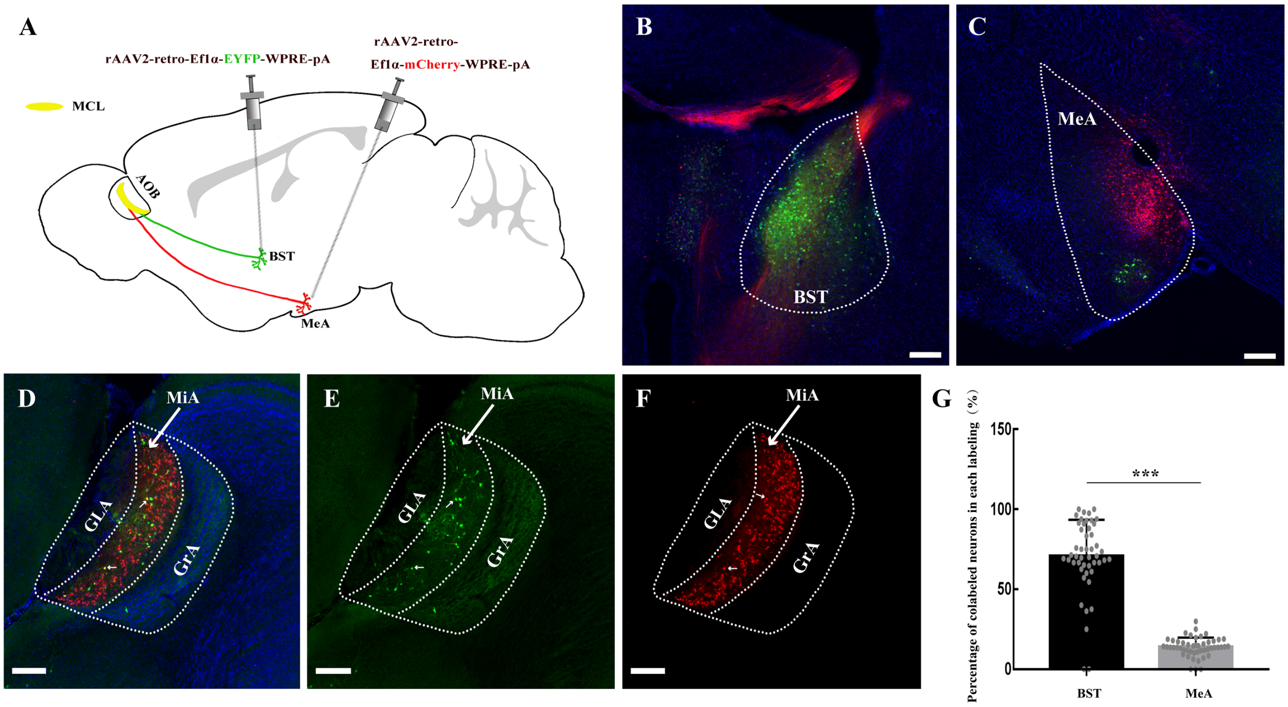

Figure 5 MiA projecting into BST and MeA simultaneously

A: Schematic. B: Injection site of rAAV2-retro-Ef1α-EYFP-WPRE-pA (in green) in BST. C: Injection site of rAAV2-retro-Ef1α-mCherry-WPRE-pA (in red) in MeA. D–F: Two kinds of rAAV2-retro overlapped in MiA after four weeks (arrows indicate co-labeled neurons). G: Percentages of co-labeled neurons in MiA among all labeled neurons from BST and MeA, respectively. ***: *P*<0.001. Scale bars: 200 μm. *n*=3.

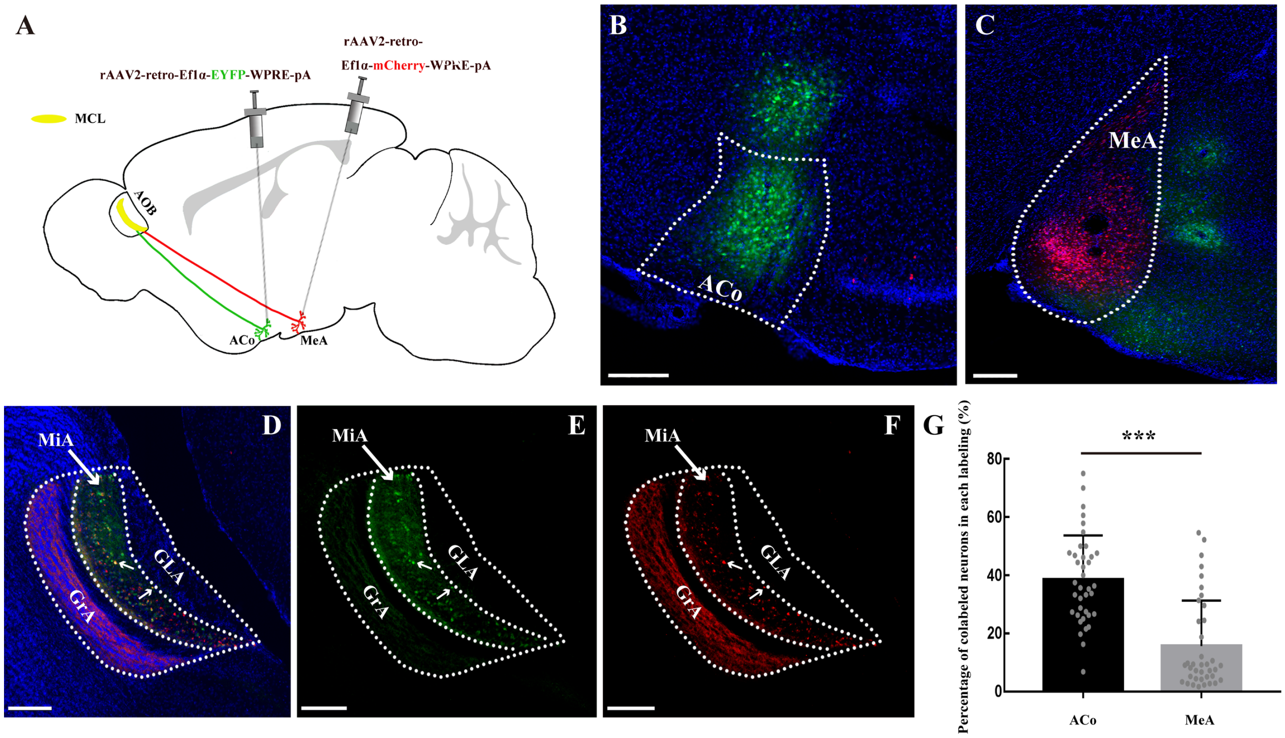

Figure 6 MiA projecting into ACo and MeA simultaneously

A: Schematic. B: Injection site of rAAV2-retro-Ef1α-EYFP-WPRE-pA (in green) in ACo. C: Injection site of rAAV2-retro-Ef1α-mCherry-WPRE-pA (in red) in MeA. D–F: Two kinds of rAAV2-retro overlapped in the MiA after four weeks (arrows indicate co-labeled neurons). G: Percentages of co-labeled neurons in MiA among all labeled neurons from ACo and MeA, respectively. ***: *P*<0.001. Scale bars: 200 μm. *n*=3.

regions. These results indicate that the dispersion characteristics of efferent projections of mitral cells in the AOB are similar to those of the MOB, that is, the axonal branches of individual mitral cells can reach all olfactory cortices (Nagayama et al., 2010). Although the dendrites, shapes, locations, and spontaneous and stimulus-induced activities of the AOB projection neurons rarely resemble those of MOB mitral cells (Larriva-Sahd, 2008; Mohrhardt et al., 2018), their transport patterns of information in the MOB and AOB may be similar, and different olfactory cortices may have different odor decoding mechanisms, eventually leading to different perceptions of odorants and pheromones.

We also found that the numbers of labeled neurons in the AOB from various cortices were significantly different, in the order BST<ACo<MeA<PMCo (Figure 1I). In addition, the percentages of co-labeled neurons from two cortices were highest in the BST, followed by the ACo and PMCo, and lowest in the MeA (Figures 2G, 3G, 4G, 5G, 6G), indicating that the number of labeled neurons in the AOB, from small to large, was in the order: BST, ACo, PMCo, and MeA. These results demonstrate that there were quantitative differences in the number of mitral cells in the AOB projecting to diverse accessory olfactory cortices, if the magnitude of the local axon terminals was the same in the rAAV-infected areas. However, given that rAAVs do not fully infect the entire targeted brain region, the number of labeled neurons in the AOB was incomplete. According to previous results, a single AOB harbors 6 842 putative mitral cells (Mohrhardt et al., 2018), which is 4–18 times greater than that labeled in our study (Figure 1I, MeA: 111.06±74.39, PMCo: 117.12±82.213, BST: 26.05±20.061, ACo: 48.3±36.943; approximately 15 slices in one AOB). Therefore, we cannot conclude that there are differences in the number of neurons in the AOB projecting into different brain regions. However, there may be significant differences in the number of neurons projecting to the same area in different brain regions, suggesting that each mitral cell in the AOB could project to a different number of neurons in different cortices, but this requires more sophisticated single-cell markers for detection and validation.

In addition, we found that there was no significant difference in the projection pattern between the aAOB and pAOB, although their sources of input are isolated from each other (Dulac & Torello, 2003; Riviere et al., 2009). Nevertheless, only the aAOB or pAOB showed retrograde labeling, but limitedly (Figure 2F, form BST; Figure 3E, form ACo). These results are similar to previous research, which used anterograde and retrograde chemical tract-tracing methods in rats and demonstrated that apart from common vomeronasal-recipient areas, only the aAOB projects to the BST, medial division, and posteromedial part (BSTMPM), and only the pAOB projects to the dorsal anterior amygdale (AAd), deep cell layers of the bed nucleus of the accessory olfactory tract

(BAOT), and anteroventral MeA (MeAV) (Mohedano-Moriano et al., 2007). The midline separating the aAOB and pAOB is determined by the boundary of Gαi2 labeling between the anterior and posterior glomerular layer (GLA), which is roughly perpendicular to the AOB (Marking et al., 2017). Because of the larger local diffusion range of rAAVs, we cannot suggest significant anatomical and functional differences between the aAOB and pAOB, but their axonal projection patterns have a certain degree of convergence (von Campenhausen & Mori, 2000).

Finally, we found reciprocal projections between cortices, such as the ACo and PMCo (Figure 3B, C), MeA and PMCo (Figure 4B, C), MeA and BST (Figure 5B, C), and MeA and ACo (Figure 6B, C), which suggests that these brain regions regulate each other. Combined with previous results, these findings indicate that the way in which information is decoded in the accessory olfactory cortex remains unknown. Moreover, we found that no neurons in the MOB were labeled from the above-mentioned accessory olfactory cortices, including the CoA and MeA, which have been reported to receive inputs from the MOB (Kang et al., 2009). Whether the information convergence point of the MOS and AOS is the hypothalamus or the cortical amygdala (Kang et al., 2009; Perez-Gomez et al., 2015), or even direct connections between the MOB and AOB at the very beginning (Vargas-Barroso et al., 2015), is still controversial, requiring additional experiments with more sophisticated single-cell labeling tools to enable verification.

Our study provides an effective method for labeling mitral cells in the AOB of mice and demonstrated that their axonal projection pattern was the same as in the MOB, i.e., dispersion characteristics of efferent projections to each cortex through a large number of axonal branches. Moreover, we found no significant differences between the aAOB and pAOB in projections to the BST, ACo, MeA, and PMCo, although their inputs were distinguishable from the apical and basal VNO (Figure 7). Further single-cell labeling and recordings are necessary to elucidate the projection patterns and information encoding of individual mitral cells in the aAOB and pAOB and whether individual cortical neurons sample information across segregated AOB pathways. It would be useful to study what pheromone information is represented in the different accessory olfactory cortices and to understand how the brain processes pheromone signals to elicit stereotypical behavioral responses.

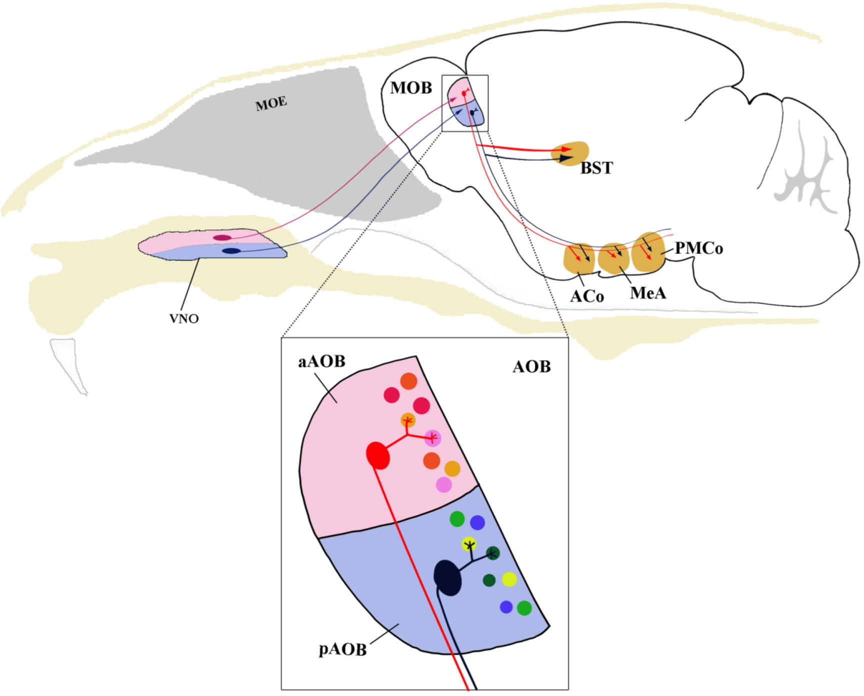

Figure 7 Schematic of afferent projections in accessory olfactory system of mice

COMPETING INTERESTS

The authors declare that they have no competing interests.

AUTHORS' CONTRIBUTIONS

X.P.R., X.T.Z, and F.Q.X. designed the study. N.Z. and X.P.R. supervised the analyses. N.Z., Z.Z.W., S.W.W., F.J.Y., C.L., and X.P.R. performed labeling and statistics. N.Z. and X.P.R wrote the manuscript with the other authors' input. A.M. polished the manuscript. N.Z and X.P.R revised the manuscript. All authors read and approved the final version of the manuscript.

ACKNOWLEDGEMENTS

We thank Dr. Ling-Ling Xu (Wuhan Institute of Physics and Mathematics) for maintaining and managing the optical platform.

REFERENCES

Ackels T, Drose DR, Spehr M. 2016. In-depth physiological analysis of defined cell populations in acute tissue slices of the mouse vomeronasal organ. *Journal of Visuallized Experiments*, **115**: e54517.

Breer H, Fleischer J, Strotmann J. 2006. The sense of smell: multiple olfactory subsystems. *Cellular and Molecular Life Sciences*, **63**: 1465−1475.

Doving KB, Trotier D. 1998. Structure and function of the vomeronasal organ. *Journal of Experimental Biologyl*, **201**: 2913−2925.

Dulac C, Torello AT. 2003. Molecular detection of pheromone signals in mammals: from genes to behaviour. *Nature Reviews Neuroscience*, **4**: 551−562.

Dulac C, Wagner S. 2006. Genetic analysis of brain circuits underlying pheromone signaling. *Annual Review of Genetics*, **40**: 449−467.

Ghosh S, Larson SD, Hefzi H, Marnoy Z, Cutforth T, Dokka K, Baldwin KK. 2011. Sensory maps in the olfactory cortex defined by long-range viral tracing of single neurons. *Nature*, **472**: 217−220.

Halpern M, Martinez-Marcos A. 2003. Structure and function of the vomeronasal system: an update. *Progress in Neurobiology*, **70**(3): 245−318.

Holy TE. 2018. The accessory olfactory system: Innately specialized or microcosm of mammalian circuitry?. *Annual review of neuroscience*, **41**: 501−525.

Kang N, Baum MJ, Cherry JA. 2009. A direct main olfactory bulb projection to the 'vomeronasal' amygdala in female mice selectively responds to volatile pheromones from males. *The European Journal of Neuroscience*, **29**(3): 624−634.

Krieger J, Schmitt A, Lobel D, Gudermann T, Schultz G, Breer H, Boekhoff I. 1999. Selective activation of G protein subtypes in the vomeronasal organ upon stimulation with urine-derived compounds. *The Journal of Biological Chemistry*, **274**(8): 4655−4662.

Larriva-Sahd J. 2008. The accessory olfactory bulb in the adult rat: a cytological study of its cell types, neuropil, neuronal modules, and interactions with the main olfactory system. *The Journal of Comparative Neurology*, **510**(3): 309−350.

Leinders-Zufall T, Brennan P, Widmayer P, S PC, Maul-Pavicic A, Jager M, Li XH, Breer H, Zufall F, Boehm T. 2004. MHC class I peptides as chemosensory signals in the vomeronasal organ. *Science*, **306**(5698): 1033−1037.

Leinders-Zufall T, Lane AP, Puche AC, Ma W, Novotny MV, Shipley MT, Zufall F. 2000. Ultrasensitive pheromone detection by mammalian vomeronasal neurons. *Nature*, **405**: 792−796.

Marking S, Krosnowski K, Ogura T, Lin W. 2017. Dichotomous distribution of putative cholinergic interneurons in mouse accessory olfactory bulb. *Frontiers in Neuroanatomy*, **11**: 10.

Miyamichi K, Amat F, Moussavi F, Wang C, Wickersham I, Wall NR, Taniguchi H, Tasic B, Huang ZJ, He Z, Callaway EM, Horowitz MA, Luo L. 2011. Cortical representations of olfactory input by trans-synaptic tracing. *Nature*, **472**: 191−196.

Mohedano-Moriano A, Pro-Sistiaga P, Ubeda-Banon I, Crespo C, Insausti R, Martinez-Marcos A. 2007. Segregated pathways to the vomeronasal amygdala: differential projections from the anterior and posterior divisions of the accessory olfactory bulb. *The European Journal of Neuroscience*, **25**(7): 2065−2080.

Mohrhardt J, Nagel M, Fleck D, Ben-Shaul Y, Spehr M. 2018. Signal detection and coding in the accessory olfactory system. *Chemical Senses*, **43**(9): 667−695.

Moriya-Ito K, Endoh K, Fujiwara-Tsukamoto Y, Ichikawa M. 2013. Three-dimensional reconstruction of electron micrographs reveals intrabulbar circuit differences between accessory and main olfactory bulbs. *Frontiers in Neuroanatomy*, **7**: 5.

Nagayama S, Enerva A, Fletcher ML, Masurkar AV, Igarashi KM, Mori K, Chen WR. 2010. Differential axonal projection of mitral and tufted cells in the mouse main olfactory system. *Frontiers in Neural Circuits*, **4**: 120.

Perez-Gomez A, Bleymehl K, Stein B, Pyrski M, Birnbaumer L, Munger SD, Leinders-Zufall T, Zufall F, Chamero P. 2015. Innate predator odor aversion driven by parallel olfactory subsystems that converge in the ventromedial hypothalamus. *Current Biology*, **25**(10): 1340−1346.

Riviere S, Challet L, Fluegge D, Spehr M, Rodriguez I. 2009. Formyl peptide receptor-like proteins are a novel family of vomeronasal chemosensors. *Nature*, **459**: 574−577.

Sosulski DL, Bloom ML, Cutforth T, Axel R, Datta SR. 2011. Distinct representations of olfactory information in different cortical centres. *Nature*, **472**: 213−216.

Spehr M, Spehr J, Ukhanov K, Kelliher KR, Leinders-Zufall T, Zufall F. 2006. Parallel processing of social signals by the mammalian main and accessory olfactory systems. *Cellular Molecular Life Sciences*, **63**: 1476−1484.

Su CY, Menuz K, Carlson JR. 2009. Olfactory perception: receptors, cells, and circuits. *Cell*, **139**: 45−59.

Takami S, Graziadei PP. 1991. Light microscopic Golgi study of mitral/tufted cells in the accessory olfactory bulb of the adult rat. *The Journal of Comparative Neurology*, **311**(1): 65−83.

Urban NN, Castro JB. 2005. Tuft calcium spikes in accessory olfactory bulb mitral cells. *The Journal of Neuroscience: the Official Journal of the Society for Neuroscience*, **25**(20): 5024−5028.

Vargas-Barroso V, Ordaz-Sanchez B, Pena-Ortega F, Larriva-Sahd JA. 2015. Electrophysiological evidence for a direct link between the main and accessory olfactory bulbs in the adult rat. *Frontiers in Neuroscience*, **9**: 518.

von Campenhausen H, Mori K. 2000. Convergence of segregated pheromonal pathways from the accessory olfactory bulb to the cortex in the mouse. *The European Journal of Neuroscience*, **12**(1): 33−46.

Yokosuka M. 2012. Histological properties of the glomerular layer in the mouse accessory olfactory bulb. *Experimental Animals*, **61**(1): 13−24.

Yoles-Frenkel M, Kahan A, Ben-Shaul Y. 2018. Temporal response properties of accessory olfactory bulb neurons: limitations and opportunities for decoding. *The Journal of Neuroscience*, **38**(21): 4957−4976.

Yonekura J, Yokoi M. 2008. Conditional genetic labeling of mitral cells of the mouse accessory olfactory bulb to visualize the organization of their apical dendritic tufts. *Molecular and Cellular Neuroscience*, **37**(4): 708−718.

Zhu X, Lin K, Liu Q, Yue X, Mi H, Huang X, He X, Wu R, Zheng D, Wei D, Jia L, Wang W, Manyande A, Wand J, Zhang Z, Xu F. 2020. Rabies virus pseudotyped with CVS-N2C glycoprotein as a powerful tool for retrograde neuronal network tracing. *Neuroscience Bulletin*, **36**(3): 202−216.

ZOOLOGICAL RESEARCH

Exploring the reproductive ecology of the tropical semifossorial snake *Ninia atrata*

Teddy Angarita-Sierra[1,2,3,*], Cesar Alejandro López-Hurtado[2]

[1] *Tropical Organism Biology Research Group*, *Universidad Nacional de Colombia*, *Bogotá* 111321, *Colombia*
[2] *Yoluka ONG*, *Fundación de Investigación en Biodiversidad y Conservación*, *Bogotá* 110931, *Colombia*
[3] *Vicerrectoria de Investigación*, *Universidad Manuela Beltrán*, *Bogotá* 110231, *Colombia*

ABSTRACT

Based on histological analyses and field studies, this research describes the reproductive ecology of a population of *Ninia atrata* snakes inhabiting an oil palm plantation. Furthermore, through a multivariate approach, we explored the main drivers of reproductive output in *N. atrata*. Results showed that prey abundance and food intake were crucial variables contributing to reproductive output. Multiple linear regression models showed that neonates had high sensitivity (R^2=55.29%) to extreme changes in climate, which was strongly related to slug and snail abundance variability and microhabitat quality. Reproductive cycles were markedly different between the sexes, being continuous in males and cyclical in females. Despite this variation, reproductive cycles at the population level were seasonal semi-synchronous. Constant recruitment of neonates all year, multiple clutches, high mating frequency, and continuous sperm production characterized the reproductive phenology of *N. atrata*. In addition, a significant number of previtellogenic females presented oviductal sperm as well as uterine scars, suggesting a high precocity in the species. The main drivers of reproductive output also differed between the sexes. In females, clutch size and secondary follicle variability were highly related to stomach bolus volume, fat body area, and body mass. In males, height of piles of palm leaves and body mass, rather than intrinsic reproductive traits, were the main drivers of sperm production. Nevertheless, in both cases, the relationship between body mass, prey abundance, and food intake suggests that *N. atrata* follows the income breeding strategy to compensate for reproductive costs and to maximize fitness.

Keywords: Continuous male reproduction; Clutch mass; Income breeding; Iteroparity; Spermatogenesis; Oogenesis; Reproductiveeffort; El Niño-Southern Oscillation (ENSO)

INTRODUCTION

Since the early efforts of Fitch (1970) to elucidate the reproductive cycles of tropical reptiles, research on the reproductive phenology of tropical snakes has increased in response to the historical disparity between temperate and tropical zone studies (Mathies, 2011). In particular, researchers in the South American tropics of Brazil and

---

Received: 21 June 2019; Accepted: 29 November 2019; Online: 11 December 2019

Foundation items: This work was supported by the Faculty of Sciences and Project Management Program of the Welfare Office of the Universidad Nacional de Colombia under Grant Nos. 3733, 1150, 1302, 1567, and 3093; Colciencias Scholarship Doctoral Program under Grant No. 6172; Yoluka NGO, Biodiversity and Conservation Research Foundation under Grant No. 001 – 2014; Universidad Manuela Beltrán under act 13072019 and Palmasol S.A. Ac001–2014

*Corresponding author, E-mail: teddy.angarita@yoluka.org.co

DOI: 10.24272/j.issn.2095-8137.2020.015

Argentina have expanded our knowledge about the phenology and reproductive traits of more than 10 elapid species (Almeida-Santos et al., 1998, 2006; Ávila et al, 2010; Valdujo et al., 2002), 10 viper species (Almeida-Santos et al., 1999, 2006; Almeida-Santos & Salomao, 2002; Hartmann et al., 2004; Janeiro-Cinquini, 2004; Leão et al., 2014; Marques et al., 2013; Monteiro et al., 2006; Nogueira et al., 2003), nine boine species (Bretona & Chiaraviglio, 2003; Chiaraviglio, 2006; Miranda et al., 2017; Pizzatto, 2005; Pizzatto & Marques, 2007; Rivas et al., 2007), and 26 colubrid species (Alencar et al., 2012; Ávila et al., 2006; Balestrin & Di-Bernardo, 2005; Bizerra et al., 2005; Braz et al., 2014; da Costa-Prudente et al., 2014; Dos Santos-Acosta et al., 2006; Gaiarsa et al., 2013; Goldberg, 2004b, 2006 Gomes & Marques, 2012; Gualdrón-Durán et al., 2019; Hartmann et al., 2002; Leite et al., 2009; López & Giraudo, 2008; Marques, 1996; Marques et al., 2009; Marques & Puorto, 1998; Pizzatto et al., 2008; Pizzatto & Marques, 2002; Scartozzoni et al., 2009; Silva & Vadez, 1989; Vitt, 1996).

The above contributions have shown that the reproductive biology of tropical snakes diverges from the uniformly seasonal and highly synchronous patterns seen in species from temperate zones. Tropical snakes exhibit both seasonal and aseasonal reproductive cycles. However, aseasonal reproduction is not the rule in the tropics, in fact, truly aseasonal (continuous) reproduction by tropical females is rare (Brown & Shine, 2006b; Saint Girons & Pfeffer, 1972; Shine, 2003). Tropical snake reproduction includes multiple phenologies and high variability among populations, as well as within individuals of the same population (Mathies, 2011; Pizzatto et al., 2008). Most species also have broad seasonal reproductive schedules and exhibit intersexual divergence in reproductive cycles (e.g., *Naja*, *Bungarus*, *Calliophis*, Pizzatto et al., 2008; Saint Girons & Pfeffer, 1972).

Despite the enormous efforts to understand the reproductive biology of snakes, fewer studies have been conducted on tropical fossorial and semifossorial snakes than on terrestrial and arboreal snakes (Braz et al., 2014). This is due to the cryptic behavior, secretive microhabitats, and lower encounter rates of fossorial and semifossorial snakes, which makes them an elusive research object. Therefore, their natural history and ecology remain poorly understood, which limits our assessment of their reproductive seasonality, energy acquisition timescale, reproductive expenditure, and sexual maturation age or size. In Colombia, the semifossorial snake *Atractus marthae* (Meneses-Pelayo & Passos, 2019) has been the only snake species with a detailed reproductive study. *Atractus marthae* populations inhabit the cloud forests (>2 400 m a.s.l.) of the northeastern Andes of Colombia, with females reported to have an asynchronous reproductive stage, aseasonal and discontinuous reproductive cycle, and single clutch per year, whereas males present spermatozoa in testes and ducts, as well as hypertrophied of the sexual segment of male kidney (SSK) throughout the year (Guladrón-Durán et al., 2019). However, given the dearth of reproductive information among Colombian snakes, comparison between the reproductive ecology of snakes from highlands and lowlands is difficult, limiting our understanding of the general reproductive patterns of snakes in the tropical Andes.

Ninia atrata (Hallowell, 1845) is a semifossorial tropical snake widely distributed in South America. It ranges from Western Panama, Colombia, Ecuador, Venezuela to Trinidad and Tobago (Angarita-Sierra, 2009, 2014, 2015; Ingrasci, 2011; McCranie & Wilson, 1995; Medina-Rangel, 2015; Mesa-Joya, 2015; Rivas et al., 2012). Despite its broad distribution and high abundance in disturbed or transformed habitats, its reproductive biology has been largely ignored (Angarita-Sierra, 2015; Lynch, 2015). Currently, details on clutch size and birth-size in northern South American populations have only been reported as anecdotal observations (Lancini, 1979; Natera-Mumaw et al., 2015; Roze, 1966). Silva & Valdez (1989) reported a hatchling period from June to September in populations located on the northern hills of Caracas, Venezuela.

Herein, we explored the reproductive biology of *N. atrata* in order to improve our understanding of the reproductive features of semifossorial tropical snakes. Our study consisted of three main goals: (1) To provide a detailed description of female and male annual reproductive cycles, minimum size at sexual maturity, mating frequency, recruitment, clutch size, and egg features. (2) To analyze the relationship between reproductive traits of *N. atrata*, prey abundance, and food intake, as well as variability during extreme El Niño-Southern Oscillation (ENSO) climatic events. (3) To explore the main drivers of reproductive output of the population under study.

MATERIALS AND METHODS

Study area and climate variability

We studied *N. atrata* snakes inhabiting the oil palm plantation (*Elaeis guineensis* Jacq. 1897) of Palmasol S. A., located at Vereda La Castañeda, the municipality of San Martin, Department of Meta, Colombia (N3° 31', W73° 32'; Figure 1). This locality has a monomodal climate (rainy season from April to November and dry season from December to March) with an annual rainfall of the 3 070 mm and high temperatures year-round (>26 °C). According to the Colombian Institute of Hydrology, Meteorology, and Environmental Studies (IDEAM Spanish acronym), the El Niño ENSO recorded between 2016 and 2017 was the strongest of the last 20 years (IDEAM, 2016). Therefore, climatic variability was categorized as good and bad climatic years, where good years represent the sampling period from August 2014 to December 2015 without ENSO effects, and bad years represent the sampling period from January 2016 to April 2017 under ENSO effects.

We monitored the temperature and relative humidity of microhabitats using four thermo-hygrometers (EBI20-TH1 Ebro®). These devices were placed over three consecutive days per sampling visit, with three at the base of different piles of palm leaves and one at the base of an epiphytic cushion. These sites were randomly selected. A fifth thermo-hygrometer was placed at a height of 1.5 m on a randomly

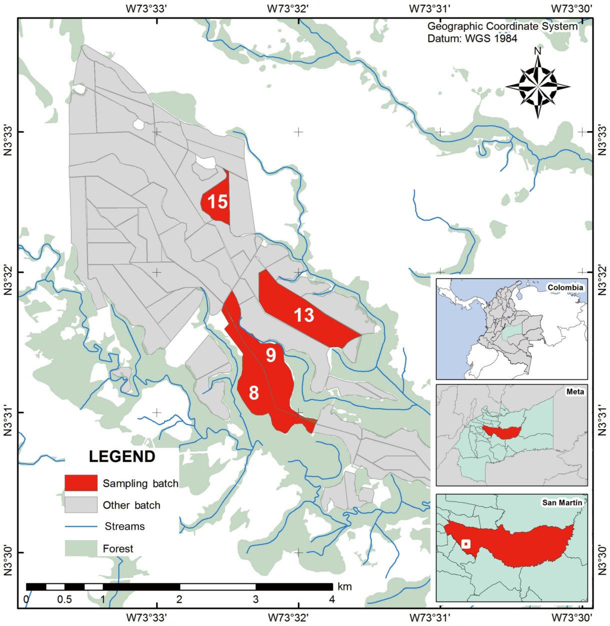

Figure 1 Study area

Oil palm plantation (*Elaeis guineensis* Jacq. 1897) of Palmasol S. A. Sampling batches 8, 9, 13, and 15 are in red

selected palm tree trunk. We configured the thermo-hygrometers to record temperature and relative humidity readings on a per minute basis, resulting in a total of 138 240 measurements and 2 304 h of sampling effort per thermo-hygrometer.

Sampling and data collection

Data were obtained during four plantation production batches (8, 9, 13, 15; Figure 1), in which piles of oil palm leaves are stacked following pruning. We sampled from August 2014 to June 2017, spending three days per sampling visit (*n*=32). No sampling was conducted in September 2014 or May 2015 due to logistic constraints.

Snake searching was conducted in a total of 4 563 palm leaf piles (microhabitat 1) and 304 epiphytic cushions attached to the base of palm trees (microhabitat 2) from 0730 h to 1730 h, totaling 1 189 h of sampling effort per researcher. Palm leaf piles and epiphytic cushions were searched by raking to a depth of 5–15 cm over a 3–5 min period, with all hand-captured prey items (e.g., snails, earthworms, slugs, and leeches) and snakes recorded. We used the height (cm) of the palm leaf piles and epiphytic cushions as surrogate estimators of microhabitat quality. This is because greater habitat height likely provided better refuge for the snakes due to lower microclimate variability, larger number of prey, and greater security against predators (Angarita-Sierra, 2015; Angarita-Sierra & Lozano-Daza, 2019; Lynch, 2015; Weatherhead & Madsen, 2006).

All caught snakes were measured (snout-vent length (SVL); tail length (TL)) using a measuring tape (±0.1 cm) and weighed (Mass) using a Pesola® dynamometer of 50 g (±0.1 g). We calculated the sexual size dimorphism index (SSD) following Gibbons & Lovich (1990) and determined the ratio between the SVL of the larger and smaller sex. The ratio is defined as positive when females are larger and negative when males are larger (with SSD=1.0 when SVL is equal between the two sexes). We recorded snake health (presence/ absence of tick, mycoses, or injuries) by external examination, as well as sex, umbilicus scars, and secondary sexual traits in males (development degree of chin tubercles). We also recorded the presence of food and reproductive condition by palpation and by contrast light on the snake body from the dorsal to ventral surface.

Snakes captured in batch 13 (*n*=275) were used in the mark-recapture experiments to test whether females could produce more than one clutch during the same reproductive season. Thus, these snakes were branded on their ventral scales following the procedures described by Dorcas & Willson (2009) using an Aaron Medical Change-A-Tip cautery unit Bovie® (Winne et al., 2006). We determined the sex of the branded snakes by inserting a blunt probe through the cloaca orifice following procedures described by Blanchard & Finster (1933). Afterward, all branded individuals were released at the same place in which they were captured.

We transported gravid females and eggs found in the field to the lab in individual terraria. The females were provided with food and water *ad libitum*. The captive environment was maintained to resemble the conditions of the oil palm plantation (photoperiod regime: 12 h light/12 h darkness; temperature: 26.21±0.61 °C and 65.64±3.52 h). Once females laid their eggs, we collected, measured, inspected, and monitored their temperature throughout incubation (26.21±0.61 °C; 65.64±3.52 h) using an infrared thermometer (CGHM-H13). Finally, when hatchlings were born, we measured, individually marked, and released them with their mothers at the place where she was captured.

Reproductive data acquisition

In total, 150 snakes from batches 8, 9, and 15 were euthanized with an injection of lidocaine 2% ($C_{14}H_{22}N_2O$) in the heart, then fixed with 10% formalin, and preserved in 70% ethanol. All specimens were deposited in the reptile collection of the Instituto de Ciencias Naturales (ICN) of the Universidad Nacional de Colombia. We determined sex of the collected snakes by abdominal dissection and direct gonad observation.

Afterward, the reproductive tracts were fixed in 10% buffered formalin and then used to make histological slides following Luna (1968) to determine reproductive stage, as well as spermatogenesis and oogenesis cycles. We registered microscopic reproductive traits following the procedures described by Krohmer et al., (2004), Balestrin & Di-Bernardo (2005), and Ramos-Pallares et al. (2015). Sperm abundance and time of spermatogenesis were based on counts (three replicates) in cross-sections of seminiferous tubules chosen at random using a light microscope under 40× magnification (Fox, 1952).

Based on digital pictures and ImageJ v1.52 software (Schneider et al., 2012), we obtained the following macroscopic reproductive variables from sacrificed male and female snakes: size of hypertrophy SSK, testicular volume (mm^3), width of distal end of deferent duct (mm), oviductal width (mm), number and diameter of previtellogenic and vitellogenic follicles (mm), and width and length of oviductal eggs (mm).

We considered sexually mature males as the smallest (SVL) male having spermatozoa in their testes, and sexually mature females as the smallest female with vitellogenic follicles or oviductal eggs. We calculated relative fecundity (RF) and relative clutch mass (RCM) following Iverson (1987) and Seigel & Fitch (1984), respectively. We classified female reproductive condition as previtellogenic (only translucent tiny follicles), vitellogenic (yellowish yolky follicles), ovigerous (with oviductal eggs), or vitellogenic and ovigerous (with vitellogenic follicles and oviductal eggs simultaneously). We employed histological cuts to evaluate and validate the macroscopic state of the follicles, which allowed us to allocate an unbiased reproductive state for both males and females. Finally, we used the presence or absence of sperm in the oviducts and infundibulum as a surrogate estimator of mating season.

Statistical analysis

We assessed differences in the sex ratio among mature males and females each month using the *G*-test and Chi-square (χ^2) test. We compared size at sexual maturity between males and females using *t*-test and assessed the assumptions of normality and homoscedasticity based on Kolmogorov-Smirnov and Levene tests, respectively (Guisande-Gonzáles et al., 2014). We evaluated monthly intersexual variations (synchrony) in female and male reproductive stages, as well as time variation (seasonality) using the χ^2 test and *G*-test. Likewise, we employed one-way analysis of variance (ANOVA) to compare the oviduct distal width between female reproductive stages.

Based on multiple regression analyses of 150 collected snakes (females=79, males=71), we explored the main drivers of reproductive output of the *N. atrata* population under study. We first considered the following variables: SVL (Var 1), body mass (Var 2), primary follicle number (Var 3), secondary follicle number (Var 4), fat body area (Var 5), stomach volume (Var 6), height of piles of palm leaves (Var 9), testicular volume (Var 10), SSK width (Var 11), and width of distal end of deferent duct (Var 12). We then measured stomach bolus and fat bodies through digital pictures with ImageJ v1.52 (Schneider et al., 2012). We calculated fat body area (mm^2) as the sum of each small fat body area attached to the digestive and reproductive tract of each individual. We estimated testes and stomach bolus volume employing the ellipsoid formula (equation 1):

$$V = \frac{3}{4}{}''\pi\left(\frac{w}{2}\right)^2\left(\frac{l}{2}\right) \qquad (1)$$

where, V=testes volume estimated or stomach bolus, *w*=width, and *l*=length.

We next used clutch size and sperm count as dependent variables, with all remaining variables considered independent. Both dependent and independent variables were square roottransformed using the Tukey's staircase transformation method described by Erickson & Nosanchuk (1977).

We evaluated assumptions of normality, autocorrelation, and homoscedasticity using the Kolmogorov-Smirnov test, Durbin-Watson test, and Breusch-Pagan test, respectively. We tested multicollinearity between the previously named variables using the variance inflation factor (VIF) with a threshold of 10. To select the "best" regression model based on the variables evaluated, we employed the Akaike Information Criterion (AIC; Akaike, 1973).

We analyzed recruitment variability during ENSO events, employing neonatal abundance as the dependent variable and height of piles of palm leaves (Var 9) and prey abundance observed in microhabitats (snails, slugs, earthworms, leeches; Angarita-Sierra & Lozano-Daza, 2019) as independent variables.

Finally, to estimate the contribution of all independent variables to the regression models, we employed a hierarchical partitioning method (Chevan & Sutherland, 1991). All statistical analyses were performed using Rwizard 3.0 (Guisande-Gonzáles et al., 2014) and the following R packages: StatR (Guisande-Gonzáles et al., 2014), hier. part (Walsh & MacNally, 2015), nortest (Gross, 2015), lmtest (Hothorn et al., 2017), and usdm (Naimi, 2015).

RESULTS

From all batches sampled, we caught a total of 425 specimens of *N. atrata* (males=209, females=216), with an SSD index of 0.16. The sex ratio showed no significant differences between months (χ^2=15.89, *P*=0.145, *n*=425), climate season (χ^2=2.30, *P*=0.1286, *n*=425), or batches sampled (χ^2=0.93, *P*=0.61, *n*=425). In contrast, significant differences in snake abundance were observed between good and bad years (χ^2=176.15, *P*<0.0001, *n*=425; Figure 2). Health condition was recorded as a potential variable affecting reproductive output. However, through the whole sampling period, only 11 specimens (2.6%) suffered poor condition (ticks *n*=1; mycoses *n*=8; injury=2). Therefore, these variables were excluded from analyses and we considered the *N. atrata* population under study to be healthy.

Female reproductive cycle and activity

According to the macroscopic reproductive traits observed in 79 *N. atrata* females, the smallest female with vitellogenic follicles, indicating sexual maturity, was 270 mm SVL. All females larger than 270 mm SVL (48%) were in some stage of reproduction (Table 1). Females were asynchronous in reproductive stage between months or climate years (χ^2 months=27.374, *P*=0.44; χ^2 climate years=3.05, *P*=0.38). All reproductive stages were observed throughout the year. Oviduct width exhibited significant differences among female reproductive stages (ANOVA *F*=13.7, *P*<0.000 1), with the oviduct being less wide in previtellogenic females than the

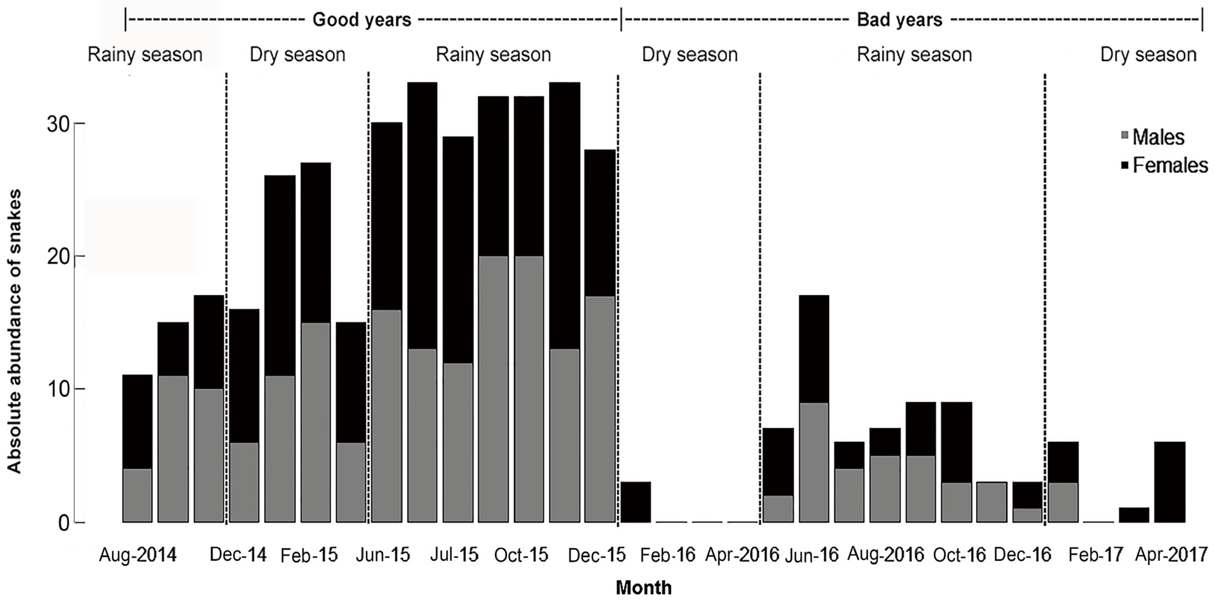

Figure 2 Abundance and population sex ratio of *Ninia atrata* through sampling period (2014−2017)

Table 1 Mean values of female reproductive features

Female reproductive stage	SVL (mm)	Mass (g)	Oviduct length (mm)	Sperm in oviduct	Uterine scar	No. primary follicles	No. secondary follicles	No. eggs
Previtellogenic	205.05 (120−246) *n*=38	4.94 (1.08−9.42) *n*=34	4.00 (0.91−9.75) *n*=38	Present (40%) Absent (60%) *n*=43	Present (15%) Absent (85%) *n*=38	5.71 (1−10) *n*=38	Absent	Absent
Vitellogenic	313.57 (270−353) *n*=14	12.01 (8.33−17.09) *n*=14	9.19 (2.59−16.85) *n*=14	Present (87.5%) Absent (12.5%) *n*=16	Present (20%) Absent (80%) *n*=10	7.21 (3−10) *n*=14	2.36 (1−5) *n*=10	Absent
Ovigerous	335.08 (278−370) *n*=12	15.88 (13.33−19.8) *n*=11	9.06 (4.10−13.49) *n*=12	Present (83.3%) Absent (16.7%) *n*=12	Present (100%) *n*=12	8.66 (5−13) *n*=12	Absent	3.25 (2−4) *n*=12
Vitellogenic and ovigerous	315.68 (320−370) *n*=5	15.02 (12.35−19.1) *n*=5	10.13 (5.19−14.4) *n*=5	Present (100%) *n*=7	Present (100%) *n*=5	10 (7−14) *n*=5	1.8 (1−3) *n*=5	2.8 (2−4) *n*=5

remaining reproductive stages. However, differences in oviduct width among females at ovigerous, vitellogenic, and vitellogenic-ovigerous stages were not significant (ANOVA F= 0.14, P=0.86). Thus, an oviduct width larger than 6.14±3.85 mm indicated sexual maturity. Nonetheless, a high degree of oviduct width overlap was observed among female reproductive stages, suggesting that this macroscopic character is not an accurate predictor of sexual maturity (Figure 3).

In the 79 adult females examined, primary follicles were present throughout the year. However, in mid-June, most follicles began to enlarge, reaching a maximum in November to January until the beginning of the dry season (Figure 4A). Likewise, the greatest abundance of primary follicles was observed in January to March and September to November. Consequently, secondary follicles were only observed from April to November (rainy season), with abundance and size increasing gradually, reaching the greatest size in the October to November period (Figure 4B).

We observed mating signals at all female reproductive stages. However, the number of immature females exhibiting mating signals was significantly lower than that of mature females (χ^2=20.14, P<0.001, n=79). As expected, the frequency of uterine scars was significantly higher in females at ovigerous and vitellogenic stages (χ^2=44.32, P<0.001, n=79). Notwithstanding, uterine scars also were observed in six previtellogenic females, four of which had sperm inside the infundibulum and two of which had sperm inside the oviduct. Mature females had sperm inside their infundibulum or oviduct almost the entire year (except December), indicating that copulation is continuous even for females not ready to mate. We observed eggs throughout the year, though the greatest

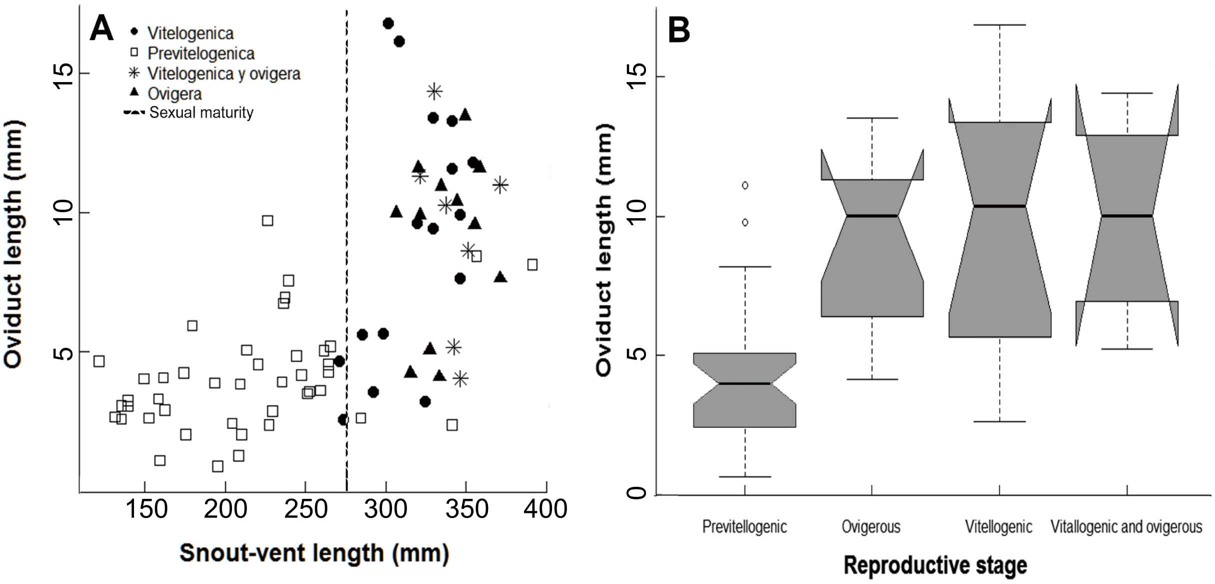

Figure 3 Variation in oviduct width

A: Scatterplot depicting relationship between snout-vent length (SVL) and distended degree of oviduct (mm). B: ANOVA showing oviduct length differences between female reproductive stages

abundance was recorded in September to December (Figure 4C). Based on the incubation of three clutches oviposited by three gravid females, the estimated birth-time was 108±1.41 d/egg. Clutch size ranged from 1–4 eggs (2.44±1.02, *n*=34). We recaptured two female snakes who produced eggs twice in the same reproductive season (first capture in July and recapture in November). Also, during the dissection of snakes collected in August to November from batches 8 and 9, we recorded five females with vitellogenic follicles and oviductal eggs simultaneously, indicating that females could produce more than one clutch per reproductive season.

Neonates were also observed throughout most of the year (except July), with three abundance peaks during the recruitment season. The greatest recruitment peak occurred during the early dry season (January–February). A second moderate recruitment peak was observed in September, and a third pronounced recruitment peak occurred at the end of the rainy season (November). The greatest dearth occurred during the first half of the rainy season (June–July; Figure 4D). Based on the birth of eight neonates, birth-size was estimated to be 114.63±10.69 mm SVL and 1.91±0.74 g of body mass. Likewise, RCM and RF were highly variable and ranged from 4.32% to 8.54% (7.21±1.14%, *n*=16) and 2.72% to 12.74% (7.28±3.01%, *n*=34), respectively.

We observed a remarkable decrease in neonates between good and bad climate years. Based on the presence or absence of the ENSO, the number of neonates declined significantly, from 57 in good years to four in bad years (10.557, *P*=0.001, *n*=61). Despite this, we observed a clear synchronization between recruitment peaks and prey abundance in years without ENSO effects. Increased snail and slug abundance coincided with increased neonate abundance over the same time period (Figure 5). This relationship was confirmed by multiple regression analysis, with neonate abundance being strongly correlated with slug and snail abundance, but not with other prey (R^2=0.46, *P*= 0.032; Figure 6). Nonetheless, when the height of piles of palm leaves was included in the analysis, it provided a better model, explaining 55.29% (*P*=0.011) of the neonate abundance variability observed (Table 2).

Male reproductive activity

Ninia atrata males exhibited early sexual activity. The smallest male with sperm in their testes, indicating sexual maturity, was 145 mm SVL, and the largest male without sperm was 212 mm SVL. These males represent the extreme body-size limits of sexual maturity. However, 98.60% (*n*=71) of males larger than 187 mm SVL had sperm in their testes and deferent duct. The smallest male with metamorphosing spermatocytes was 137 mm SVL.

Based on macroscopic examination of the male gonads, testes showed noticeable size variation throughout the year. Testicular size gradually changed, decreasing from February to August and increasing from August to November. Maximum volume was attained in April (beginning of rainy season) and October-November (end of rainy season) and was 136.4% greater than the minimum testicular volume observed in August (mid rainy season; Figure 7A). Despite a lack of mature male samples in December, January, and March, our data suggests that testicular volume declines at the beginning of the dry season but increases mid-way through.

Likewise, macroscopic sexual features such as SSK and distal end of deferent duct exhibited a similar monthly

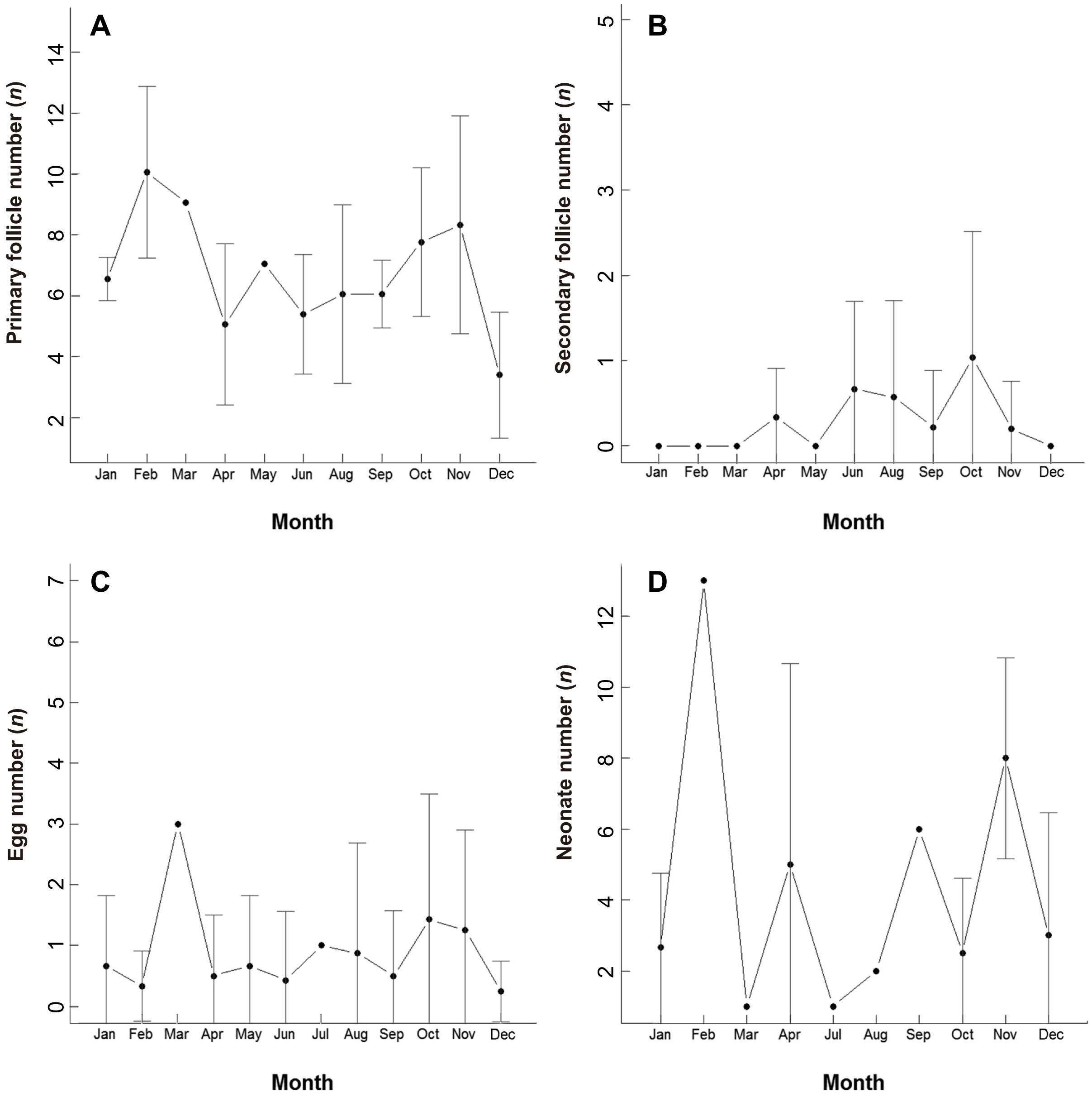

Figure 4 Monthly variability of female reproductive traits and neonates

Black dots represent means, black bars represent standard deviation. A: Absolute values of primary follicles. B: Absolute values of secondary follicles. C: Absolute values of eggs found during sampling period and in dissected reproductive tracts. D: Absolute values of neonates during sampling period

variability pattern as observed for testicular volume (Figure 7C–D). Indeed, monthly variability of these traits was closely related to testis size (R_{SSK}^2 =0.68, P<0.000 1, n=71; $R_{\text{deferent duct}}^2$= 0.45, P<0.000 1, n=71). In contrast, sperm production was not correlated with monthly variability in macroscopic male sexual features (R_{SSK}^2 =0.031, P=0.15, n=69; $R_{\text{Testis volume}}^2$=0.028, P=0.18, n=71; $R_{\text{deferent duct}}^2$=0.033, P=0.14, n=71), indicating that testicular volume, SSK hypertrophy, and deferent duct width are not concordant with spermatogenic activity. Sperm production was present for most of the year, including the dry and rainy seasons. Specifically, production increased gradually from April to November and reached a maximum in July–August (mid rainy season) without significant decline once production began (Figure 7B).

Conversely, significant differences in the size of males with either weak or prominent chin tubercles were found (ANOVA F=37.28, P<0.000 1, n=71). The weak condition was generally associated with males within the SVL range of 135–241 mm (168.16±2.02, n=12), although two larger males (SVL=276

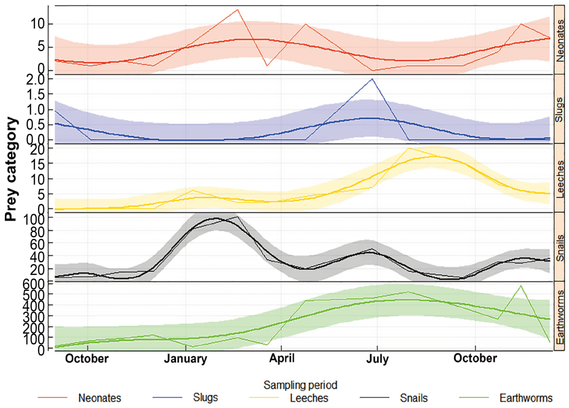

Figure 5 Temporal prey abundance variation and neonates of *Ninia atrata* during years without ENSO effects (2014−2015)

Scale of Y-axis represents abundance values. Shaded area represents 95% confidence intervals. Zigzag lines represent abundance values at each sampling period

and 280) exhibited this condition even though they had reached the minimum size of sexual maturity. In contrast, the prominent condition was generally associated with males within the SVL range of 183–354 mm, in accordance with the results that 98.60% (*n*=71) of males of this size have sperm in their testes and deferent duct. Despite this, three smaller-sized males (SVL=146, 154, and 175) also had prominent chin tubercles. In fact, the SVL ranges of chin tubercle condition showed a high degree of overlap (46.53%), indicating that this secondary sexual character may not be an accurate predictor of male reproductive stage.

Reproductive cycles and mating

We found notable differences in the reproductive cycles between the sexes. First, males showed a continuous cyclical pattern, in which spermatogenesis, gonads, and SSK were active throughout the year. Although they did show reduced activity during the dry and mid rainy seasons, they never displayed total regression or quiescence. In contrast, females showed a cyclical pattern in which oogenesis, gonads, and accessory organs become inactive or absent during the dry season. Second, size at sexual maturity was significantly different between the sexes (*t*=9.54, *P*<0.000 1, *n*=150), with males and females attaining sexual maturity at 56% and 86% of mean adult SVL, respectively. Finally, higher sperm and vitellogenic follicle production were not synchronized. While maximum sperm abundance occurred from July to August (mid rainy season), maximum vitellogenic follicle abundance occurred from October to November (end of rainy season).

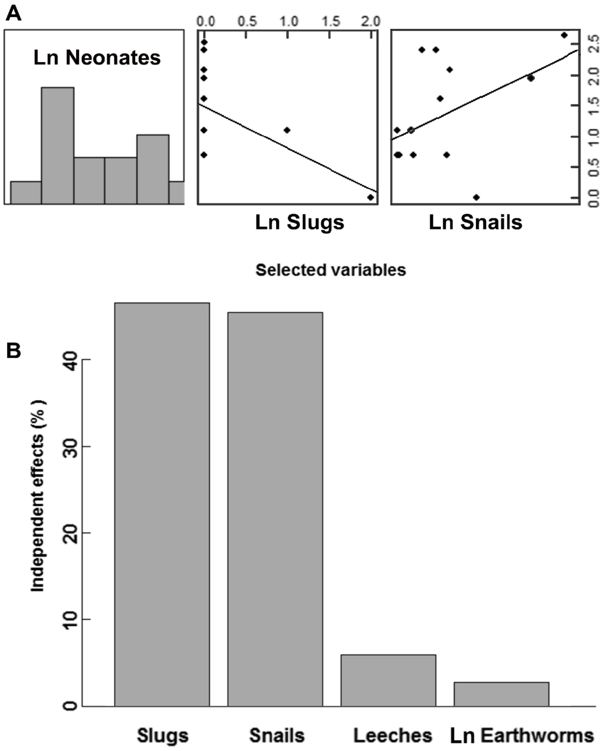

Figure 6 Multiple regression models related to neonate and prey abundances

Plots depicting linear regressions between neonate abundance (A) and prey abundance (B) Relative contributions of variables. Ln Neonates: Logarithm-transformed neonate abundance. Ln Earthworms: Logarithm-transformed earthworm abundance Ln Snails: Logarithm-transformed snail abundance. Ln Slugs: Logarithm-transformed slug abundance

Despite the divergence in reproductive cycles between sexes, sperm production and follicle maturation patterns indicated that the reproductive cycle was seasonal at the population level. Both sexes presented a synchronized increase in reproductive output through the rainy season, with highest abundance from June to November. Even though no mating behaviors were observed among individuals of *N. atrata*, the high frequencies of oviductal sperm, as well as sperm production and follicle maturation, suggest two main mating pulses, one at the beginning of the rainy season (April) and one at the end of the rainy season (October–November). However, mating signals were present all year, including the dry season (Figure 8).

The seasonal reproductive cycle of *N. atrata* was closely correlated with the strong climate seasonality of the study area, as well as prey and hatchling abundance. For instance, the greatest recruitment peak occurred in the mid dry season, which coincided with the increase in snail abundance and greatest production of primary follicles, whereas the greatest recruitment dearth was observed in the mid rainy season, which coincided with the decline in snail abundance and maximum sperm production (Figures 7–8).

Main drivers of reproductive output in *Ninia atrata*

The main drivers of reproductive output in *N. atrata* diverged between the sexes. In females, multiple regression analysis indicated that clutch size was strongly correlated with almost all reproductive traits evaluated (Table 2). However, among

Table 2 Multiple regression analysis models

Model	R^2	AIC	dAIC	*df*	Nor. test *P* value	Hom. test *P* value	Aut. test *P* value
Clutch size versus female reproductive drivers							
Clutch size vs. Var2+Var3+Var4	0.70	–90.62	0.0	1	0.07	0.35	0.63
Clutch size vs. Var2+Var3+Var4+Var5+Var6		–89.16	–1.46	1			
Clutch size vs. Var1+Var2+Var3+Var4+Var5+Var6		–87.28	–2.98	1			
Clutch size vs. Var1+Var2+Var3+Var4+Var5+Var6+Var9		–85.35	–5.39	1			
Secondary follicles versus female reproductive drivers							
Secondary follicles vs. Var2+Var5+Var6	0.42	11.18	0.0	1	0.17	0.36	0.87
Secondary follicles vs. Var2+Var5+Var6+Var9		11.69	0.51	1			
Secondary follicles vs. Var2+Var3+Var5+Var6+Var9		13.24	2.06	1			
Secondary follicles vs. Var1+Var2+Var3+Var5+Var6		15.21	4.03	1			
Sperm count versus male reproductive traits and environmental variables							
Sperm count vs. Var2+Var6+Var9	0.198	–166.21	0.0	1	0.07	0.34	0.2
Sperm count vs. Var1+Var2+Var6+Var9		–165.20	–1.01	1			
Sperm count vs. Var1+Var2+Var6+Var9+Var10		–163.32	–2.89	1			
Sperm count vs. Var1+Var2+Var6+Var9+Var10+Var11		–161.38	–4.83	1			
Neonates versus prey abundances							
Neonates vs. Slugs+Snails	0.46	–9.06	0.0	1	0.34	0.50	0.46
Neonates vs. Slugs+Snails+Leeches		–7.60	1.46	1			
Neonates vs. Slugs+Snails+Leeches+Earthworms		–6.41	2.65	1			
Neonates versus prey abundances and height of piles of palm leaves							
Neonates vs. Var9+Snails	0.55	–11.59	0.0	1	0.83	0.43	0.92
Neonates vs. Var9+Snails+ Slugs		–11.49	–0.10	1			
Neonates vs. Var9+Snails+ Slugs+Leeches		–10.55	–1.04	1			
Neonates vs. Var9+Snails+ Slugs+Leeches+Earthworms		–8.65	–2.94				

AIC: Akaike information criterion, employed to select“best model”, was used to test whether environmental factors rather than intrinsic reproductive traits are main drivers of reproductive output. Var1: Snout-vent length, Var2: Body mass, Var3: Primary follicles number, Var4: Secondary follicles number, Var5: Fat body area, and Var6: Stomach bolus volume, Var9: Height of piles of palm leaves, Var10: Testicular volume, Var11: Width of sexual segment of kidney, and Var12: Distal width of deferent duct. R^2: Proportion of variance for reproductive output explained by microenvironment or reproductive intrinsic trait variables. Nor. test: Kolmogorov-Smirnov test for normality; Hom. test: Breusch -Pagan test for homoscedasticity; Aut. test: Durbin-Watson test for autocorrelation.

these variables, the "best model" was comprised of the number of primary and secondary follicles and body mass, which explained 70.63% (P<0.000 1) of clutch size variability. Given the importance of secondary follicles in clutch size, a second multiple regression analysis was carried out exploring the relationships among secondary follicles, maternal traits, and height of piles of palm leaves (Figure 9). As a result, secondary follicle variability was highly correlated with stomach bolus volume, fat body area, and body mass. These variables composed the "best model" and explained 44% (P= 0.003) of secondary follicle variability. Similarly, female SVL, but not the remaining variables, was significantly related to egg mass (F=7.64, P=0.014, n=17), indicating that larger females produced heavier eggs.

In males, body mass, height of piles of palm leaves, and stomach volume, rather than intrinsic reproductive traits, showed the greatest contribution to sperm production (R^2= 0.198, P<0.001; Table 2). This result agrees with the discordance observed between sperm production and monthly variation in testicular volume and size of SSK (Figure 10).

DISCUSSION

In general, the reproductive ecology of *N. atrata* followed typical patterns reported in tropical snakes. First, early male maturation at a smaller size than females agrees with the common pattern among oviparous, small or median sized dipsadid species (Dos Santos-Acosta et al., 2006; Parker & Plummer, 1987; Pizzatto et al., 2008). Indeed, Goldberg (2004a) reported a similar maturation size for *N. maculata* (Peters, 1861) in which the smallest spermiogenic male was 179 mm SVL and the smallest vitellogenic female was 190 mm SVL.

Second, the reproductive cycles of both males and females were asynchronous, whereas the reproductive cycle at the population level was seasonal semi-synchronous, which agrees with the patterns observed in several tropical snakes with diverse phylogenetic histories, such as *Atractus marthae*

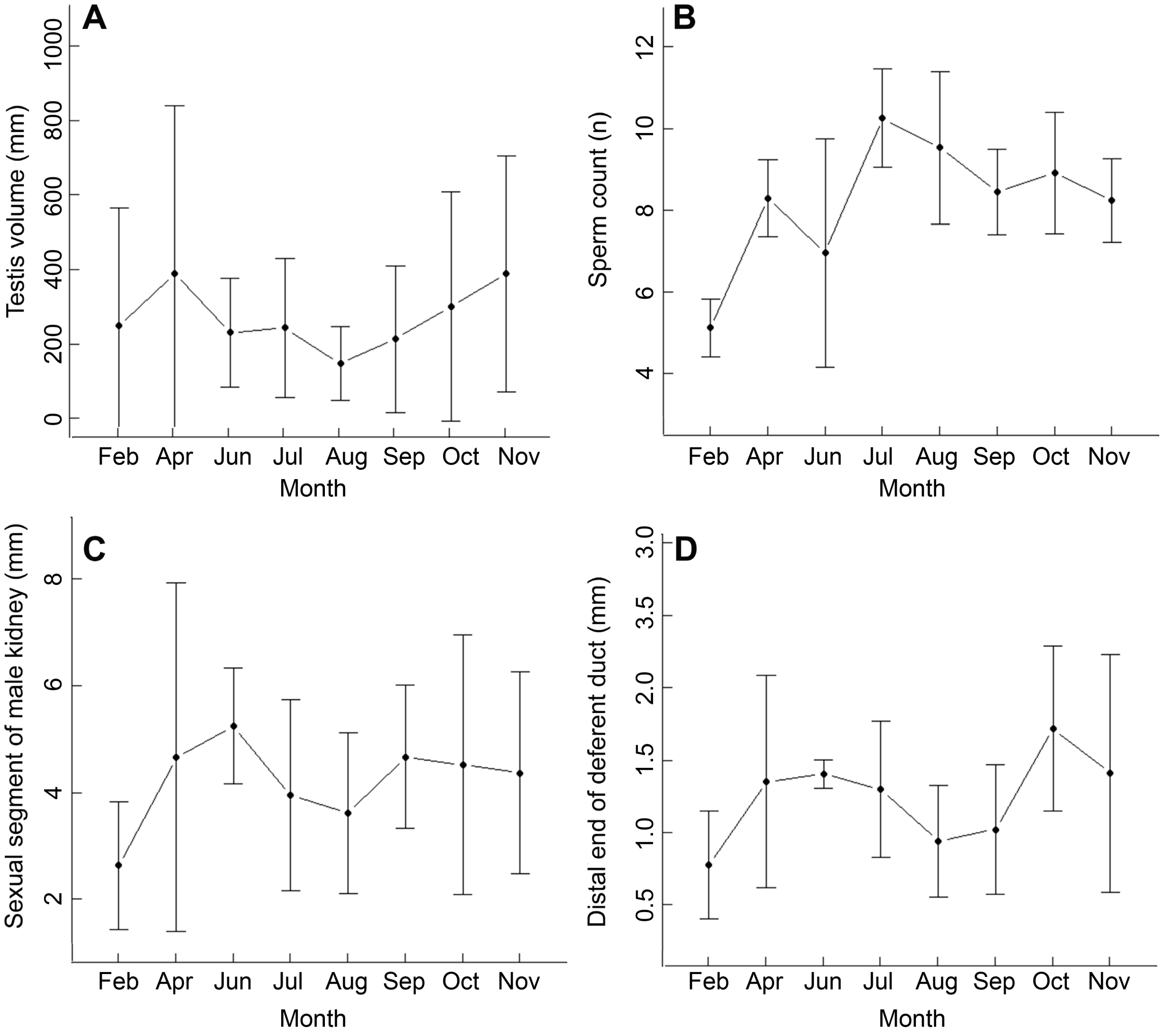

Figure 7 Monthly variability of male reproductive traits

Black dots represent means, black bars represent standard deviation. A: Absolute values of testis volume. B: Average values of sperm count per individual. C: Width of sexual segment of male kidney. D: Width of distal end of deferent duct

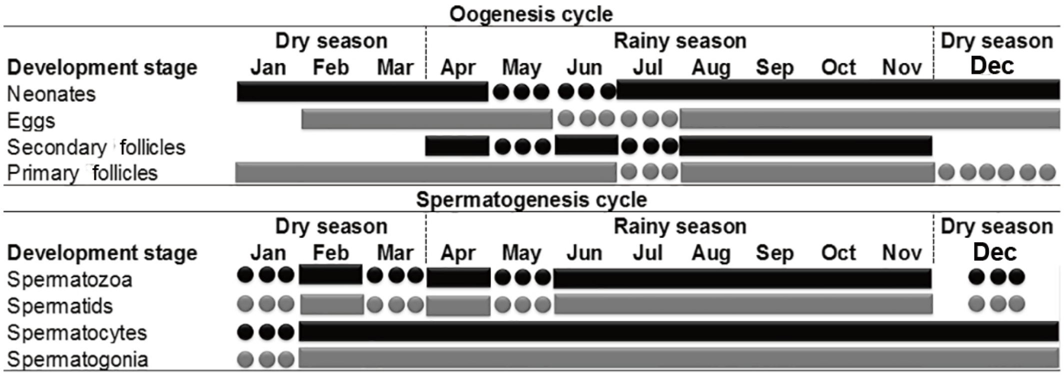

Figure 8 Oogenesis and spermatogenesis cycles in *Ninia atrata*

Females: 79, Males: 71. Boxes: Observed, dotted line: Inferred

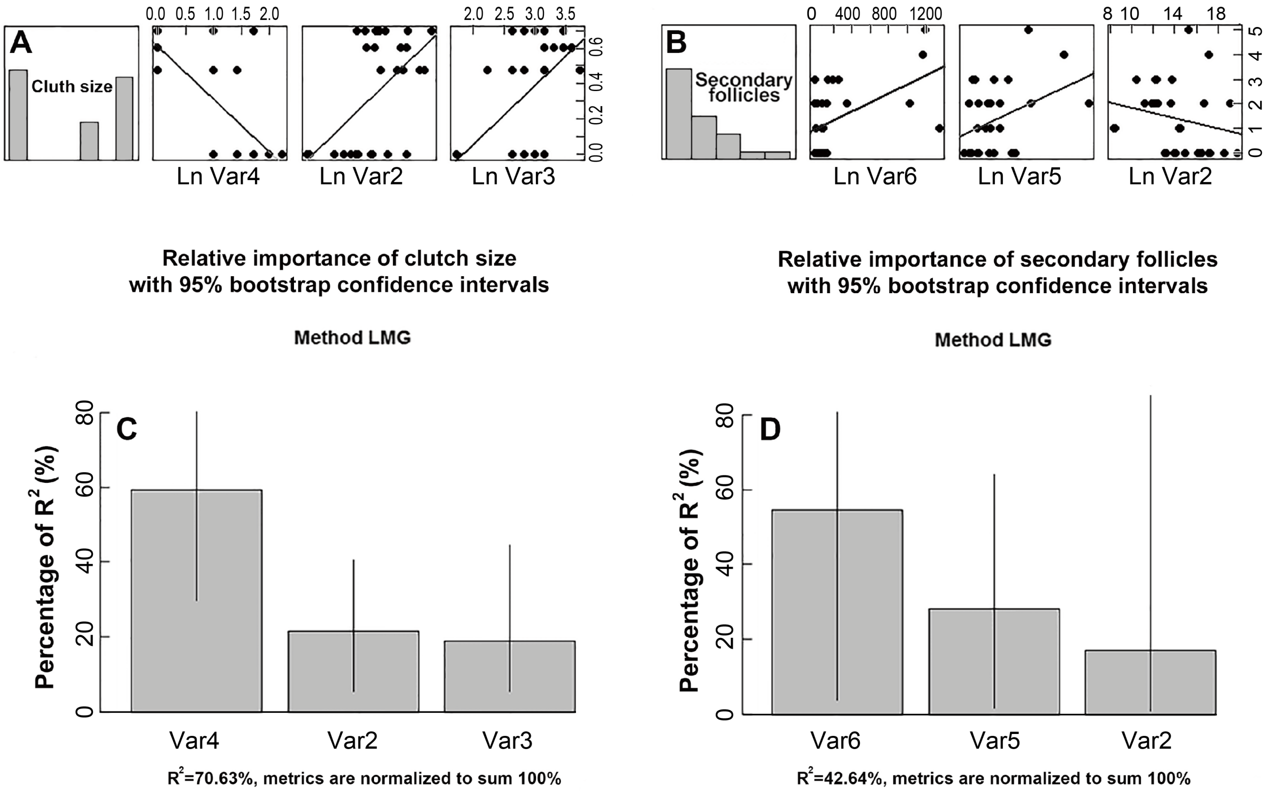

Figure 9 Multiple regression models related to clutch size and secondary follicles with environmental variables and intrinsic reproductive traits

A, B: Plots depicting linear regressions between clutch size and secondary follicles with variables, respectively. C, D: Relative contributions of variables composing“best regression model”for clutch size and secondary follicles, respectively. Var2: Body mass; Var3: Primary follicles number; Var4: Secondary follicles number; Var5: Fat body area; Var6: Stomach bolus volume

(Meneses-Pelayo & Passos, 2019), *Sibynomorphus* spp., (Schlegel, 1837), *Atractus reticulatus* (Boulenger, 1885), *Drymobius margaritiferus* (Schlegel, 1837), *Dipsas albifrons* (Sauvage, 1884), *Mastigodryas melanolomus* (Cope, 1868), *Micrurus lemniscatus* (Linnaeus, 1758), and others (Goldberg, 2006; Marques et al., 2013; Pizzatto et al., 2008).

Third, the presence of several vitellogenic-ovigerous females during the reproductive season, constant recruitment of neonates year-round, frequent mating evidence all year independent of season, and presence of previtellogenic females with sperm in their oviduct or infundibulum agrees with the patterns reported for numerous tropical snakes, such as *Erythrolamprus aesculapii* (Linnaeus, 1758), *Erithrolamprus bizona* (Jan, 1863), *Mastigodryas bifossatus* (Raddi, 1820), *Tropidonophis mairii* (Grey, 1841), and others, in which multiple clutches, high mating frequency, and continuous sperm production characterize their reproductive phenology (Brown & Shine, 2006a; Goldberg, 2004b, 2006 Marques, 1996). This suggests that immature females are willing or are forced by males to mate.

In contrast, the body size-fecundity relationship observed in *N. atrata* moves away from the expected correlation between SVL and reproductive output in tropical snakes (Miranda et al., 2017; Shine & Madsen, 1997). In *N. atrata*, SVL was shown to be a poor morphological predictor of fecundity. In particular, SVL was only significantly correlated with egg mass, presumably reflecting physical constraints on clutch volume (Shine, 1991). In contrast, body mass was shown to be a better morphological predictor for both sexes, as this trait was persistently selected in all regression models assessed. Male body mass had the strongest contribution (>50%) to sperm production. Similarly, female body mass in all regression models evaluated explained 20% of the reproductive output and occupied the second or third place of importance, after traits such as secondary follicle number, stomach bolus volume, or fat body area. Nonetheless, sperm production was poorly explained by the variables assessed (R^2=19.88%). Thus, future studies should clarify which microenvironment variables or intrinsic reproductive traits can determine the reproductive output observed in *N. atrata* males.

Food intake and prey abundance were crucial variables contributing to reproductive output in *N. atrata*. The high association of vitellogenic or ovigerous females with stomach content, as well as the great importance of stomach bolus volume as an explanatory variable of secondary follicle variability and sperm production, rather than fat bodies or

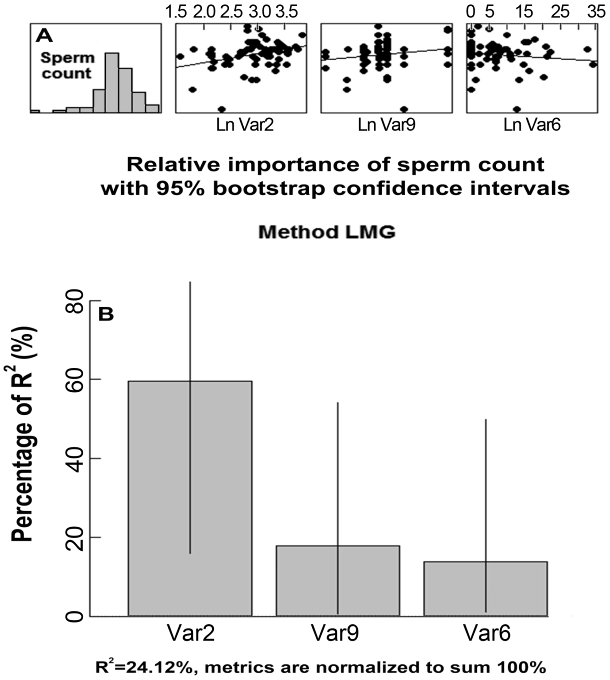

Figure 10 Multiple regression models related to sperm production with environmental variables and intrinsic reproductive traits

A: Plots depicting linear regression models between sperm count with variables. B: Relative contributions of variables composing "best regression model"for sperm count. Var2: Body mass; Var6: Stomach bolus volume; Var9: Height of piles of palm leaves

SVL, indicated a strong link between *N. atrata* reproductive output and food intake. In addition, the strong link observed between recruitment peaks and prey abundance is in agreement with the results of Shine (2003), who argued that even in the tropics, seasonal reproductive cycles would be favored because they reflect the variability of operative environmental factors, as well as the temporal shifts in reproductive trade-offs.

Similarly, the remarkable decrease in neonates and significant differences in snake abundance during ENSO events emphasized the high sensitivity of *N. atrata* to extreme climate changes. The variabilities of operative environmental factors such as height of palm leaf piles and prey availability (mainly snail abundance) were demonstrated to be the main drivers of *N. atrata* abundance variability (Angarita-Sierra & Lozano-Daza, 2019).

The above evidence suggests that *N. atrata* populations follow an income breeding strategy (Jönsson, 1997) in order to compensate for the demands of reproduction and to maximize fitness. This result agrees with the observed feeding patterns, i.e., largest females had significantly higher stomach bolus volumes than the largest males, intersexual dietary divergence, and notable disparity in food intake between the sexes (Angarita-Sierra & Lozano-Daza, 2019). Moreover, unlike tropical snakes that exhibit a seasonal shift in their reproductive strategies (from capital breeding to income breeding or vice versa, e. g., *Tropidonophis mairii* (Brown & Shine, 2006a)), *N. atrata* maintained the same reproductive strategy, despite the extreme climatic variability due to ENSO.

Income breeders are rare among ectotherms because of the high energetic costs associated with the muscle and organ maintenance needed to sustain their highly active mode of feeding (Bonnet et al., 1998). However, the *N. atrata* population in the oil palm plantation had a huge amount of prey available year-round, allowing them to reduce their energetic costs of acquisition without exceeding the energetic costs that would have to be expended in reproduction or other activities (Angarita-Sierra & Lozano-Daza, 2019). Hence, the income breeding strategy observed in this population could be strongly influenced by habitat. However, more empirical data are needed to elucidate whether reproductive strategy switches with habitat type or is a conservative life-history trait of the species.

Finally, macroscopic reproductive traits were shown to be an inaccurate proxy for reproductive activity in both sexes. In particular, testicular volume and SSK were not associated with sperm production. Likewise, oviduct distal width and presence of chin tubercles exhibited wide variance, which made it difficult for accurate maturity size determination. The accuracy of macroscopic reproductive traits as a proxy for reproductive cycle evaluation has been questioned previously (Braz et al., 2014; Mathies, 2011). In fact, it has been observed that histological analysis invalidates macroscopically determined maturity in fish, lizards, and fossorial snakes (Boretto & Ibargüengoytía, 2006; Braz et al., 2014; Fernández et al., 2017; Vitale et al., 2006). Nonetheless, this topic has been poorly explored in snake reproductive studies due to the historical and widespread use of macroscopic reproductive traits in comparisons between different studies (Pizzatto & Marques, 2006, 2007). Therefore, for future comparison between *N. atrata* populations or related taxa, we recommend employing histological assessment to avoid spurious results that could distort the relationships among reproductive cycles, environmental factors, and reproductive trade-offs.

SCIENTIFIC FIELD SURVEY PERMISSION INFORMATION

Permission for field surveys in the municipality of San Martin, Department of Meta, Colombia was granted by the National Environmental Licensing Authority (ANLA). Project approval (No. 27212 under resolution No. 0255 of 14 March 2014) was issued by the National Environmental Licensing Authority (ANLA).

COMPETING INTERESTS

The authors declare that they have no competing interests.

AUTHORS' CONTRIBUTIONS

T. A. S designed the study, collected data, conducted experiments in the field, analyzed data, and wrote the manuscript. C. A. L. H. collected data, conducted experiments in the field, and processed the data. T.A.S and C.A.

L. H. discussed and revised the manuscript. All authors read and approved the final version of the manuscript.

ACKNOWLEDGEMENTS

We thank all students, friends, relatives, and volunteers for their help and support during fieldwork. We give special thanks to Luisa F. Montaño-Londoño for her love and support during this study; Jhon Infante-Betacour, a member of the Yoluka Ong, for general support and help with maps; Fabio I. Daza, John Murphy, and David A. Sanchez for manuscript review; Maria Argenis Bonilla-Gómez and John D. Lynch for support, advice, and allowing us to use the equipment under their care; Xavier Marquínez Casas and Adriana Jerez for allowing us to use their histology lab. We especially thank Francisco Javier Ruiz, Instituto Nacional de Salud, for his support and allowing us to use the facilities under his care during reproductive studies. We thank Ivan Leonardo Niño for his support during fieldwork and laboratory procedures. We thank Martha P. Ramirez, Ezequiel González-León, Luis E. Gualdrón, and Maria F. Calvo, Laboratory of Vertebrate and Reproductive Biology, Universidad Industrial de Santander for their support and teachings on reproductive biology. Special thanks to Maria Clara Borda and Mauricio Acuña for support and freedom to seek snakes at Palmasol S. A., and Elizabeth Moreno-Domínguez, coordinator of the Project Management Program of Universidad Nacional de Colombia, for her support. Finally, we thank the anonymous reviewers for their careful reading of our manuscript and their many insightful comments and suggestions.

REFERENCES

Akaike H. 1973. Information theory and an extension of the maximum likelihood principle. *In*: Petrovand BN, Caski F. Proceeding of the Second International Symposium on Information Theory. Budapest: Akademiai Kiado, 1–451.

Alencar LRV, Galdino CAB, Nascimento LB. 2012. Life history aspects of *Oxyrhopus trigeminus* (Serpentes: Dipsadidae) from two sites in Southeastern Brazil. *Journal of Herpetology*, **46**(1): 9−13.

Almeida-Santos SM, Aguiar LF, Balestrin RL. 1998. Serpentes: *Micrurus frontalis* (coral snake). *Male combat. Herpetological Review*, **29**: 242.

Almeida-Santos SM, Pizzato L, Marques OA. 2006. Intra-sex synchrony and inter-sex coordination in the reproductive timing of the Atlantic coral snake *Micrurus corallinus* (Elapidae) in Brazil. *Herpetological Journal*, **16**(4): 371−376.

Almeida-Santos SM, Salomão MG. 2002. Reproduction in neotropical pitvipers, with emphasis on species of the genus *Bothrops*. *In*: Schett G, Höggren M, Douglas ME, Greene HW. Biology of the Vipers. Oklahoma: Eagle Mountain Publishing, 445–514.

Almeida-Santos SM, Salomão MG, Peneti EA, Sena PS, Guimarães ES. 1999. Predatory combat a tail wrestling in hierarchical contests of the Neotropical rattlesnake *Crotalus durissus terrificus* (Serpentes: Viperidae). *Amphibia-Reptila*, **20**: 88−96.

Angarita-Sierra T. 2009. Variatión Geográphic de *Ninia atrata* en Colombia (Colubridae: Dipsadinae). *Papéis Avulsos de Zoologia*, **49**(2): 277−288.

Angarita-Sierra T. 2014. Hemipenial morphology in the semifossorial snakes of the Genus *Ninia* and a new species from Trinidad, West Indies (Serpentes: Dipsadidae). *South American Journal of Herpetology*, **9**(2): 114−130.

Angarita-Sierra T. 2015. Repertoire of antipredator displays in the semifossorial snake *Ninia atrata* (Hallowell, 1845) (Serpentes: Dipsadidae). *Herpetological Notes*, **8**(2015): 339−344.

Angarita - Sierra T, Lozano - Daza SA. 2019. Life is uncertain, eat dessert first: Feeding ecology and prey-predator interactions of the coffee snake Ninia atrata. *Journal of Natural History*, **53**(23-24): 1401−1420.

Ávila RW, Ferreira VL, Arruda JA. 2006. Natural history of the South American water snake *Helicops leopardinus* (Colubridae: Hydropsini) in the Pantanal, Central Brazil. *Journal of Herpetology*, **40**(2): 274−279.

Ávila RW, Kawashita-Ribeiro RA, Ferreira VL, Strüssmann C. 2010. Natural history of the coral snake *Micrurus pyrrhocryptus* Cope 1862 (Elapidae) from semideciduous forests of western Brazil. *South American Journal of Herpetology*, **5**(2): 97−101.

Balestrin RL, Di-Bernardo M. 2005. Reproductive biology of *Atractus reticulatus* (Boulenger, 1885) (Serpentes, Colubridae) in southern Brazil. *Herpetological Journal*, **15**(3): 195−199.

Bizerra A, Marques OA, Sazima I. 2005. Reproduction and feeding of the colubrid snake *Tomodon dorsatus* from South-eastern Brazil. *AmphibiaReptilia*, **26**(1): 33−38.

Blanchardi FN, Finster EB. 1933. A method of marking living snakes for future recognition, with a discussion of some problems and results. *Ecology*, **14**(4): 334−347.

Bonnet X, Bradshaw D, Shine R. 1998. Capital versus income breeding: an ectothermic perspective. *Oikos*, **83**(2): 333−342.

Boretto JM, Ibargüengoytía NR. 2006. Asynchronous spermatogenesis and biennial female cycle of the viviparous lizard *Phymaturus antofagastensis* (Liolaemidae): reproductive responses to high altitudes and temperate climate of Catamarca, Argentina. *Amphibia-Reptilia*, **27**(1): 25−36.

Boulenger GA. 1885. Second list of reptiles and batrachians from the province Rio Grande do Sul, Brazil sent to the Natural History Museum by Dr. *H. van Ihering. Annals and Magazine of Natural History*, **5**(16): 85−88.

Braz HB, Kasperoviczus KN, Almeida-Santos SM. 2014. Reproductive ecology and diet of the fossorial snake *Phalotris lativittatus* in the Brazilian Cerrado. *Herpetological Journal*, **24**: 49−57.

Bretona M, Chiaraviglio M. 2003. Reproductive biology, mating aggregations, and sexual dimorphism of the Argentine *Boa constrictor* (Boa constrictor occidentalis). *Journal of Herpetology*, **37**(3): 510−516.

Brown GP, Shine R. 2006a. Reproductive ecology of a tropical natricine snake, *Tropidonophis mairii* (Colubridae). *Journal of Zoology*, **258**(1): 63−72.

Brown GP. Shine R. 2006b. Why do most tropical animals reproduce seasonally? Testing hypotheses on an Australian snake. *Ecology*, **87**(1): 133−143.

Chevan A, Sutherland M. 1991. Hierarchical partitioning. *The American Statistician*, **45**: 90−96.

Chiaraviglio M. 2006. The effects of reproductive condition on thermoregulation in the Argentina *Boa constrictor* (Boa constrictor occidentalis) (Boidae). *Herpetological Monographs*, **20**(1): 172−177.

Cope ED. 1868. An examination of the Reptilia and Batrachia obtained by the Orton Expedition to the Equador and the upper Amazon, with notes on other species. *Proceedings of the Academy of Natural Sciences of Philadelphia*, **20**: 96−140.

da Costa-Prudente AL, Costa-Menks A, da Silva FM, Maschio GF. 2014. Diet and reproduction of the Western Indigo Snake *Drymarchon corais* (Serpentes: Colubridae) from the Brazilian Amazon. *Herpetological Notes*, **7**: 99−108.

Dorcas ME, Willson JD. 2009. Innovative methods for studies of snake ecology and conservation. *In*: Mullin SJ, Seigel R. Snakes Ecology and Conservation. New York: Cornell University Press, 45–37.

Dos Santos-Acosta MC, Prudente AL, Di-Bernardo M. 2006. Reproductive biology of *Tantilla melanocephala* (Linnaeus, 1758) (Serpentes, colubridae) from Eastern Amazonia, Brazil. *Journal of Herpetology*, **40**(4): 556−559.

Erickson BH, Nosanchuk TA. 1977. Understanding Data. New York: McGraw-Hill, 1–351.

Fernández JB, Medina M, Kubisch EL, Scolaro JA, Ibargüengoytía NR. 2017. Reproductive strategies in males of the world's southernmost lizards. *Integrative Zoology*, **12**(2): 132−147.

Fitch HS. 1970. Reproductive cycles in lizards and snakes. *Museum of Natural History Miscellaneous Publication*, **52**: 1−247.

Fox W. 1952. Seasonal variation in the male reproductive system of Pacific Coast garter snakes. *Journal of Morphology*, **90**(3): 481−553.

Gaiarsa MP, De Alencar LR, Martins M. 2013. Natural history of Pseudoboine snakes. *Papéis Avulsos de Zoologia*, **53**(19): 261−283.

Gibbons JW, Lovich JE. 1990. Sexual dimorphism in turtles with emphasis on the slider turtle (*Trachemys scripta*). *Herpetological Monographs*, **4**: 1−29.

Goldberg SR. 2004a. Reproduction in the coffee snake, *Ninia maculata* (Serpentes: Colubridae), from Costa Rica. *Texas Journal of Science*, **56**(1): 81−84.

Goldberg SR. 2004b. Notes on reproduction in the false coral snakes, *Erythrolamprus bizona* and *Erythrolamprus mimus* (Serpentes: Colubridae) from Costa Rica. *Texas Journal of Science*, **56**(2): 171−174.

Goldberg SR. 2006. Reproductive cycle of the salmon-bellied racer, *Mastigodryas melanolomus* (Serpentes, Colubridae), from Costa Rica. *Phylomedusa*, **5**(8): 145−148.

Gomes CA, Marques OA. 2012. Food habits, reproductive biology, and seasonal activity of the dipsadid snake, *Echinanthera undulata* (Wied, 1824), from the Atlantic forest in Southeastern Brazil. *South American Journal of Herpetology*, **7**(3): 233−240.

Grey JE. 1841. A catalogue of the species of reptiles and Amphibia hitherto described as inhabiting Australia, with a description of some new species from Western Australia. *Journals of Two Expeditions of Discovery in Northwest London: Cambridge Library Collection History of Oceania*: 422−449.

Gross J. 2015. Test for Normality. An Online Reference. Version 1.4.0 (16 April 2018). Viena: http://CRAN.R-project.org/package=nortest.

Gualdrón-Durán LE, Calvo-Castellanos MF, Ramírez-Pinilla MP. 2019. Annual reproductive activity and morphology of the reproductive system of an Andean population of Atractus (Serpentes, Colubridae). *South American Journal of Herpetology*, **14**(1): 58−70.

Guisande-Gonzáles C, Vaamonde-Liste A, Barreiro-Felpeto A. 2014. RWizard. An Online Reference. Version 4.0 16 April 2018). Vigo: http://www.ipez.es/RWizard/Download.html.

Hallowell E. 1845. Descriptions of reptiles from South America, supposed to be new. *Proceedings of the Academy of Natural Sciences of Philadelphia*, **2**: 241−247.

Hartmann MT, Del Grande ML, Da Costa-Gondim J, Mendes MC, Marques OAV. 2002. Reproduction and activity of the snail-eating snake, Dipsas albifrons (Colubridae), in the Southern Atlantic Forest in Brazil. *Studies on Neotropical Fauna and Environment*, **37**(2): 111−114.

Hartmann MT, Marques OAV, Almeida-Santos SM. 2004. Reproductive biology of the southern Brazilian pitviper *Bothrops neuwiedi pubescens* (Serpentes, Viperidae). *Amphibia-Reptilia*, **25**(1): 77−85.

Hothorn T, Zeileis A, Farebrother RW, Cimmins C, Milo G, Mitchell D. 2017. Testing Linear Regression Models. An Online Referece Version 0.9-35 16 April 2017). Viena: http://CRAN.R-project.org/package=lmtest.

IDEAM (Colombian Institute of Hydrology, Meteorology, and Environmental Studies). 2016. Current weather conditions. An Online Referece (16 Apr. 2017). Bogotá: http://www.ideam.gov.co/web/tiempo-y-clima/prediccion-climatica. (in Spanish)

Ingrasci MJ. 2011. Molecular Systematics of the Coffee Snakes, Genus Ninia (Colubridae: Dipsadinae). Ph. D. Dissertation, University of Texas, Arlington, United States of America.

Iverson JB. 1987. Patterns of relative fecundity in snakes. *Florida Science*, **50**(4): 223−233.

Jan G. 1863. Systematic enumeration of the ophidians belonging to the coronellidae group. *Archive for Zoology Anatomy and Physiology*, **2**(2): 213−330.

Janeiro - Cinquini TRF. 2004. Reproductive capacity of *Bothrops jararaca* (Serpentes, Viperidae). *Iheringia Série Zoologia*, **94**(4): 429−431.

Jönsson KI. 1997. Capital and income breeding as alternative tactics of resource use in reproduction. *Oikos*, **78**(1): 57−66.

Krohmer RW, Martinez D, Mason RT. 2004. Development of the renal sexual segment in immature snakes: effect of sex steroid hormones. *Comparative Biochemistry and Physiology-Part A: Molecular & Integrative Physiology*, **139**(1): 55−64.

Lancini AR. 1979. Snakes of Venezuela. Caracas: Arimitano Editors. (in Spanish)

Leão SM, Pelegrim N, De Campos-Nogueira C, Albuquerque-Brandão R. 2014. Natural history of *Bothrops itapetiningae* Boulenger, 1907 (Serpentes: Viperidae: Crotalinae), an endemic species of the Brazilian Cerrado. *Journal of Herpetology*, **48**(3): 324−331.

Leite PT, Nunes SDF, Kaefer IL, Cechin SZ. 2009. Reproductive biology of the swamp racer *Mastigodryas bifossatus* (Serpentes: Colubridae) in subtropical Brazil. *Zoologia*, **26**(1): 12−18.

Linnaeus C. 1758. Systema naturæ per regna tria naturæ, secundum classes, ordines, genera, species, cum characteribus, differentiis, synonymis, locis. Tomus I. Laurentii Salvii, Holmiæ.

López MS, Giraudo AR. 2008. Ecology of the snake *Philodryas patagoniensis* (Serpentes, Colubridae) from Northeast Argentina. *Journal of Herpetology*, **42**(3): 474−480.

Luna LG. 1968. Manual of histologic staining methods of the armed forces institute of pathology. 3rd edn. New York: McGraw-Hill, 111–112.

Lynch JD. 2015. The role of plantations of the African Palm (Elaeis guiensis JACQ.) in the conservation of snakes in Colombia. *Caldasia*, **37**(1): 169−182.

Marques OAV. 1996. Reproductive biology of the coral snake *Erythrolamprus aesculapii* Linnaeus (Colubridae), in the Southeastern of Brazil. *Revista Brasileira de Zoologia*, **13**(3): 747−753.

Marques OAV, Almeida-Santos SM, Rodrigues M, Camargo R. 2009. Mating and reproductive cycle in the Neotropical colubrid snake *Chironius bicarinatus*. *South American Journal of Herpetology*, **4**(1): 76−80.

Marques OAV, Pizzato L, Almeida-Santos SM. 2013. Reproductive strategies of new world coral snakes, genus Micrurus. *Herpetologica*, **69**(1): 58−66.

Marques OAV, Puorto G. 1998. Feeding, reproduction, and growth in the crowned snake *Tantilla melanocephala* (Colubridae), from southeastern Brazil. *Amphibia-Reptilia*, **19**(3): 311−318.

Mathies T. 2011. Reproductive cycles of tropical snakes. *In*: Aldridge RD, Sever DM. Reproductive Biology and Phylogeny of Snakes. New Hampshire: CRC Press, 511–550.

McCranie JR, Wilson LD. 1995. Two new species of colubrid snakes of the genus *Ninia* from Central America. *Journal of Herpetology*, **29**(2): 224−232.

Medina-Rangel GF. 2015. *Ninia atrata* geographic distribution. *Herpetological Review*, **46**(4): 574−575.

Meneses-Pelayo E, Passos P. 2019. New polychromatic species of Atractus (Serpentes: Dipsadidae) from the eastern portion of the Colombian Andes. *Copeia*, **107**(2): 250−261.

Mesa-Joya FL. 2015. First record of *Ninia atrata* Hallowell, 1845 (Squamata: Colubridae) from Sierra Nevada de Santa Marta, northern Colombia. *Check List*, **11**(112): 1−3.

Miranda EP, Ribeiro RP Jr., Camera BF, Barros M, Draque J, Micucci P, Waller T, Strüssmann C. 2017. Penny and penny laid up will be many: large yellow anacondas do not disregard small prey. *Journal of Zoology*, **301**(4): 301−309.

Monteiro C, Montgomery CE, Spina F, Sawaya RJ, Martins M. 2006. Feeding, reproduction, and morphology of *Bothrops mattogrossensis* (Serpentes, Viperidae, Crotalinae) in the Brazilian Pantanal. *Journal of Herpetology*, **40**(3): 408−413.

Naimi B. 2015. Uncertainty analysis for species distribution models. An Online Reference. Version 1.1 (16 April 2017). Viena: https://cran.r-project.org/web/packages/usdm.

Natera–Mumaw M, Esqueda–Gozález LP, Castelaín–Fernández M. 2015. Snakes Atlas of Venezuela. Santiago de Chile, Dimacofi Negocios Avanzados S.A., 1–441. (in Spanish)

Nogueira C, Sawaya R, Martins M. 2003. Ecology of the pitviper, *Bothrops moojeni*, in the Brazilian Cerrado. *Journal of Herpetology*, **37**(4): 653−659.

Parker WS, Plummer MV. 1987. Population ecology. *In*: Seigel RA, Collins JT, Novak SS. Snakes: Ecology and Evolutionary Biology. New York: MacMillan Publisher Company, 253–301.

Peters WCH. 1861. About new serpents of the king Zoological Museum: *Typhlops striolatus*, *Geophidium dubium*, *Streptophorus* (*Ninia*) *maculatus*, *Elaps hippocrepis*. *Monthly Reports of the Royal Prussian Academy of Sciences in Berlin*, **1861**: 922−925.

Pizzatto L. 2005. Body size, reproductive biology and abundance of the rare pseudoboini snakes genera *Clelia* and *Boiruna* (Serpentes, Colubridae) in Brazil. *Phyllomedusa*, **4**(2): 111−122.

Pizzatto L, Cantor M, De Oliveira JL, Marques OAV, Capovilla V, Martins M. 2008. Reproductive ecology of dipsadine snakes, with emphasis on South American Species. *Herpetologica*, **64**(2): 168−179.

Pizzatto L, Marques OAV. 2002. Reproductive biology of the false coral snake *Oxyrhopus guibei* (Colubridae) from southeastern Brazil. *AmphibiaReptilia*, **23**(4): 495−504.

Pizzatto L, Marques OAV. 2006. Interpopulational variation in sexual dimorphism, reproductive output, and parasitism of *Liophis miliaris* (Colubridae) in the Atlantic forest of Brazil. *Amphibia-Reptilia*, **27**(1): 37−46.

Pizzatto L, Marques OAV. 2007. Reproductive ecology of boine snakes with emphasis on Brazilian species and a comparison to pythons. *South American Journal of Herpetology*, **2**(2): 107−122.

Raddi G. 1820. Of some new species of Brazilian reptiles and plants. *Memories of Mathematics and Physics of the Italian Society of Sciences Based in Modena*, **18**: 313−343.

Ramos-Pallares E, Anaya-Rojas JM, Serrano-Cardozo VH, Ramirez-Pinilla MP. 2015. Feeding and reproductive ecology of *Bachia bicolor* (Squamata: Gymnophthalmidae) in urban ecosystems from Colombia. *Journal of Herpetology*, **49**(1): 108−117.

Rivas JA, Muñoz MC, Burghardt GM, Thorbjarnarson JB. 2007. Sexual size dimorphism and the mating system of the green anaconda (*Eunectes murinus*). *In*: Henderson RW, Powell R. Biology of Boas and Pythons. Oklahoma: Eagle Mountain Publishers, 340–362.

Rivas G, Molina CR, Ugueto GN, Barros TR, Barrio-Amorós CL, Kok PJR. 2012. Reptiles of Venezuela: an updated and commented checklist. *Zootaxa*, **3211**: 1−64.

Roze JA. 1966. Taxonomy and Zoogeography of Ophidians from Venezuela. Caracas: Universidad Central de Venezuela, 1–362. (in Spanish)

Saint Girons H, Pfeffer P. 1972. Notes on the ecology of the snakes of Cambodia. *Zoologische Mededelingen*, **47**: 5−87.

Sauvage HE. 1884. On some reptiles from the Museum of Natural History collection. *Bulletin Société Philom*, **7**(8): 142−146.

Scartozzoni RR, Da Graça-Salomão M, Almeida-Santos SM. 2009. Natural history of the Vine Snake *Oxybelis fulgidus* (Serpentes, Colubridae) from Brazil. *South American Journal of Herpetology*, **4**(1): 81−89.

Schlegel H. 1837. Essay on the Physiognomy of Snake. Descriptive Part. Shonekat M.H, Amsterdam. (in French)

Schneider CA, Rasband WS. Eliceiri KW. 2012. NIH Image to ImageJ: 25 years of image analysis. *Nature Methods*, **9**(7): 671−675.

Seigel RA, Fitch HS. 1984. Ecological patterns of relative clutch mass in snakes. *Oecologia*, **61**(3): 293−301.

Shine R. 1991. Intersexual dietary divergence and the evolution of sexual dimorphism in snakes. *The American Naturalist*, **138**(1): 103−122.

Shine R. 2003. Reproductive strategies in snakes. *Proceedings of the Royal Society B: Biological Sciences*, **270**(1519): 995−1004.

Shine R, Madsen T. 1997. Prey abundance and predator reproduction: Rats and pythons on tropical Australia floddplain. *Ecology*, **78**(4): 1078−1086.

Silva JL, Vadez J. 1989. Rhythm of activity and period of hatching of some ophidians of the North of Venezuela. *Acta Biológica Venezuelica*, **12**(3-4): 88−96.

Valdujo PH, Nogueira C, Martins M. 2002. Ecology of *Bothrops neuwiedi pauloensis* (Serpentes: Viperidae: Crotalinae) in the Brazilian Cerrado. *Journal of Herpetology*, **36**(2): 169−176.

Vitale F, Svedäng H, Cardinale M. 2006. Histological analysis invalidates macroscopically determined maturity ogives of the Kattegat cod (*Gadus morhua*) and suggests new proxies for estimating maturity status of individual fish. *ICES Journal of Marine Science*, **63**(3): 485−492.

Vitt LJ. 1996. Ecological observations on the tropical colubrid snake Leptodeira annulata. *Herpetological Natural History*, **4**(1): 69−76.

Weatherhead PJ, Madsen T. 2006. Linking behavioral ecology to conservation objectives. *In*: Mullin SJ, Seigel R. Snakes Ecology and Conservation. New York: Cornell University Press, 221–243.

Walsh C, Macnally R. 2015. Hierarchical Partitioning. An Online Reference Version 1.0-4 16 April 2017). Viena: http://CRAN.R-project.org/package=hier.part.

Winne CT, Willson JD, Adrews KM, Reed RN. 2006. Efficacy of marking snakes with disposable medical cautery units. *Herpetological Review*, **37**(1): 52−54.

ZOOLOGICAL RESEARCH

Morphological and ecological divergence in two populations of European glass lizard, *Pseudopus apodus* (Squamata: Anguidae)

Olga Jovanović Glavaš[1], Paula Počanić[2], Vanja Lovrić[2], Lorena Derežanin[2], Zoran Tadić[2,*], Duje Lisičić[2,*]

[1] *Department of Biology*, *University of Osijek*, *Osijek* 31000, *Croatia*

[2] *Department of Animal Physiology*, *Faculty of Science*, *University of Zagreb*, *Zagreb* 10000, *Croatia*

ABSTRACT

The European glass lizard, *Pseudopus apodus* (Pallas, 1775), is a large, legless lizard with wide distribution across south-eastern Europe and eastern and central Asia. To date, morphological diversification among populations on a geographically small scale has not yet been reported in this lizard. Thus, we investigated the morphological variations and corresponding differences in habitat utilization between two populations of *P. apodus* inhabiting the same biogeographical zone within a relatively close geographic area. We hypothesized that minor differences in habitat could induce a significant level of morphological differentiation, thus indicating morphological plasticity in this species on a small geographical scale. We sampled 164 individuals (92 from the Croatian mainland and 72 from the island of Cres). Results showed that *P. apodus* indeed exhibited morphological differences between populations in the same biogeographical zone within a relatively close geographic area, with the Cres Island individuals being generally larger than the individuals from the mainland. Some ecological characteristics were similar in both populations (e.g., soil temperature, distance to hiding place), whereas others were distinct (e.g., air temperature and humidity). In addition, vegetation cover differed between the two sites, with more vegetation present on the mainland than on the island. Furthermore, the Cres Island population showed clear sexual dimorphism, which was absent in the mainland population.

Keywords: Mediterranean; Morphology; Sauria; Sexual dimorphism

INTRODUCTION

The European glass lizard or sheltopusik, *Pseudopus apodus*, (Pallas, 1775), is a large legless lizard. With a total length of up to 120 cm (Arnold, 2002) and tail length around 150% of its body length (Obst, 1981), it is the largest lizard in Europe and the only extant species of this genus. It is diurnal, crepuscular, and often active after rain (Arnold, 2002). It lives in Asia Minor and central Asia and throughout southeastern Europe and the Balkans up to the eastern Adriatic coast (Jandzik et al., 2018). The existence of two previously recognized subspecies (Obst, 1978, 1981), i.e., nominal *P. apodus apodus* from the eastern range and *P. a. thracius* from the western range, was recently confirmed by molecular data (Jandzik et al., 2018). However, several issues remain regarding the third, southern clade,

---

Open Access

Received: 20 September 2019; Accepted: 27 February 2020; Online: 28 February 2020

Foundation items: This work was partly supported through grant 119-0000000-1285 of the Ministry of Science of the Republic of Croatia to Z.T.

*Corresponding authors, E-mail: duje.lisicic@biol.pmf.hr

DOI: 10.24272/j.issn.2095-8137.2020.025

which, according to molecular analyses, also deserves a subspecies status (Jandzik et al., 2018). In addition to molecular analysis, morphological variation between the two subspecies is evident; however, in some populations, morphometric data from the original description of the subspecies (Obst, 1978, 1981) have not yet been confirmed (e.g., Jordanian population; Rifai et al., 2005). Furthermore, despite being relatively common in certain areas, there is a paucity of data on its ecology. Sexual dimorphism in this species is not very prominent, as is typical for anguids (Çiçek et al., 2014; Thomas & Hedges, 1998), although recent studies from Kukushkin & Dovgal (2018) found sexual dimorphism in a population from the Steppe Crimea.

Contemporary literature on this species indicates a level of morphological variation within the subspecies *P. a. thracius* (Obst, 1981; Rifai et al., 2005), although only between distant populations inhabiting different biogeographical zones, and accordingly, under the influence of different environmental conditions. In this study, we investigated the morphological differences between two populations of *P. a. thracius* in relative geographic proximity within the same biogeographical zone. One population was from the Croatian mainland and the other was from the island of Cres. We chose an island population to ensure that the level of migration between populations was minimal and that populations were isolated from one another. In addition, it is common for isolated populations to display some divergence, as recorded in other reptile species (e.g., *Testudo graeca*, Carretero et al., 2005; *Podarcis siculus*, Herrel et al., 2008; *Notechis scutatus*, Aubret, 2015).

We expect that slight differences in physical and ecological conditions between the two sites (such as composition of predatory fauna, temperature, and precipitation) may also influence species morphology, given that such conditions are known to influence the morphology of species that exhibit greater phenotypic plasticity (e.g., *Podarcis siculus*; Herrel et al., 2008). We speculate that morphological divergence will be found between the studied populations, thereby indicating morphological plasticity in *P. apodus*, even on a small geographical scale.

We anticipated that body size would differ between the insular and mainland populations, possibly due to Foster's rule (Foster, 1964). On the one hand, lizards tend to grow larger on islands (Owens et al., 2006; Pafilis et al., 2009; Palkovacs, 2003) due to high intraspecific competition or predation relaxation. On the other hand, large-bodied animals may adopt smaller body forms when in insular populations in response to limited natural resources (Lomolino, 2005). As such, the issue of body size on islands remains highly debated (Itescu et al., 2018). Habitat usage of *P. apodus* is very diverse and data obtained so far show that usage highly depends on population geography and habitat type; preferences diverge between dense vegetation in the Caucasian regions (Alekperov, 1978), rocky slopes and shrubs in Crimea (Shcherbak, 1966), rivers and oases in middle Asia (Bogdanov, 1986), to the humid and dense vegetation in Bulgaria (Telenchev et al., 2017). Due to the similarity of our study sites, we expected to find only small differences in habitat usage between the two populations.

MATERIALS AND METHODS

Study sites

We chose sites with similar climatic and vegetation properties, yet separated enough that morphological variability could manifest. We studied two populations located 200 km apart: a Croatian mainland population (Klis, central Dalmatia, Croatia; DMS N43°33′, E16°31′) and an island population (Island of Cres, Croatia; DMS N44°41′, E14°24′) on the eastern Adriatic Coast (Figure 1). Both sites lay within the Eumediterranean biogeographical zone, therefore sharing similar vegetation and climatic characteristics (Horvatić, 1963). An Eumediterranean climate is characterized by hot, dry summers and mild, rainy winters. Vegetation on both sites is comprised of Mediterranean macchia interspersed with pastures or small patches of agricultural land, particularly olive groves.

Cres Island is the largest Croatian island within the Eumediterranean zone of evergreen vegetation, i.e., *Quercion ilicis* alliance (Topić, 2001), with an abundant *P. apodus* population. Due to its size, Cres Island shows variability in vegetation communities similar to that observed on the mainland (Horvatić, 1963). Klis was chosen as a random site within the same zone, where the population of *P. apodus* is large enough for the study (personal observation).

The mainland study site (Klis) is located a few kilometers from the coast on the south-facing slopes at an elevation of 115–235 m a.s.l. The site is divided into two neighboring locations of roughly 200 m×300 m. The island of Cres is 4.2 km from the mainland, measuring 66 km×12 km (405.8 km^2). The Cres study site is situated in the southern part of the island on the southern slopes at an elevation of 30–110 m a.s.l. It consists of three neighboring locations, two of similar size (100 m×200 m) and a third larger one (200 m×300 m).

Although extremely similar in vegetation and climate, the two sites still express differences in faunal composition, especially that of predatory species. In Klis, predators like wolves (*Canis lupus*), foxes (*Vulpes vulpes*), stone marten (*Martes foina*), least weasel (*Mustela nivalis*), and badgers (*Meles meles*) are common, but are mostly absent from Cres, except for the stone marten and least weasel (Sušić & Radek, 2007). Although both martens and weasels typically feed on small mammals (Nowak, 1991), stone martens have been recorded preying on *P. apodus* (Georgiev & Raichev, 2009), though this is considered uncommon. In addition, dissimilarities in mammalian fauna may influence other components of the food chain, thus generating differences between locations. On the other hand, a species known to prey upon *P. apodus*, the short-toed eagle (*Circaetus gallicus*; e.g., Bakaloudis et al., 1998), is present at both sites (Tutiš et al., 2013) and thus should not create different predation pressure between sites.

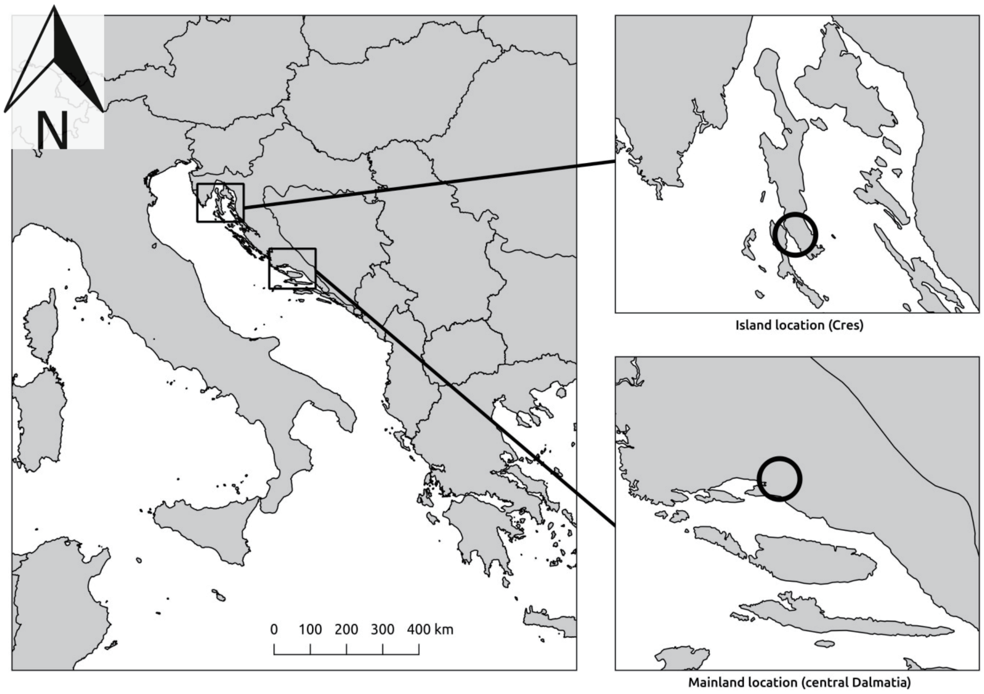

Figure 1 Geographical location of mainland (Klis, Croatia) and island (Cres) populations included in study
Enlarged locations on right are not drawn to scale.

Data collection

A pilot study carried out in 2011 at both sites showed that *P. apodus* is most abundant during spring. Consequently, this study was performed from mid-April to the end of June over a period of two years at both sites (2011, 2014), as well as in 2012 at the mainland (Klis) site. Each site (mainland and island) was checked for the presence of animals over five consecutive days. Surveys were conducted all day, from sunrise to late dusk. For each animal located, the following morphological parameters were recorded using a hand-held meter with a precision of 1 mm, rope, pair of calipers with a precision of 0.01 mm, and 600 g Pesola spring scale with a precision of 5 g: total body length (TL), snout-vent length (SVL), body width near head (BWH–thinnest part of body after head), body width at mid-body (BWM–widest part at mid-body region), body width near cloaca (BWC–body width at cloaca), tail length (TLL), body mass (BM), head length (HL), head width (HW), head height (HH), mouth length (ML), mouth width (MW), interorbital distance (IOD), and internarial distance (IND) (see Figure 2A for head dimension measurements). Based on these data, we calculated the HL/HW ratio, which is often used to differ between subspecies (Obst, 1978). All captured animals were marked to avoid duplicating the results. If the same animal was re-captured, only the environmental data were recorded. In some specimens, the tail was partially missing, and this condition was also recorded. All applicable international, national, and/or institutional guidelines for the care and use of animals were strictly followed. All animal sample collection protocols complied with the current laws of the Republic of Croatia.

We recorded several physical characteristics of the environment at the site of capture: i.e., air temperature, soil temperature, air humidity, air movement, and air pressure, recorded using a Kestrel 4000 Pocket Weather Tracker (precision of 0.1 °C, wind speed 3% of reading, relative humidity (RH) 3%, and barometric pressure 1.5 hPa) and a K-type Thermocouple (Appa Technology Corp., Taiwan, China, precision of 0.1 ℃). In addition, we measured six microhabitat characteristics at each site of individual animal capture: (a) microhabitat type (seven subtypes: (1) open meadow with grass less than 10 cm in height–usually pasture or mowed meadow; (2) open meadow with grass more than 10 cm in height–usually untended meadow; (3) ground, surrounded by bushes; (4) bush; (5) under object–e.g., log, branch, stone; (6) open stonewall–typical stonewall that allows animal to pass through its crevices from one side to the other; and (7) closed stonewall–stonewall bordered on one side with earth or rocks, animal can enter only from one side and hide deep inside crevices); (b) substrate type (five subtypes: (1) dry vegetation; (2) earth with grass; (3) earth with rocks; (4) earth; and (5) stone); (c) nearest hiding place (five subtypes: (1) pile of rocks, under stones or in stonewall; (2) stones covered with bushes; (3) under log, branch, or manmade debris; (4) under dense bush; and (5) dense grass or herbaceous plants); (d) approximate distance of animal to hiding place (measured in cm, from the central point of animal's body); (e) vegetation cover (measured as approximative percentage of predefined subtype in a radius of 5 m around each capture site: (1) total

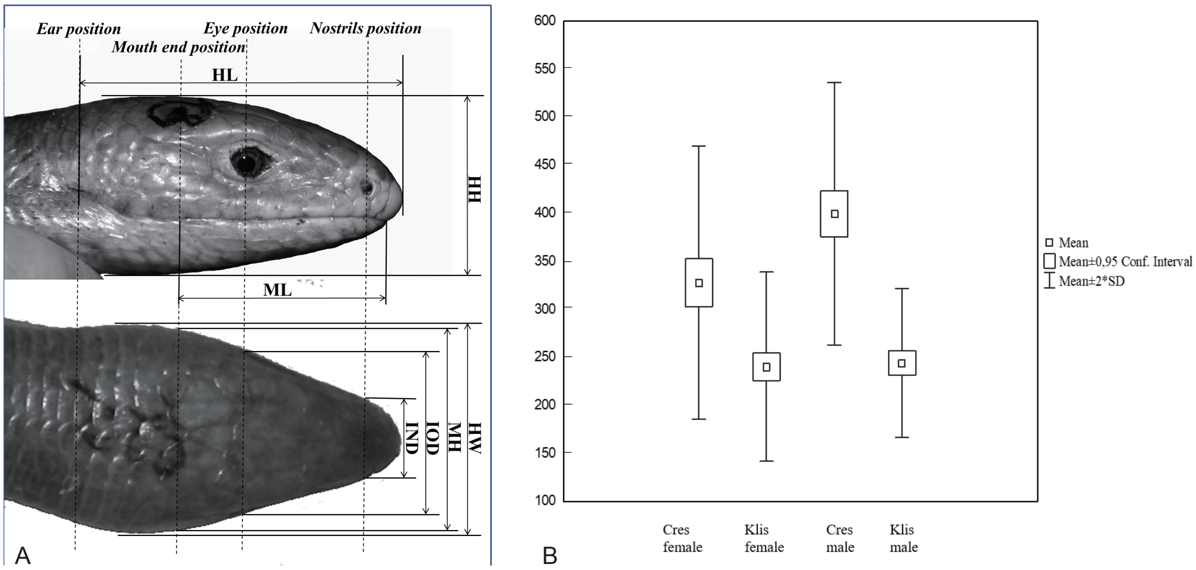

Figure 2 Head dimension measurements of *P. apodus* (A) and scaled mass index (SMI) values for Cres Island and Klis shown separately for each sex (B)

HL: Head length; HW: Head width; HH: Head height; ML: Mouth length; MW: Mouth width; IOD: Interorbital distance; IND: Internarial distance.

cover of vegetation; (2) short vegetation up to 10 cm; (3) herbaceous vegetation up to 50 cm; (4) shrubby vegetation; and (5) tree vegetation); and (f) other habitat characteristics besides vegetation (measured as approximative percentage of predefined subtype in a radius of 5 m around each capture site: (1) stone walls; (2) soil; (3) gravel/small stones; (4) concrete; and (5) rocks and stones). Hiding places were defined as any place where the animal can hide and not to be visible by a predator such as a fox or buzzard, e.g., hole in ground, crevice between rocks, under a log or boulder, or in dense vegetation. After measuring, the animals were released at the site of capture.

Scaled mass index (SMI) and residual analysis

General morphometric measurements (e.g., SVL, total length, head measurements) can be informative of the ecology of the species, and their variation can provide an indication of ecological or evolutionary processes, such as responses to predation or sexual selection pressure (Losos, 1990; Meiri, 2008). In that context, different indices are commonly used to summarize these data, including the SMI.

Body condition was estimated from mass/length data, and the SMI was calculated according to Peig & Green (2009). This index represents an improvement over previously used condition indices as it is based on the central principle of scaling, and includes many methodological, biological, and conceptual advantages (Peig & Green, 2009). Here, the calculation was carried out in three steps. First, to identify the extreme values, we plotted the recorded length (L) and mass (M) data of all individuals. Second, we calculated the scaling exponent b_{SMA} by standardized major axis regression on ln-transformed data using online software (Bohonak & van der Linde, 2004). Third, we calculated the SMI using the formula:

$$\hat{M}i = Mi\left[\frac{L0}{Li}\right]^{bSMA} \qquad (1)$$

where M_i and L_i are the body mass and total length of individual *i*, respectively, and L_0 is the arithmetic mean of L. The SMI was calculated separately for each site and sex.

Statistical analysis

All statistical analyses were carried out using Statistica software (TIBCO Software Inc, 2018). Due to their very low number (four), juveniles were excluded from the analyses. Morphometric data were analysed using multivariate analysis of covariance (MANCOVA), with site and sex as factors and SVL as the covariate. Subsequent univariate analysis of covariance (ANCOVA) was run for each variable separately. Values obtained for SMI were tested with a Kruskal-Wallis test (K-W Test). In addition, tail condition (intact vs. partial; autotomy rate) was analysed using log-linear model analysis to compare groups (sex and site). The HL/HW ratio was tested for normality and then used for *t*-test.

Ecological and physical habitat data (e.g., air temperature, soil temperature, air movement, relative humidity, air pressure, and distance to hiding place) and vegetation cover data were log transformed and then used for two separate factor analyses. Ecological and physical habitat data, as well as vegetation cover data, were checked for correlation. As no variables showed correlation (all values were between –0.7 and 0.7), none seemed to be redundant. Extracted factors for each dataset were analysed using MANOVA to test for site, sex, and interaction between site and sex. Data on the time of day were not included in the analyses as Mann-Whitney *U*-test showed no significant differences regarding when the animals were caught.

RESULTS

During the three years of study, we caught 164 animals in total, including 92 from Klis (49 females, 40 males, and three juveniles) and 72 from Cres Island (34 females, 37 males, and one juvenile). This species exhibited marked differences in coloration between juveniles and adults: juveniles were gray with black patches and spots, and had coarse scales, whereas adults were uniformly brown with smooth and shiny scales. As we did not catch animals intermediate in color/pattern, differentiation between juveniles and adults was considered straightforward.

Morphology

Individuals from Cres were generally larger than individuals from Klis, which was the case for all morphometric traits (Table 1). Morphometric data analysis showed an influence of site (MANCOVA; F=9.20, *P*<0.05) and sex (MANCOVA; F=23.12, *P*<0.05) on almost all examined variables. The only variables not influenced by sex were TLL (ANCOVA; F=0.11, *P*=0.74) and BWM (ANCOVA; F=2.39, *P*=0.12) and not influenced by site were TLL (ANCOVA; F=2.05, *P*=0.16) and IND (ANCOVA; F=2.08, *P*=0.15). Similarly, significant interactions between site and sex (MANCOVA; F=2.18, *P*<0.05) were detected, indicating that males and females differed in morphology depending on the site. Variables not affected by this interaction were HH (ANCOVA; F=3.59, *P*=0.06), ML (ANCOVA; F=2.88, *P*=0.09), IOD (ANCOVA; F=0.10, *P*=0.76), BWM (ANCOVA; F=1.64, *P*=0.20), BWC (ANCOVA; F=3.23, *P*=0.08), and TLL (ANCOVA; F= 0.68, *P*=0.41). All morphometric variables were influenced by SVL as a covariate (MANCOVA; F=25.71, *P*<0.05), except for TLL (ANCOVA; F=0.89, *P*=0.35). We excluded TL from this analysis as it was strongly correlated to TLL and SVL as a covariate. Log-linear model analysis of tail condition against site and sex showed that the interaction between site and tail condition, as well as site and sex, was not significant, but the interaction between tail condition and sex was highly significant (Table 2; *df*=1; *P*=0.001). The HL/HW ratio (Table 3) showed no differences between the sites, but was slightly lower in males than in females, though not significantly (*P*>0.05).

The SMI differed significantly between two populations, with the Cres population having higher values (K-W Test; *P*<0.05), indicating that the animals from Cres were larger than those from Klis. A within-population comparison of Cres individuals showed that males had higher SMI values (K-W Test; *P*<0.05) than females. The individuals from Klis, however, did not show such differences between the sexes (K-W Test; *P*>0.05; Table 4, Figure 2B).

Table 1 Means±*SD*, including range (in parenthesis), and MANCOVA results for morphometric measurements at each site

	Cres		Klis		MANCOVA site×sex	MANCOVA sex	MANCOVA site
	F (*n*=34)	M (*n*=37)	F (*n*=49)	M (*n*=40)			
TL (cm)	89.01±5.36 (79.10–98.00)	91.80±5.95 (78.50–107.40)	84.07±6.95 (55.60–95.7)	82.96±6.78 (64.50–97.60)	–	–	–
SVL (cm)	34.99±2.60 (30.50–40.50)	37.34±2.54 (31.30–41.9)	32.74±2.85 (24.00–39.90)	32.87±2.11 (28.30–36.50)	–	–	–
HL (mm)	40.45±4.40 (25.77–52.30)	48.58±5.73 (36.32–69.62)	37.44±3.67 (26.32–43.37)	41.15±3.47 (34.97–49.83)	*P*<0.05	*P*<0.05	*P*<0.05
HW (mm)	22.40±1.91 (19.65–29.82)	27.23±2.89 (19.50–31.20)	20.27±1.33 (16.39–23.03)	27.23±2.89 (18.59–27.14)	*P*<0.05	*P*<0.05	*P*<0.05
HH (mm)	21.34±1.89 (18.99–27.72)	25.76±2.87 (19.87–33.57)	20.27±1.68 (16.54–24.26)	22.65±1.81 (18.66–26.38)	n.s.	*P*<0.05	*P*<0.05
ML (mm)	20.53±3.11 (17.18–29.71)	24.93±3.51 (20.63–38.29)	18.16±1.96 (13.71–23.20)	20.17±2.05 (15.70–25.51)	n.s.	*P*<0.05	*P*<0.05
MW (mm)	18.75±1.92 (16.03–25.81)	22.37±1.98 (17.64–25.24)	17.24±1.66 (13.73–20.82)	18.67±1.72 (15.21–22.70)	*P*<0.05	*P*<0.05	*P*<0.05
IOD (mm)	15.03±2.21 (7.86–19.52)	17.00±2.40 (8.86–21.66)	13.49±1.26 (11.36–16.78)	14.58±1.31 (10.74–17.45)	n.s.	*P*<0.05	*P*<0.05
IND (mm)	6.81±0.68 (5.80–8.37)	8.03±0.88 (6.10–9.34)	6.59±0.55 (5.25–7.61)	7.02±0.61 (5.71–8.33)	*P*<0.05	*P*<0.05	n.s.
BWH (mm)	21.36±1.83 (18.47–25.43)	24.48±2.69 (18.18–29.96)	19.29±1.86 (16.12–25.11)	20.30±1.90 (16.72–26.95)	*P*<0.05	*P*<0.05	*P*<0.05
BWM (mm)	26.78±3.17 (20.96–32.38)	29.40±3.91 (22.61–36.65)	23.44±3.35 (18.24–31.44)	23.64±2.17 (18.76–30.2)	n.s.	n.s.	*P*<0.05
BWC (mm)	22.14±1.76 (19.35–28.39)	24.13±1.88 (20.20–29.48)	19.56±1.52 (16.16–23.44)	19.95±1.11 (17.40–22.86)	n.s.	*P*<0.05	*P*<0.05
TLL (cm)	52.99±4.68 (44.10–59.70)	52.11±6.58 (19.90–57.50)	49.55±9.43 (0.70–60.50)	50.00±5.96 (33.40–63.80)	n.s.	n.s.	n.s.
BM (g)	325.29±63.87 (220–490)	404.11±79.54 (220–552)	240.45±57.24 (105–400)	243.48±36.09 (150–315)	*P*<0.05	*P*<0.05	*P*<0.05

F: Female; M: Male. *n*: Number of individuals. TL: Total length; SVL (co-variate): Snout-vent length; HL: Head length; HW: Head width; HH: Head height; ML: Mouth length; MW: Mouth width; IOD: Interorbital distance; IND: Internarial distance; BWH: Body width near head; BWM: Body width at mid-body; BWC: Body width near cloaca; TLL: Tail length; BM: Body mass. –: Not available; n.s.: Not significant.

Table 2 Number of individuals with intact and autotomized tails at both sites and for both sexes

	Klis		Cres	
Tail condition	M	F	M	F
Original	9	17	6	20
Autotomized	31	32	31	14

In both populations, females had significantly more often intact tails than males ($P<0.05$). F: Female; M: Male.

Table 3 Means±*SD* of head length (HL) to head width (HW) ratios (HL/HW) for studied populations

Site	M	F
Klis	1.81±0.14	1.85±0.15
Cres	1.78±0.19	1.82±0.14

M: Male; F: Female. *t*-test showed no significant differences between sexes or between sites. ($P>0.05$).

Table 4 Scaled mass index (SMI)

Locality	*n*	Sex	b_{SMA}	95 % CI	L_0	SMI
Cres	34	F	3.24	2.20, 4.28	89.01	327.98
	34	M	3.89	2.85, 4.93	92.78	398.69
Klis	48	F	3.59	2.84, 4.34	84.66	239.38
	39	M	2.08	1.49, 2.66	83.43	243.94

n: Number of individuals; F: Female; M: Male; b_{SMA}: Scaling exponent; L_0: Arithmetic mean of L (individual total length).

Ecological variables

Mean recorded values of physical habitat data showed slight differences between the two sites, with Cres Island having lower average recorded temperature and humidity but higher air pressure than Klis (Table 5). Factor analysis of ecological and physical habitat data yielded three factors that explained 71.52% of the variability. Air and soil temperature showed significant factor loadings for factor 1 (0.81 and 0.84), relative humidity and air pressure for factor 2 (–0.74 and 0.77), and distance to hiding place for factor 3 (–0.77). MANOVA of the extracted factors showed differences between the two sites ($F=31.40$, $P<0.05$, Partial $\eta^2=0.49$), but not between the sexes ($F=0.82$, $P=0.49$, Partial $\eta^2=0.03$) nor the interaction between sex and site ($F=0.42$, $P=0.74$, Partial $\eta^2=0.02$).

Total vegetation, short vegetation up to 10 cm, herbaceous vegetation up to 50 cm, and tree vegetation were more abundant in Klis, whereas shrubby vegetation was more prominent on Cres. Factor analysis of the variables describing vegetation cover yielded two factors that explained 67.97% of the variability. Total and herbaceous vegetation showed significant factor loadings for factor 1 (0.91 and 0.78) and short vegetation up to 10 cm showed significant factor loadings for factor 2 (0.80). MANOVA of extracted factors showed differences between the two sites ($F=18.98$, $P<0.05$, Partial $\eta^2=0.20$), but no differences between the sexes ($F=1.12$, $P=0.33$, Partial $\eta^2=0.01$) nor the interaction between sex and site ($F=1.55$, $P=0.22$, Partial $\eta^2=0.02$).

Table 5 Measured parameters of physical and ecological habitat data with significant factor loadings from a factor analysis expressed as means±*SD*

Variable	Cres	Klis
Recorded air temperature (°C)	21.6±4.3	24.3±5.5
Annual air temperature (°C)	15.3*	16.1*
Recorded soil temperature (°C)	19.4±4.0	19.5±2.5
Air movement	2.1±2.2	2.1±1.9
Relative air humidity at capture site (%)	43.0±10.5	56.1±13.5
Annual air humidity (%)	70.4*	58.1*
Recorded air pressure (hPa)	1 010.7±4.0	999.9±6.3
Annual air pressure (hPa)	1 009.6*	1 000.4*
Distance to hiding place	223.8±319.4	226.6±318.1

*: Taken from Meteorological and Hydrological Service of Croatia (Zaninović et al., 2008); standard deviation (*SD*) data not available.

DISCUSSION

In our study, we compared the morphology and ecology of two populations of European glass lizard, one insular (Cres) and one from the mainland (Klis). The ecological and physical habitat data showed that the studied locations differed in the amount of vegetation, with less vegetation being present in the Cres site. Vegetation cover is an important variable that influences *P. apodus* distribution within the habitat, with individual distribution differing between different vegetation types (Telenchev et al., 2017). However, to truly differentiate to what extent our data represent true habitat or transitional habitat, we still lacked detailed information on species vagility and habitat use. Currently available data on vagility of *P. apodus*, based on a single research, show that recaptured individuals were found the furthest 5 m away from the site of their previous capture, suggesting very low mobility in this species (Telenchev et al., 2017).

In addition, two of the measured physical parameters, i.e., air temperature and relative humidity, were higher on Klis (Table 5). Interestingly, data from the Meteorological and Hydrological Service of Croatia for both areas showed only slight differences in annual temperature (less than 1 °C between locations) but larger differences in annual relative humidity. The annual humidity data correspond well to our mainland location data, but the island location showed almost two times higher values compared to our data. This finding indicates that humidity may be a parameter that makes a difference between the island and mainland locations. Yet, some parameters were strikingly similar at both sites, e.g., soil temperature (which corresponds to the temperature experienced by the animal when it is hiding underground) did not differ between sites. Humidity can directly affect vegetative growth, but in our case less vegetation was present at the island site. Another important difference between the sites was the macro- and meso-faunal composition. Cres lacks many of the predators present in the Klis area (e.g., medium-sized predators like foxes or badgers). The lack of larger predators could be connected to vegetation cover, i.e., wild (deer) and domestic (sheep) grazers are present all over Cres, thus limiting vegetative growth (Dumančić, 1992; Sušić & Radek, 2007). The absence or removal of top predators can lead to simplified or degraded habitats, which impact lower trophic levels (Estes et al., 2001; Ripple & Beschta, 2004; Soulé et al., 2003), and might be the case on Cres. However, according to our results, the detected vegetation and humidity differences between the two selected habitats did not directly influence the presence of either sex or how they use the habitat (for ecological parameters see section Materials and methods–Data collection). In addition, during preliminary study, we observed no animals during mid-summer at either site, consistent with the fact that they are most active at temperatures between 22 °C and 31 °C (Telenchev et al., 2015) and estivate under higher air temperatures (Abe, 1995; Buhlmann, 1995; Storey, 2001). Overall, the studied populations did not differ significantly in the general ecological parameters recorded.

The most influenced phenotypic character, dependent on habitat and important from an evolutionary perspective, is body size (Werner & Gilliam, 1984). It is also the most important trait in niche determination (Blanckenhorn, 2000; Janzen, 1993; Wikelski, 2005). In general, both of our studied populations could be regarded as morphologically small, as all animals measured were smaller than those reported in the original description of *P. a. thracius* (where numerous individuals were recorded with a SVL greater than 400; Obst, 1978). In addition, the HL/HW ratios in our populations were slightly lower than the average from the original description (1.82), although they fell within the range (1.72–2.12, Obst, 1978; Table 3).

Comparative analysis of morphological data showed strong discrimination between the two study populations. Animals from Cres were larger than those from Klis. The higher SMI values for the Cres animals also suggest better physical fitness (Cooper et al., 2009). The smaller body size observed in Klis may indicate stronger predation pressure, as many predators are absent from Cres Island (e.g., foxes and badgers, Sušić & Radek, 2007). This predation risk may influence not only survival, but also the size of the animals. In addition, predation pressure can influence population age structure, i.e., a higher number of older individuals being captured by predators can decrease the overall size of individuals as size in reptiles is commonly dependent on age (Tomašević Kolarov et al., 2010).

Another possible explanation for the larger body size could be the abundance of potential prey items. *Pseudopus apodus* is a generalist, although arthropod and mollusc prey are dominant, with some vertebrates (Rifai et al., 2005). Rifai et al. (2005) showed dominance of different prey items at different localities (e.g., orthopterans in Jordan, coleopterans in Caucasus, molluscs in Crimea). On the other hand, food abundance is often higher on large islands, which may influence not only body size, but also species density (Pafilis et al., 2009).

On Cres, the lack of predators and possibly higher food abundance, may have influenced the size of the studied individuals, which could be a plastic trait. However, this must be confirmed experimentally, as some traits show more plasticity (e.g., hindlimb length in *Anolis sagrei*, Losos et al., 2000), whereas others are more conservative (e.g., dry mass growth rate in *Sceloporus graciosus*, Sears & Angilletta, 2003).

Apart from the size differences between populations, we also detected intersexual size differences within the Cres population, with males being significantly larger than females. In both populations, males had larger heads than females, but this difference was more prominent in Cres. Larger heads imply bigger muscles and greater bite force (Sagonas et al., 2014; Santana et al., 2010), which may evolve for a number of reasons (Christiansen & Wroe, 2007; Dewar et al., 2015; Dollion et al., 2017; Jones & Ruff, 2011; Vincent & Herrel, 2007). A greater bite force can allow an animal to extend its food niche, enabling it to feed on larger or harder prey items (Herrel et al., 2001; Verwaijen et al., 2002; Wyckmans et al., 2007) or to eat different types of food, such as plants (Herrel et al., 2004a, 2004b, 2008; Sagonas et al., 2014). The larger head (accompanied with larger body size) in *P. apodus* is crucial for mating success, as male to male combat has been observed in this species (Jablonski, 2018) and individuals that can inflict stronger bites are more likely to win such contests. Therefore, larger individuals may be more successful in mating, which could, through intrasexual selection, result in the increased size of males in the population. Intersexual selection may also play a role, with females preferring larger individuals as a sign of better general fitness. This pronounced sexual dimorphism in morphology was observed in all morphometric variables in the Cres population, which was characterized by larger, more robust males compared to females.

However, there was an exception, with TLL being slightly longer in females than in males. This was the only morphometric variable that was not influenced by sex, location, or by the interaction between site and sex. This finding is surprising, as all other parameters indicated that the animals from Cres were generally larger. Log-model analysis confirmed this difference and clearly showed that males suffer more often from autotomy than females (see Table 2). Tail autotomy is directly connected to predator evasion strategies in lizards (Higham et al., 2013). This suggests that the observed TLL values may be dependent on increased predation and that males are more active and exposed to predation than females. Intrasexual selection (e.g., male-male fights) is unlikely to have a significant influence on the occurrence of autotomy, as observations on male to male combat have shown no bites to the tail region (Jablonski, 2018). This is an interesting finding as previous study suggests that *P. apodus* lizards rarely autotomize their tails (Obst, 1981).

The general differences between populations observed in this paper could also be a consequence of the island effect (e.g., Foster 's rule). On islands that lack predators, lizards tend to increase their body size in order to reduce intraspecific competition (Case, 1978; Meiri, 2008). In addition, selection on islands with reduced predation risk may favor larger males, resulting in larger body size in future generations (Case, 1978). This may partially explain the phenomenon we observed, as *P. apodus* may be very aggressive towards conspecifics during the breeding period (Lisičić pers. observ.; Jablonski, 2018). However, detailed studies on territoriality and sexual selection in this species are lacking.

The evolutionary background of the detected intrapopulation differences is speculative. Even though *P. apodus* is common on many islands along the eastern Adriatic coast, information on its dispersal history is limited. Island populations of *P. apodus* are probably remnants from the last Ice Age when most islands in this region were connected to the mainland, some 10 000–15 000 years ago, as was the case with the herpetofauna on other Mediterranean islands (Corti et al., 1999). Previous experiments on the reciprocal introduction of the Italian wall lizard (*Podarcis siculus*) on two Adriatic islets have shown that even for genetically identical populations, 35 years of separation can result in profound morphological, behavioural, and physiological differences (Herrel et al., 2008). These differences confirm the plasticity of this species in terms of dietary shift, which can be observed in skull dimensions, dentition, gut morphology, and digestive performance (Herrel et al., 2008; Vervust et al., 2010).

Detailed genetic data on our studied populations are not available, so we can only speculate to what extent these differences result from environmental and/or genetic variability. The only genetic data on these populations refer to the subspecies (Jandzik et al., 2018), which show very low genetic diversity within the whole range of the *P. a. thracius* subspecies, both at the nuclear and mitochondrial level. It has also been suggested that *P. apodus* has lower genetic plasticity than the genus *Anguis*, possibly explaining its much narrower distribution (Jandzik et al., 2018).

Genetic data that can account for the evolutionary history in some lizard species, e.g., genetic data of *Podarcis erhardii* in Greece suggests that spatial fragmentation contributes more to genetic variation than geographic proximity (Hurston et al., 2009), should be taken with caution as *P. apodus* obviously differs in this aspect from other European lizards. Certainly, detailed genetical analyses would contribute to a better understanding of the underlying causes of the observed plasticity.

Regardless of the causal mechanism, morphological differences between the two studied populations were evident. Here, we showed that *P. apodus* exhibited morphological differences between two geographically close populations inhabiting the same biogeographical zone. Specifically, not only did we observe an increase in body size but also clear sexual dimorphism in the island population compared with the mainland population. This indicates that phenotypic plasticity occurs, even on a small geographical scale, in *P. apodus*. However, more studies on different populations of *P. apodus* are needed to confirm the level of phenotypic plasticity on a wider scale and to put it in a broader ecological context.

SCIENTIFIC FIELD SURVEY PERMISSION INFORMATION

Fieldwork in both localities in Croatia was partly supported through grant 119-0000000-1285 of the Ministry of Science of the Republic of Croatia. Permission for the field survey was issued by Department of Nature Protection, Ministry of Culture of the Republic of Croatia (permit No.: UP/I-612-07/10-33/762, 532-08-01-01/3-10-02 issued 29 June 2010), and by the Ministry of Environmental and Nature Protection of the Republic of Croatia (permit No.: UP/I-612-07/14/48/77, 517-07-1-1-1-14-4 issued 04 June 2014).

COMPETING INTERESTS

The authors declare that they have no competing interests.

AUTHORS'CONTRIBUTIONS

D.L. and Z.T. designed the study and revised the manuscript. O.J.G. performed the analyses and wrote the manuscript. D.L., P.P., V.L., and L.D. conducted the fieldwork. All authors read and approved the final version of the manuscript.

ACKNOWLEDGMENTS

We thank Herrel A. for reading the manuscript and for suggestions to improve it. We also want to thank P.L. and S.L. for unlimited logistical support during field work.

REFERENCES

Abe AS. 1995. Estivation in South American amphibians and reptiles. *Brazilian Journal of Medical and Biological Research*, **28**(11–12): 1241−1247.

Alekperov AM. 1978. Amphibians and reptiles of Azerbaijan. Elm, Baku.

Arnold EN. 2002. Reptiles and Amphibians of Europe. 2nd ed. Princeton: Princeton University Press.

Aubret F. 2015. Island colonisation and the evolutionary rates of body size in insular neonate snakes. *Heredity*, **115**(4): 349−356.

Bakaloudis DE, Vlachos CG, Holloway GJ. 1998. Habitat use by short-toed eagles *Circaetus gallicus* and their reptilian prey during the breeding season in Dadia Forest (north-eastern Greece). *Journal of Applied Ecology*, **35**(6): 821−828.

Blanckenhorn WU. 2000. The evolution of body size: what keeps organisms small?. *The Quarterly Review of Biology*, **75**(4): 385−407.

Bogdanov OP. 1986. Presmikayushchiesya Srednei Azii. Tashkent, Uzbekistan, Ukituvchi. (in Russian)

Bohonak AJ, van der Linde K. 2004(2016-03-28). RMA: software for reduced major axis regression, Java version. http://www.kimvdlinde.com/professional/rma.html.

Buhlmann KA. 1995. Habitat use, terrestrial movements, and conservation of the turtle, *Deirochelys reticularia* in Virginia. *Journal of Herpetology*, **29**(2): 173−181.

Carretero M, Znari M, Macé J, Harris DJ. 2005. Morphological divergence among populations of *Testudo graeca* from west-central Morocco. *Animal*

Biology, **55**(3): 259−279.

Case TJ. 1978. A general explanation for insular body size trends in terrestrial vertebrates. *Ecology*, **59**(1): 1−18.

Christiansen S, Wroe S. 2007. Bite forces and evolutionary adaptations to feeding ecology in carnivores. *Ecology*, **88**(2): 347−358.

Çiçek K, Tok CV, Hayretdağ S, Ayaz D. 2014. Data on the food composition of European glass lizard, *Pseudopus apodus* (Pallas, 1775) (Squamata: Anguidae) from Canakkale (Western Anatolia, Turkey). *Acta Zoologica Bulgarica*, **66**(3): 433−436.

Cooper Jr W, Pérez-Mellado V, Hawlena D. 2009. Morphological traits affect escape behaviour of the Balearic lizards (*Podarcis lilfordi*). *Amphibia-Reptilia*, **30**(4): 587−592.

Corti C, Masseti M, Delfino M, Pérez-Mellado V. 1999. Man and herpetofauna of the Mediterranean islands. *Revista Española de Herpetologia*, **13**: 83−100.

Dewar EW, Crocker CA, Bauchiero AV, Livingstone JP. 2015. Is skull shape related to aggressive displays in Pinnipeds?. *FASEB Journal*, **29**(S1): 696−698.

Dollion AY, Measey GJ, Cornette R, Carne L, Tolley KA, da Silva JM, Boistel R, Fabre AC, Herrel A. 2017. Does diet drive the evolution of head shape and bite force in chameleons of the genus *Bradypodion*?. *Functional Ecology*, **31**(3): 671−684.

Dumančić D. 1992. Improvement of lawn production in Mediterranean as a precondition for sheep and goat farming. *Agronomski Glasnik*, **1–88**: 105−111.

Estes J, Crooks K, Holt RD. 2001. Predators, ecological role of. *In*: Levin SA. Encyclopedia of Biodiversity. San Diego: Academic Press, 857−878.

Foster JB. 1964. Evolution of mammals on islands. *Nature*, **202**(4929): 234−235.

Georgiev D, Raichev E. 2009. A record of Horned viper *Vipera ammodytes* (L.) in the diet of the Stone marten *Martes foina* (Erxl.) (Mammalia: Mustelidae) in Bulgaria. *ZooNotes*, **5**: 1−2.

Herrel A, Van Damme R, Vanhooydonck B, De Vree F. 2001. The implications of bite performance for diet in two species of lacertid lizards. *Canadian Journal of Zoology*, **79**(4): 662−670.

Herrel A, Vanhooydonck B, Van Damme R. 2004a. Omnivory in lacertid lizards: adaptive evolution or constraint?. *Journal of Evolutionary Biology*, **17**(5): 974−984.

Herrel A, Vanhooydonck B, Joachim R, Irschick DJ. 2004b. Frugivory in polychrotid lizards: effects of body size. *Oecologia*, **140**(1): 160−168.

Herrel A, Huyghe K, Vanhooydonck B, Backeljau T, Breugelmans K, Grbac I, Van Damme R, Irschick DJ. 2008. Rapid large-scale evolutionary divergence in morphology and performance associated with exploitation of a different dietary resource. *Proceedings of the National Academy of Sciences of the United States of America*, **105**(12): 4792−4795.

Higham TE, Russell AP, Zani PA. 2013. Integrative biology of tail autotomy in lizards. *Physiological and Biochemical Zoology*, **86**(6): 603−610.

Horvatić S. 1963. Biogeographical position and articulation of our coast in the light of modern phytocenological research. *Acta Botanica Croatica*, **22**: 27−81.

Hurston H, Voith L, Bonanno J, Foufopoulos J, Pafilis P, Valakos E, Anthony N. 2009. Effects of fragmentation on genetic diversity in island populations of the Aegean wall lizard *Podarcis erhardii* (Lacertidae, Reptilia). *Molecular Phylogenetics and Evolution*, **52**(2): 395−405.

Itescu Y, Schwarz R, Donihue CM, Slavenko A, Roussos SA, Sagonas K, Valakos ED, Foufopoulos J, Pafilis P, Meiri S. 2018. Inconsistent patterns of body size evolution in co-occurring island reptiles. *Journal of Biogeography*, **27**(5): 538−550.

Jablonski D. 2018. Male-male combat in *Pseudopus apodus* (Reptilia: Anguidae). *Russian Journal of Herpetology*, **25**(4): 293−298.

Jandzik D, Jablonski D, Zinenko O, Kukushkin OV, Moravec J, Gvoždík V. 2018. Pleistocene extinctions and recent expansions in an anguid lizard of the genus *Pseudopus*. *Zoologica Scripta*, **47**(1): 21−32.

Janzen FJ. 1993. An experimental analysis of natural selection on body size of hatchling turtles. *Ecology*, **74**(2): 332−341.

Jones KE, Ruff CB. 2011. Male-male combat drives bite force evolution in the absence of mastication. *FASEB Journal*, **25**(1): 867.

Kukushkin OV, Dovgal IV. 2018. Sexual dimorphism in *Pseudopus apodus* (Reptilia: Sauria: Anguidae) from the Steppe Crimea. *Ecologica Montenegrina*, **19**: 1−21.

Lomolino MV. 2005. Body size evolution in insular vertebrates: generality of the island rule. *Journal of Biogeography*, **32**(10): 1683−1699.

Losos JB. 1990. Ecomorphology, performance capability, and scaling of West Indian *Anolis* lizards: an evolutionary analysis. *Ecological Monographs*, **60**(3): 369−388.

Losos JB, Creer DA, Glossip D, Goellner R, Hampton A, Roberts G, Haskell N, Taylor P, Ettling J. 2000. Evolutionary implications of phenotypic plasticity in the hindlimb of the lizard *Anolis sagrei*. *Evolution*, **54**(1): 301−305.

Meiri S. 2008. Evolution and ecology of lizard body sizes. *Global Ecology and Biogeography*, **17**(6): 724−734.

Nowak RM. 1991. Walker's Mammals of the World. 5th ed. Baltimore: The Johns Hopkins University Press.

Obst FJ. 1978. On geographical variability of Scheltopusik, *Ophisaurus apodus* (Pallas). *Zoologische Abhandlungen Staatliches Museum für Tierkunde in Dresden*, **35**: 129−140.

Obst FJ. 1981. *Ophisaurus apodus* (Pallas, 1775)-Scheltopusik. *In*: Handbuch der Reptilien und Amphibien Europas, vol. 1. Echsen (Sauria). Akademische Verlags gesellschaft, Wiesbaden, 259–274. (in German)

Owens IP, Scott SN, Robinson SI, Clegg SM, Kikkawa J. 2006. Large body size in island-dwelling passerines: the roles of insular specialization, niche expansion and ecological release. *Acta Zoologica Sinica*, **52**(S1): 262−266.

Pafilis P, Meiri S, Foufopoulos J, Valakos E. 2009. Intraspecific competition and high food availability are associated with insular gigantism in a lizard. *Naturwissenschaften*, **96**(9): 1107−1113.

Palkovacs EP. 2003. Explaining adaptive shifts in body size on islands: a life history approach. *Oikos*, **103**(1): 37−44.

Peig J, Green AJ. 2009. New perspectives for estimating body condition from mass/length data: the scaled mass index as an alternative method. *Oikos*, **118**(12): 1883−1891.

Rifai L, Baker MA, Al Shafei D, Disi AM, Manhasneh A, Amr Z. 2005. *Pseudopus apodus* (Pallas, 1775) from Jordan, with notes on its ecology (Sqamata: Sauria: Anguidae). *Herpetozoa*, **18**(3–4): 133−140.

Ripple WJ, Beschta RL. 2004. Wolves and the ecology of fear: can predation risk structure ecosystems?. *BioScience*, **54**(8): 755−766.

Sagonas K, Pafilis P, Lymberakis P, Donihue CM, Herrel A, Valakos ED. 2014. Insularity affects head morphology, bite force and diet in a Mediterranean lizard. *Biological Journal of the Linnean Society*, **112**(3):

469−484.

Santana SE, Dumont ER, Davis JL. 2010. Mechanics of bite force production and its relationship to diet in bats. *Functional Ecology*, **24**(4): 776−784.

Sears MW, Angilletta Jr MJ. 2003. Life-history variation in the sagebrush lizard: phenotypic plasticity or local adaptation?. *Ecology*, **84**(6): 1624−1634.

Shcherbak NN. 1966. Amphibians and Reptiles of the Crimea (Herpetologia Taurica). Kiev: Naukova Dumka. (in Russian).

Soulé ME, Estes JA, Berger J, del Rio CM. 2003. Ecological effectiveness: conservation goals for interactive species. *Conservation Biology*, **17**(5): 1238−1250.

Storey KB. 2001. Turning down the fires of life: Metabolic regulation of hibernation and estivation. *In*: Storey KB. Molecular Mechanisms of Metabolic Arrest. Oxford: BIOS Scientific Publishers, 1–21.

Sušić G, Radek V. 2007. Biodiversity through ponds of Cres Island. Istraživačko-edukacijski centar za zaštitu prirode Eko Centar Insulae, Beli. (in Croatian)

Telenchev I, Simeonovska-Nikolova D, Natchev N, Tzankov N. 2015. A preliminary study on the habitat selection of European glass lizard (*Pseudopus apodus*) in southeast Bulgaria. *In*: First National Conference of Biotechnology. Sofia, 2014.

Telenchev I, Simeonovska-Nikolova D, Tzonev R. 2017. Habitat use and activity of European glass lizard, *Pseudopus apodus* (Pallas, 1775), in southeastern Bulgaria. *Turkish Journal of Zoology*, **41**(2): 286−293.

Thomas R, Hedges SB. 1998. New anguid lizard (*Diploglossus*) from Cuba. *Copeia*, **1998**(1): 97−103.

TIBCO Software Inc. 2018. Statistica (data analysis software system), version 13. http://tibco.com.

Tomašević Kolarov N, Ljubisavljević K, Polović L, Džukić G, Kalezić ML. 2010. The body size, age structure and growth pattern of the endemic Balkan Mosor rock lizard (*Dinarolacerta mosorensis* Kolombatović, 1886). *Acta Zoologica Academiae Scientiarum Hungaricae*, **56**(1): 55−71.

Topić J. 2001. Vegetation (Flora) of Croatia. *In*: Lovstvo JJ. Croatia: Strossmayer University of Osijek, 105–124. (in Croatian)

Tutiš V, Kralj J, Radović D, Ćiković D, Barišić S. 2013. Red Data Book of Birds of Croatia. Republic of Croatia: Ministry of Environmental and Nature Protection, State Institute for Nature Protection.

Vervust B, Pafilis P, Valakos ED, Van Damme R. 2010. Anatomical and physiological changes associated with a recent dietary shift in the lizard *Podarcis sicula*. *Physiological and Biochemical Zoology*, **83**(4): 632−642.

Verwaijen D, Van Damme R, Herrel A. 2002. Relationships between head size, bite force, prey handling efficiency and diet in two sympatric lacertid lizards. *Functional Ecology*, **16**(6): 842−850.

Vincent SE, Herrel A. 2007. Functional and ecological correlates of ecologically-based dimorphisms in squamate reptiles. *Integrative and Comparative Biology*, **47**(2): 172−188.

Werner EE, Gilliam JF. 1984. The ontogenetic niche and species interactions in size-structured populations. *Annual Review of Ecology and Systematics*, **15**: 393−425.

Wikelski M. 2005. Evolution of body size in Galapagos marine iguanas. *Proceedings of the Royal Society B: Biological Sciences*, **272**(1576): 1985−1993.

Wyckmans M, Van Wassenbergh S, Adriaens D, Van Damme R, Herrel A. 2007. Size-related changes in cranial morphology affect diet in the catfish *Clariallabes longicauda*. *Biological Journal of the Linnean Society*, **92**(2): 323−334.

Zaninović K, Gajić-Čapka M, Perčec Tadić M, Vučetić M, Bajić A, Cindrić K, Cvitan L, Katušin Z, Kaučić D, Likso T, Lončar E, Lončar Ž, Mihajlović D, Pandžić K, Patarčić M, Srnec L, Vučetić V. 2008. Atlas of Croatia 1961–1990, 1971–2000. Zagreb: Meteorological and Hydrological Service of Croatia.

ZOOLOGICAL RESEARCH

Spatial and temporal patterns of amphibian species richness on Tianping Mountain, Hunan Province, China

DEAR EDITOR,

Exploring species richness patterns across space and time can help in understanding species distribution and in formulating conservation strategies. Among taxa, amphibians are of utmost importance as they are highly sensitive to environmental changes due to their unique life histories (Zhong et al., 2018). Here, we investigated the spatial and temporal patterns of amphibian species richness on Tianping Mountain in China. Specifically, we established 10 transects at low to high elevations, and sampled amphibians in April, June, August, and October 2017. Our results demonstrated that amphibian species composition and richness varied significantly at both spatial and temporal scales and were associated with gradients of environmental change in microhabitats on Tianping Mountain.

Biodiversity is a hot topic in community ecological research and exhibits a strong relationship with ecosystem functioning (Wang & Brose, 2018; Zhao et al., 2018). Although biodiversity consists of multiple components, species richness is a fundamental measurement underlying various ecological concepts and models (Gotelli & Colwell, 2011). Exploring species richness patterns across space and time can help to understand the distribution of organisms (Fu et al., 2006), reveal the mechanism of species coexistence (Hu et al., 2011), formulate conservation strategies (Olds et al., 2016), and assess environmental changes (Butchart et al., 2010).

Spatial patterns of species richness are usually tested along altitudinal or latitudinal gradients at the local and regional scales, respectively. At the local scale, species richness typically exhibits two types of response along elevational gradients; i.e., it decreases continuously or displays a hump-shaped relationship with increasing elevation (Rahbek, 1995, 2004). These relationships can be explained by environmental factors such as climate, area, and habitat heterogeneity (Cruz-Elizalde et al., 2016; Hernández-Salinas & Ramírez-Bautista, 2012; McCain, 2009; Rahbek, 1995; Sanders et al., 2003) or can be attributed to mid-domain effects, with increasing species distribution overlap towards the center of a bounded geographic domain free of environmental gradients (Colwell et al., 2004; Wu et al., 2013a). At the larger geographic scale (e.g., latitudinal gradients), species richness can increase from the poles to the tropics (e.g., global data of amphibians, birds, and mammals; Marin & Hedges, 2016). This is likely because tropical areas have greater historical lineages and higher environmental heterogeneity than temperate zones (Jansson et al., 2013; Stevens, 2011). In contrast, marine species richness along latitudinal gradients (for both vertebrates and invertebrates, and all species together) is bimodal, with a dip in richness occurring at the equator (Chaudhary et al., 2017). This relationship is strongly determined by temperature, which can influence animal biology and productivity within ecosystems (Chaudhary et al., 2017).

Temporal environmental fluctuations (e.g., seasonality) can also control species composition and richness (Tonkin et al., 2017). The unique assemblages observed at specific times of the year depend on the ecological conditions of each season (Chesson, 2000), and have been well documented in different fauna. For instance, temporal changes in bird species richness can be attributed to seasonal migration (Somveille et al., 2015). In terms of fish communities, species richness and assemblages can vary seasonally due to minimization of interspecific competition for resources (Shimadzu et al., 2013). Therefore, exploring temporal (seasonal) patterns of species richness can help to understand species coexistence and ecosystem stability (Thibaut & Connolly, 2013).

Although numerous studies have examined spatial (e.g.,

Received: 11 September 2019; Accepted: 13 January 2020; Online: 15 January 2020

Foundation items: This study was supported by the Strategic Priority Research Program of the Chinese Academy of Sciences (XDA23080101), National Natural Science Foundation of China (31700353), Biodiversity Survey and Assessment Project of the Ministry of Ecology and Environment, China (2019HJ2096001006), West Light Foundation of the Chinese Academy of Sciences (2016XBZG_XBQNXZ_B_007), and China Biodiversity Observation Networks (Sino BON)

DOI: 10.24272/j.issn.2095-8137.2020.017

Acharya et al. 2011; Bhattarai et al., 2004; Fu et al., 2007; Gojo Cruz et al., 2018; Kraft et al., 2011; Khatiwada et al., 2019; Wu et al., 2013a, 2013b) and temporal patterns (e.g., Bender et al., 2017; Shimadzu et al., 2013; Tonkin et al., 2017) of species richness in different taxa separately, empirical studies are still needed for simultaneous quantification. This is because both space and time can affect the distribution and activities of species at the local scale. For instance, species belonging to different spatial guilds may exploit different habitat types. Population size may increase at different times as species can adapt to changes in temporal environmental conditions over their life cycle (Shimadzu et al., 2013). This is especially true for amphibians due to their restricted distribution ranges as well as their seasonal migration for spawning and after metamorphosis (Fei et al., 2009). Therefore, in the present study, we focused on the spatial and temporal (seasonal) changes in species richness in amphibians distributed on Tianping Mountain, China. Specifically, we (1) revealed the amphibian species assemblages along elevational gradients, as well as those in different seasons, (2) explored the environmental factors that determined species composition, and (3) tested the spatial and temporal patterns of species richness. Methodological details are provided in the Supplementary Materials.

In total, 15 species belonging to seven families were recorded during the four sampling sessions (Supplementary Table S1). Results showed that amphibian assemblages changed along the elevational gradients. Overall, the dominant species recorded at the low, mid-, and high elevation transects included *Amolops ricketti* and *Odorrana schmackeri*, *Paramegophrys liui*, and *Paa boulengeri* and *Leptobrachium boringii*, respectively (Figure 1A). The amphibian assemblages also exhibited strong temporal shifts during the four seasons. The dominant species in April, June, August, and October were *Paramegophrys liui* and *L. boringii*, *Megophrys sangzhiensis* and *Pseudohynobius flavomaculatus*, *O. margaretae* and *O. schmackeri*, and *Paa boulengeri* and *A. ricketti*, respectively (Figure 1B).

The redundancy analysis (RDA) results were significant when testing the effects of environmental factors on amphibian species composition (P=0.005). The first two axes explained 31.73% of the variation (20.13% and 11.60%, respectively). Among the 16 environmental factors, air humidity, water temperature, altitude, tree number, canopy density, shrub coverage, fallen leaf coverage, fallen leaf depth, and water conductivity had significant effects on species composition (P<0.05). Juvenile and adult *O. schmackeri*, adult *A. chunganensis*, juvenile and adult *A. ricketti*, and adult *Fejervarya multistriata* were positively associated with water temperature and water conductivity, but were negatively associated with altitude, tree number, canopy density, and fallen leaf depth. In contrast, juvenile *Bufo gargarizans*, adult *L. boringii*, and adult *Paramegophrys liui* were positively associated with altitude, tree number, canopy density, and fallen leaf depth, but were negatively correlated with water temperature and water conductivity. In addition, adult *Feirana quadranus*, adult *Pseudorana sangzhiensis*, adult *O. margaretae*, juvenile and adult *Paa boulengeri*, adult *M. sangzhiensis*, and adult *Rhacophorus chenfui* were positively associated with shrub coverage and air humidity. In contrast, adult *Hyla gongshanensis* and juvenile *Pseudohynobius flavomaculatus* were negatively associated with shrub coverage and air humidity (Figure 1C).

Overall, total amphibian species richness increased significantly along elevational gradients when incorporating data from all four sampling sessions (R^2=0.53, P=0.010; Figure 1D), indicating that more species were detected at high elevation sites. However, the response of species richness to elevational gradients differed each month. Specifically, there were no significant changes in April and August (R^2=–0.12, P=0.844; R^2=–0.06, P=0.519), but a significant increase and U-shaped relationship were observed in June and October, respectively (R^2=0.38, P=0.034; R^2=0.70, linear term: P=0.009, quadratic term: P=0.014; Figure 1E). At the temporal scale, total species richness varied significantly among the different months (Friedman test; χ^2=16.129, df=3, P=0.001). Specifically, species richness in April was significantly lower than that in August (W=17, P=0.011), but was significantly higher than that in October (W=76, P=0.044). Species richness in October was significantly lower than that in June (W=93, P=0.001) and August (W=97, P<0.001). However, there was no significant difference in species richness between April and June (W=24.5, P=0.052) or between June and August (W=43, P=0.612; Figure 1F).

Overall, our results indicated that amphibian species assemblages varied along elevational gradients. Specifically, *A. ricketti* and *O. schmackeri* were the dominant species at the low elevation transects. However, these species, as well as *F. multistriata* and *H. gongshanensis*, were restricted to transects below 800 m a.s.l. (i.e., were not recorded at mid- or high elevations). Results also showed that *Paramegophrys liui* was dominant at the mid-elevation transects, whereas *Paa boulengeri* and *L. boringii* were dominant at the high elevation transects. In addition, we found one high elevation-restricted species (*Pseudorana sangzhiensis*). These results support previous claims that elevations associated with specific habitat conditions (e.g., temperature and vegetation variation) are important for determining amphibian species distribution (Khatiwada et al., 2019; Meza-Joya & Torres, 2016) and provide specific spatial niches for species. We also found that temporal niche utilization differed among the amphibians, with dominant species changing from *Paramegophrys liui* and *L. boringii* in April, to *Pseudohynobius flavomaculatus* in June, *O. schmackeri* in August, and *Paa boulengeri* and *A. ricketti* in October. Some species were also seasonally restricted. For instance, *Paramegophrys liui* was not detected after June, *O. schmackeri* and *M. sangzhiensis* were only active in June and August, and *Pseudorana sangzhiensis* was only recorded in August. These results could be attributed to breeding times and temperature adaptations (Fei et al., 2009; Snyder & Weathers, 1975). Therefore, our results are in agreement with previous studies, which state that *Paramegophrys liui* and *L.*

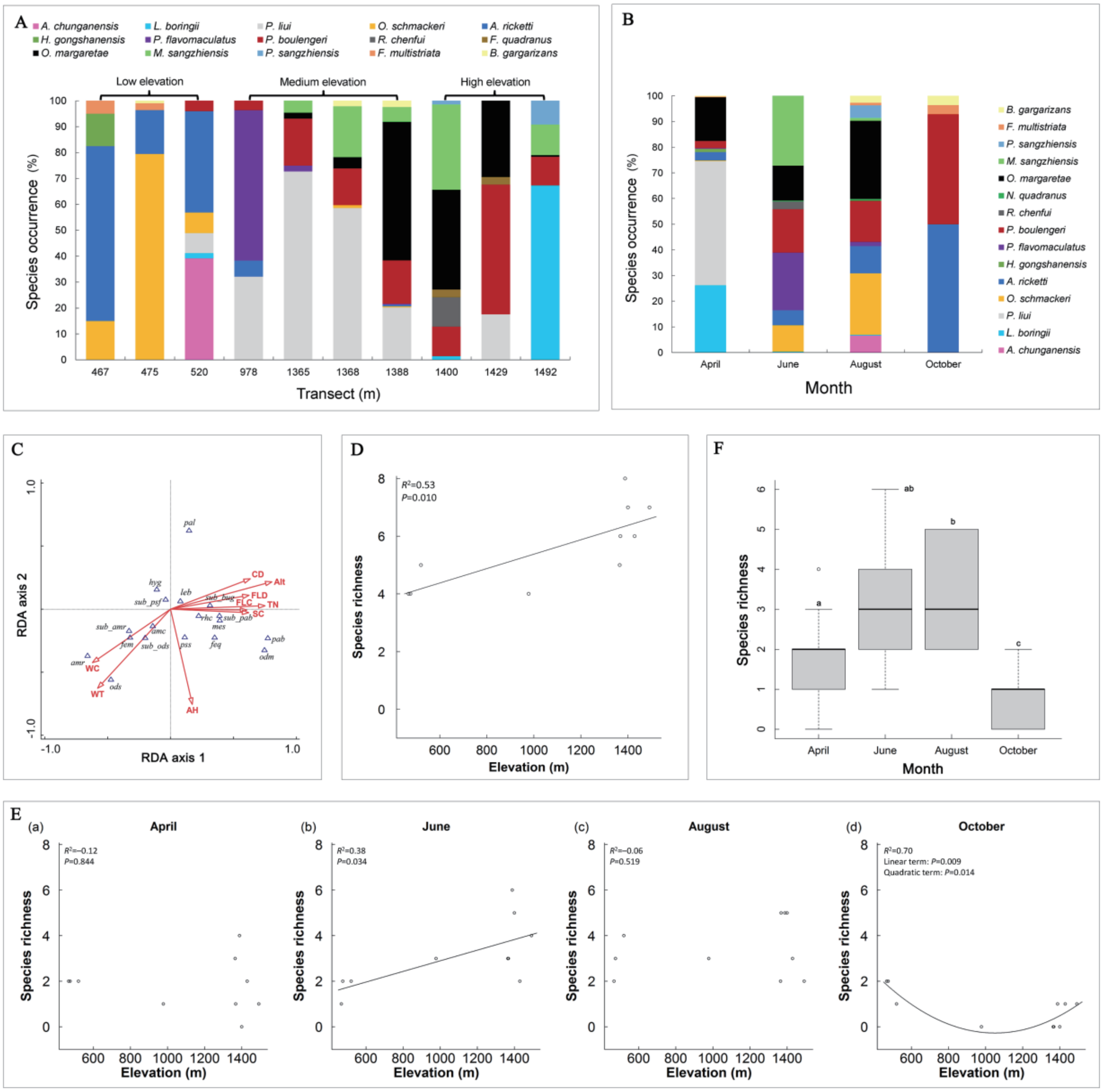

Figure 1 Spatial and temporal patterns of amphibian species richness on Tianping Mountain.

A: Species occurrence (percentage of individuals) in different sampling transects. B: Species occurrence (percentage of individuals) in different months. C: Redundancy analysis (RDA) of relationships among environmental factors and amphibian species composition. Length of environmental vector indicates degree of correlation. Only significant variables (P<0.05) are depicted. Abbreviations of environmental factors and amphibian species are listed in Supplementary Table S1 and Table S2, respectively. D: Relationship between total amphibian species richness and elevation. E: Relationship between amphibian species richness and elevation each month. F: Temporal changes in amphibian species richness over four months. Different letters on top of error bars indicate significant difference between pairwise months (P<0.05).

boringii breed in April–July and February–April, respectively (Fei et al., 2009, 2012), whereas *O. schmackeri* and *M. sangzhiensis* usually breed in June–August (Fei et al., 2009, 2012). We also sampled several species in all seasons (e.g., *Paa boulengeri* and *A. ricketti*), which may be related to their broader temperature adaptation range (Fei et al., 2009, 2012).

Previous studies have indicated that *Paramegophrys liui* and *L. boringii* usually require high elevation habitats with broad vegetation coverage (Fei et al., 2009, 2012), which provide good breeding sites. This may explain why their abundance was positively correlated with environmental factors such as canopy density, fallen leaf depth, and tree number. However, their abundance was negatively correlated with water temperature as their breeding season occurs from March to June under relatively low temperatures (Fei et al., 2012; Yu & Lu, 2010). Juvenile *B. gargarizans* exhibited similar patterns as *P. liui* and *L. boringii*, which was probably because they recently underwent metamorphosis from water bodies. However, *A. chunganensis*, *A. ricketti*, and *O. schmackeri* were negatively associated with altitude, as these species prefer large, strong-flowing streams with low vegetation cover, which were more common at the lower elevation transects with higher temperatures (Wu et al., 2015; Xiong et al., 2005). The observations for *F. multistriata* at low elevations could be attributed to their high abundance in and preference for lowland paddy fields close to large streams. Unsurprisingly, *F. quadranus*, *Pseudorana sangzhiensis*, *O. margaretae*, *Paa boulengeri*, *M. sangzhiensis*, and *R. chenfui* were positively associated with shrub coverage and air humidity, as these conditions provide diverse food items such as insects, snails, and crabs (Huang et al., 2011; Yuan & Wen, 1990). In contrast, *H. gongshanensis* and juvenile *Pseudohynobius flavomaculatus* were negatively correlated with air humidity and shrub coverage as they inhabit paddy fields close to streams (Liao & Lu, 2010) and small ponds covered by rocks (Fei et al., 2009), respectively.

In contrast with many earlier studies (e.g., Hu et al., 2011; Khatiwada et al., 2019), total amphibian species richness increased continuously along the elevational gradients, with more species detected at higher elevations. This observation is interesting as most previous studies suggest that amphibian species richness should exhibit a hump-shaped response to elevation due to mid-domain effects (e.g., amphibians in Hengduan Mountain, China; Fu et al., 2006; amphibians in tropical Andes; Meza-Joya & Torres, 2016) or decrease continuously with elevation (e.g., eastern Nepal Himalaya; Khatiwada et al., 2019). This is because high elevations (e.g., >3 000 m on Hengduan Mountains and eastern Nepal Himalaya; Hu et al., 2011; Khatiwada et al., 2019) usually correspond to low temperatures, with fewer amphibian species able to survive in cold regions (Funk et al., 2012). Our conflicting results could be attributed to the limited elevation of transects selected on Tianping Mountain (<1 500 m), with temperature not a primary limiting factor of amphibian species richness at the spatial scale. In addition, our results could also be attributed to the larger heterogeneity of habitats at higher elevations on Tianping Mountain (Cao et al., 1997), which could support more amphibian species (Hernández-Salinas & Ramírez-Bautista, 2012; Meza-Joya & Torres, 2016). It was not surprising that more species were observed in June and August as these months occur in the active season (warmer and wetter climate conditions) for most amphibian species, with their populations increasing in suitable habitats (Bickford et al., 2010).

In conclusion, the present study demonstrated the spatial and temporal patterns of amphibian species richness on Tianping Mountain in Hunan Province, China. Future studies should focus on more facets of biodiversity to better understand the roles of spatial and temporal variation in community assembly processes of mountain-dwelling amphibians. As the spatial and temporal niches of amphibian species were different, specific conservation strategies should be implemented. Furthermore, we confirmed that amphibian species occurrence was strongly determined by biotic and abiotic features of their microhabitats, which mediated species composition along the elevational transects. Because microhabitats are easily affected by human disturbance, long-term monitoring should be conducted to investigate the relationship between amphibian diversity and environmental change.

SCIENTIFIC FIELD SURVEY PERMISSION INFORMATION

Field sampling was approved by the Management Office of the Badagongshan Nature Reserve (No. BDGSNR201204002). Animals collection and measurement protocols were approved by the Animal Care and Use Committee of Chengdu Institute of Biology (No. CIB2010031015).

SUPPLEMENTARY DATA

Supplementary data to this article can be found online.

COMPETING INTERESTS

The authors declare that they have no competing interests.

AUTHORS' CONTRIBUTIONS

T.Z. and J.P.J. conceived and designed the study. W.B.Z., C.L.Z., C.L.L., B.Z., D.X., and T.Z. collected the data. W.B.Z. and T.Z. analyzed the data and wrote the first draft of the manuscript. C.L.Z., W.Z., and J.P.J. commented on the manuscript. All authors read and approved the final version of the manuscript.

ACKNOWLEDGEMENTS

We are grateful to the managers for access to Badagongshan National Nature Reserve and to Yu-Long Li, Bi-Wu Qin, and Wen-Bo Fan for their help during fieldwork. We also thank Xiao-Xiao Shu for drawing the sampling site map.

Wen-Bo Zhu[1,2], Chun-Lin Zhao[1,3], Chun-Lin Liao[4], Bei Zou[1], Dan Xu[1,5], Wei Zhu[1], Tian Zhao[1,*], Jian-Ping Jiang[1,*]

[1] *CAS Key Laboratory of Mountain Ecological Restoration and Bioresource Utilization* & *Ecological Restoration Biodiversity Conservation*, *Key Laboratory of Sichuan Province*, *Chengdu Institute of Biology*, *Chinese Academy of Sciences*, *Chengdu*, *Sichuan* 610041, *China*

[2] *University of Chinese Academy of Sciences*, *Beijing* 100049, *China*

[3] *Key Laboratory of Southwest China Wildlife Resources Conservation (Ministry of Education)*, *China West Normal University*, *Nanchong*, *Sichuan* 637009, *China*
[4] *National Nature Reserve of Badagongshan*, *Sangzhi*, *Hunan* 427100, *China*
[5] *College of Animal Science and Technology*, *Southwest University*, *Chongqing* 400715, *China*
*Corresponding authors, E-mail: zhaotian@cib.ac.cn; jiangjp@cib.ac.cn

REFERENCES

Acharya BK, Sanders NJ, Vijayan L, Chettri B. 2011. Elevational gradients in bird diversity in the Eastern Himalaya: an evaluation of distribution patterns and their underlying mechanisms. *PLoS One*, **6**(12): e29097.

Bender IMA, Kissling WD, Böhning-Gaese K, Hensen I, Kühn I, Wiegand T, Dehling DM, Schleuning M. 2017. Functionally specialised birds respond flexibly to seasonal changes in fruit availability. *Journal of Animal Ecology*, **86**(4): 800−811.

Bhattarai KR, Vetaas OR, Grytnes JA. 2004. Fern species richness along a central Himalayan elevational gradient, Nepal. *Journal of Biogeography*, **31**(3): 389−400.

Bickford D, Howard SD, Ng DJJ, Sheridan JA. 2010. Impacts of climate change on the amphibians and reptiles of Southeast Asia. *Biodiversity and Conservation*, **19**(4): 1043−1062.

Butchart SHM, Walpole M, Collen B, van Strien A, Scharlemann JPW, Almond REA, Baillie JEM, Bomhard B, Brown C, Bruno J, Carpenter KE, Carr GM, Chanson J, Chenery AM, Csirke J, Davidson NC, Dentener F, Foster M, Galli A, Galloway JN, Genovesi P, Gregory RD, Hockings M, Kapos V, Lamarque JF, Leverington F, Loh J, McGeoch MA, McRae L, Minasyan A, Morcillo MH, Oldfield TEE, Pauly D, Quader S, Revenga C, Sauer JR, Skolnik B, Spear D, Stanwell-Smith D, Stuart SN, Symes A, Tierney M, Tyrrell TD, Vie JC, Watson R. 2010. Global biodiversity: indicators of recent declines. *Science*, **328**(5982): 1164−1168.

Cao T, Qi C, Yu X. 1997. Studies on species diversity of *Fagus lucida* communities on the Badagongshan Mountain, Hunan. *Chinese Biodiversity*, **5**(2): 112−120. (in Chinese)

Chaudhary C, Saeedi H, Costello MJ. 2017. Marine species richness is bimodal with latitude: a reply to Fernandez and Marques. *Trends in Ecology & Evolution*, **32**(4): 234−237.

Chesson P. 2000. Mechanisms of maintenance of species diversity. *Annual Review of Ecology and Systematics*, **31**(1): 343−366.

Colwell RK, Rahbek C, Gotelli NJ. 2004. The mid-domain effect and species richness patterns: what have we learned so far?. *The American Naturalist*, **163**(3): E1−E23.

Cruz-Elizalde R, Ramírez-Bautista A, Hernández-Ibarra X, Wilson LD. 2016. Species diversity of amphibians from arid and semiarid environments of the Real de Guadalcázar State Reserve, San Luis Potosí, Mexico. *Natural Areas Journal*, **36**(3): 302−309.

Fei L, Hu S, Ye C, Tian W, Jiang J, Wu G, Li J, Wang Y. 2009. Fauna Sinica, Amphibia, Vol.2, Anura. Beijing: Science Press. (in Chinese)

Fei L, Ye C, Jiang J. 2012. Colored Atlas of Chinese Amphibians and Their Distributions. Chengdu, China: Sichuan Publishing House of Science & Technology. (in Chinese)

Fu C, Hua X, Li J, Chang Z, Pu Z, Chen J. 2006. Elevational patterns of frog species richness and endemic richness in the Hengduan Mountains, China: geometric constraints, area and climate effects. *Ecography*, **29**(6): 919−927.

Fu C, Wang J, Pu Z, Zhang S, Chen H, Zhao B, Chen J, Wu J. 2007. Elevational gradients of diversity for lizards and snakes in the Hengduan Mountains, China. *Biodiversity and Conservation*, **16**(3): 707−726.

Funk WC, Caminer M, Ron SR. 2012. High levels of cryptic species diversity uncovered in Amazonian frogs. *Proceedings of the Royal Society B: Biological Sciences*, **279**(1734): 1806−1814.

Gojo Cruz PHP, Afuang LE, Gonzalez JCT, Griezo WSM. 2018. Amphibians and reptiles of Luzon Island, Philippines: the herpetofauna of Pantabangan-Carranglan watershed, Nueva Ecija Province, Caraballo Mountain range. *Asian Herpetological Research*, **9**(4): 201−223.

Gotelli NJ, Colwell RK. 2011. Estimating species richness. *In*: Magurran AE, McGill BJ. Frontiers in Measuring Biodiversity. New York, USA: Oxford University Press, 39–54.

Hernández-Salinas U, Ramírez-Bautista A. 2012. Diversity of amphibian communities in four vegetation types of Hidalgo State, Mexico. *The Open Conservation Biology Journal*, **6**(1): 1−11.

Hu J, Xie F, Li C, Jiang J. 2011. Elevational patterns of species richness, range and body size for spiny frogs. *PLoS One*, **6**(5): e19817.

Huang H, Gong D, Zhang Y. 2011. Primary observation of the ecological habits of *Rana guadranus* in Tianshui City of Gansu Province. *Journal of Anhui Agriculture Science*, **39**(8): 4749−4752. (in Chinese)

Jansson R, Rodríguez-Castañeda G, Harding LE. 2013. What can multiple phylogenies say about the latitudinal diversity gradient? A new look at the tropical conservatism, out of the tropics, and diversification rate hypotheses. *Evolution*, **67**(6): 1741−1755.

Khatiwada JR, Zhao T, Chen Y, Wang B, Xie F, Cannatella DC, Jiang J. 2019. Amphibian community structure along elevation gradients in eastern Nepal Himalaya. *BMC Ecology*, **19**(1): 19.

Kraft NJB, Comita LS, Chase JM, Sanders NJ, Swenson NG, Crist TO, Stegen JC, Vellend M, Boyle B, Anderson MJ, Cornell HV, Davies KF, Freestone AL, Inouye BD, Harrison SP, Myers JA. 2011. Disentangling the drivers of diversity along latitudinal and elevational gradients. *Science*, **333**(6050): 1755−1758.

Liao W B, Lu X. 2010. Age structure and body size of the Chuanxi Tree Frog *Hyla annectans chuanxiensis* from two different elevations in Sichuan (China). *Zoologischer Anzeiger-A Journal of Comparative Zoology*, **248**(4): 255−263.

Marin J, Hedges SB. 2016. Time best explains global variation in species richness of amphibians, birds and mammals. *Journal of Biogeography*, **43**(6): 1069−1079.

McCain CM. 2009. Global analysis of bird elevational diversity. *Global Ecology and Biogeography*, **18**(3): 346−360.

Meza-Joya FL, Torres M. 2016. Spatial diversity patterns of *Pristimantis* frogs in the Tropical Andes. *Ecology and Evolution*, **6**(7): 1901−1913.

Olds BP, Jerde CL, Renshaw MA, Li Y, Evans NT, Turner CR, Deiner K, Mahon AR, Brueseke MA, Shirey PD, Pfrender ME, Lodge DM, Lamberti GA. 2016. Estimating species richness using environmental DNA. *Ecology and Evolution*, **6**(12): 4214−4226.

Rahbek C. 1995. The elevational gradient of species richness: a uniform pattern?. *Ecography*, **18**(2): 200−205.

Rahbek C. 2004. The role of spatial scale and the perception of large-scale species-richness patterns. *Ecology Letters*, **8**(2): 224−239.

Sanders NJ, Moss J, Wagner D. 2003. Patterns of ant species richness along elevational gradients in an arid ecosystem. *Global Ecology and Biogeography*, **12**(2): 93−102.

Shimadzu H, Dornelas M, Henderson PA, Magurran AE. 2013. Diversity is maintained by seasonal variation in species abundance. *BMC Biology*, **11**(1): 98.

Snyder GK, Weathers WW. 1975. Temperature adaptations in amphibians. *The American Naturalist*, **109**(965): 93−101.

Somveille M, Rodrigues ASL, Manica A. 2015. Why do birds migrate? A macroecological perspective. *Global Ecology and Biogeography*, **24**(6): 664−674.

Stevens RD. 2011. Relative effects of time for speciation and tropical niche conservatism on the latitudinal diversity gradient of phyllostomid bats. *Proceedings of the Royal Society B: Biological Sciences*, **278**(1717): 2528−2536.

Thibaut LM, Connolly SR. 2013. Understanding diversity-stability relationships: towards a unified model of portfolio effects. *Ecology Letters*, **16**(2): 140−150.

Tonkin JD, Bogan MT, Bonada N, Rios-Touma B, Lytle DA. 2017. Seasonality and predictability shape temporal species diversity. *Ecology*, **98**(5): 1201−1216.

Wang S, Brose U. 2018. Biodiversity and ecosystem functioning in food webs: the vertical diversity hypothesis. *Ecology Letters*, **21**(1): 9−20.

Wu Q, Wang Y, Ding P. 2015. Ontogenetic shifts in diet of the piebald odorous frog *Odorrana schmackeri* in the Thousand Island Lake. *Chinese Journal of Zoology*, **50**(2): 204−213. (in Chinese)

Wu Y, Colwell RK, Rahbek C, Zhang C, Quan Q, Wang C, Lei F. 2013. Explaining the species richness of birds along a subtropical elevational gradient in the Hengduan Mountains. *Journal of Biogeography*, **40**(12): 2310−2323.

Wu Y, Yang Q, Wen Z, Xia L, Zhang Q, Zhou H. 2013. What drives the species richness patterns of non-volant small mammals along a subtropical elevational gradient?. *Ecography*, **36**(2): 185−196.

Xiong J, Yang D, Liao Q, Kang Z. 2005. Population monitor of *Amolops ricketti* in Hupingshan National Nature Reserve of Hunan. *Sichuan Journal of Zoology*, **24**(3): 403−406. (in Chinese)

Yu TL, Lu X. 2010. Sex recognition and mate choice lacking in male Asiatic toads (*Bufo gargarizans*). *Italian Journal of Zoology*, **77**(4): 476−480.

Yuan F, Wen X. 1990. Initial study of life habits and diet compisition of *Paa boulengeri* in Western Jiangxi Province. *Chinese Journal of Zoology*, **25**(2): 17−21. (in Chinese)

Zhao T, Wang B, Shu G, Li C, Jiang J. 2018. Amphibian species contribute similarly to taxonomic, but not functional and phylogenetic diversity: inferences from amphibian biodiversity on Emei Mountain. *Asian Herpetological Research*, **9**(2): 110−118.

Zhong M, Yu X, Liao W. 2018. A review for life-history traits variation in frogs especially for anurans in China. *Asian Herpetological Research*, **9**(3): 165−174.

ZOOLOGICAL RESEARCH

A new species of the genus *Amolops* (Anura: Ranidae) from Yunnan, China

DEAR EDITOR,

A new species of the genus *Amolops*, *Amolops tuanjieensis* **sp. nov.**, is described from Yunnan, China. The new species can be distinguished by the following characters: dorsolateral folds present; dorsal and ventral surfaces smooth; top of head and dorsum brown-red with irregular gray and dark spots; flank green; side of head black, from tip of snout, diffusing posteriorly to axilla, continuing as black streak below edge of dorsolateral fold; SVL 39.5–40.4 mm in males, 56.8–60.7 mm in females; tympanum distinct; supratympanic fold indistinct; vomerine teeth in two oblique rows between choanae, closer to each other than choanae; vocal sacs present; nuptial pads present; outer metatarsal tubercle absent, supernumerary tubercles absent; all fingertips expanded into discs; limbs dorsally brown with dark brown bars and irregular dark brown blotches.

The genus *Amolops* Cope, 1865 is distributed throughout Southeast Asia, southern China, and southern and eastern Himalaya. The genus currently contains 59 species (Frost, 2019), 18 of which belong to the *Amolops monticola* species group (Lyu et al., 2019a), characterized by smooth skin, side of head dark with light-colored upper lip stripe extending to axilla, and dorsolateral folds present (Jiang et al., 2016; Stuart et al., 2010; Yuan et al., 2018), including *Amolops aniqiaoensis* Dong, Rao, and Lü, 2005, *Amolops akhaorum* Stuart, Bain, Phimmachak, and Spence, 2010, *Amolops archotaphus* (Inger and Chanard, 1997), *Amolops bellulus* Liu, Yang, Ferraris, and Matsui, 2000, *Amolops chakrataensis* Ray, 1992, *Amolops chunganensis* (Pope, 1929), *Amolops compotrix* (Bain, Stuart, and Orlov, 2006), *Amolops cucae* (Bain, Stuart, and Orlov, 2006), *Amolops chayuensis* Sun, Luo, Sun and Zhang, 2013, *Amolops daorum* (Bain, Lathrop, Murphy, Orlov, and Ho, 2003), *Amolops gerbillus* (Annandale, 1912), *Amolops iriodes* (Bain and Nguyen, 2004), *Amolops mengyangensis* Wu and Tian, 1995, *Amolops monticola* (Anderson, 1871), *Amolops mengdingensis* and Yu, Wu, Yang, 2019, *Amolops nyingchiensis* Jiang, Wang, Xie, Jiang, and Che, 2016, *Amolops vitreus* (Bain, Stuart, and Orlov, 2006) and *Amolops wenshanensis* Yuan, Jin, Li, Stuart, and Wu, 2018. There are ten species of *A. monticola* group in China (*A. aniqiaoensis*, *A. bellulus*, *A. chunganensis*, *A. chayuensis*, *A. gerbillus*, *A. mengyangensis*, *A. monticola*, *A. nyingchiensis*, *A. wenshanensis* and *A. mengdingensis*) and four occur in Yunnan including *A. bellulus*, *A. mengyangensis*, *A. wenshanensis*, and *A. mengdingensis* (Frost, 2019; Yu et al., 2019).

During recent fieldwork at Tuanjie Township, Gengma Dai and Wa Autonomous County, Yunnan Province, China (Figure 1A), five *Amolops* specimens were collected. These specimens resemble members of the *A. monticola* group in that they have smooth skin, light-colored upper lip stripe extending to axilla, and dorsolateral folds present. Based on morphological comparison and molecular phylogenetic analyses, we considered these specimens to represent a new species of the genus *Amolops*, which is described herein.

Specimens were fixed in 80% ethanol and then stored in 80% ethanol. Muscle tissues were preserved in 99% ethanol. Specimens were deposited at Guangxi Normal University (GXNU).

Total genomic DNA was extracted from the muscle tissues of the five individuals. Fragments encoding partial 16S rRNA (*16S*), partial cytochrome oxidase subunit I (*COI)*, and complete NADH dehydrogenase subunit 2 (*ND2*) genes were amplified and sequenced following the protocols of Yu et al. (2019). All new sequences were deposited in GenBank under accession Nos. MN832750–MN832759 and MN832772–MN832776 (Supplementary Table S1). The phylogenetic position of these individuals in *Amolops* was reconstructed based on the three fragments using Bayesian inference (BI) (see Supplementary Methods). Sequence divergence (uncorrected *P* distance) was calculated in MEGA 7 (Kumar et

---

Open Access

Received: 28 June 2019; Accepted: 24 December 2019; Online: 04 March 2020

Foundation items: This work was supported by the National Natural Science Foundation of China (31872212) and Guangxi Key Laboratory of Rare and Endangered Animal Ecology, Guangxi Normal University (18-A-01-08)

DOI: 10.24272/j.issn.2095-8137.2020.018

al., 2016).

Morphometric data were taken using digital calipers to the nearest 0.1 mm. Measurements followed Fei et al. (1999) (Supplementary Methods). Comparative morphological data of *Amolops* were taken from previous publications (Anderson, 1871; Annandale, 1912; Bain et al., 2003, 2006; Bain & Truong, 2004; Dever et al. 2012; Dong et al., 2005; Fei et al., 2009; Inger & Chanard, 1997; Jiang et al., 2016; Liu et al., 2000; Lu et al. 2014; Lyu et al., 2018, 2019a, 2019b; Orlov & Ho, 2007; Pope, 1929; Rao & Wilkinson, 2007; Ray, 1999; Stuart et al., 2010; Sung et al., 2016; Wu & Tian, 1995; Yu et al., 2019; Yuan et al., 2018).

The specimens from Tuanjie Township represented a distinct lineage and sister taxon to the clade consisting of *A. akhaorum*, *A. archotaphus*, *A. mengdingensis*, *A. mengyangensis*, *A. daorum*, and *A. iriodes*, with strong support (Figure 1B). In addition, the new specimens possess a combination of morphological characters different from all known congeners. Therefore, we describe them as a new species of the genus *Amolops* below.

Taxonomic account

Amolops tuanjieensis **sp. nov.** (Figures 1C–J; Table 1)

Holotype: GXNU YU110005, adult male, collected on 18 April 2019 by Guo-Hua Yu from Tuanjie Township (N23°32'54.00", E99°20'12.00"; Figure 1A), Gengma Dai and Wa Autonomous County, Yunnan Province, China.

Paratypes: GXNU YU110003, GXNU YU110007, and GXNU YU110034, three adult females; GXNU YU110006, adult male, collected at the same time as the holotype from the type locality by Guo-Hua Yu.

Etymology: The specific epithet is named for the type locality, Tuanjie Township, Gengma Dai and Wa Autonomous County, Yunnan Province, China. We suggest the English common name as "Tuanjie cascade frog" and the Chinese common name as "团结湍蛙".

Diagnosis: *Amolops tuanjieensis* **sp. nov.** differs from other members in the genus *Amolops* by the following characters: (1) SVL 39.5–40.4 mm in males and 56.8–60.7 mm in females; (2) dorsolateral folds present; (3) side of head dark with light-colored upper lip stripe extending to axilla; (4) skin on dorsal and ventral surfaces smooth; (5) tympanum distinct, less than half of eye diameter; (6) supratympanic fold indistinct; (7) vomerine teeth in two oblique rows between choanae, closer to each other than to choanae; (8) top of head and dorsum brown-red with irregular black and gray spots; (9) loreal regions dark black; (10) lateral green; (11) pineal body present; (12) nuptial pad velvety; (13) two external subgular vocal sacs in males; (14) all fingertips expanded; (15) two palmar tubercles present; (16) inner metatarsal tubercle oval, outer metatarsal tubercle absent; (17) supernumerary tubercles absent.

Description of holotype (all measurements in mm; see Table 1): GXNU YU110005, adult male (SVL 39.5 mm); head longer

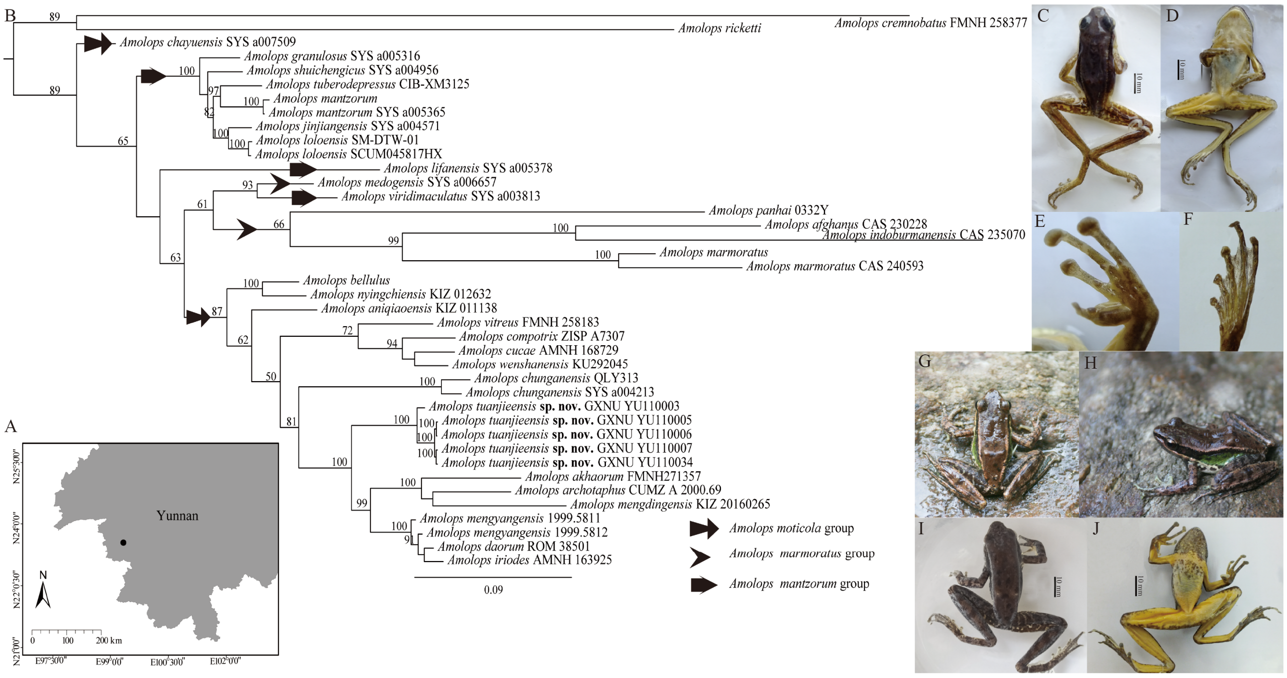

Figure 1 Collection site of *Amolops tuanjieensis* sp. nov. from Yunnan, China (A) and Bayesian phylogram of *Amolops* species inferred from a combination of 16S rRNA, *CO1*, and *ND2* (B). Dorsal (C) and ventral (D) views of holotype of *Amolops tuanjieensis* sp. nov. (GXNU YU110005) in preservative. Ventral view of hand (E) and foot (F) of holotype in preservative. Dorsal (G) and lateral (H) views of paratype of *Amolops tuanjieensis* (GXNU YU110034) in life and dorsal (I) and ventral (J) views of paratype (GXNU YU110034) in preservative Numbers above branches are Bayesian posterior probabilities (only values above 50% are shown).

Table 1 Measurements (mm) of holotype and paratypes of *Amolops tuanjieensis* sp. nov.

	GXNU YU110003	GXNU YU110005(Holotype)	GXNU YU110006	GXNU YU110007	GXNU YU110034
Sex	♀	♂	♂	♀	♀
SVL (Snout-Vent Length)	60.7	39.5	40.4	57.3	56.8
HL (Head Length)	20.2	13.7	14.7	18.6	18.6
HW (Head Width)	20.1	11.7	12.9	18.0	18.1
SL (Snout Length)	9.1	5.5	6.5	8.2	7.5
IND (Internarial Distance)	6.4	4.4	4.3	6.2	6.4
IOD (Interorbital Distance)	6.2	4.1	3.9	6.1	6.3
UEW (Upper Eyelid Width)	5.6	4.0	4.0	4.3	4.5
ED (Eye Diameter)	8.4	5.7	5.9	7.9	7.7
TD (Tympanum Diameter)	3.1	2.7	2.6	2.6	2.1
FHL (Forearm and Hand Length)	34.4	22.5	19.2	30.1	31.9
THL (Thigh Length)	31.1	20.6	20.3	29.4	33.7
TL (Tibia Length)	36.7	24.1	24.8	35.7	37.0
TFL (Length of Foot and Tarsus)	50.3	34.0	31.8	45.1	48.6
FL (Foot Length)	28.3	18.3	19.1	26.0	29.7
F3DSC (Horizontal Diameter of Digital Disc of Finger III)	3.1	1.9	1.6	2.3	3.1

(HL 13.7 mm) than wide (HW 11.7 mm); snout obtusely pointed, projecting beyond margin of lower jaw; canthus rostralis distinct; loreal region sloping, concave; nostrils oval, lateral, closer to eye than snout tip; internarial distance (IND 4.4 mm) larger than interorbital distance (IOD 4.1 mm); upper eyelid width (UEW 4.0 mm) narrower than interorbital space; tympanum distinct (TD 2.7 mm), less than half eye diameter (ED 5.7 mm); supratympanic fold indistinct; vomerine teeth in two oblique rows between choanae, closer to each other than to choanae; tongue attached anteriorly, cordiform deeply notched posteriorly (Figure 1C–D).

Forelimbs moderately long with slender fingers; relative length of fingers I<II<IV<III; all fingertips expanded into discs with circummarginal grooves; webbing between fingers absent; subarticular tubercles prominent and rounded, formula 1, 1, 2, 2; supernumerary tubercle present; two metacarpal tubercles, oval (Figure 1E).

Hindlimbs long, tibiotarsal articulation reaching beyond tip of snout; tibia length (TL 24.1 mm) longer than thigh length (THL 20.6 mm) and foot length (FL 18.3 mm); relative length of toes I<II<III<V<IV; all toe tips expanded into discs with circummarginal and transverse grooves; webbing between toes well developed, webbing formula I1–2II2–2III1–2IV2–1V; subarticular tubercles distinct, formula 1, 1, 2, 3, 2; inner metatarsal tubercle prominent, oval; outer metatarsal tubercle absent; supernumerary tubercles absent (Figure 1F).

Wide and flattened dorsolateral fold present; skin on dorsal and ventral surfaces smooth; dorsal limbs smooth; flanks granular; small warts above vent.

Color of holotype in life: Top of head and dorsum brown-red with irregular gray and dark spots; side of head black, from tip of snout, diffusing posteriorly to axilla, continuing as black streak below edge of dorsolateral fold; golden upper lip stripe extending to axilla; narrow golden stripe along above edge of dorsolateral fold; limbs dorsally brown with dark brown bars and irregular dark brown blotches; upper part of flanks green with dark blotches, lower part of flanks white with large dark blotches.

Color of holotype in preservative: Top of head and dorsum red-black; dorsal surface of limbs yellow with black bands; dorsolateral fold gray-white; lateral faded to black; throat, chest, venter, and ventral surface of limbs light yellow, scattered with light blotches on chest (Figure 1C–F).

Male secondary sexual characteristics: Adult males possess nuptial pads covering dorsal surface of base of first finger; two external subgular vocal sacs with slit-like opening at posterior of jaw.

Morphological variation: Measurements of holotype and paratypes are given in Table 1. The new species is sexually dimorphic, with females being obviously larger than males and having no vocal sacs or nuptial pads. Paratype GXNU YU110034 has more streaks on throat and chest than others (Figure 1G–J).

Distribution and ecology: The new species is known only from the type locality (Supplementary Figure S1). The holotype and paratypes were found on leaves and small branches, less than 1 m above the ground along a stream. No tadpoles or vocal recordings were collected for the new species.

Comparisons: Within the *A. monticola* group, the new species (SVL 39.5–40.4 mm in males, 56.8–60.7 mm in females) is distinguishable from *A. akhaorum* (SVL 34.9–37.2 mm in males), *A. chakrataensis* (SVL 55.0 mm in females), *A. chunganensis* (SVL 34.0–39.0 mm in males, SVL 44.0–54.0 mm in females), *A. daorum* (SVL 34.8–38.1 mm in males, SVL 53.3–57.6 mm in females), and *A. wenshanensis* (SVL 35.7–39.9 mm in males, SVL 43.7–45.6 mm in females) by having larger body size and from *A. aniqiaoensis* (SVL

52.0 mm in males), *A. bellulus* (SVL 45.9–50.1 mm in males, SVL 63.6 mm in females), *A. cucae* (SVL 40.7–44.6 mm in males, SVL 65.9–68.0 mm in females), *A. chayuensis* (SVL>42.0 mm in males), and *A. nyingchiensis* (SVL 48.5–58.3 mm in males) by having smaller body size. The new species further differs from *A. akhaorum*, *A. aniqiaoensis*, *A. archotaphus*, *A. compotrix*, *A. cucae*, *A. chayuensis*, *A. daorum*, *A. iriodes*, *A. mengyangensis*, *A. mengdingensis*, *A. vitreus*, and *A. wenshanensis* by dorsum red-brown (vs. green); from *A. archotaphus* and *A. chunganensis* by distinct dorsolateral folds present (vs. weakly developed); and from *A. bellulus* and *A. nyingchiensis* by vocal sacs present (vs. absent). *Amolops tuanjieensis* **sp. nov.** is further distinguished from *A. chakrataensis* by supratympanic fold absent (vs. distinct) and from *A. archotaphus*, *A. compotrix*, *A. cucae*, and *A. vitreus* by outer metatarsal tubercle absent (vs. present). The new species differs from *A. gerbillus* by distinct tympanum present (vs. small or indistinct) and finger webbing absent (vs. rudimentary webbing between fingers III and IV) and from *A. monticola* by dorsum brown-red (vs. dorsal surface brown or yellow), limb dorsally brown with dark brown bars (vs. upper surface of legs grayish, obscurely banded), and line from eye to glandular fold absent (vs. pale bluish line from eye along glandular fold present).

Amolops tuanjieensis **sp. nov.** differs from members of the *Amolops marmoratus* group (*A. afghanus* (Günther, 1858), *A. marmoratus* (Blyth, 1855), *A. medogensis* Li and Rao, 2005, *A. indoburmanensis* Dever, Fuiten, Konu and Wilkinson, 2012, and *A. panhai* Matsui and Nabhitabhata, 2006) by distinctive dorsolateral folds present (vs. absent).

Compared to the *Amolops mantzorum* group, *Amolops tuanjieensis* **sp. nov.** can be easily distinguished from *A. lifanensis* (Liu, 1945), *A. loloensis* (Liu, 1950), *A. mantzorum* (David, 1872), *A. tuberodepressus* Liu and Yang, 2000, *A. xinduqiao* (Fei, Ye, Wang, and Jiang, 2017), and *A. viridimaculatus* (Jiang, 1983) by dorsolateral folds present (vs. absent in all) and from *A. jinjiangensis* Su, Yang, and Li, 1986, *A. shuichengicus* Lyu and Wang, 2019, and *A. granulosus* (Liu and Hu, 1961) by having two external vocal sacs (vs. vocal sac absent in *A. jinjiangensis* and *A. shuichengicus* and vocal sac internal in *A. granulosus*).

In addition, *Amolops tuanjieensis* **sp. nov.** differs from *Amolops caelumnoctis* Rao & Wilkinson, 2007 and *Amolops splendissimus* Orlov & Ho, 2007, both of which occur in Yunnan but are not assigned to any species group, by having smaller body size (SVL 36.9–40.2 mm in males, SVL 64.3 mm in females vs. SVL 71.3–73.7 mm in males, SVL 78.0–90.6 mm in females in *A. caelumnoctis* and SVL 62.6–75.6 mm in males, SVL 69.3–96.8 mm in females in *A. splendissimus*), dorsolateral folds present (vs. absent), white upper lip stripe present (vs. absent), two external subgular vocal sacs present (vs. vocal sac absent), and light yellow spots on dorsum absent (vs. numerous small light yellow spots on dorsum present in *A. caelumnoctis* and *A. splendissimus*).

In China, there are ten other *Amolops* species that belong to three species groups, but are not distributed in Yunnan, including the *A. ricketti* group (*A. albispinus* Sung, Wang and Wang, 2016, *A. ricketti*, *A. sinensis* Lyu, Wang and Wang, 2019, *A. wuyiensis* (Liu and Hu, 1975), *A. yatseni* Lyu, Wang and Wang, 2019, and *A. yunkaiensis* Lyu, Wang, Liu, Zeng and Wang, 2018), *A. daiyunensis* group (*A. daiyunensis* (Liu and Hu, 1975) and *A. hongkongensis* (Pope and Romer, 1951)), and *A. hainanensis* group (*A. hainanensis* (Boulenger, 1900) and *A. torrentis* (Smith, 1923)) according to Lyu et al. (2019a). *Amolops tuanjieensis* **sp. nov.** can be distinguished from these species by distinctive dorsolateral folds present (vs. absent). Moreover, the new species differs from *A. albispinus*, *A. ricketti*, *A. sinensis*, *A. wuyiensis*, *A. yatseni*, *A. daiyunensis*, *A. hongkongensis*, *A. hainanensis*, and *A. torrentis* by two external subgular vocal sacs present (vs. absent in *A. albispinus*, *A. ricketti*, *A. sinensis*, *A. yatseni*, and *A. hainanensis*, and two internal vocal sacs present in *A. wuyiensis*, *A. daiyunensis*, *A. hongkongensis*, and *A. torrentis*).

Comments: In China, species of *Amolops* have been assigned to different species groups based on morphological characters (Fei et al., 2009). However, consistent with Lyu et al. (2019a), our phylogenetic analysis revealed that the division of some species groups needs further investigation. Firstly, *A. chayuensis*, which was placed in the *A. monticola* group by Sun et al. (2013) based on the presence of dorsolateral folds, did not group together with the clade consisting of the new species and other members of the same group, indicating that the *A. monticola* group is not monophyletic and that assignment of species groups based on dorsolateral folds only is problematic. Comprehensive morphological and molecular comparisons using *A. monticola* data are necessary to clarify the division of the *A. monticola* group.

In addition to the problems at the species group level in *Amolops*, species diversity within this genus also needs further investigation. *Amolops marmoratus*, which has been confused with *A. afghanus* and *A. indoburmanensis* (Dever et al., 2012; Lyu et al., 2019a), is mainly distributed in southern Tibet, as well as Myanmar, Bangladesh, Nepal, and eastern Himalaya in India (Frost, 2019), with distribution in Thailand according to Chan-ard (2003). This species is certainly known from Myanmar, but the statuses of other populations remain problematic (Frost, 2019). In this study, we found that the genetic distance between *A. marmoratus* from Thailand and *A. marmoratus* from Myanmar reached 4.48% for the 16*S* sequences, indicating that *A. marmoratus* from Thailand possibly represents a cryptic species.

NOMENCLATURAL ACTS REGISTRATION

The electronic version of this article in portable document format represents a published work according to the International Commission on Zoological Nomenclature (ICZN), and hence the new names contained in the electronic version are effectively published under that Code from the electronic edition alone (see Articles 8.5–8.6 of the Code). This published work and the nomenclatural acts it contains have been registered in

ZooBank, the online registration system for the ICZN. The ZooBank LSIDs (Life Science Identifiers) can be resolved and the associated information can be viewed through any standard web browser by appending the LSID to the prefixhttp://zoobank.org/.

Publication LSID:
urn:lsid:zoobank.org:pub:473C9146-DD0F-47DC-B65E-15419876E314.
Amolops tuanjieensis LSID:
urn:lsid:zoobank.org:act:1D52BBEE-8306-485F-AF87-692B9F2C3547.

SCIENTIFIC FIELD SURVEY PERMISSION INFORMATION

Permission for field surveys in Gengma County, Yunnan Province was granted by the Forestry Bureau of Gengma County.

SUPPLEMENTARY DATA

Supplementary data to this article can be found online.

COMPETING INTERESTS

The authors declare that they have no competing interests.

AUTHOR CONTRIBUTIONS

G.H.Y. and Z.J.W conceived and designed the study. Y.L.G performed the experiments, analyzed the data, and prepared the manuscript. G.H.Y. collected materials. All authors read and approved the final version of the manuscript.

ACKNOWLEDGEMENTS

We would like to thank Rui Cheng and Yong-Qi Wang for their technical support.

Yu-Lu Gan[1,2], Guo-Hua Yu[1,2,*], Zheng-Jun Wu[1,2,*]

[1] *Key Laboratory of Ecology of Rare and Endangered Species and Environmental Protection (Guangxi Normal University)*, *Ministry of Education*, *Guilin*, *Guangxi* 541004, *China*

[2] *Guangxi Key Laboratory of Rare and Endangered Animal Ecology*, *College of Life Science*, *Guangxi Normal University*, *Guilin*, *Guangxi* 541004, *China*

*Corresponding authors, E-mail: yugh2018@126.com; wu_zhengjun@aliyun.com

REFERENCES

Anderson J. 1871. A list of the reptilian accession to the Indian Museum, Calcutta, from 1865 to 1870, with a description of some new species. *The Journal of the Asiatic Society of Bengal*, **40**(2): 12−39.

Annandale N. 1912. Zoological results of the Abor expedition, 1911-1912. I. Batrachia. *Records of the Indian Museum*, **8**: 7−36.

Bain RH, Lathrop A, Murphy RW, Orlov NL, Cuc HT. 2003. Cryptic species of a cascade frog from Southeast Asia: taxonomic revisions and description of six new species. *American Museum Novitates*, **3417**: 1−60.

Bain RH, Nguyen TQ. 2004. Herpetofaunal diversity of Ha Giang Province in northeastern Vietnam, with descriptions of two new species. *American Museum Novitates*, **3453**: 1−42.

Bain RH, Stuart BL, Orlov NL. 2006. Three new Indochinese species of cascade frogs (Amphibia: Ranidae) allied to *Rana archotaphus*. *Copeia*, **2006**(1): 43−59.

Blyth E. 1855. Report of the Curator; Zoological Department, for March meeting. *The Journal of the Asiatic Society of Bengal*, **24**: 187−188.

Boulenger GA. 1900. On the reptiles, batrachians, and fishes collected by the late Mr. John Whitehead in the interior of Hainan. *Proceedings of the Zoological Society of London*, **4**: 956−962.

Chan-ard T. 2003. A Photographic Guide to Amphibians in Thailand. Bangkok, Thailand: Darnsutha Press Co., Ltd. (in Thai)

David A. 1872. Rapport adressé a MM. les Professeurs-Administráteurs du Museum d'histoire naturelle. *Nouvelles Archives du Muséum d'Histoire Naturelle*, **7**: 75−100.

Dever JA, Fuiten AM, Konu Ö, Wilkinson JA. 2012. Cryptic torrent frogs of Myanmar: An examination of the *Amolops marmoratus* species complex with the resurrection of *Amolops afghanus* and the identification of a new species. *Copeia*, **2012**(1): 57−76.

Dong BJ, Rao DQ, Lü SQ. 2005. *Amolops aniqiaoensis. In*: Zhao WG, Rao DQ, Lü SQ, Dong BJ. (Eds.), Herpetological Surveys of Xizang Autonomous Region 2. Medog. *Sichuan Journal of Zoology*, **24**: 250−253. (in Chinese)

Fei L, Hu SQ, Ye CY, Huang YZ. 2009. Fauna Sinica. Amphibia. Vol. 2 *Anura*. Beijing: Science Press, 957. (in Chinese)

Fei L, Ye CY, Huang YZ, Liu MY. 1999. Atlas of Amphibians of China. Zhengzhou, China: Henan Publishing House of Science and Technology Press, 432. (in Chinese)

Fei L, Ye CY, Wang YF, Jiang K. 2017. A new species of the genus *Amolops* (Anura: Ranidae) from high-altitude Sichuan, southwestern China, with a discussion on the taxonomic status of *Amolops kangtingensis*. *Zoological Research*, **38**(3): 138−145.

Frost DR. 2019. Amphibian Species of the World: and Online Reference. Version 6.0. New York, USA: American Museum of Natural History. Available from http://research.amnh.org/herpetology/amphibia/index.html/.

Günther AC. 1858. Catalogue of the Batrachia Salientia in the Collection of the British Museum. London: British Museum of Natural History, 160.

Inger RF, Chanard T. 1997. A new species of ranid frog from Thailand, with comments on *Rana livida* (Blyth). *Natural History Bulletin of the Siam Society*, **45**: 65−70.

Jiang K, Wang K, Yan F, Xie J, Zhou D, Liu W, Jiang J, Li C, Che J. 2016. A new species of the genus *Amolops*(Amphibia: Ranidae) from southeastern Tibet, China. *Zoological Research*, **37**(1): 31−40.

Jiang YM. 1983. A new species of genus *Staurois* (Ranidae)-*Staurois viridimaculatus*. *Acta Herpetologica Sinica*, **2**(3): 71. (in Chinese)

Kumar S, Stecher G, Tamura K. 2016. MEGA7: molecular evolutionary genetics analysis version 7.0 for bigger datasets. *Molecular Biology and Evolution*, **33**(7): 1870−1874.

Li PP, Rao DQ. 2005. *Amolops medogensis. In*: Zhao WG, Rao DQ, Lü SQ, Dong BJ. (Eds.), Herpetological Surveys of Xizang Autonomous Region 2. Medog. *Sichuan Journal of Zoology*, **24**: 250−253. (in Chinese)

Liu CC. 1945. New frogs from west China. *Journal of the West China Border Research Society, Series B*, **15**: 28−44.

Liu CC. 1950. Amphibians of Western China. *Fieldiana: Zoology Memoirs*, **2**: 4−400.

Liu CC, Hu SQ. 1961. Tailless Amphibians of China. Beijing: Science Press, 364. (in Chinese)

Liu CC, Hu SQ. 1975. Report on three new species of Amphibia from Fujian Province. *Acta Zoologica Sinica*, **21**: 265−271. (in Chinese)

Liu WZ, Yang DT, Ferraris C, Matsui M. 2000. *Amolops bellulus*: a new species of stream-breeding frog from western Yunnan, China (Anura: Ranidae). *Copeia*, **2000**(2): 536−541.

Liu WZ, Yang DT. 2000. A new species of *Amolops* (Anura: Ranidae) from Yunnan, China, with a discussion of karyological diversity in *Amolops*. *Herpetologica*, **56**(2): 231−238.

Lu B, Bi K, Fu JZ. 2014. A phylogeographic evaluation of the *Amolops mantzorum* species group: Cryptic species and plateau uplift. *Molecular Phylogenetics & Evolution*, **73**(1): 40−52.

Lyu ZT, Huang LS, Wang J, Li YQ, Chen HH, Qi S, Wang YY. 2019b. Description of two cryptic species of the *Amolops ricketti* group (Anura, Ranidae) from southeastern China. *Zookeys*, **812**: 133−156.

Lyu ZT, Wu J, Wang J, Sung YH, Liu ZY, Zeng ZC, Wang X, Li YY, Wang YY. 2018. A new species of *Amolops* (Anura: Ranidae) from southwestern Guangdong, China. *Zootaxa*, **4418**(6): 562−576.

Lyu ZT, Zeng Z, Wan H, Yang J, Li Y, Pang H, Wang Y. 2019a. A new species of *Amolops* (Anura: Ranidae) from China, with taxonomic comments on *A. liangshanensis* and Chinese populations of *A. marmoratus*. *Zootaxa*, **4609**(2): 247−268.

Matsui M, Nabhitabhata J. 2006. A new species of *Amolops* from Thailand (Amphibia, Anura, Ranidae). *Zoological Science*, **23**(8): 727−732.

Orlov NL, Ho CT. 2007. Two new species of cascade ranids of *Amolops* genus (Amphibia: Anura: Ranidae) from Lai Chau Province (Northwest Vietnam). *Russian Journal of Herpetology*, **14**(3): 211−229.

Pope CH. 1929. Four New Frogs from Fukien Province, China. New York: The American Museum of Natural History. (in Chinese)

Pope CH, Romer JD. 1951. A new Ranid frog (*Staurois*) from the colony of Hongkong. *Fieldiana Zoology*, **31**: 609−612.

Rao DQ, Wilkinson JA. 2007. A new species of *Amolops* (Anura: Ranidae) from southwest China. *Copeia*, **2007**(4): 913−919.

Ray P. 1992. Two new hill-stream frogs of the genus *Amolops Cope* (Amphibia: Anura: Ranidae) from Uttar Pradesh (India). *Indian Journal of Forestry*, **15**: 346−350.

Ray P. 1999. Systematic studies on the amphibian fauna of the District Dehradun, Uttar Pradesh, India. *Memoirs of the Zoological Survey of India*, **18**(3): 1−102.

Smith MA. 1923. On a collection of reptiles and batrachians from the island of Hainan. *Journal of the Natural History Society of Siam*, **6**: 195−212.

Stuart BL, Bain RH, Phimmachak S, Spence K. 2010. Phylogenetic systematics of the *Amolops monticola* group (Amphibia: Ranidae), with description of a new species from northwestern Laos. *Herpetologica*, **66**(1): 52−66.

Su CY, Yang DT, Li SM. 1986. A new species of *Amolops* from the Hengduan Shan Mountains. *Acta Herpetologica Sinica*, **5**: 204−206. (in Chinese)

Sun GZ, Luo WX, Sun HY, Zhang GY. 2013. A new species of cascade frog from Tibet: China-*Amolops chayuensis* (Amphibian: Ranidae). *Forestry Construction*, **20**(5): 14−16. (in Chinese)

Sung YH, Hu P, Wang J, Liu HL, Wang YY. 2016. A new species of *Amolops* (Anura: Ranidae) from southern China. *Zootaxa*, **4170**(3): 525−538.

Wu GF, Tian WS. 1995. A new *Amolops* Species from Southern Yunnan. *In*: Zhao E. (Ed.), Amphibian Zoogeographic Division of China. A Symposium Issued to Celebrate the Second Asian Herpetological Meeting Held at Ashgabat, Turkmenistan 6 to 10 September 1995. *Sichuan Journal of Zoology*, *Supplement*, 51-52. (in Chinese)

Yu GH, Wu ZJ, Yang JX. 2019. A new species of the *Amolops monticola* group (Anura: Ranidae) from southwestern Yunnan, China. *Zootaxa*, **4577**(3): 548−560.

Yuan Z, Jin J, Li J, Btuart BL, Wu J. 2018. A new species of cascade frog (Amphibia: Ranidae) in the *Amolops monticola* group from China. *Zootaxa*, **4415**(3): 498−512.

ZOOLOGICAL RESEARCH

A new species of the genus *Sinomicrurus* (Serpentes: Elapidae) from China and Vietnam

DEAR EDITOR,

A new species of *Sinomicrurus* Slowinski, Boundy, and Lawson, 2001 is described herein based on a series of specimens. The new species, *Sinomicrurus peinani* **sp. nov**., occurs in southern China and northern Vietnam. *Sinomicrurus peinani* **sp. nov**. is distinguished from its congeners by the following combination of characters: (1) 30–35 black cross-bands on body and tail; (2) 13 dorsal scale rows throughout, all smooth; (3) white belly with black cross-bands or irregular spots; (4) broad white transverse bar on top of head with inverted V-shaped anterior margin, white bar wider than anterior black bar; and (5) frontal V-like, 1.3 times as long as wide. In addition, new occurrences of *S. houi* in Guangxi, China, and Vietnam are discussed.

Sinomicrurus Slowinski, Boundy, and Lawson, is a group of small to medium-sized Asian coral snakes (Slowinski et al., 2001; Zhao, 2006). They are widely distributed in eastern and southeastern Asia, ranging from Nepal in the west to Japan in the east and from Hunan, China, in the north to Taiwan, China, in the south (Zhao, 2006).

Previously, members of the genus *Sinomicrurus* were contained within *Calliophis* Gray (Slowinski et al., 2001; Zhao et al., 1998). However, phylogenetic analyses based on morphological characters and cytochrome *b* sequences suggested that the Asian coral snakes fell into three major clades (Slowinski et al., 2001). Thus, Slowinski et al. (2001) erected a new genus *Sinomicrurus* to accommodate the northern tropical/subtropical mainland species, including *C. hatori* (Takahashi, 1930), *C. japonicas* (Günther, 1868), *C. kelloggi* (Pope, 1928), *C. macclellandi* (Reinhardt, 1844), and *C. sauteri* (Steindachner, 1913). Recently, Peng et al. (2018) described a new species from Hainan Island, China. Thus, six species are recognized presently within this genus.

In recent decades, a series of field surveys have been conducted in southern China (Guangxi) and Vietnam, involving the collection of several *Sinomicrurus* coral snakes. Further study based on morphological comparisons and genetic data indicated they were different from all putative species of this genus. Thus, we evaluated these specimens as a new species, which is described herein.

Twenty-one specimens of *Sinomicrurus* collected from China were morphologically examined (Supplementary Appendix S1). Scalation, color pattern, and body proportions were recorded and measured. Measurements of body and tail lengths were taken with a ruler to the nearest 1 mm; other measurements were taken with a slide caliper to the nearest 0.1 mm. Meristic characters were recorded on both sides. Ventral scales were counted following Dowling (1951). For comparison, characters of other *Sinomicrurus* species were taken from previous publications (Peng et al., 2018; Pope, 1935; Stejneger, 1907; Zhao, 2006; Zhao et al., 1998).

Abbreviations used for measurements and meristic characters are as follows: SVL (snout-vent length): distance between tip of snout and cloaca; TaL (tail length): distance between cloaca and tip of tail; DS: dorsal scales; VS: ventral scales; SC: subcaudal scales; IL: infralabials; SL: supralabials; Tem: temporals; Lo; Loreals; Poo: postoculars; Pro: preoculars; CB: number of cross-bands on body. All specimens are deposited in Yibin University (YBU), Sichuan, China.

In total, 25 individuals representing three Chinese species and one unidentified taxon were sequenced and analyzed (Supplementary Appendix S2). Genomic DNA was extracted from liver samples preserved in 85% alcohol using Tissue DNA kits (Omega Bio-Tek, Inc., USA). A partial sequence for the mitochondrial cytochrome c oxidase I (*COI*) was amplified

---

Received: 26 June 2019; Accepted: 30 January 2020; Online: 28 February 2020

Foundation items: This study was supported by the Strategic Priority Research Program of the Chinese Academy of Sciences (XDA 20050201, XDA19050303), National Natural Science Foundation of China (NSFC31372152), Southeast Asia Biodiversity Research Institute, Chinese Academy of Sciences (CAS) (Y4ZK111B01: 2017CASSEABRIQG002), International Partnership Program of CAS (152453KYSB20170033), and Animal Branch of the Germplasm Bank of Wild Species, CAS (Large Research Infrastructure Funding)

DOI: 10.24272/j.issn.2095-8137.2020.023

using the primer chmf/chmr and cycling parameters provided in Che et al. (2012). The double-stranded products were sequenced by a commercial company (Genewiz, China), with the sequences then edited manually using SeqMan in Lasergene v15.1 (DNASTAR Inc., USA) (GenBank accession Nos.: MN 685872–MN685896). An additional nine sequences representing *S. sauteri*, *S. hatori*, *S. macclellandi*, and *S. kelloggi* were retried from GenBank and added to the dataset for subsequent analyses (Supplementary Appendix S2). *Micrurus nigrocinctus* and *M. lemniscatus* were chosen as outgroups based on previous work (Pyron et al., 2013).

We reconstructed phylogenetic relationships using Bayesian inference (BI) and Maximum likelihood (ML) methods. Prior to analyses, the optimal evolutionary models for each codon position were selected using PartitionFinder under Bayesian Information Criterion (BIC) (Lanfear et al., 2012). BI analysis was performed using MrBayes v3.2.2 (Ronquist et al., 2012). All searches were performed with two independent runs, with each initiating a random tree. Each run consisted of four Markov chains (three heated and one cold chain) estimated for 5×10^6 million generations and sampled every 2 000 generations, with 25% of initial samples discarded as burn-in. Convergence was assessed by examining effective sample sizes (ESS) (ESS>200) and likelihood plots through time in TRACER v1.4 (Rambaut & Drummond, 2007). The resulting trees were combined to calculate posterior probabilities (PP) for each node in a 50% majority-rule consensus tree. The ML trees were constructed using RaxML v7.2.6 (Stamatakis, 2008) with the GTRCAT model under the same partitioning scheme as Bayesian analysis. Branch support was assessed using 1 000 non-parametric bootstrap (BS) topological replicates. Pairwise distances (*P*-distances) between in-group taxa were calculated in Mega 6.0 (Kumar et al., 2008; Tamura et al., 2013).

Taxonomy

Sinomicrurus peinani **sp. nov. (**Figure 1A–D; Table 1)

Holotype: YBU 16086, adult female, from Cangwu County (N23.65°, E111.56°), Guangxi, China, elevation of ~30 m a.s.l.; collected on 05 June 2016.

Paratypes (three specimens): YBU 16054, female; YBU 16066, male; YBU 16067, female. Same locality and date as holotype.

Diagnosis: All examined specimens possessed a small to medium-sized body, varying from 368 mm to 620 mm, as well as: (1) 30–35 black cross-bands on body and tail; (2) 13 dorsal scale rows throughout, all smooth; (3) white belly with black speckles or bands; (4) broad white transverse bar on top of head with inverted V-shaped anterior margin, white bar wider than anterior black bar; and (5) frontal V-like, 1.3 times as long as wide.

Description of holotype: Adult female. Total length 550 mm, tail length 45 mm. Body rather slender; head short, broad, and rounded with obtuse muzzle. Rostral trapezoidal, 1.5 times as broad as deep. Internasals large and square, slightly wider than long, in contact with each other and with rostral. Prefrontals pentagonal, length equal to width. Frontal V-shaped, nearly 1.3 times as long as wide. Supraoculars large, twice as long as broad, shorter than frontals. Parietals large, 1.6 times as long as broad. Single loreal, large; one preocular, longer than wide; two postoculars, one below other. Two temporals, one behind other, in contact with supralabials. Seven supralabials on each side, third and fourth bordering eye. Six infralabials, second smallest, first four touching chin-shield; two pairs of chin-shields, in contact with each other.

Dorsal scales in 13 rows throughout, all smooth. Ventrals 219+4, cloaca scale divided. Subcaudals 28, paired; dorsal tail scale rows reduced from six to four at sixth subcaudal. Tail short and tip pointed.

Dorsal surface brownish, with 27+3 regular, narrow, black transverse bands edged with yellow, each band in contact with cross-band on belly, forming closed ring. Quadrangular spots or irregular short bands between rings on belly. Black rings occasionally not reaching abdomen, forming half rings. Head black above with very broad white transverse bar behind eyes. Anterior margin inverted V-shaped white band, extending to prefrontals; posterior margin nearly straight, exceeding end of frontals; white bar wider than anterior black bar, yellowish white below, with 47+5 cross-bars or quadrangular spots.

Ecological notes: The specimens were found in meadowland in bamboo forest (Figure 1A). An individual of *Achalinus* sp. was found in the stomach of *Sinomicrurus peinani* **sp. nov**. No data on diet or reproduction are available.

Etymology: The species is named after Professor Pei-Nan Yu, a distinguished doctor in China, in recognition of his great contribution to the treatment of snakebite. We suggest the following common names for this species: “广西华珊瑚蛇” (Chinese) and Guangxi coral snake (English).

Description of paratypes: The three paratypes are similar to the holotype in body color and pattern. A summary of the morphological and meristic data of the three paratypes is given in Table 1.

Distribution: This species is currently known from China (Cangwu, Guangxi) and Vietnam (Cao Bằng and Vinh Phuc). The speciemens from Vietnam were unavailable for examination, but molecular phylogeney indicated that they should be conspecific with those from Cangwu, Guangxi, China (Supplementary Appendix S3).

Phylogenetic position: Both BI and ML analyses recovered a consistent topology, with slight disagreement in support values in some nodes (Figure 1C). In the BI tree, all individuals of *Sinomicrurus* formed a monophyly with high support (1.00 PP and 100% BS). Within *Sinomicrurus*, the two species (*S. sauteri* and *S. hatori*) endemic to Taiwan, China formed the basal lineage. *Sinomicrurus kelloggi* and the recently described *S. houi* Peng, Wang, Ding, Zhu, Luo, Yang, Huang, Lv, & Huang, 2017, formed a highly supported lineage (1.00 PP and 100% BS). All putative individuals of *S. macclellandi* formed a monophyly with high support indices (1.00 PP and 97% BS), which was sister to a well-supported monophyly

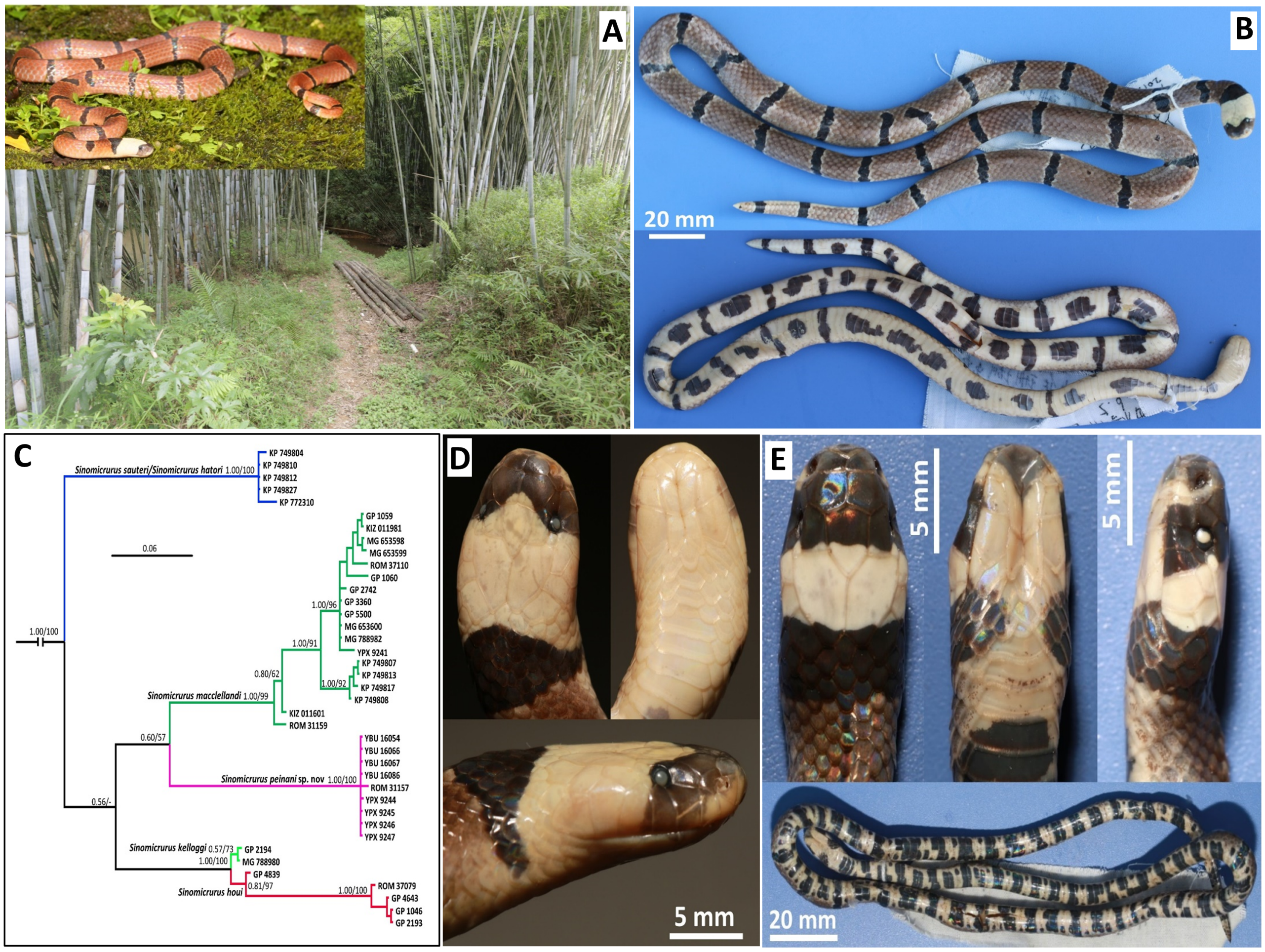

Figure 1 Holotype and phylogenetic position of *Sinomicrurus peinani* sp. nov.

A: General view of holotype (YBU 16086) in life and habitat of new species *Sinomicrurus peinani* **sp. nov.** B: Dorsal and ventral views of holotype (YBU 16086) in preservative. C: Bayesian 50% majority-rule consensus tree inferred from *COI*. Posterior probabilities and bootstrap support values for clades are shown adjacent to nodes to which they refer. D: Dorsal, ventral, and lateral views of head of holotype (YBU 16086) in preservative. E: Dorsal, ventral, and lateral views of head and ventral view of belly of *Sinomicrurus macclellandi* (YBU 14127) from Sichuan Province, China.

Table 1 Morphological characters of the type specimens of *Sinomcrurus peinani* sp. nov.

Specimens	Sex	SVL (mm)	TaL (mm)	DS	VS	SC	IL	SL	Tem	Lo	Poo	Pro	CB
YBU16086	F	550	45	13-13-13	210	28	7/7	6/6	1+1/1+1	0	2/2	1/1	27+3
YBU16054	F	575	45	13-13-13	208	27	7/7	6/6	1+1/1+1	0	2/2	1/1	26+3
YBU16066	M	335	33	13-13-13	217	28	7/7	6/6	1+1/1+1	0	2/2	1/1	31+4
YBU16067	F	500	49	13-13-13	225	28	7/7	6/6	1+1/1+1	0	2/2	1/1	32+4

For abbreviations, see text. F: Female; M: Male.

consisting of several individuals from Wuzhou and Guangxi, China and from Vietnam with poor support (0.60 PP and 57% BS). However, unexpectedly, all samples of *S. m. swinhoei* (Denburgh) were nested within the nominated subspecies (Figure 1C). In addition, two specimens from Guangxi, China and Vietnam formed a well-supported clade (97% BS) with all samples of *S. houi* from Hainan, China.

Uncorrected *P*-distances between each in-group taxa/lineage of *Sinomicrurus* ranged from 1.3% (between *S. sauteri* and *S. hatori*) to 14.6% (between *S. houi* and *S. macclellandi*) (Supplementary Appendix S4).

Based on a combination of morphological comparisons and molecular phylogenies, we deemed these specimens to represent an undescribed species, which we described herein.

Remarks

DNA barcoding based on *COI* is widely applied for rapid and unambiguous identification of species and can be used to screen for potentially cryptic species (Che et al., 2012; Liu et al., 2015). Our results indicated that the genetic distances between the new species and its congeners were much higher than that between other congeners (Supplementary Appendix S4), as well as that between other snakes (Liu et al., 2015), indicating that *Sinomicrurus peinani* **sp. nov.** should sever as a specific rank.

In addition to the large genetic distances between the new species and its congeners, *Sinomicrurus peinani* **sp. nov.** can also be differentiated by various phenotypic characters. The new species differs from *S. sauteri*, *S. hatori*, and *S. japonicus* by black longitudinal stripes on body absent (vs. present) (Günther, 1868; Steindachner, 1913; Takahashi, 1930). *Sinomicrurus peinani* **sp. nov.** is distinct from *S. houi* and *S. kelloggi* by 13 rows of dorsal scales throughout (vs. 15) and broad white band on top of head (vs. two narrow white bands) (Peng et al., 2018; Pope, 1928; Smith, 1943).

Sinomicrurus macclellandi currently contains four subspecies (Vogel, 2006). Besides the nominate form, which is mainly found in mainland China (Zhao, 2006), *S. m. swinhoei* (van Denburgh, 1912) is endemic to Taiwan, China, *S. m. iwasakii* (Maki, 1935) is endemic to Japan, and *S. m. univirgatus* (Günther, 1868) occurs in India and Nepal. *Sinomicrurus peinani* **sp. nov.** differs from *S. m. univirgatus* by its different body pattern, with the latter having black vertebral strip and transverse bars restricted to sides of body, or absent altogether (Günther, 1868). *Sinomicrurus peinani* **sp. nov.** can be distinguished from the other three subspecies by broad white transverse band with inverted V-shaped anterior margin on top of head (vs. two white bands with straight margin) and V-shaped frontal (vs. spindle-shaped frontal), small and not closely arranged cross-bands and spots (Figure 1D) (vs. more closely arranged black cross-bands and spots on belly, such that abdomen appears dark black, Figure 1E) (Reinhardt, 1844; Maki, 1935; van Denburgh, 1912; Zhao, 2006). *Sinomicrurus peinani* **sp. nov.** can be distinguished from *S. macclellandi* by white band on top of head wider than anterior black band vs. white band generally as wide as anterior black band. Historically, several other names have been allied to *S. macclellandi*, e.g., *Calliophis macclellandi gorei* Wall, 1910 and *Calliophis macclellandi concolor* Wall, 1925, with the first described from India and the latter described from Myanmar. Nevertheless, the new species differs from both by having black transverse bars on body (vs. without) (Wall, 1910, 1925).

Sinomicrurus houi Peng, Wang, Ding, Zhu, Luo, Yang, Huang, Lv, & Huang was originally described only from Hainan, China and was thus regarded as endemic to that area (Peng et al., 2018). However, our molecular phylogenetic results suggested that several closely situated specimens from Guangxi, China and Vietnam formed a monophyly with *S. houi* from Hainan, China indicating that *S. houi* may occur on the Asian mainland and may not be endemic to Hainan, China alone. Unexpectedly, the *S. m. swinhoei* samples were nested within those from mainland China (*S. m. macclellandi*), indicating that the intraspecific relationship and taxonomy of *S. macclellandi* need to be further studied.

NOMENCLATURAL ACTS REGISTRATION

The electronic version of this article in portable document format represents a published work according to the International Commission on Zoological Nomenclature (ICZN), and hence the new names contained in the electronic version are effectively published under that Code from the electronic edition alone (see Articles 8.5–8.6 of the Code). This published work and the nomenclatural acts it contains have been registered in ZooBank, the online registration system for the ICZN. The ZooBank LSIDs (Life Science Identifiers) can be resolved and the associated information can be viewed through any standard web browser by appending the LSID to the prefixhttp://zoobank.org/.

Publication LSID:
urn:lsid:zoobank.org:pub:DB71DFD6-4CE8-448C-8217-926E055D626E.
Sinomicrurus peinani LSID:
urn:lsid:zoobank.org:act:8FF100CF-421D-4769-A343-D7B93B02DACC.

SCIENTIFIC FIELD SURVEY PERMISSION INFORMATION

This field survey was approved by the Department of Forestry of Guangxi Zhuang Autonomous Region, China and Vietnam Adiministration of Forestry (982/TCLN-BTTN).

SUPPLEMENTARY DATA

Supplementary data to this article can be found online.

COMPETING INTERESTS

The authors declare that they have no competing interests.

AUTHORS' CONTRIBUTIONS

Q.L., P.G., and J.C. designed the study; P.G., J.W.Y., P.W., S.N.N., and R.W.M. collected specimens; P.G. collected morphological data; Q.L. and S.B.H. collected genetic data; Q.L. performed molecular and phylogenetic analyses and prepared the manuscript; P.G. and J.C. revised the manuscript. All authors read and approved the final version of the manuscript.

ACKNOWLEDGEMENTS

We appreciate P.L. Yu, Y.L. Xie, J.X. Yang, Z.J. Zhang, K. Jiang, N. Orlov, and K. Li for assistance in field work; M. Yu, D. Wang, J.Q. Jin, and H.M. Chen for assistance in lab work; G.H. Zhong for drawing the map; and K. Jiang for providing references. We thank the Department of Forestry of Guangxi for permission to undertake field survey. We would like to thank Vietnam Administration of Forestry issued the permit and provided local helps during the fieldwork. We extend our sincere gratitude to Amy Lathrop (Royal Ontario Museum, Canada) for the help during the tissue loan.

Qin Liu[1], Jiao-Wen Yan[2], Shao-Bing Hou[3,4], Ping Wang[1],
Sang Ngoc Nguyen[5], Robert W. Murphy[6], Jing Che[3,*],
Peng Guo[1,*]

[1] *College of Life Sciences and Food Engineering*, *Yibin University*, *Yibin*, *Sichuan* 644007, *China*
[2] *Fisheries*, *Animal* & *Veterinary Sciences Bureau of Cangwu County*, *Wuzhou*, *Guangxi* 543115, *China*
[3] *State Key Laboratory of Genetic Resources and Evolution*, *Kunming Institute of Zoology*, *Chinese Academy of Sciences*, *Kunming*, *Yunnan* 650223, *China*
[4] *Kunming College of Life Science*, *University of Chinese Academy of Sciences*, *Kunming*, *Yunnan* 650204, *China*
[5] *Institute of Tropical Biology*, *Vietnam Academy of Science and Technology (VAST)*, *Ho Chi Minh City*, *Vietnam*
[6] *Centre for Biodiversity and Conservation Biology*, *Royal Ontario Museum*, *Toronto*, *Ontario M5S 2C6*, *Canada*
*Corresponding authors, E-mail: chej@mail.kiz.ac.cn; ybguop@163.com

REFERENCES

Che J, Chen HM, Yang JX, Jin JQ, Jiang K, Yuan ZY, Murphy RW, Zhang YP. 2012. Universal COI primers for DNA barcoding amphibians. *Molecular Ecology Resource*, **12**(2): 247−258.

Dowling HG. 1951. A proposed standard system of counting ventrals in snakes. *British Journal of Herpetology*, **1**(5): 97−99.

Günther A. 1868. Sixth account of new species of snakes in the collection of the British Museum. *Annals and Magazine of Natural History*, **4**(1): 413−429.

Kumar S, Nei M, Dudley J, Tamura K. 2008. MEGA: a biologist-centric software for evolutionary analysis of DNA and protein sequences. *Briefings in Bioinformatics*, **9**(4): 299−306.

Lanfear R, Calcott B, Ho SYW, Guindon S. 2012. PartitionFinder: combined selection of partitioning schemes and substitution models for phylogenetic analyses. *Molecular Biology and Evolution*, **29**(6): 1695−1701.

Liu Q, Zhu F, Zhong GH, Wang YY, Fang M, Xiao R, Cai YS, Guo P. 2015. COI-based barcoding of Chinese vipers (Reptilia: Squamata: Viperidae). *Amphibia-Reptilia*, **36**(4): 361−372.

Maki M. 1935. A new poisonous snake (*Calliophis iwasakii*) from Loo-Choo. *Transactions of the Natural History Society of Formosa, Taihoku*, **25**: 216−219.

Peng LF, Wang LJ, Ding L, Zhu YW, Luo J, Yang DC, Huang RY, Lv SQ, Huang S. 2018. A new species of the genus *Sinomicrurus* Slowinski, Boundy and Lawson, 2001(Squamata: Elapidae) from Hainan Province, China. *Asian Herpetological Research*, **9**(2): 65−73.

Pope CH. 1928. Seven new reptiles from Fukien Province, China. *American Museum Novitates*(320): 1−6.

Pope CH. 1935. The Reptiles of China: Turtles, Crocodilians, Snakes, Lizards. New York: American Museum of Natural History.

Pyron RA, Burbrink FT, Wiens JJ. 2013. A phylogeny and revised classification of Squamata, including 4161 species of lizards and snakes. *BMC Evolutionary Biology*, **13**(1): 93.

Rambaut A, Drummond AJ. 2007(2018-03-23). Tracer v 1.4. http://tree.bio.ed.ac.uk/software/tracer.

Reinhardt JT. 1844. Description of a new species of venomous snake, *Elaps Macclellandi*. *Calcutta Journal of Natural History*, **4**: 532−534.

Ronquist F, Teslenko M, van der Mark P, Ayres DL, Darling A, Höhna S, Larget B, Liu L, Suchard MA, Huelsenbeck JP. 2012. MrBayes 3.2: efficient Bayesian phylogenetic inference and model choice across a large model space. *Systematic Biology*, **61**(3): 539−542.

Slowinski JB, Boundy J, Lawson R. 2001. The phylogenetic relationships of Asian coral snakes (Elapidae: *Calliophis* and *Maticora*) based on morphological and molecular characters. *Herpetologica*, **57**(2): 233−245.

Smith MA. 1943. The Fauna of British India, Ceylon and Burma, Including the whole of the Indo-Chinese Sub-region. Reptilia and Amphibia, Vol. III, Serpentes. London: Taylor & Francis Ltd.

Stamatakis A, Hoover P, Rougemont J. 2008. A rapid bootstrap algorithm for the RAxML web servers. *Systematic Biology*, **75**(5): 758−771.

Steindachner F. 1913. Über zwei neue Schlangenarten aus Formosa. *Anzeiger der Kaiserlichen Akademie der Wissenschaften in Wien, Mathematisch-Naturwissenschaftliche Klasse*, **50**: 218−220.

Stejneger LH. 1907. Herpetology of Japan and Adjacent Territory. Washington: Bulletin of United States National Museum.

Takahashi S. 1930. Synopsis of the Terrestrial Snakes of JapanTokyo: Shunyo-do. (in Japanese)

Tamura K, Stecher G, Peterson D, Filipski A, Kumar S. 2013. MEGA6: molecular evolutionary genetics analysis version 6.0. *Molecular Biology and Evolution*, **30**(12): 2725−2729.

van Denburgh J. 1912. Concerning certain species of reptiles and amphibians from China, Japan, the Loo Choo Islands, and Formosa. *Proceedings of the California Academy of Sciences*, **3**(10): 187−258.

Vogel G. 2006. Venomous Snakes of Asia. Frankfurt am Main: Edition Chimaira.

Wall F. 1910. Notes on snakes collected in Upper Assam. Part II. *The Journal of the Bombay Natural History Society*, **19**(4): 825−845.

Wall F. 1925. Notes on snakes collected in Burma in 1924. *The Journal of the Bombay Natural History Society*, **30**(4): 805−821.

Zhao EM, Huang MH, Zong Y. 1998. Fauna Sinica: Reptilia Vol. 3. Squamata Serpentes. Beijing: Science Press. (in Chinese)

Zhao EM. 2006. Snakes of China (I). Hefei: Anhui Sciences and Technology Publishing House. (in Chinese)

ZOOLOGICAL RESEARCH

Preliminary study on fine structures of subcortical nuclei in rhesus monkeys by *ex vivo* 9.4 T MRI

DEAR EDITOR,

Changes in fine structures of the brain over a life span can have robust effects on neural activity and brain function, which both play crucial roles in neurodegenerative diseases. Clinically, however, low-resolution MRI only provides limited information about fine brain structures. Here, using high-resolution 9.4 T MRI, we established a set of structural images and explored the fine structures of the claustrum, hippocampus, amygdala complex, and subregions of the amygdala complex (BLA, including lateral, basal, and accessory basal subnuclei) in rhesus macaque (*Macaca mulatta*) brains. Based on these high-resolution images, we were able to discriminate the subregional boundaries accurately and, at the same time, obtain the volume of each brain nuclei. Thus, advanced high-resolution 9.4 T MRI not only provides a new strategy for early diagnosis of neurodegenerative diseases, but also provides the ability to observe fine structural changes in the brain across a life span.

The basolateral complex of the amygdala (BLA), including the lateral, basal, and accessory basal subnuclei, is an important region receiving information from the cortex and subcortical nuclei, including the hippocampus, and transferring information to other parts of the amygdala (Huang et al., 2013; Pikkarainen et al., 1999; Sah et al., 2003; Saunders et al., 1988). Neuroimaging studies have significantly expanded our knowledge of brain structure and function during postnatal development and aging, as well as the progression of neurological and psychological disorders (Knickmeyer et al., 2010; Shaw et al., 2008; Sowell et al., 2002a, 2002b). The introduction of 9.4 T MRI technology has greatly facilitated subcortical classification of brain regions with fine dimensions (Kwan et al., 2017). With its high resolution, we can accurately discriminate subregional boundaries and obtain the volume of each brain nucleus. As an advanced imaging device, 9.4 T MRI provides a new strategy for the early diagnosis of neurodegenerative diseases and can further clarify fine structural changes in the central nervous system over a life span.

Three female rhesus monkeys aged from 12 to 20 years old were used in this study. Postmortem brains of the monkeys were provided by the Kunming Primate Research Center (KPRC) of the Chinese Academy of Sciences (CAS). Details on age and brain volume are provided in Table 1. The brains were acquired following approved protocols from the Kunming Institute of Zoology (KIZ), CAS. Briefly, the monkeys were deeply anesthetized with an overdose of sodium pentobarbital (50 mg/kg i.m.) and perfused transcardially with 0.9% saline followed by 10% buffered formalin. The brains were removed from the skulls and submerged in a 500 mL solution of 4% paraformaldehyde (PFA). Each brain was positioned in an oval-shaped container filled with FOMBLIN® perfluoropolyether (Solvay Specialty Polymers, Italy). The container was generated by 3D printing and was adapted to the outer surface of the brain so that the brain tissue was held steady during scanning. Brains immersed in perfluoropolyether were vacuumed for at least 3 d under 0.1 atmospheric pressure to remove all air bubbles in the sample before the MRI scans. One half of each brain was selected and cut into 50 μm sections through the amygdala along the horizontal plane. Sections were stained with Cresyl violet. All animal care and experimental procedures were carried out in strict accordance with the guidelines for the National Care and Use of Animals approved by the National Animal Research Authority (China) and the Institutional Animal Care and Use Committee (IACUC) of KIZ, CAS, and were approved by the Ethics Committee of KIZ and KPRC, KIZ, CAS (AAALAC

Received: 05 September 2019; Accepted: 30 December 2019; Online: 06 January 2020

Foundation items: This work was supported by the Chinese Academy of Sciences (Y406541141 and 1100050210), National Natural Science Foundation of China (91649119), and Ministry of Science and Technology of China (2015CB755605 and 2016YFC1305902) to J.L.L., National Natural Science Foundation of China (91649101), National Key Research and Development Program of China (2016 YFC1300500-503), Hefei Science Center (2017HSC-KPRD003), and Hefei Institutes of Physical Science (YZJJ201702) to K.Z.

DOI: 10.24272/j.issn.2095-8137.2020.013

Table 1 Specimen information

Specimen ID	Age (Years)	Brain volume (mL)	Cerebellum volume (cm^3)	Hippocampus		Amygdala		Lateral nucleus (L)		Basal nucleus (B)		Accessory basal nucleus (AB)		Claustrum	
				Left	Right	Left	Right	Left	Right	Left	Right	Left	Right	Left	Right
05076	12	73	8.02	482.868	477.4	192.81	196.56	54.34	61.74	36.71	42.48	59.2	60.68	170.345	176.97
00006	18	93	8.57	528.901	539.1	193.62	204.06	50.46	58.59	46.22	44.61	61.72	60.67	200.424	182.19
98374	20.3	93	8.22	528.901	560.6	253.79	262.58	63.51	70.98	38.82	38.45	66.24	67.37	172.501	186.77

accredited).

MRI was performed on a 9.4 Tesla 40 cm MRI system (a superconducting magnet of 9.4 T/400 PS, Agilent Inc., USA, equipped with Avance HD BioSpec console, Bruker BioSpin MRI GmbH, Germany) with a patented transceiver coil. To acquire high-quality MRI images, a newly patented conformal radiofrequency (RF) coil (Chinese Patent application 201710191106.8) based on the standard quadrature RF excitation/receive configuration was used. To achieve high sensitivity, the coil was designed with half open brain-conformal surface mode and composed of 16 distributed resonant elements with quadrature ports. Therefore, only one ^{1}H channel was used but with sufficient sensitivity for high-resolution imaging. The maximal inner diameter of the coil was 95 mm, which is appropriate to hold the container and produce RF-illuminating volume for the entire brain.

For each macaque brain, T_2* weighted images of FLASH (Fast Low Angle Shot) 2D and 3D sequences were acquired. The 2D images were acquired with the following settings: TR/TE=2 900 ms/14 ms, flip angle=80°, resolution=208 μm×182 μm, slice thickness=0.5 mm, matrix size=384×384, 104 slices, acquisition time=18 m 30 s, band kHz. The FLASH 2D images were acquired eight times separately and averaged to achieve high-resolution images with a better signal-to-noise ratio (SNR). For the 3D images, the following settings were applied: TR/TE=45 ms/13 ms, flip angle=10°, voxel size=155 μm×155 μm×155 μm, matrix size=515×420×354, acquisition time=1 h 51 m 30 s, band kHz.

Currently, there is no precedent for subfield segmentation of the amygdala. In addition, standard analysis software cannot perform automatic segmentation of the amygdala subfields at the above resolution. Manual segmentation of 9.4 T images can be achieved with reference to an atlas (Saleem & Logothetis, 2012) using the ITK-SNAP package. Here, MRI segmentation of the hippocampus, amygdala, basolateral complex in the amygdala (BLA, including the lateral, basal, and accessory basal nuclei), and claustrum were manually performed with reference to the atlas "A Combined MRI and Histology Atlas of the Rhesus Monkey Brain in Stereotaxic Coordinates" (Saleem & Logothetis, 2012). The atlas, which also contains histological sections and images, clearly shows the boundaries of each nucleus for segmentation. The segmented regions were only regions of interest (ROI) and did not exactly match specific histological nuclei. The subregions of interest in the amygdala (sROI) were close to the BLA (ROIs of lateral nucleus, basal nucleus, and accessory basal nucleus, briefly denoted as L, B, AB, and claustrum).

To segment the fine structures on MRI images correctly, both MRI resolution and contrast are crucial parameters. Compared to histological sections before (Figure 1B, middle panel) and after staining (Figure 1B, right panel), the shapes of the subfields in the amygdala on MRIs closely matched those of the subfields in the corresponding histological staining section. This finding laid the foundation for our segmentation of MRI images. After 9.4 T MRI segmentation, we obtained a more accurate nucleus volume than that achieved using 3 T MRI, which was limited by voxel-like reconstruction (voxel size=310 μm×310 μm×300 μm) (Figure 1A). Image intensity was corrected to remove bias before quantitative image segmentation. Image contrast between the amygdala, hippocampus, and claustrum (Figure 1A) was sufficient to identify the landmarks of their structures; however, it was difficult to distinguish the boundaries of each subfield in the BLA and claustrum from the 3 T MRI images (uMR 790 United Imaging Inc., China). The 3D T2 sequences at 3 T were acquired with the following settings: TR=2 500 ms, TE=440.8 ms, flip angle=58°, averages=2, time=30 min, echo chain length=120, matrix size=512×512×300, FOV=80 mm×80 mm, voxel size: 800 μm×800 μm×800 μm. At the same time, by comparing the histological sections with the MRI images, we found that the MRI images exhibited strong similarity with images from low magnification microscopy. With 3 T MRI images, this could be helpful for locating the boundaries of deep brain nuclei due to the large volume of brain tissue in non-human primates. However, in order to explore the spatial location of deep nuclei in the brain, high-resolution MRI is also necessary.

To discriminate the fine structures of the subcortical nuclei, the ROIs of the hippocampus, amygdala, and BLA were segmented and depicted (Figure 1C). The boundaries of the sROIs were manually delineated for each image in the horizontal plane. The volumes of the sROIs were then obtained in ITK-SNAP after completing segmentation. As the sample brains were formalin-fixed and firmly attached in the device during the MRI scans, there were no respiratory disturbances, as are found in live monkeys, so averaging the multiple scans significantly improved the SNR. Thus, the volumes of the hippocampus, amygdala, claustrum, and amygdala subfields were more precise using the 9.4 T MRI images due to the higher resolution and smaller error of the ultra-high magnetic field strength.

In this study, using ultra-high-resolution 9.4 T MRI, we

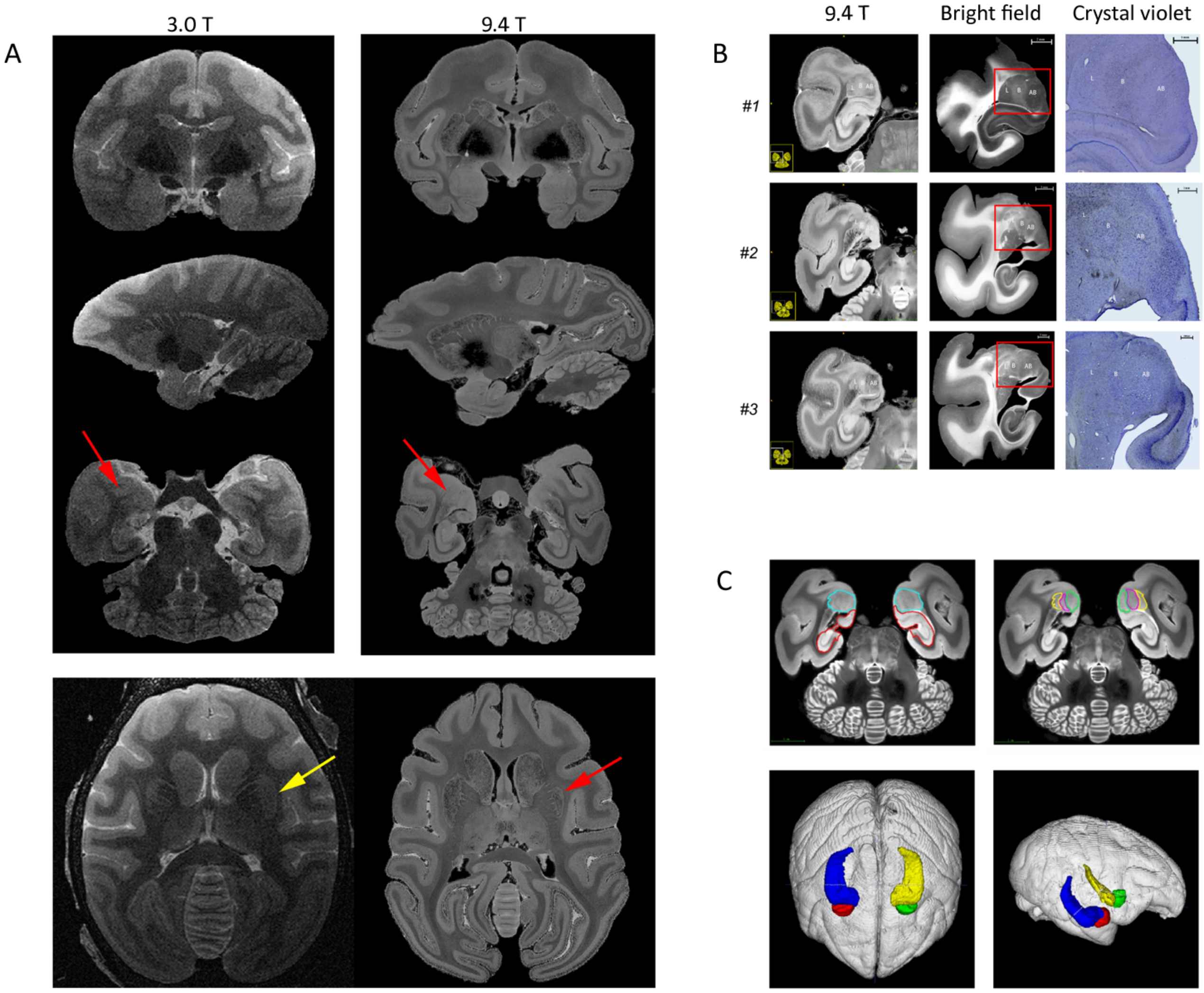

Figure 1 Comparison of 3 T and 9.4 T MRI images of rhesus monkey brains

A: MRI images of coronal (top row), sagittal (middle row), and horizontal (bottom row) planes acquired at 3 T 3D FLASH (left column) and 9.4 T 3D FLASH (right column). Red arrows indicate location of amygdala. Amygdala subfields are more easily identified on 9.4 T MRI images than on 3 T MRI images. Region (reconstruction voxel size: 310 μm×310 μm×300 μm, yellow arrow) of claustrum is obscured in 3 T MRI slice, especially right side of brain. In contrast, 9.4 T MRI images (voxel size: 155 μm×155 μm×155 μm, red arrow) easily show boundary of claustrum. B: Representative images of 9.4 T 2D FLASH MRI, bright field (black background), and crystal violet staining of right amygdala at each age stage. One monkey brain from each age group was selected for section staining. Each row represents right-side of amygdala of sample brain, which was cut and photographed. Left column shows horizontal MRI images close to position of sections in middle column. Middle column shows sections before staining. Staining of ROIs in red frame is shown in right column. Subnuclei in amygdala can be seen clearly on MRI images and sections before and after crystal violet staining (amygdala subfield: L: Lateral nuclei, B: Basal nuclei, AB: Accessory basal nuclei). Scale bars: 1 mm. C: Manual segmentation of amygdala and hippocampus. With high-resolution, 9.4 T MRI images show clear boundaries of each amygdala subregion. 3D models show exact positions of bilateral amygdala and hippocampus in monkey brains.

observed the fine structures in the amygdala, hippocampus, and BLA in the rhesus macaque brain. In contrast, the fine structures were not sufficiently clear for segmentation when using 3 T MRI. Clinically, psychological disturbances related to emotion and memory usually involve the amygdala, hippocampus, and their association (Sharp 2017; Yang & Wang, 2017). The BLA is the information entrance to the amygdala from the cortex and subcortical regions, such as the hippocampus. The lateral nucleus in the BLA is responsible for receiving extrinsic sensory information from the sensory thalamus and sensory cortices, and for output to other amygdala nuclei, including the basal and accessory basal nuclei (Janak & Tye, 2015; Pitkanen & Amaral, 1998). The BLA has reciprocal connections with the cortex and hippocampus, and thus information from the BLA can have a broad influence throughout the cortex (Saunders et al., 1988). Thus, by segmentation of all deep nuclei within fine brain structures, we can accurately obtain their volumes.

The current study was based on high-resolution 9.4 T MRI scans of *ex-vivo* rhesus macaque brains. The next step will be to undertake anatomical research of rhesus macaque brains *in-vivo* and to obtain high-resolution MRI images over their entire lifespan. Such research can supplement histological studies, which can lose information on fine structural changes over long periods of time. In addition, because of the large volume of brain tissue in rhesus monkeys, tissue removal by optical techniques is not ideal for understanding the spatial structures of deep brain nuclei. Therefore, high-resolution MRI images are essential for studying the fine structures of the brain, especially deep nuclei.

In conclusion, our findings suggest that the use of ultra-high-resolution MRI images to display the microstructures of the brain is an essential technique. In the future, it would be interesting to identify the connections among subcortical nuclei in the brains of live macaques following behavioral training and testing using simultaneous fMRI.

COMPETING INTERESTS

The authors declare that they have no competing interests.

AUTHORS' CONTRIBUTIONS

J.L.L. and K.Z. initiated the project. H.Z.C. and H.Y.Y. designed the experiments. J.L.L. organized and supervised the whole project. H.Z.C. collected macaque brain samples and performed perfusion and fixation; H.Y.Y. and H.Z.C. performed MRI scanning and data collection; H.Z.C., K.Z., and J.L.L. drafted the manuscript, with input from all other authors. All authors read and approved the final version of the manuscript.

Huan-Zhi Chen[1,3], Hong-Yi Yang[2], Kai Zhong[2,5],
Jia-Li Li[1,4,6,*]

[1] *Key Laboratory of Animal Models and Human Disease Mechanisms of Chinese Academy of Sciences* & *Yunnan Province*, *Kunming Institute of Zoology*, *Chinese Academy of Sciences*, *Kunming*, *Yunnan* 650223, *China*
[2] *High Magnetic Field Laboratory*, *Hefei Institutes of Physical Science*, *Chinese Academy of Sciences*, *Hefei*, *Anhui* 230031, *China*
[3] *Kunming College of Life Science*, *University of Chinese Academy of Sciences*, *Kunming*, *Yunnan* 650223, *China*
[4] *CAS Center for Excellence in Animal Evolution and Genetics*, *Chinese Academy of Sciences*, *Kunming*, *Yunnan* 650223, *China*
[5] *CAS Center for Excellence in Brain Science and Intelligence Technology*, *Chinese Academy of Sciences*, *Hefei*, *Anhui* 230031, *China*
[6] *Kunming Primate Research Center of the Chinese Academy of Sciences*, *Kunming Institute of Zoology*, *Chinese Academy of Sciences*, *Kunming*, *Yunnan* 650223, *China*

*Corresponding author, E-mail: lijiali@mail.kiz.ac.cn

REFERENCES

Huang Y, Coupland NJ, Lebel RM, Carter R, Seres P, Wilman AH, Malykhin NV. 2013. Structural changes in hippocampal subfields in major depressive disorder: a high-field magnetic resonance imaging study. *Biological Psychiatry*, **74**(1): 62−68.

Janak PH, Tye KM. 2015. From circuits to behaviour in the amygdala. *Nature*, **517**(7534): 284−292.

Knickmeyer RC, Styner M, Short SJ, Lubach GR, Kang C, Hamer R, Coe CL, Gilmore JH. 2010. Maturational trajectories of cortical brain development through the pubertal transition: unique species and sex differences in the monkey revealed through structural magnetic resonance imaging. *Cerebral Cortex*, **20**(5): 1053−1063.

Kwan BYM, Salehi F, Kope R, Lee DH, Sharma M, Hammond R, Burneo JG, Steven D, Peters T, Khan AR. 2017. Evaluation of ex-vivo 9.4 T MRI in post-surgical specimens from temporal lobe epilepsy patients. *Journal of Neuroradiology*, **44**(6): 377−380.

Pikkarainen M, Ronkko S, Savander V, Insausti R, Pitkanen A. 1999. Projections from the lateral, basal, and accessory basal nuclei of the amygdala to the hippocampal formation in rat. *The Journal of Comparative Neurology*, **403**(2): 229−260.

Pitkanen A, Amaral DG. 1998. Organization of the intrinsic connections of the monkey amygdaloid complex: projections originating in the lateral nucleus. *The Journal of Comparative Neurology*, **398**(3): 431−458.

Sah P, Faber ES, Lopez De Armentia M, Power J. 2003. The amygdaloid complex: anatomy and physiology. *Physiological Reviews*, **83**(3): 803−834.

Saleem KS, Logothetis NK. 2012. A Combined MRI and Histology Atlas of the Rhesus Monkey Brain in STereotaxic Coordinates. Amsterdam Boston: Academic Press.

Saunders RC, Rosene DL, Van Hoesen GW. 1988. Comparison of the efferents of the amygdala and the hippocampal formation in the rhesus monkey: II. Reciprocal and non-reciprocal connections. *The Journal of Comparative Neurology*, **271**(2): 185−207.

Sharp BM. 2017. Basolateral amygdala and stress-induced hyperexcitability affect motivated behaviors and addiction. *Translational Psychiatry*, **7**(8): e1194.

Shaw P, Kabani NJ, Lerch JP, Eckstrand K, Lenroot R, Gogtay N, Greenstein D, Clasen L, Evans A, Rapoport JL, Giedd JN, Wise SP. 2008. Neurodevelopmental trajectories of the human cerebral cortex. *The Journal of Neuroscience: The Official Journal of the Society for Neuroscience*, **28**(14): 3586−3594.

Sowell ER, Thompson PM, Peterson BS, Mattson SN, Welcome SE, Henkenius AL, Riley EP, Jernigan TL, Toga AW. 2002a. Mapping cortical gray matter asymmetry patterns in adolescents with heavy prenatal alcohol exposure. *NeuroImage*, **17**(4): 1807−1819.

Sowell ER, Thompson PM, Rex D, Kornsand D, Tessner KD, Jernigan TL, Toga AW. 2002b. Mapping sulcal pattern asymmetry and local cortical surface gray matter distribution in vivo: maturation in perisylvian cortices. *Cerebral Cortex*, **12**(1): 17−26.

Yang Y, Wang JZ. 2017. From structure to behavior in basolateral amygdala-hippocampus circuits. *Frontiers in Neural Circuits*, **11**: 86.

ZOOLOGICAL RESEARCH

Hyperactive reactive oxygen species impair function of porcine Sertoli cells via suppression of surface protein ITGB1 and connexin-43

DEAR EDITOR,

Gap junctions regulate intercellular communication between Sertoli cells and germ cells in male testes and play vital functions in spermatogenesis. Many factors in animal breeding and husbandry can induce oxidative stress, which can impair the testis microenvironment and male animal fertility. However, the underlying mechanisms are largely unknown. Recently, we identified that androgen signals promote the expression of connexin-43 (Cx43), a key component of gap junctions, to regulate spermatogenesis. Thus, we asked whether hyperactive reactive oxygen species (ROS) can impair gap junctions by interfering with Cx43 in porcine testes. Using a porcine Sertoli cell *in vitro* system, we found that hyperactive ROS caused extensive apoptosis in Sertoli cells, remarkable decrease in Cx43 expression, and failed maintenance of co-cultured spermatogonial stem cells (SSCs), indicating that ROS impaired the function of Sertoli cells and promoted loss of SSCs. This observation provides a possible mechanism for the impact of ROS on fertility of male animals.

As germline stem cells residing in the testicular basal membrane, SSCs are responsible for producing functional sperm (Shinohara et al., 1999). The capacity of spermatogenesis determines the fertility of male animals. One spermatogonial stem cell in the seminiferous tubules is embraced by two Sertoli cells to form a unique structure called a niche. The testicular microenvironment is composed of several types of supporting cells. For example, specialized Sertoli cells are located at the base of testicular seminiferous tubules and exhibit multiple functions, such as protection of SSCs and provision of extrinsic signals for spermatogenesis (Naughton, 2006), Moreover, they promote germ-cell differentiation, meiosis, and transformation into spermatozoa (Phillips et al., 2010). Therefore, it is important to understand the physiological and metabolic characteristics of Sertoli cells in male reproduction. Many types of intercellular interactions between SSCs and Sertoli cells have been identified, including gap junctions (Xia et al., 2005). Gap junctions are a type of cellular interaction involved in diverse biological processes. They are closely related to spermatogenesis, with earlier studies revealing potential signaling pathways that influence the fate of spermatogonia and spermatocytes in differentiation and migration (Xia et al., 2005). Cx43 is an important gap junction protein (Laird et al., 1991). Cx43 is synthesized and trafficked through the endoplasmic reticulum like a typical integral membrane protein (Musil & Goodenough, 1993), and has been identified as a pivotal molecule regulating blood-testis barrier dynamics (Li et al., 2009). These observations indicate that Cx43 in Sertoli cells is closely associated with spermatogenesis.

Among the many harmful factors impacting livestock reproduction, oxidative stress has been well studied. ROS have been shown to decrease sperm and oocyte quality in rodents (Lane et al., 2014), porcines (Kang et al., 2013), bovines (Arias et al., 2017), and humans (Prasad et al., 2016). ROS exhibit diverse derivations, such as ultraviolet radiation, X-rays, gamma rays, and atmospheric pollutants (Nisar et al., 2013). These various sources of ROS imply an inevitable threat to male fertility in animal breeding and husbandry. In addition to the impact on spermatogonia, oxidative stress also affects the function of Sertoli cells (Liu et al., 2018). Sertoli cells reside in the basal membrane of seminiferous tubules and regulate germ cell fate via direct interaction or release of signaling molecules (Johnson et al., 2008). Many regulatory patterns have been identified, i.e., androgen controls the permeability of the blood-testis barrier to regulate SSC differentiation (Meng et al., 2005). Our previous studies

---

Received: 28 November 2019; Accepted: 05 March 2020; Online: 05 March 2020

Foundation items: This work was supported by a project funded by the Priority Academic Program Development of Jiangsu Higher Education Institutions (PAPD) and National Innovation and Entrepreneurship Training Program for Undergraduates (201910307021Y)

DOI: 10.24272/j.issn.2095-8137.2020.024

revealed that androgen regulates ITGB1, a key molecule for SSC homing, via WT1 in Sertoli cells (Wang et al., 2019), and regulates Cx43 protein expression in Sertoli cells (Xia et al., 2020). These observations suggest that androgen signaling participates in the regulatory process of SSC fate via the intercellular molecules between Sertoli cells and SSCs. Thus, we asked whether oxidative stress affects these pivotal molecules in Sertoli cells, which directly influence spermatogonia fate.

Here, we investigated the impact of oxidative stress on Sertoli cells using an *in vitro* system and determined the expression of Sertoli cell markers and apoptosis ratio. The results demonstrated that the hyperactive ROS disturbed the expression of Cx43 in Sertoli cells and affected the co-cultured SSCs in this system, suggesting that the hyperactive ROS impaired the function of Cx43. The detailed materials and methods are available in the Supplementary Online file.

After purification differential adhesion and hypotonic treatment to remove germ cells, followed by 24 h culture, Sertoli cells displayed polygonal morphology and the nucleus was clearly visible (Figure 1A). Reverse Transcription-polymerase chain reaction (RT-PCR) verified the expression of Sertoli cell markers Cx43, WT1, AMH, and SOX9 (Figure 1B). The expression of WT1 was also detected using immunofluorescence to identify the purity of the isolated cells (Figures 1C–F). Statistical analysis revealed that the purity of the Sertoli cells was over 80% (Figure 1G). Collectively, purified Sertoli cells from 7-d-old porcines were obtained.

To investigate the impact of ROS on Sertoli cell growth status, 1×10^5 Sertoli cells cultured in 24-well plates were supplemented with various doses of H_2O_2. No obvious morphological changes were observed at low H_2O_2 doses (10

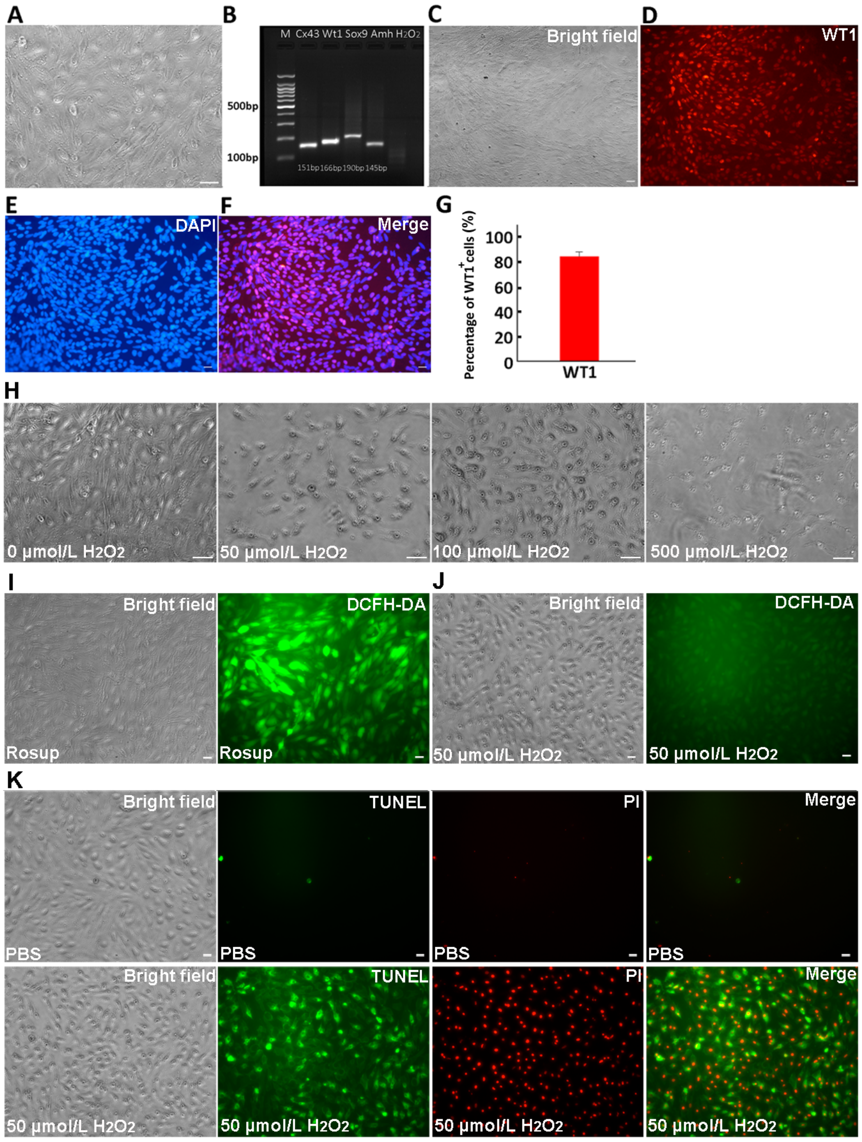

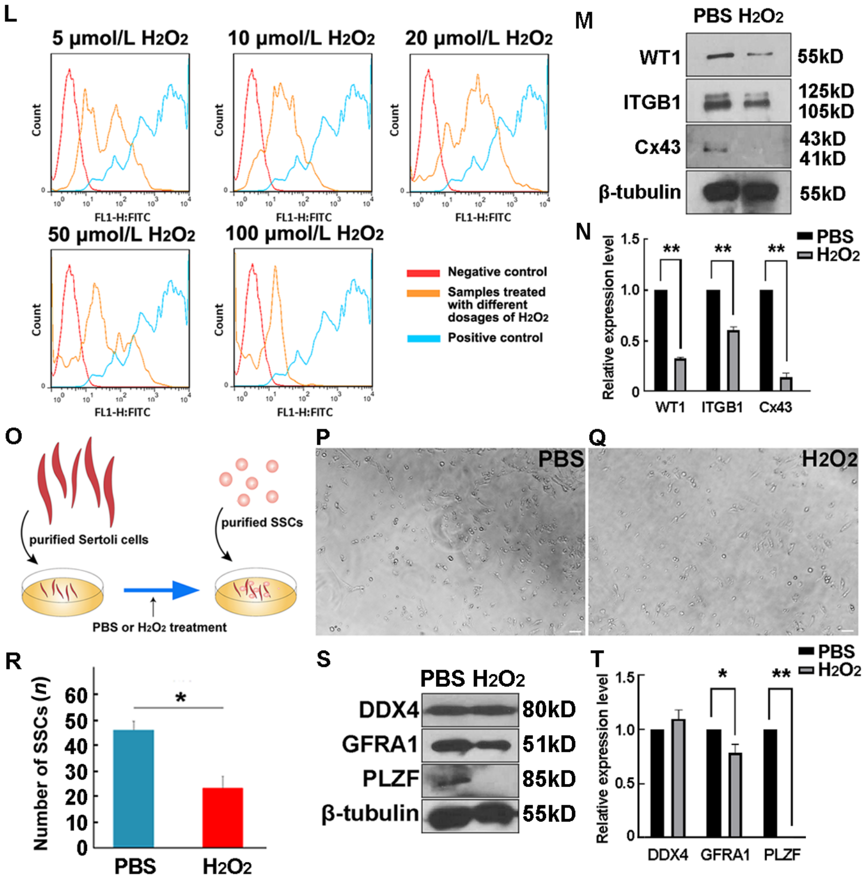

Figure 1 Hyperactive reactive oxygen species (ROS) disturbed expression of Cx43 in Sertoli cells and affected co-cultured SSCs

A: Purified Sertoli cells were plated on dishes for culture. B: Expression levels of Sertoli cell markers, Cx43, WT1, AMH, and Sox9, were detected in purified Sertoli cells by RT-PCR, *n*=3. C−F: Purity of Sertoli cells was determined using IF staining against WT1 (C: Bright field; D: WT1; E: DAPI; F: Merge). G: Percentage of WT1$^+$ cells is presented as mean percentage±*SEM*, *n*=5. H: Morphology of Sertoli cells treated with 0, 50 μmol/L H_2O_2, 100 μ mol/L H_2O_2, or 500 μmol/L H_2O_2 is shown. I, J: Images of DCFH-DA fluorescence were taken for positive control group (Rosup provided by the Reactive Oxygen Species Assay Kit, Beyotime) (I) and 50 μmol/L H_2O_2-treated group, *n*=5 (J). K: Apoptosis signal detection using Annexin V-FITC/PI kit. PBS- and 50 μmol/L H_2O_2-treated groups, *n*=5. L: ROS levels in Sertoli cells treated with different concentrations of H_2O_2 (5, 10, 20, 50, or 100 μmol/L, *n*=3) were analyzed by flow cytometry. M, N: Sertoli cells treated with PBS or 50 μmol/L H_2O_2 for 48 h were harvested to detect protein levels of WT1, ITGB1, and Cx43 using Western blotting, with data presented as means±*SEM*, *n*=3, **: *P*<0.01 (N). O: Schematic of Sertoli cell and SSC co-culture system. P, Q: Morphology of co-culture of SSCs maintained with PBS- (P) or H_2O_2- (Q) treated Sertoli cells for 48 h is displayed. R: Number of SSCs in PBS- or H_2O_2-treated Sertoli cells was statistically analyzed, *n*=3. S, T: Protein levels of DDX4, GFRA1, and PLZF in PBS- and H_2O_2-treated SSCs were analyzed using Western blotting; Data are presented as mean percentage±*SEM*, *n*=3, *: *P*<0.05, **: *P*<0.01 (*t*-test) (T). Scale bars: 20 μm.

μmol/L and 20 μmol/L, data not shown). However, as the dosage increased, cell number decreased and cell morphology changed and began to shrink. Obvious impact on cell morphology was observed at a H_2O_2 concentration of 50 μmol/L. The cell structure also changed, with a large number of cells showing atrophy when the H_2O_2 concentration increased to 100 μmol/L, and extensive Sertoli cell death observed when the H_2O_2 concentration increased to 500 μmol/L (Figure 1H). We then performed dichloro-dihydro-fluorescein diacetate (DCFH-DA) fluorescent dye staining to detect ROS levels; however, only a weak ROS signal was detected at the dose of 50 μmol/L H_2O_2 (Figure 1I, J). Subsequently, the Sertoli cells (1×10^4) were stained with Annexin V-FITC/PI for apoptosis ratio analysis under ROS stress. We found that when cells were treated with 50 μmol/L H_2O_2, the number of apoptotic cells increased significantly (Figure 1K). In addition, many necrotic cells were observed in the group treated with 250 μmol/L H_2O_2 (data not shown), indicating that a high dose of H_2O_2 was lethal to Sertoli cells. We further clarified the dosage effect of H_2O_2 on Sertoli cells using flow cytometry. Two major populations were observed based on ROS levels, with the proportion of the higher-level ROS population increasing in the 20 μmol/L H_2O_2 group, but decreasing in the 50 μmol/L H_2O_2 and 100 μmol/L H_2O_2

groups (Figure 1L). This was likely due to increasing ROS levels causing extensive death of Sertoli cells. It is also worth noting that the induced ROS signal clearly appeared under 5 μmol/L H_2O_2 (Figure 1L), indicating that Sertoli cells were sensitive to H_2O_2 stimulation.

As a key gap junction protein, the expression level of Cx43 is closely related to Sertoli cell function (Xia et al., 2005). Thus, we treated Sertoli cells with phosphate-buffered saline (PBS) or 50 μmol/L H_2O_2 for 48 h to test the possible effects of ROS on Cx43 expression. Western blotting revealed that Cx43 expression was significantly down-regulated in the 50 μmol/L H_2O_2-treated group compared with the PBS-treated group (Figure 1M). In addition, the expression levels of WT1, a Sertoli cell marker, and ITGB1, a key surface molecule for Sertoli cell-SSC interaction, were significantly decreased (Figure 1M, N). Collectively, these observations indicate that the structure and function of Sertoli cells were impaired under ROS stress.

As an important component of the testicular microenvironment, the damage induced by H_2O_2 should affect SSC maintenance. To test this hypothesis, Sertoli cells were treated with PBS or 50 μmol/L H_2O_2 for 24 h and then co-cultured with purified SSCs for 48 h (Figure 1O). Compared with the PBS-treated group, the number of SSCs decreased significantly in the H_2O_2-treated group (Figure 1P, R). Further analysis demonstrated that the expression levels of SSC markers GFRA1 and PLZF were down-regulated after H_2O_2 treatment (Figure 1S, T), thus indicating that the number of undifferentiated spermatogonia was reduced. However, there was no significant difference in the level of DDX4 in the PBS and H_2O_2 treatment groups, which may be due to an increase in the number of differentiated spermatogonia in the H_2O_2 treated group. These results suggest that the impaired Sertoli cells affected the maintenance of SSCs and probably led to differentiation.

Although *in vitro* culture of porcine SSCs is still a challenging project, recent studies have taken a step forward in the long-term maintenance and establishment of porcine SSC lines (Sun et al., 2019). In this study, a co-culture system was used to explore the impact of a representative harmful factor, ROS, on Sertoli cell function. Although high levels of ROS in germlines are known to be risky, knowledge regarding the impact of ROS on Sertoli cells is limited. In particular, the influence on Sertoli cell-germ cell interactions remains poorly identified. This directly determines the capacity of spermatogenesis, as demonstrated by the successful establishment of tree shrew spermatogonial stem cells with Sertoli feeder cells in culture systems (Li et al., 2017).

ROS are mainly produced by mitochondria during cell metabolism in various cell types (Scherz-Shouval et al., 2007). Studies have demonstrated that ROS play regulatory roles in various stem cells. For example, ROS are instantaneously generated during embryoid development and regulate cardiotypic development in embryonic stem cell-derived embryoid bodies (Sauer et al., 2000). ROS signaling regulates the cellular pathways involved in neuronal differentiation and neuronal stem cell proliferation (Vieira et al., 2011). Increased ROS levels drive hematopoietic stem cell differentiation (Ludin et al., 2014). However, ROS may play very different roles in different types of stem cells. In some types of stem cells, ROS induce apoptosis, while in others, ROS may promote self-renewal. In male germlines, the effects of ROS are interesting. Although ROS are generally considered harmful to spermatogenesis, previous study has reported that the self-renewal of SSCs requires a certain level of ROS, with no significant effects observed at 30 μmol/L H_2O_2, but with proliferation inhibited by the addition of >100 μmol/L H_2O_2 (Morimoto et al., 2015). However, our data revealed that even low doses of H_2O_2 disturbed Sertoli cell maintenance and inhibited expression of key surface functional proteins, indicating that SSCs and Sertoli cells may have different tolerances to ROS stress. In the co-culture system, we observed a reduced number of SSCs maintained with H_2O_2-treated Sertoli cells. Expression levels of undifferentiated markers GFRA1 and PLZF decreased markedly, but total germ cell marker DDX4 was not altered. Based on our previous studies (Wang et al., 2019; Xia et al., 2020), loss of ITGB1 or Cx43 facilitates SSC differentiation. Thus, impaired Sertoli cell function by ROS can lead to loss of SSCs and promotion of SSC differentiation, and differentiated germ cells possibly compensate the expression of DDX4. Notably, some studies have reported that antioxidants, such as lycopene (Krishnamoorthy et al., 2013) and genistein (Zhang et al., 2017), eliminate ROS in Sertoli cells and rescue spermatogenesis, indicating some potential ways to protect fertility of boars.

Collectively, the impact of ROS on two pivotal surface proteins in Sertoli cells was revealed, and an *in vitro* model confirmed that this damage affected the maintenance of spermatogonia, implying potential damage to the testicular niche. However, further studies using *in vivo* models are required, including studies on the link between ROS dosage in Sertoli cells and SSC fate.

SUPPLEMENTARY DATA

Supplementary data to this article can be found online.

COMPETING INTERESTS

The authors declare that they have no competing interests.

AUTHORS' CONTRIBUTIONS

K.Z. proposed the ideas. D.C.Z. drafted the manuscript. R.C., Y.H.C., J.J.W. and C.Y. revised the manuscript. All authors read and approved the final version of the manuscript.

Dan-Chen Zhang[1], Rong Chen[1], Yi-Hui Cai[1],
Jing-Jing Wang[1], Chang Yin[1], Kang Zou[1,*]

[1] *Germline Stem Cells and Microenvironment Lab*, *College of Animal Science and Technology*, *Nanjing Agricultural University*,

Nanjing, *Jiangsu* 210095, *China*
*Corresponding author, E-mail: kangzou@njau.edu.cn

REFERENCES

Arias ME, Andara K, Briones E, Felmer R. 2017. Bovine sperm separation by Swim-up and density gradients (Percoll and BoviPure): Effect on sperm quality, function and gene expression. *Reproductive Biology*, **17**(2): 126−132.

Johnson L, Thompson Jr D, Varner DD. 2008. Role of Sertoli cell number and function on regulation of spermatogenesis. *Animal Reproduction Science*, **105**(1-2): 23−51.

Kang JT, Kwon DK, Park SJ, Kim SJ, Moon JH, Koo OJ, Jang G, Lee BC. 2013. Quercetin improves the *in vitro* development of porcine oocytes by decreasing reactive oxygen species levels. *Journal of Veterinary Science*, **14**(1): 15−20.

Krishnamoorthy G, Selvakumar K, Venkataraman P, Elumalai P, Arunakaran J. 2013. Lycopene supplementation prevents reactive oxygen species mediated apoptosis in Sertoli cells of adult albino rats exposed to polychlorinated biphenyls. *Interdisciplinary Toxicology*, **6**(2): 83−92.

Laird DW, Puranam KL, Revel JP. 1991. Turnover and phosphorylation dynamics of connexin43 gap junction protein in cultured cardiac myocytes. *Biochemical Journal*, **273**(1): 67−72.

Lane M, McPherson NO, Fullston T, Spillane M, Sandeman L, Kang WX, Zander-Fox L. 2014. Oxidative stress in mouse sperm impairs embryo development, fetal growth and alters adiposity and glucose regulation in female offspring. *PLoS One*, **9**(7): e100832.

Li CH, Yan LZ, Ban WZ, Tu Q, Wu Y, Wang L, Bi R, Ji S, Ma YH, Nie WH, Lv LB, Yao YG, Zhao XD, Zheng P. 2017. Long-term propagation of tree shrew spermatogonial stem cells in culture and successful generation of transgenic offspring. *Cell Research*, **27**(2): 241−252.

Li MWM, Mruk DD, Lee WM, Cheng CY. 2009. Connexin 43 and plakophilin-2 as a protein complex that regulates blood-testis barrier dynamics. *Proceedings of the National Academy of Sciences of the United States of America*, **106**(25): 10213−10218.

Liu LQ, Chang XL, Zhang YB, Wu CH, Li R, Tang LM, Zhou ZJ. 2018. Fluorochloridone induces primary cultured Sertoli cells apoptosis: Involvement of ROS and intracellular calcium ions-mediated ERK1/2 activation. *Toxicology in Vitro*, **47**: 228−237.

Ludin A, Gur-Cohen S, Golan K, Kaufmann KB, Itkin T, Medaglia C, Lu XJ, Ledergor G, Kollet O, Lapidot T. 2014. Reactive oxygen species regulate hematopoietic stem cell self-renewal, migration and development, as well as their bone marrow microenvironment. *Antioxidants & Redox Signaling*, **21**(11): 1605−1619.

Meng J, Holdcraft RW, Shima JE, Griswold MD, Braun RE. 2005. Androgens regulate the permeability of the blood-testis barrier. *Proceedings of the National Academy of Sciences of the United States of America*, **102**(46): 16696−16700.

Morimoto H, Kanatsu-Shinohara M, Shinohara T. 2015. ROS-generating oxidase *Nox3* regulates the self-renewal of mouse spermatogonial stem cells. *Biology of Reproduction*, **92**(6): 147.

Musil LS, Goodenough DA. 1993. Multisubunit assembly of an integral plasma membrane channel protein, gap junction connexin43, occurs after exit from the ER. *Cell*, **74**(6): 1065−1077.

Naughton KC, Jain S, Strickland AM, Gupta A, Milbrandt J. 2006. Glial cell-line derived neurotrophic factor-mediated RET signaling regulates spermatogonial stem cell fate. *Biology of Reproduction*, **74**(2): 314−321.

Nisar NA, Sultana M, Waiz HA, Para PA, Dar SA. 2013. Oxidative stress - threat to animal health and production. *International Journal of Livestock Research*, **3**(2): 76−83.

Phillips BT, Gassei K, Orwig KE. 2010. Spermatogonial stem cell regulation and spermatogenesis. *Philosophical Transactions of the Royal Society B: Biological Sciences*, **365**(1546): 1663−1678.

Prasad S, Tiwari M, Pandey AN, Shrivastav TG, Chaube SK. 2016. Impact of stress on oocyte quality and reproductive outcome. *Journal of Biomedical Science*, **23**(1): 36.

Sauer H, Rahimi G, Hescheler J, Wartenberg M. 2000. Role of reactive oxygen species and phosphatidylinositol 3-kinase in cardiomyocyte differentiation of embryonic stem cells. *FEBS Letters*, **476**(3): 218−223.

Scherz-Shouval R, Shvets E, Fass E, Shorer H, Gil L, Elazar Z. 2007. Reactive oxygen species are essential for autophagy and specifically regulate the activity of Atg4. *The EMBO Journal*, **26**(7): 1749−1760.

Shinohara T, Avarbock MR, Brinster RL. 1999. β_1-and α6-integrin are surface markers on mouse spermatogonial stem cells. *Proceedings of the National Academy of Sciences of the United States of America*, **96**(10): 5504−5509.

Sun YZ, Liu ST, Li XM, Zou K. 2019. Progress in *in vitro* culture and gene editing of porcine spermatogonial stem cells. *Zoological Research*, **40**(5): 343−348.

Vieira HLA, Alves PM, Vercelli A. 2011. Modulation of neuronal stem cell differentiation by hypoxia and reactive oxygen species. *Progress in Neurobiology*, **93**(3): 444−455.

Wang JJ, Li JM, Xu W, Xia Q, Gu YZ, Song WX, Zhang XY, Yang Y, Wang W, Li H, Zou K. 2019. Androgen promotes differentiation of PLZF+ spermatogonia pool via indirect regulatory pattern. *Cell Communication and Signaling*, **17**(1): 57.

Xia Q, Zhang DC, Wang JJ, Zhang XY, Song WX, Chen R, Li H, Xie WH, Zou K. 2020. Androgen indirectly regulates gap junction component connexin 43 through *Wilms tumor-1* in Sertoli cells. *Stem Cells and Development*, **29**(3): 169−176.

Xia WL, Mruk DD, Lee WM, Cheng CY. 2005. Cytokines and junction restructuring during spermatogenesis-a lesson to learn from the testis. *Cytokine & Growth Factor Reviews*, **16**(4−5): 469−493.

Zhang LD, Gao M, Zhang TD, Chong T, Wang ZM, Zhai XQ, Wu ZZ, Li HC. 2017. Protective effects of Genistein against Mono-(2-ethylhexyl) phthalate-induced oxidative damage in prepubertal sertoli cells. *BioMed Research International*, **2017**: 2032697.

ZOOLOGICAL RESEARCH

The anatomy of the skin of the Chinese tree shrew is very similar to that of human skin

DEAR EDITOR,

The Chinese tree shrew (*Tupaia belangeri chinensis*) is a small mammal closely related to primates. It has a small body size, low maintenance cost, and a relatively short reproductive cycle, all of which has made it the ideal model for the study of a variety of human diseases. In this study, we compared the anatomy of the skin of the Chinese tree shrew with that of the rhesus macaque, mouse and human, with the intention of providing the basic data required for the creation of skin disease models using this animal. Paraffin sections, hematoxylin-eosin (H&E) staining, masson staining and immunohistochemical techniques were used to examine the dorsal skin structure of the Chinese tree shrew. The epidermis was shown to be composed of 1–2 layers of cells. There were hair follicles, sebaceous glands and sweat glands in the dermis and the subcutaneous tissue, with apocrine glands being more common than eccrine glands. Both Keratin5 (KRT5) and Keratin10 (KRT10) were expressed in the skin of the Chinese tree shrew, with a localization in the cytoplasm. Overall, the skin morphology and histology of the Chinese tree shrew was basically the same as that of the human. We propose that the Chinese tree shrew has a strong potential to be used for creating animal models to help elucidate the molecular mechanisms underlying a variety of skin diseases.

Animal models have been used extensively with great benefit in the study of many human diseases (Yao et al., 2015). To date, a variety of animals, including fruit fly, zebrafish, frog, mouse, rat, rabbit, dog, pig, and rhesus macaque, have been used in studies looking at a variety of human diseases (Buchholz, 2015; Buffalo et al., 2019; Jiang et al., 2011; Xue et al., 2014). Each animal has its own merits and disadvantages when considering the wide range of human skin disease. For example, rodents are commonly used in biomedical researches of skin, such as psoriatic murine model induced by imiquimod (Chuang et al., 2018) and inflammatory mouse model of Behçet's disease induced by HSV-1 (Islam & Sohn, 2018), but the species disparity sometimes makes them difficult to extrapolate (van der Worp et al., 2010). Non-human primates (NHP), like rhesus macaques, are genetically closer to humans and have significant benefits in medical research (Buffalo et al., 2019; Zhang et al., 2014). NHP has been used to explore responses of *Leishmania (Viannia) braziliensis* cutaneous infection to N-methylglucamine antimoniate (Teva et al., 2005) and as SIVmac239-infected model for studying HIV infection (Zhang et al., 2019), to name a few. The NHP model has been proved to be the best model for biomedical researches. However, there are also some disadvantages of using NHP as the resources are not easy to obtain and the costs are relatively high. Therefore, there is an urgent need to find an appropriate animal which is not only genetically close to humans, but is also economic, easily obtainable and able to thrive in the laboratory.

The Chinese tree shrew is a small mammal that has a rat-sized body size (100−150 g), a low-cost of maintenance, a short reproductive cycle, and a moderate life span (6−8 years), as well as being closely related to primates (Fan et al., 2019; Xu et al., 2012; Yao, 2017; Zheng et al., 2014). During the past five decades, the Chinese tree shrew has been used as an animal model in the study of infectious diseases, myopia, cancer, metabolic diseases, and brain disorders (Guo et al., 2019; Xiao et al., 2017; Yao, 2017; Zheng et al., 2014). These Chinese tree shrew studies have increased our understanding of the basic biology of life and the molecular mechanisms underlying disease (Yao, 2017).

In this study, we examined the skin structure of the Chinese tree shrew and compared it to that of the rhesus macaque, mouse and human, to explore the potential for using the Chinese tree shrew in dermatological research. Chinese tree shrews were purchased from the Kunming Primate Research Center (KPRC) of the Chinese Academy of Sciences (CAS),

---

Received: 23 January 2020; Accepted: 04 March 2020; Online: 04 March 2020

Foundation items: This study was supported by the Chinese Academy of Sciences (CAS zsys-02) and CAS "Light of West China" Program (xbzg-zdsys-201909)

DOI: 10.24272/j.issn.2095-8137.2020.028

Kunming Institute of Zoology (KIZ), CAS. A total of six animals of different ages (1 month, and 1, 3, 4, 4.5 and 6 years old) were used. We also obtained the skin tissues of two rhesus macaques (age <1 month), which had died from diarrhea, from KPRC, KIZ, CAS. Six-week old C57BL/6 mice (*n*=3) were purchased from Shanghai SLAC Laboratory Animal Co., Ltd. Dorsal skin samples from these animals were fixed in 4% paraformaldehyde for later processing. All experimental procedures were performed according to the guidelines approved by the Institutional Review Board of KIZ, CAS (approved No. 2015-012).

The dorsal skin samples, previously fixed in 4% paraformaldehyde, were paraffin embedded (vertical embedded) and 10-μm-thick sections were cut from the tissue blocks. The tissue sections were treated with either H&E staining or masson staining (Masson's Trichrome Stain Kit (Solarbio, G1340, China)). For the immunohistochemical staining, the prepared 10 μm sections were dewaxed, rehydrated, washed with PBS, infiltrated in citrate buffer and heated for 30 min for antigen retrieval. After blocking and further incubation with primary antibodies at 4 °C overnight, the reaction was developed using the Super Vision two-step kit (Boster, SV0001, SV0002, USA) which included the secondary antibodies followed by DAB (Vector Laboratories, PK-4002, USA) staining. Harris hematoxylin (Baso, BA4041, China) was used for nuclear staining. Primary antibodies were Keratin 5 (D4U8Q) mAb (Cell Signaling Technology, #25807, USA) and Cytokeratin 10 (4A27) mAb (Santa Cruze Biotechnology, sc-70907, USA), and were used for staining KRT5 and KRT10 in skin tissue sections, respectively.

The skin of the Chinese tree shrew was composed of epidermis, dermis and the subcutaneous tissue (Figure 1A). As is known to all that human epidermis is composed of stratum corneum, stratum granulosum, stratum spinosum and stratum basal (Paus & Cotsarelis, 1999; Tobin, 2006). However, the epidermis of the Chinese tree shrew only consisted of 1–2 layers of keratinocyte cells, which was thinner than that of the human, but similar to those of the rhesus macaque and the mouse (Figure 1A–D). There were basal cells in the skin tissue composition of tree shrews because they are required for the replacement of dead cells in the epidermis. The dermis of the Chinese tree shrew showed multiple fibroblast fibers, together with blood vessels, epidermal appendages and inflammatory cells (Figure 1A). Collagen fibers, arranged in bundles, were the main fibers in the dermis, and showed blue by masson staining (Figure 1A). The subcutaneous tissue of the Chinese tree shrew was composed of loose connective and adipose tissues, which connected dermis and muscles. There were many sweat glands in the subcutaneous tissue, of which apocrine glands accounted for the highest proportion (Figure 1A). The composition of the epidermis, dermis and appendages of the rhesus macaque was similar to that of the Chinese tree shrew (Figure 1A).

The appendages of the Chinese tree shrew included hair follicles, sebaceous glands and sweat glands. Sweat glands and sebaceous glands increased in size and became more abundant with age (Figure 1E). The sweat glands were significantly distributed around the top of the hair bulbs (Figure 1E), just as eccrine sweat glands associated with the hair follicle within a defined compartment of dermal white adipose tissue in the human (Poblet et al., 2018), to form an “adnexal skin unit” along with the pilosebaceous unit. It was possible that there was some relationship between each component of this superstructure to form a common homeostatic tissue environment (Poblet et al., 2018). The mature hair follicles in the skin tissue of the Chinese tree shrew contained melanocytes. The sebaceous gland of the Chinese tree shrew was composed of acini and the short duct opening into the hair follicle as well as the epidermis (Figure 1E). However, in the human, the duct of the sebaceous gland normally opens into the hair follicle and goes directly into the epidermis under pathological conditions (Zouboulis et al., 2016). Surprisingly, the apocrine glands in the dorsal skin of the Chinese tree shrew were more prominent, while the eccrine glands were few (Figure 1E). This pattern was different to that seen in the rhesus macaque and human where eccrine glands are dominant (Best et al., 2019). By contrast, in the mouse eccrine glands are only present in the paw pad (Chee et al., 2017). The concentration of apocrine glands in the dorsal skin of the Chinese tree shrew may make it a suitable model animal for the study of apocrine gland-related diseases. In mammals, the hair follicle is a cyclical organ (Baker & Murray, 2012; Paus & Cotsarelis, 1999), and this is the same in the Chinese tree shrew (Figure 1E). As the thickness of the epidermis changed in the hair follicle cycle, it was significantly thicker in the anagen than the telogen (Figure 1E, F). The arrector pili muscle in the skin of the rhesus macaque was more obvious than that of the Chinese tree shrew, while sweat glands were uncommon in the rhesus macaque (Figure 1A). The eccrine glands were the dominant sweat glands in the rhesus macaque (Figure 1G). In the dorsal skin sections taken from the mouse, there were almost no sweat glands, and the sebaceous glands were also not obvious (Figure 1B).

Cytokeratin is a characteristic marker of epithelial cells and has a great significance in the epidermis and adnexal diseases (Moll et al., 1982). We studied the expression of KRT5 and KRT10 in the skin of the Chinese tree shrew. KRT5 dimerizes with keratin 14 forming the intermediate filaments to make up the cytoskeleton of basal epithelial cells, and has an active role in epidermolysis bullosa simplex, Dowling-Degos disease and some other dermatologic diseases (Lane et al., 1992; Tryon et al., 2019). KRT10 was observed in a group of tough, fibrous proteins that form the structural framework of keratinocytes and was produced in keratinocytes in the outer layer of the skin (Müller et al., 2006). KRT10 is associated with epidermolytic hyperkeratosis (Morais et al., 2009; March et al., 2019). We found that KRT5 and KRT10 were both expressed in the skin of the Chinese tree shrew. Specifically, KRT5 was expressed in the whole epidermis except for the stratum corneum (Figure 1H), while KRT10 was expressed mainly in the outer layer of the epidermis (Figure 1H). In terms of the epidermal appendages, KRT5 was expressed in the outer root sheath of hair follicles, sebaceous glands (especially in the basal cells in the outer layer) and sweat glands (the outer wall of the gland expressing more) (Figure 1H). In contrast, KRT10 was expressed mainly in the follicular epithelium above the follicular infundibulum, sebaceous and sweat glands, especially in the internal wall of these glands (Figure 1H). The expression pattern showed that both KRT5 and KRT10 were expressed in the cytoplasm (Figure 1H). The expression patterns of KRT5 and KRT10 in the skin of the Chinese tree shrew were similar to those observed in the rhesus macaque (Figure 1H) and human (Zhong et al., 2000).

In conclusion, we showed that the skin histology of the Chinese tree shrew was generally like that of human skin. There was a consistent composition of epidermal appendages and a similar expression pattern of some keratins between the Chinese tree shrew and human. The similarity of the skin

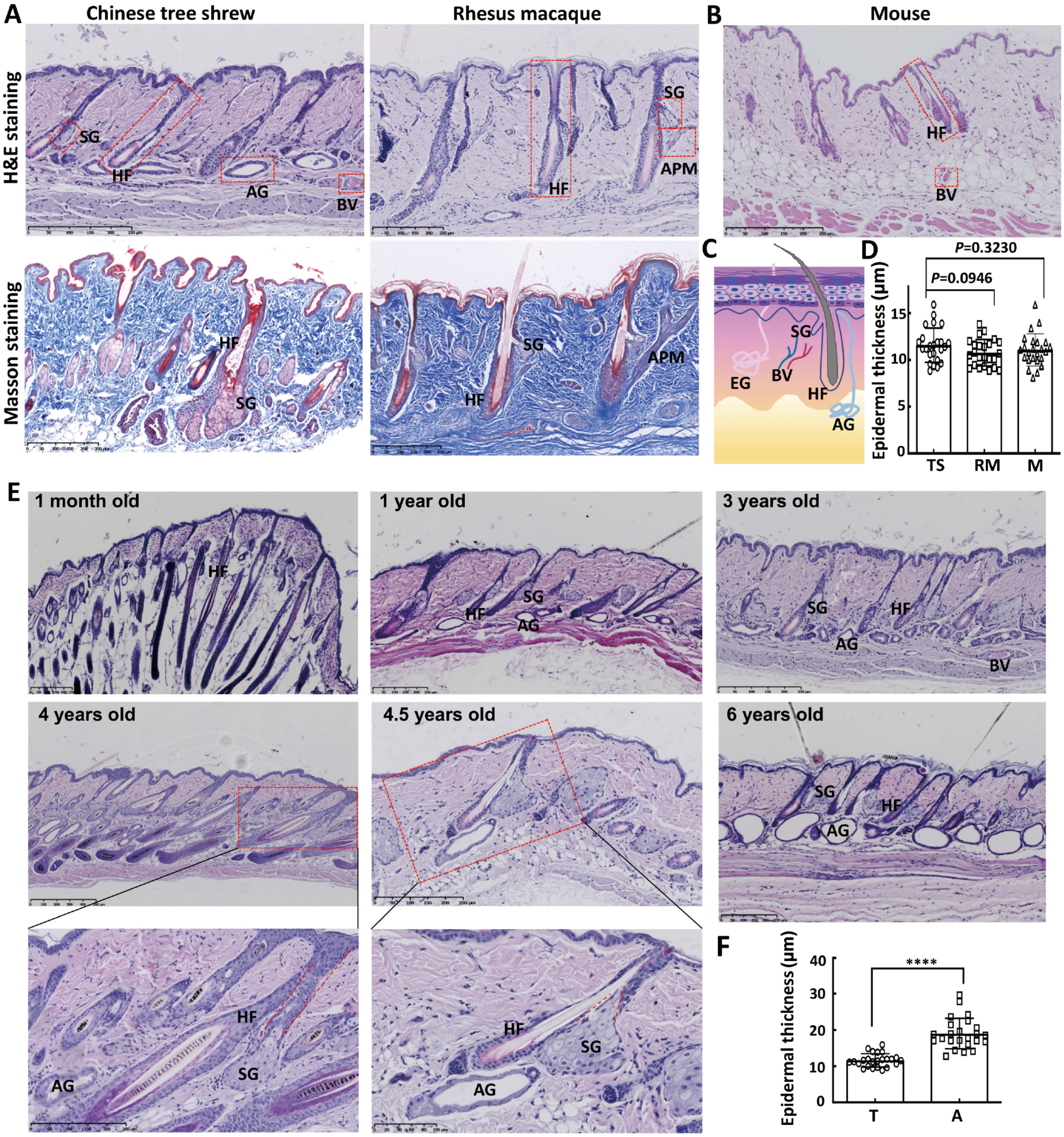

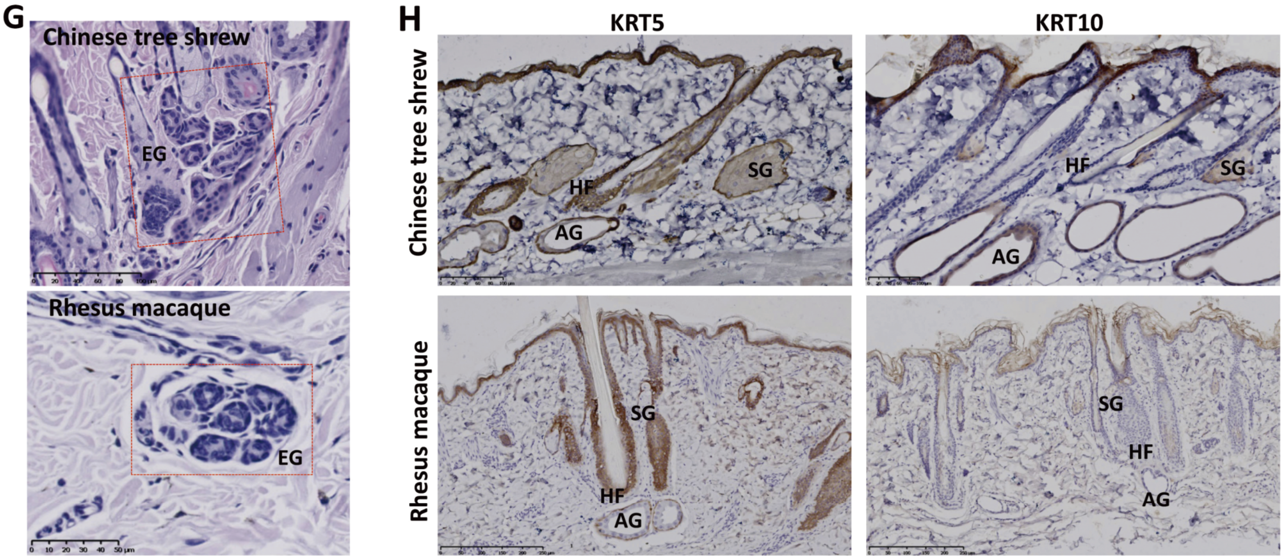

Figure 1 Comparison of the skin morphology and histology, and KRT5 and KRT10 expression pattern of the Chinese tree shrew and rhesus macaque

A: Hematoxylin and eosin (H&E) staining (*upper*) and masson staining (*below*) for the dorsal skin of the Chinese tree shrew and rhesus macaque. B: H&E staining for the dorsal skin of mouse. C: Cartoon of normal human skin. D: Comparison of the epidermal thickness among the Chinese tree shrew, rhesus macaque and mouse. The *P*-values were based on Student's *t*-test. E: H&E staining for the dorsal skin tissues of the Chinese tree shrews with different ages. The pilosebaceous unit and the apocrine glands were further demonstrated in the boxed skin tissues of the Chinese tree shrews of 4 years old and 4.5 years old, respectively. The hair follicle cycle in the skin tissues of 1-month old and 4 years old tree shrews indicated the late-anagen stage. F: Comparison of the epidermal thickness between telogen and anagen stages. ****: $P<0.000\,1$, Student's *t*-test. G: H&E staining for the eccrine gland of the Chinese tree shrew (*upper*) and rhesus macaque (*below*). H: The expression of KRT5 and KRT10 in the skin tissues of the Chinese tree shrew and rhesus macaque. The labeled abbreviations are hair follicle (HF), sebaceous gland (SG), apocrine gland (AG), eccrine gland (EG), arrector pili muscle (APM), and blood vessel (BV), tree shrew (TS), rhesus macaque (RM), mouse (M), telogen (T), anagen (A).

structure of the Chinese tree shrew relative to non-human primates and human may provide a solid basis for using this animal in further studies of human skin diseases, following the recent study into creating a Chinese tree shrew model of basal cell carcinoma (Jiang et al., 2017) and successful genetic modifications of this animal (Li et al., 2017). All those features of the Chinese tree shrew have laid the foundation for the use of this animal as a model for the study of human skin diseases.

COMPETING INTERESTS

The authors have no conflicts of interest to declare.

AUTHORS' CONTRIBUTIONS

X.Y.M. and Y.G.Y. designed this study. J. Z., R.C.L. and X.Y.M. performed the experiments and drafted the initial manuscript. L.B.L. provided key samples. Y.G.Y. and M.Z. revised the manuscript. All authors read and approved the final version of the manuscript.

ACKNOWLEDGEMENTS

We thank Zhao-Yuan Wang, Bing-Xi Yan and Yuan Zhou from Department of Dermatology, Second Affiliated Hospital, Zhejiang University School of Medicine for critical comments and Dr. Ian Logan for language editing this manuscript.

Jing Zhang[1], Rong-Can Luo[2], Xiao-Yong Man[1], Long-Bao Lv[4], Yong-Gang Yao[2,3,4,5,*], Min Zheng[1,*]

[1] *Department of Dermatology*, *Second Affiliated Hospital*, *Zhejiang University School of Medicine*, *Hangzhou*, *Zhejiang* 310009, *China*
[2] *Key Laboratory of Animal Models and Human Disease Mechanisms of the Chinese Academy of Sciences* & *Yunnan Province*, *Kunming Institute of Zoology*, *Chinese Academy of Sciences*, *Kunming*, *Yunnan* 650223, *China*
[3] *Kunming College of Life Science*, *University of Chinese Academy of Sciences*, *Kunming*, *Yunnan* 650204, *China*
[4] *Kunming Primate Research Center of the Chinese Academy of Sciences*, *Kunming Institute of Zoology*, *Chinese Academy of Sciences*, *Kunming*, *Yunnan* 650223, *China*
[5] *KIZ-CUHK Joint Laboratory of Bioresources and Molecular Research in Common Diseases*, *Kunming Institute of Zoology*, *Chinese Academy of Sciences*, *Kunming*, *Yunnan* 650223, *China*
*Corresponding authors, E-mail: yaoyg@mail.kiz.ac.cn; minz@zju.edu.cn

REFERENCES

Baker RE, Murray PJ. 2012. Understanding hair follicle cycling: a systems approach. *Current Opinion in Genetics & Development*, **22**(6): 607−612.

Best A, Lieberman DE, Kamilar JM. 2019. Diversity and evolution of human eccrine sweat gland density. *Journal of Thermal Biology*, **84**: 331−338.

Buchholz DR. 2015. More similar than you think: frog metamorphosis as a model of human perinatal endocrinology. *Developmental Biology*, **408**(2): 188−195.

Buffalo EA, Movshon JA, Wurtz RH. 2019. From basic brain research to treating human brain disorders. *Proceedings of the National Academy of Sciences of the United States of America*, **116**(52): 21617−26172.

Chee MK, Jo SK, Sohn KC, Kim CD, Lee JH, Lee YH. 2017. Effects of Brn2 overexpression on eccrine sweat gland development in the mouse paw. *Biochemical and Biophysical Research Communications*, **490**(3): 901−905.

Chuang SY, Lin CH, Sung CT, Fang JY. 2018. Murine models of psoriasis and their usefulness for drug discovery. *Expert Opinion on Drug Discovery*, **13**(6): 551−562.

Fan Y, Ye MS, Zhang JY, Xu L, Yu DD, Gu TL, Yao YL, Chen JQ, Lv LB, Zheng P, Wu DD, Zhang GJ,Yao YG. 2019. Chromosomal level assembly and population sequencing of the Chinese tree shrew genome. *Zoological Research*, **40**(6): 506−521.

Guo L, Frost MR, Siegwart JT Jr, Norton TT. 2019. Gene expression signatures in tree shrew sclera during recovery from minus-lens wear and during plus-lens wear. *Molecular Vision*, **25**: 311−328.

Islam SMS, Sohn S. 2018. HSV-induced systemic inflammation as an animal model for Behçet's disease and therapeutic applications. *Viruses*, **10**(9): 511.

Jiang HJ, Feng F, Dong ED. 2011. Model animals and animal models of human diseases. *Chinese Bulletin of Life Sciences*, **23**(3): 234−238. (in Chinese)

Jiang LP, Shen QS, Yang CP, Chen YB. 2017. Establishment of basal cell carcinoma animal model in Chinese tree shrew (*Tupaia belangeri chinensis*). *Zoological Research*, **38**(4): 180−190.

Lane EB, Rugg EL, Navsaria H, Leigh IM, Heagerty AH, Ishida-Yamamoto A, Eady RA. 1992. A mutation in the conserved helix termination peptide of keratin 5 in hereditary skin blistering. *Nature*, **356**(6366): 244−246.

Li CH, Yan LZ, Ban WZ, Tu Q, Wu Y, Wang L, Bi R, Ji S, Ma YH, Nie WH, Lv LB, Yao YG, Zhao XD, Zheng P. 2017. Long-term propagation of tree shrew spermatogonial stem cells in culture and successful generation of transgenic offspring. *Cell Research*, **27**(2): 241−252.

Müller FB, Huber M, Kinaciyan T, Hausser I, Schaffrath C, Krieg T, Hohl D, Korge BP, Arin MJ. 2006. A human keratin 10 knockout causes recessive epidermolytic hyperkeratosis. *Human Molecular Genetics*, **15**(7): 1133−1141.

March OP, Lettner T, Klausegger A, Ablinger M, Kocher T, Hainzl S, Peking P, Lackner N, Rajan N, Hofbauer JP, Guttmann-Gruber C, Bygum A, Koller U, Reichelt J. 2019. Gene editing- mediated disruption of epidermolytic ichthyosis-associated *KRT10* alleles restores filament stability in keratinocytes. *Journal of Investigative Dermatology*, **139**(8): 1699−1710.

Moll R, Franke WW, Schiller DL, Geiger B, Krepler R. 1982. The catalog of human cytokeratins: Patterns of expression in normal epithelia, tumors and cultured cells. *Cell*, **31**(1): 11−24.

Morais P, Mota A, Baudrier T, Lopes JM, Cerqueira R, Tavares P, Azevedo F. 2009. Epidermolytic hyperkeratosis with palmoplantar keratoderma in a patient with KRT10 mutation. *European Journal of Dermatology*, **19**(4): 333−336.

Paus R, Cotsarelis G. 1999. The biology of hair follicles. *New England Journal of Medicine*, **341**(7): 491−497.

Poblet E, Jimenez F, Escario-Travesedo E, Hardman JA, Hernández-Hernández I, Agudo-Mena JL, Cabrera-Galvan JJ, Nicu C, Paus R. 2018. Eccrine sweat glands associate with the human hair follicle within a defined compartment of dermal white adipose tissue. *British Journal of Dermatology*, **178**(5): 1163−1172.

Teva A, Porrozzi R, Oliveira-Neto MP, Grimaldi Jr GJ. 2005. Responses of *Leishmania* (*Viannia*) *braziliensis* cutaneous infection to N-methylglucamine antimoniate in the rhesus monkey (*Macaca mulatta*) model. *Journal of Parasitology*, **91**(4): 976−978.

Tobin DJ. 2006. Biochemistry of human skin-our brain on the outside. *Chemical Society Reviews*, **35**(1): 52−67.

Tryon RK, Tolar J, Preusser SM, Riddle MJ, Keene DR, Bower M, Thyagarajan B, Ebens CL. 2019. A homozygous frameshift variant in the *KRT5* gene is compatible with life and results in severe recessive epidermolysis bullosa simplex. *JAAD Case Report*, **5**(7): 576−579.

van der Worp HB, Howells DW, Sena ES, Porritt MJ, Rewell S, O'Collins V, Macleod MR. 2010. Can animal models of disease reliably inform human studies?. *PLoS Medicine*, **7**(3): e1000245.

Xiao J, Liu R, Chen CS. 2017. Tree shrew (*Tupaia belangeri*) as a novel laboratory disease animal model. *Zoological Research*, **38**(3): 127−137.

Xu L, Chen SY, Nie WH, Jiang XL, Yao YG. 2012. Evaluating the phylogenetic position of Chinese tree shrew (*Tupaia belangeri chinensis*) based on complete mitochondrial genome: implication for using tree shrew as an alternative experimental animal to primates in biomedical research. *Journal of Genetics and Genomics*, **39**(3): 131−137.

Xue LX, Zhang FZ, Sun RJ, Dong ED. 2014. Research status and perspective of disease animal models in China. *Scientia Sinica Vitae*, **44**(9): 851−860. (in Chinese)

Yao YG, Chen YB, Liang B. 2015. The 3rd symposium on animal models of primates - the application of non-human primates to basic research and translational medicine. *Journal of Genetics and Genomics*, **42**(6): 339−341.

Yao YG. 2017. Creating animal models, why not use the Chinese tree shrew (*Tupaia belangeri chinensis*)?. *Zoological Research*, **38**(3): 118−126.

Zhang MX, Song TZ, Zheng HY, Wang XH, Lu Y, Zhang HD, Li T, Pang W, Zheng YT. 2019. Superior intestinal integrity and limited microbial translocation are associated with lower immune activation in SIVmac239-infected northern pig-tailed macaques (*Macaca leonina*). *Zoological Research*, **40**(6): 522−531.

Zhang XL, Pang W, Hu XT, Li JL, Yao YG, Zheng YT. 2014. Experimental primates and non-human primate (NHP) models of human diseases in China: current status and progress. *Zoological Research*, **35**(6): 447−464.

Zheng YT, Yao YG, Xu L. 2014. Basic Biology and Disease Models of Tree Shrews. Kunming: Yunnan Science and Technology Press, 1–475. (in Chinese)

Zhong BY, Cheng B, Mai Y, Diao QC, Yin R. 2000. Study on the distribution of hair keratin in normal hair follicles by immunohistochemical staining. *Acta Academiae Medicinae Militaris Tertiae*, **22**(11): 1087−1089. (in Chinese)

Zouboulis CC, Picardo M, Ju Q, Kurokawa I, Törőcsik D, Bíró T, Schneider MR. 2016. Beyond acne: current aspects of sebaceous gland biology and function. *Reviews in Endocrine and Metabolic Disorders*, **17**(3): 319−334.

Zoological Research Editorial Board

EDITOR-IN-CHIEF

Yong-Gang Yao	Kunming Institute of Zoology, CAS, China

ASSOCIATE EDITORS-IN-CHIEF

Wai-Yee Chan	The Chinese University of Hong Kong, China
Xue-Long Jiang	Kunming Institute of Zoology, CAS, China
Yun Zhang	Kunming Institute of Zoology, CAS, China
Yong-Tang Zheng	Kunming Institute of Zoology, CAS, China

MEMBERS

Amir Ardeshir	University of California, Davis, USA
Yu-Hai Bi	Institute of Microbiology, CAS, China
Le Ann Blomberg	Beltsville Agricultural Research Center, USA
Kevin L. Campbell	University of Manitoba, Canada
Jing Che	Kunming Institute of Zoology, CAS, China
Ce-Shi Chen	Kunming Institute of Zoology, CAS, China
Jiong Chen	Ningbo University, China
Peng-Fei Fan	Sun Yat-Sen University, China
Michael H. Ferkin	University of Memphis, USA
Nigel W. Fraser	University of Pennsylvania, USA
Patrick Giraudoux	University of Franche-Comté, France
Cyril C. Grueter	The University of Western Australia, Australia
David Hillis	University of Texas at Austin, USA
Shiu-Lok Hu	University of Washington, USA
David Irwin	University of Toronto, Canada
Nina G. Jablonski	Pennsylvania State University, USA
Wei-Zhi Ji	Kunming Institute of Zoology, CAS, China
Xiang Ji	Nanjing Normal University, China
Jian-Ping Jiang	Chengdu Institute of Biology, CAS, China
Le Kang	Institute of Zoology, CAS, China
Julian Kerbis Peterhans	Roosevelt University, USA
Esther N. Kioko	National Museums of Kenya, Kenya
Randall C. Kyes	University of Washington, USA
Ren Lai	Kunming Institute of Zoology, CAS, China
David C. Lee	University of South Wales, UK
Shu-Qiang Li	Institute of Zoology, CAS, China
Wei Liang	Hainan Normal University, China
Hua-Xin (Larry) Liao	Duke University, USA
Si-Min Lin	Taiwan Normal University, China
Huan-Zhang Liu	Institute of Hydrobiology, CAS, China
Jian-Hua Liu	South China Agricultural University, China
Wen-Jun Liu	Institute of Microbiology, CAS, China
Meng-Ji Lu	University Hospital Essen, University DuisburgEssen, Germany
Masaharu Motokawa	Kyoto University Museum, Japan
Victor Benno Meyer-Rochow	University of Oulu, Finland
Nikolay A. Poyarkov, jr.	Lomonosov Moscow State University, Russia
Xiang-Guo Qiu	University of Manitoba, Canada
Rui-Chang Quan	Xishuangbanna Tropical Botanical Garden, CAS, China
Michael K. Richardson	Leiden University, The Netherlands
Christian Roos	Leibniz-Institute for Primate Research, Germany
Bing Su	Kunming Institute of Zoology, CAS, China
Kunjbihari Sulakhiya	Indira Gandhi National Tribal University, Amarkantak, India
John Taylor	University of Victoria, Canada
Christoph W. Turck	Max Planck Institute of Psychiatry, Germany
Wen Wang	Northwestern Polytechnical University, China
Fu-Wen Wei	Institute of Zoology, CAS, China
Jun-Hong Xia	Sun Yat-sen University, China
Guo-Jie Zhang	University of Copenhagen, Denmark
Ya-Ping Zhang	Chinese Academy of Sciences, China
Wu Zhou	The University of Mississippi, USA

ZOOLOGICAL RESEARCH
动物学研究
Bimonthly, Since 1980

Project for Enhancing International Impact of China STM Journals

2017
中国精品科技期刊
OUTSTANDING S&T JOURNALS OF CHINA

中国精品科技期刊 中国科技核心期刊 中国百强报刊

Editor-in-Chief: Yong-Gang Yao

Executive Editor-in-Chief: Yong-Tang Zheng

Editors: Su-Qing Liu Long Nie

Edited by Editorial Office of Zoological Research
(Kunming Institute of Zoology, Chinese Academy of Sciences, 32 Jiaochang Donglu, Kunming,
Yunnan, Post Code: 650223 Tel: +86 871 65199026 E-mail: zoores@mail.kiz.ac.cn)

Sponsored by Kunming Institute of Zoology, Chinese Academy of Sciences; China Zoological Society©

Supervised by Chinese Academy of Sciences

Published by Science Press (16 Donghuangchenggen Beijie, Beijing 100717, China)

Printed by Kunming Xiaosong Plate Making & Printing Co, Ltd

Domestic distribution by Yunnan Post and all local post offices in China

International distribution by China International Book Trading Corporation (Guoji Shudian) P.O.BOX 399,
Beijing 100044, China

Advertising Business License 广告经营许可证：滇工商广字66号

Domestic Postal Issue No.: 64-20

Price: 20.0 USD/100.0 CNY

ISSN 2095-8137